# Sheffield Hallam University

## A Sheffield Hallam University thesis

ProQuest Number: 10700895

ProQuest 10700895

# Coarse-Grained Computer Simulation of Fibre Self-Assembly

Pavel Prybytak

A thesis submitted in partial fulfilment of the requirements of

Sheffield Hallam University

for the degree of Doctor of Philosophy

January 2012

# Abstract

In this Thesis we present the results of a series of molecular computer simulation studies undertaken to investigate fibre self-assembly. The driving objective for this work has been to develop a generic coarse-grained model for peptide systems and examine its ability to exhibit free self-assembly of fibre structures at moderate computational cost.

Firstly, the development of a model is addressed. The model is based on mixtures of disc-like Gay-Berne and spherical Lennard-Jones particles. The discs represent single-site models of peptide molecules, whereas the spheres represent solvent particles. An additional parameter in the disc-sphere potential is introduced to adjust solvent quality. Using this model, depending on variables such as the solvent quality, formation of either chromonic stacks or chiral fibres is observed.

To explore the process of fibre self-assembly in more detail, larger systems are studied. Here, we find that, for a narrow temperature range, defect-free chiral fibres can freely self-assemble from an initially isotropic configuration. This occurs as a result of a complex multistage process, which can be controlled by adjusting the temperature. We study systems with different disc-disc interaction strengths and find that this parameter can be used to control the size and shape of a resultant fibre. We also investigate whether chiral fibres have a limiting radius.

Further, we introduce a modified version of the model in which the discs rims have both solvophobic and solvophilic regions. Depending on the relative sizes of these regions, a range of different structures are formed ('Toblerone', bilayer-sheet, cord, triple-helix). These complex structures comprise solvent particles as well as discs, and their variety can be understood from the geometries of the contributing particle types. The formation kinetics of these assemblies are also investigated.

*The Road Not Taken*

*Two roads diverged in a yellow wood,*
*And sorry I could not travel both*
*And be one traveler, long I stood*
*And looked down one as far as I could*
*To where it bent in the undergrowth;*

*Then took the other, as just as fair,*
*And having perhaps the better claim,*
*Because it was grassy and wanted wear*
*Though as for that the passing there*
*Had worn them really about the same,*

*And both that morning equally lay*
*In leaves no step had trodden black.*
*Oh, I kept the first for another day!*
*Yet knowing how way leads on to way,*
*I doubted if I should ever come back.*

*I shall be telling this with a sigh*
*Somewhere ages and ages hence;*
*Two roads diverged in a wood, and I -*
*I took the one less traveled by,*
*And that has made all the difference.*

*Robert Frost [1916]*

# Acknowledgements

# Advanced Studies

The following is a chronological list of related work undertaken and meetings attended during the course of study:

- IOP Winter School, Leeds, January 2009

- MERI Research Methods module, Sheffield Hallam University (2009)

- IOP Biological and Soft Matter Conference, Warwick University, April 2009

- MERI 1st Year Student Seminar Day (Poster Presentation)

- CCP5 Summer School Sheffield, University of Sheffield, July 2009 (Poster Presentation)

- NASQ Meeting, Warrington, 11 September 2009 (Oral Presentation)

- Course in MPI, HECTOR, Exeter, 14-16 September 2009

- MERI 2nd Year Student Seminar Day (Oral Presentation)

- CCP5 Annual Meeting, Sheffield Hallam University, 13-15 September 2010 (Oral Presentation)

- NSASM International Workshop, September 20-24, 2010, Dresden, Germany (Poster Presentation)

- BLCS Annual Conference, University of Nottingham, April 2011

- Geometry of Interfaces Conference, Primosten, Croatia, 3-7 October 2011

- CMMP Conference, Manchester, UK, 13-15 December 2011 (Oral Presentation)

# Contents

# Chapter 1

# Introduction

Due to their unique ability to undergo reversible and discontinuous system-wide phase change in response to different external physicochemical factors, fibre-forming systems have found broad application in various technological and biomedical applications. For example, hydrogels have been extensively used in the development of smart drug delivery systems. A hydrogel can be considered as a three-dimensional network of crosslinking fibres. Loaded with drug molecules these structures may release payload in response to changes in the local environmental conditions, such as pH, temperature, presence of small molecules or enzymes, and oxidising/reducing environment, among others. Hydrogels are also of great interest as a class of materials for use in tissue engineering and regeneration as they offer 3D scaffolds to support the growth of cultured cells. Another key application is in bio-sensing, where small chemical or physical changes in the sensing environment trigger macroscopically observable changes in material properties, thereby reporting the former, for example by gelation or nanoparticle assembly [1].

The practical importance of fibres' applications has attracted considerable attention to this class of materials. However, even though many experimental and theoretical studies have been performed on such systems, a complete understanding of their supramolecular structure and the way in which they form has yet to be

achieved. The relative complexity of the molecular units which form fibres via the processes of self-assembly, makes a full theoretical description of these systems a formidable challenge. Further, empirical observation of these macroscopic phenomena requires high spatial and temporal resolution, inaccessible to many experimental techniques. This means that computer simulation has the potential to be an effective tool here, bridging the gap between experiment and theory, and giving novel insights into the molecular basis of fibre formation.

## 1.1 Aims and Objectives

The work presented in this Thesis addresses the study of fibre self-assembly by means of molecular simulations. The aims of this study were set as follows:

- to research the self-assembly processes involved in fibre formation, in terms of a generic molecular model.

- to develop a generic coarse-grained model able to exhibit free self-assembly of fibre structures at moderate computational cost.

- to implement this model via an appropriate simulation strategy.

- to conduct a detailed study of fibre self-assembly using the developed model and associated analytical methodologies

## 1.2 Outline of the Thesis

The Thesis is organised in eight Chapters, including this brief introduction.

Chapter 2, considers experimental approaches used in the study of fibre self-assembly. Then, previous attempts to model fibre self-assembly using simulation techniques are reviewed. Attention is focussed on work which is relevant to the

results presented here, although some effort has been made to give a wider consideration.

Chapter 3 reviews computer simulation techniques relevant to the study performed here. A particular emphasis is placed on the Molecular Dynamics (MD) simulation method used in this project. This chapter also describes two important soft particle models: the Gay-Berne and Lennard-Jones model.

In chapter 4, model development and testing is described. An initial molecular model is introduced and preliminary results associated with this model are presented.

Following from these initial results, Chapter 5 presents comprehensive results of simulations of much larger systems. Systems with different parametrisations are studied and the resultant data are analysed. From this, a detailed description of the processes involved in fibre self-assembly is given.

In chapter 6, a modified version of the model is introduced in order to investigate self-assembly of aggregates which incorporate solvent particles within their structures. This modified model is then used to study how these composito-structures vary with model parametrisation. Following from these initial studies, Chapter 7 presents results of additional simulations of some of the systems from Chapter 6, conducted in constant NPT ensemble.

Finally, Chapter 8 summarises the main results of this thesis and presents conclusions and suggestions for future work.

# Chapter 2

# Studies of fibre self-assembly

The study of molecular self-assembly has become an active and diverse field of research, ranging from biomedicine and biotechnology to material science and nanotechnology. Understanding of the sequence-structure-properties relationships in self-assembling systems is crucial, in view of the rational design of new nano building blocks for biotechnological applications or new drugs. Special interest has been shown in self-assembling biodegradable materials based on proteins, polysaccharides and polypeptides [2]. This class of biological materials has considerable potential for a number of applications, including scaffolding for tissue repair in regenerative medicine, drug delivery and biological surface engineering [3]. A significant amount of existing research in the field of molecular self-assembly has been concentrated on peptide self-assembling systems. The relative simplicity of structure, simplicity in design and synthesis, make peptides an attractive model system for the study of fibre self-assembly.

## 2.1 Experimental studies of fibre self-assembly

Short aromatic peptides have been found to self-assemble into a number of different supramolecular structures such as straight hollow spherical structures, amyloid-like

fibres and nanotubes. These were first described by Reches and Gazit et. [4, 5]. Although a complete understanding of the self-assembly of these peptides has not yet been achieved, some intuition has been gained. For example, aromatic interactions (or $\pi - \pi$ interactions) are believed to play a key role in the formation of these structures. $\pi - \pi$ interactions are attractive interactions caused by intermolecular overlapping of p-orbitals in $\pi$-conjugated systems. Obviously, the larger the number of $\pi$-electrons, the stronger the interaction is. Thus, surfaces of flat aromatic rings tend to arrange themselves in stacks, contributing a free energy of formation, as well as order and directionality, to the self-assembly process [6]. Besides aromatic interactions, hydrogen bonds and ionic interactions are also present, but their contribution is less understood and explored.

Fmoc-dipeptides belong to a class of aromatic peptides. They comprise a Fmoc (9 -Fluorenylmethoxycarbonyl) protecting group and two chemical residues (the generic molecular structure of Fmoc-dipeptide is presented in Fig.2.1). By varying the chemistry of the residues, different peptides can be synthesised. For instance, if Phenylalanine is used as a residue Fmoc-Phenylalanine -Phenylalanine peptide will be synthesised. It is noteworthy that this peptide is believed to represent the smallest structural unit that can form typical amyloid-like fibres [6].
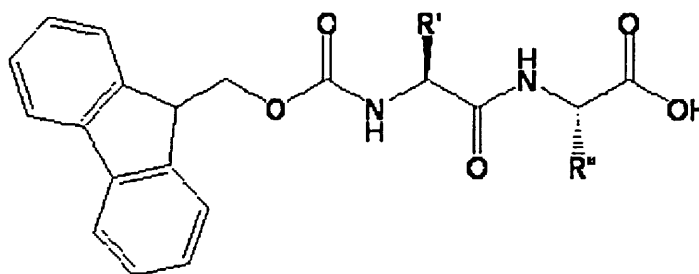


Figure 2.1:  Generic molecular structure of Fmoc-dipeptide.

The gelation behaviour of various Fmoc-dipeptides has been studied by Ulijn et al.[7], Xu et al.[8]. On changing the pH level, gel formation has been observed

for a range of these peptides, although in some cases (Fmoc-glycine-phenylalanine and Fmoc-glycine-threonine) no gelation was observed under any of the conditions tested, crystals being formed instead. CryoSEM images of the thus synthesized gels shows significant morphological variation (Fig. 2.2), indicating dependence on the amino acid sequence in the peptide. The diameters of the fibres that were observed by Ulijn et al.[7] for all peptides are summarized in Table 2.1.

| Fmoc-peptide | pH | Fibre diameter[nm] |
|:---:|:---:|:---:|
| $Gly - Gly$ | $< 4$ | $33 \pm 8$ |
| $Ala - Gly$ | $< 4$ | $30 \pm 6$ |
| $Ala - Ala$ | $< 4$ | $68 \pm 18$ |
| $Leu - Gly$ | $< 4$ | $22 \pm 5$ |
| $Phe - Gly$ | $< 4$ | $25 \pm 6$ |
| $Gly - Phe$ | $-$ | $-$ |
| $Phe - Phe$ | $< 4$ | $56 \pm 13$ |

Table 2.1:   Diameters of the Fmoc-dipeptide fibres presented in [7].
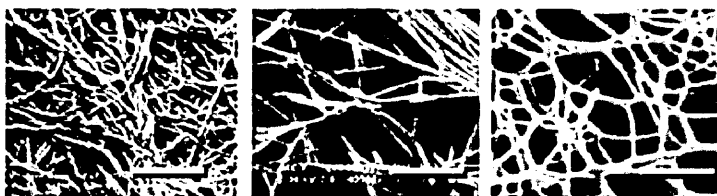


Figure 2.2:   Morphology of the Fmoc-dipeptide gels observed in [7].

The influence of the hydrophobicity of the Fmoc-dipeptides on their gel properties has been studied at Unilever Research. Storage moduli reported after 20hrs are plotted versus logP (hydrophobicity) in Fig. 2.3. These results further indicate that the molecular structure of peptide has a direct effect on the resultant gel properties.

The structure of the fibres formed by Fmoc-Phe-Phe peptide was also studied by Ulijn et al.[9]. Firstly circular dichroism (CD) was used to investigate the backbone orientation of the dipeptide within the hydrogel. Supported by Fourier transform infrared spectra (FT-IR) analysis of Fmoc-FF gel, these results indicated that molecules are predominantly in a $\beta$-sheet conformation and that the local arrangement of the peptides is possibly anti-parallel. Fluorescence spectroscopy indicated a

| Fmoc-peptide | $R_1$ | $R_2$ | LogP |
|---|---|---|---|
| $Ala - Gly$ | $CH_3$ | $H$ | 2.865 |
| $Ala - Val$ | $CH_3$ | $CH(CH_3)_2$ | 3.431 |
| $Val - Gly$ | $CH_3CH(CH_3)_2$ | $H$ | 3.644 |
| $Leu - Ala$ | $CH_2CH(CH_3)_2$ | $CH_3$ | 3.962 |
| $Phe - Ala$ | $CH_2Ph$ | $CH_3$ | 4.113 |
| $Leu - Gly$ | $CH_2CH(CH_3)_2$ | $H$ | 4.175 |
| $Phe - Gly$ | $CH_2Ph$ | $H$ | 4.326 |
| $Phe - Val$ | $CH_2Ph$ | $CH(CH_3)_2$ | 4.892 |
| $Leu - Phe$ | $CH_2CH(CH_3)_2$ | $CH_2Ph$ | 5.423 |

Table 2.2: Fmoc dipeptide sequence studied at Unilever Research along with their hydrophobicity (Log P).
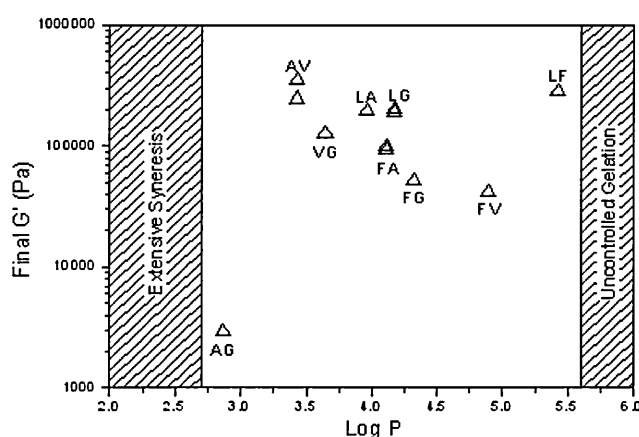


Figure 2.3: Storage moduli versus hydrophobicity for the dipeptides listed in Table 2.2.

large degree of $\pi - \pi$ stacking of the fluorenyl group, suggesting that aromatic interactions have a significant influence on fibre self-assembly. Based on these features, it was assumed that fibres are formed from twisted antiparallel $\beta$-sheets, interlocked via $\pi - \pi$ stacking of fluorenyl groups.

Detailed analysis of images obtained by transmission electron microscopy (TEM) showed that the gel is composed of an overlapping mesh of flat ribbons (Fig.2.4). Further examination of these ribbons by 2-D crystallographic analysis and wide angle X-ray scattering (WAXS) suggested that they are formed by single fibres of constant width placed side by side. The width of these individual fibres was found
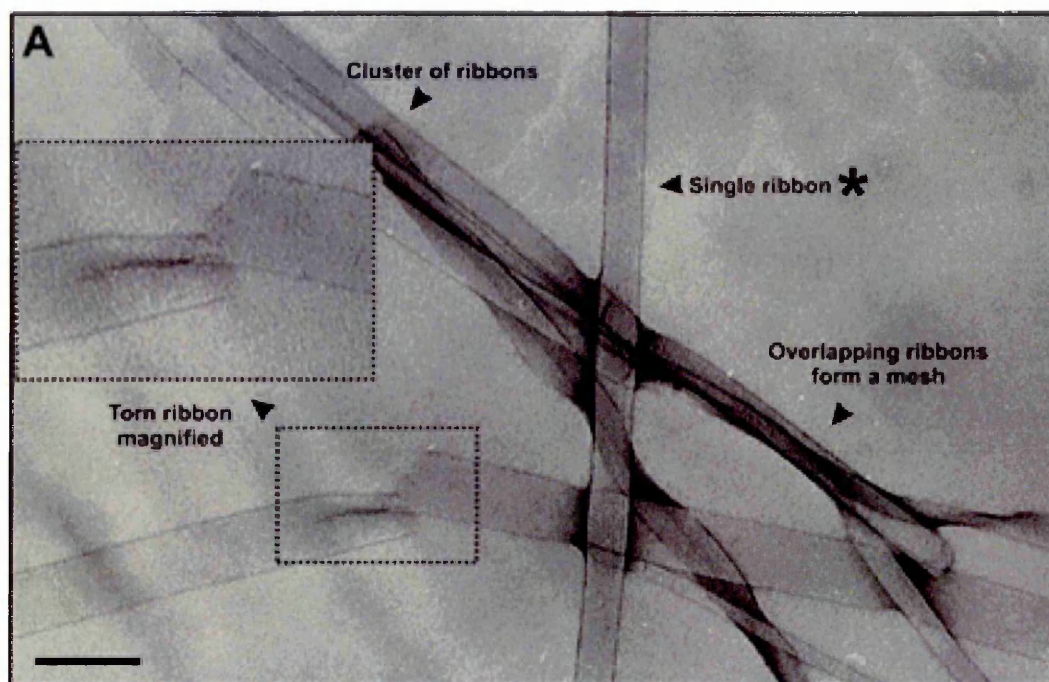
Figure 2.4: TEM image of Fmoc-Phe-Phe gel [9], showing an overlapping mesh of flat ribbons.

to be in good agreement with the proposed model structure of [9].

As can be seen from examples above, experimental techniques make it possible to study and analyse the structure of formed fibres. However little is known about the early-stages of fibres self-assembly, due to limitations of available resolutions. Nevertheless, some progress in this direction has been established. Different experimental reports suggest that fibre self-assembly is a multi-stage process involving distinct intermediate structures.

Within these, as a particular class, studies have focused on exploring formation of amyloid fibres. This is an important field of research, as an understanding of amyloid fibre self-assembly may be relevant to drug treatments for Alzheimer's and Parkinson's diseases [10, 11, 12]. This work showed that fibre formation is preceded by self-assembly of some intermediate structures (protofibres). These protofibres can be fractionated by gel-filtration chromatography and studied by electron microscopy, atomic force microscopy and X-ray fibre diffraction. There is a hypothesis that it may be these intermediate structure (protofibres) which are actually pathogenic,

but that later they detoxify by conversion to a fibre [11, 12].

An interesting example of combining experimental techniques with computer simulation to study fibre formation has been presented by M. Marini and co-workers [13]. They studied the self-assembly of the eight-residue peptide KFE8. Depending on the ionic strength of the solution, different rates of self-assembly could be achieved. The pH of the solution was, therefore, adjusted such that speed of self-assembly was considerably reduced, making it possible to study intermediate structures. AFM images and electron microscopy performed on quick-frozen aliquots taken from evolving solutions then confirmed the presence of left-handed helical ribbons a few minutes after preparation of the peptide solution. After 2 hours, the concentration of these ribbons decreased considerably and further assembly into bands of parallel filaments was observed. CD spectra collected over time indicated a steady increase in antiparallel $\beta$-sheet structures in the early stages, followed by decrease in the presence of random coils. This suggested that ribbons are intermediates in the formation of fibres. Various $\beta$-sheet configurations were constructed and their stability was tested by all-atom MD simulations. Dimension and pitch of the most stable simulated configuration was found to be in a good agreement with experimental measurements.

The pathway for the self-assembly of an $\alpha$-helical protein fibre was studied in [14] via a combination of solution-phase biophysical methods, microscopy, and peptide engineering. It was assumed that fibres form via a nucleation and growth mechanism (Fig.2.5). At first, by analysing CD spectra and analytical ultracentrifugation (AUC) data, it was concluded that when SAF peptides are mixed they combine rapidly (in less than seconds) to form sticky ended, partly helical heterodimers. After mixing is completed, and before fibrelogenesis begins, a lag phase follows. On the order of tens of minutes the system does not change spectroscopically (CD or LD) or visibly (TEM). This is characteristic of a nucleation process. Analysis of the concentration dependence of the growth curves, based on CD spectra data, was

used to estimate dimensionality of growth and the size of the nucleus. According to this analysis, the critical nucleus comprised six to eight partially folded dimers. After nucleation, subsequent linear fibre growth occured through both elongation and thickening. The first fibres were visible by TEM at 10 to 30 min. At later times (1-2 hours) it became possible to observe fibre elongation directly by LM. Additionally, a series of seeding experiments was conducted. In this, fragmented matured fibres were used as initial nuclei. These produced more and shorter fibres with increasing amounts of seed.
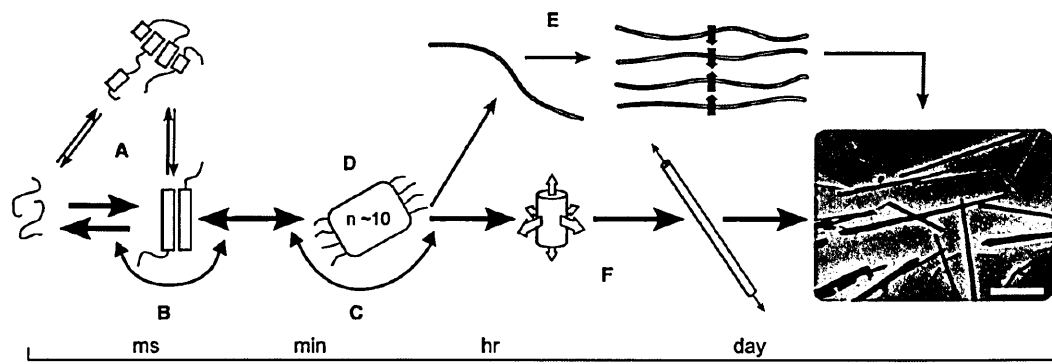


Figure 2.5: Schematic of possible pathways for fibre formation. (A) The two peptides may interact to form various oligomers that are competent for fibrelogenesis, or (B) the individual peptides may be competent for assembly. (C) Onward assembly may be immediately energetically favorable, or (D) further assembly may only be favorable once a critical nucleus has formed. (E) fibres may thicken via the bundling of fibres, or (F) the addition of material in both radial and longitudinal directions yields mature fibres as shown in the electron micrograph (scale bar: 5 $\mu$m). The pathway determined from the experiments described herein is shown in bold [14].

## 2.2  Computer simulations of fibre self-assembly

Self-assembled fibre nanostructures hold great promise for many applications. However, even though many experimental and theoretical studies have been performed on such systems, a complete understanding of their supramolecular structure and the way in which they form has yet to be achieved. The relative complexity of the molecular units which form fibres via the processes of self-assembly, makes a full theoretical description of these systems a formidable challenge. Further, empirical observation of these macroscopic phenomena requires high spatial and temporal resolution, inaccessible to many experimental techniques. This means that computer simulation has the potential to be an effective tool here, bridging the gap between experiment and theory, and giving novel insights into the molecular basis of fibre formation.

However, the inherent potential of this approach is limited by the time and length scales that can be accessed. Depending on the complexity of the building blocks and size of a system, the time scale of a processes such as fibre self-assembly is on the order of seconds, to minutes. In comparison, most MD simulations are limited to times on the order of nanoseconds. Statistical sampling (such as in MC simulation) would also require significant amount of computational resources due to the large configuration space needed to be explored in order to equlibrate and sample self-assembled nanostructure. Thus, a rigorous numerical study of this problem at the atomistic level is beyond the capability of modern computers. For this reason, in most of the presented full-atomistic simulations studies of molecular self-assembly, number of molecules (building blocks) used is limited to dozens and, in some cases, pre-assembled structures are used and tested for stability.

For instance, Chami and Wilson [15] explored the structure and dynamics of aggregates of the chromonic liquid crystal sunset yellow (SSY) in aqueous solution by carrying out a detailed atomic simulation. Here, eight SSY molecules were used

in MD simulations to study their self-assembly into a chromonic stack. Despite the number of molecules being small, it took 200 ns to observe system evolution from the initial dispersed state through formation of dimers and tetramers to development of single stack of eight molecules. Subsequently, using preformed 9 stacks of 16 molecules each, larger simulations were used to investigate chromonic columns with a loose hexagonal packing, corresponding to a nematic phase of SSY.

Often, an atomistic simulation is used just to verify the stability of a constructed (or preformed) nanostructures. Typically this approach involves constructing a wide variety of molecular packing geometries that are consistent with the dimensions found experimentally. Each of these is then evaluated by MD simulations to identify the most stable one [16, 17]. This approach enables determination of structural features as well as significant interactions that stabilize the nanofibre [18].

The limitations to time and length scales that inhibit study of the dynamics of self-assembly can be partially overcome by applying coarse-graining approaches. Coarse-graining consists of, e.g., replacing an atomistic description of a molecule with a lower-resolution (coarse-grained) model that averages and smoothes away atomistic details. The use of a coarse-grained representation of a system decreases the number of particles, degrees of freedom and interactions. This results in a considerable reduction in the computational effort required to generate physically meaningful configurations.

We consider application of this approach by analysing the example of propane coarse-graining. A propane molecule consists of 11 atoms: 3 carbon and 8 hydrogen atoms. Thus it has 30 degrees of freedom and 121 intermolecular interactions have to be calculated for each pair of molecules. In first level of approximation the number of interactions and degrees of freedom can be reduced by incorporating the hydrogen atoms into united (or heavy) atoms. In this representation, a propane molecule is described by 3 particles, and so it has 6 degrees of freedom and 9 intermolecular interactions. This step does not just decrease the number of interactions to be

calculated; it also excludes the high frequency motions of bonded hydrogen atoms and so allows for the use of a larger time step in simulations. Constraining bonds between united atoms means that two more high frequency motions can be removed, allowing further increase of the time step. Finally, the propane molecule can be represented by a single particle, which averages the behaviour of three united atoms. In this simplest representation, each molecule has three degrees of freedom and only one intermolecular interaction has to be calculated for each pair of molecules. Thus, different levels of coarse-graining can be achieved. Generally, the level chosen is dictated by the objectives of the simulations, or, in other words, by the physical and chemical properties which need to be present in the model. Once an appropriate level of coarse-graining has been chosen and united atoms have been determined, effective interactions between these coarse-grained sites have to be developed to encompass the essential properties of the system to be simulated.
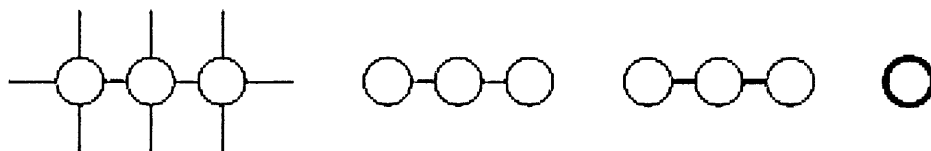
Figure 2.6:  Coarse-graining of propane.

A more contextual and involved example of coarse-grained model development is given by Marrink's work [19] developing an efficient model for lipid and surfactant systems. In this model, four-to-one mapping was used to represent the molecules, i.e. four united atoms were represented by a single interaction center. Four different coarse grained site types were defined to describe physicochemical properties of different moieties: thus combination of polar (P), nonpolar (N), apolar (C), and charged (Q) were taken to interact via Lennard-Jones (LJ) potentials of various strengths. In addition to these, charged groups interacted via the normal electrostatic Coulombic potential. To represent chain stiffness and bonded interactions

between chemically connected sites, weak harmonic potentials were used. The solvent was modeled explicitly, CG water molecules again interacting via a LJ potential. The proposed model was first verified by running bulk alkane simulations for butane, octane, dodecane, hexadecane, and eicosane (1 through 5 C particles, respectively). The results obtained for densities of liquid alkanes and mutual solubilities of alkanes in water and water in alkanes were found to be in good agreement with experimental values. Subsequently, the CG model for dipalmitoylphosphatidylcholine (DPPC) was shown to aggregate spontaneously into a bilayer. Structural, elastic, dynamic properties of the resultant self-assemblies matched the experimentally measured quantities closely. The distribution of the individual lipid components along the bilayer normal was also found to be very similar to those obtained from atomistic simulations. It was then demonstrated that phospholipids with different headgroup (ethanolamine) or different tail lengths (lauroyl, stearoyl) or unsaturated tails (oleoyl) could also be modelled with this same CG force field. Finally, the CG model was applied to nonbilayer phases. Dodecylphosphocholine (DPC) aggregated into small micelles that were structurally very similar to those modeled atomistically, and Dioleoylphosphatidylethanolamine (DOPE) formed an inverted hexagonal phase with structural parameters in agreement with experimental data. Thus, this CG model proved to be both versatile in its applications and accurate in its predictions, being computationally significantly more efficient (a gain of 3-4 orders of magnitude) than the fully atomistic version.

Nguyen and Hall at [20], following a previously proposed model [21], developed an intermediate-resolution CG model for polyalanine peptide Ac-KA14K-NH2. This model was extensively used in spontaneous fibre formation simulations. The results obtained were found to be in good qualitative agreement with experiments. Here, each amino acid residue was composed of four spheres (Fig.2.7): a three-sphere backbone comprised of united atom NH, $C_\alpha H$, and CO, and a single-bead sidechain R ($CH_3$ for alanines). Ideal backbone bond angles, $C_\alpha - C_\alpha$ distances, and residue

L-isomerization were achieved by imposing pseudobonds.
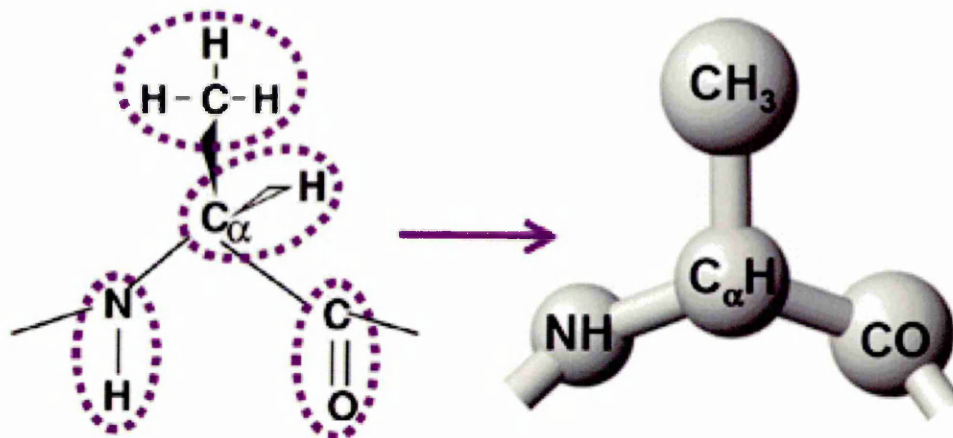


Figure 2.7: CG representation of alanine residue [21].

All forces were modelled by either hard-sphere or square-well potentials to ensure compatibility with discontinuous molecular dynamics (DMD). The solvent was modelled implicitly; its effect was factored into the energy function as a potential of mean force. Simulations indicated that fibre formation developed according to a certain sequence. Initially, the denatured peptide system stayed in a lag phase, during which some amorphous aggregates formed. These aggregates then dispersed into small $\beta$-sheets. Finally, the sheets aligned one by one, creating a small fibre, which then grew into a longer fibre (Fig.2.8).

Fibre growth was observed to occur by both $\beta$-sheet elongation and lateral addition. It was further found that fibrelization depends on temperature and peptide concentration: the critical temperature for forming fibres decreased with increasing peptide concentration. The strength of the hydrophobic interactions was also found to play an important role: depending on hydrophobicity, either fibres or amorphous structures were formed.

Bellesia and Shea [22] introduced a novel mid-resolution off-lattice coarse-grained model to investigate the self-assembly of $\beta$-sheet forming peptides. This model belongs to the same general type as Nguyen-Hall model, although it is more complex as molecular chirality was introduced via additional dihedral terms. The model was
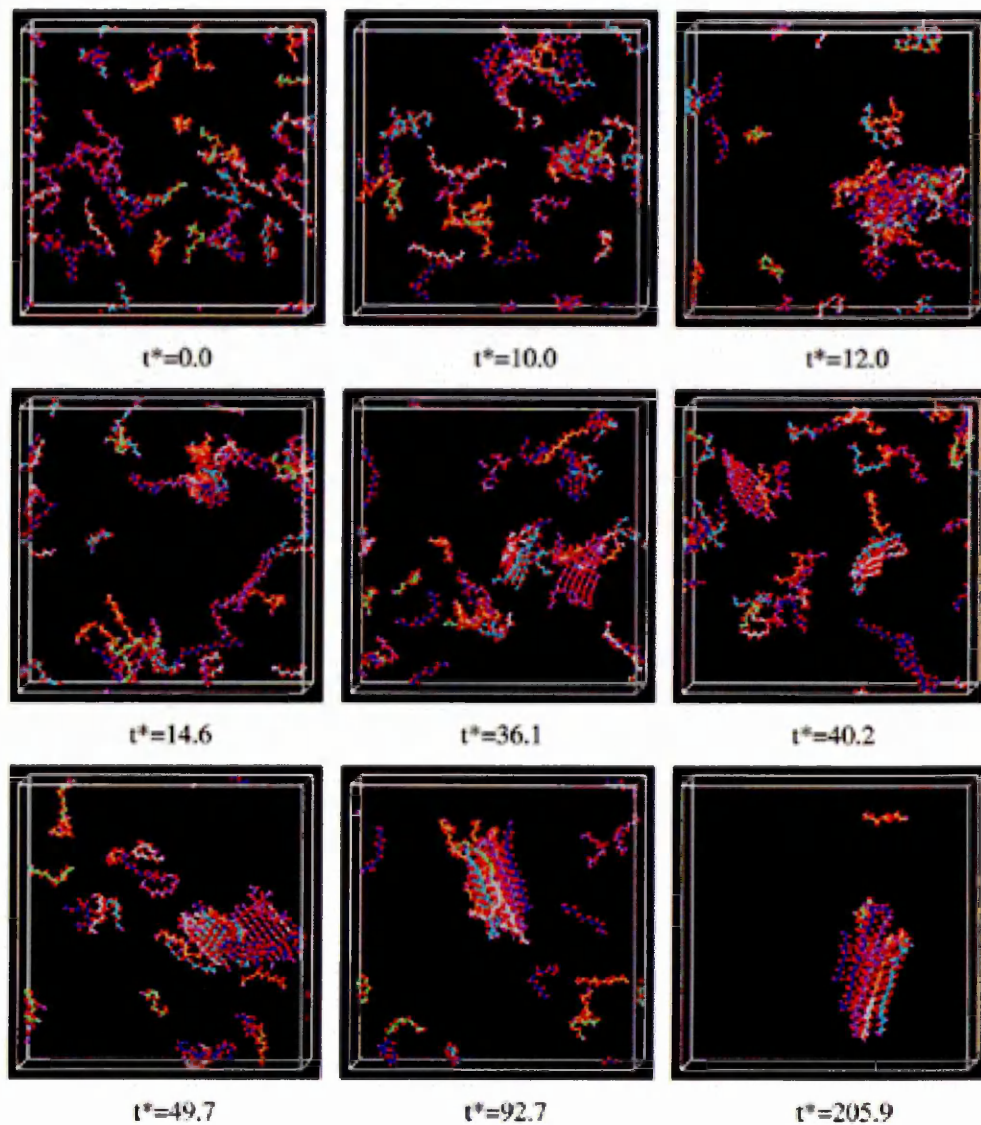
Figure 2.8: Fibrelisation process [21].

simple enough to permit the simulation of hundreds of peptides, yet detailed enough to enable the formation of twisted $\beta$-tapes, ribbons, and higher order aggregates (small protofibres consisting of triple and quadruple tapes)(Fig.2.9).

An alternative approach to bonded and nonbonded interaction potentials was used in [23, 24], where development of a CG model for diphenylalanine in aqueous solution was discussed. Here, interaction functions between CG beads were derived such that the resulting CG simulation reproduced the conformational sampling and the intermolecular interactions observed in an atomistic simulation. This is an ex-

(a)

(b)
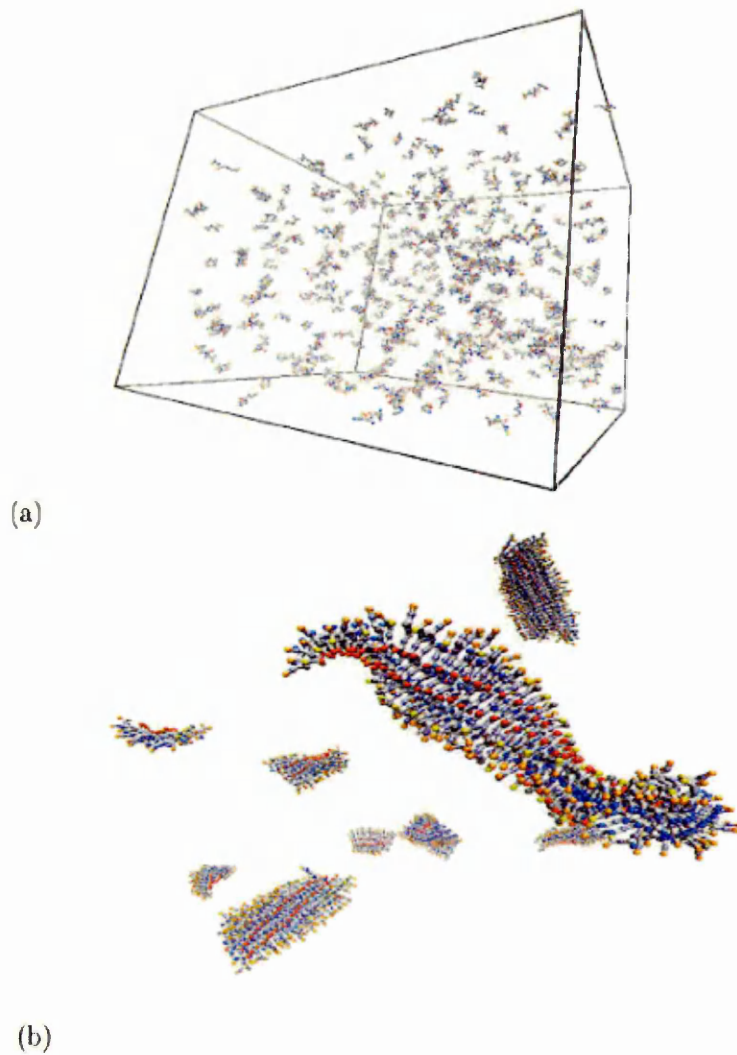
Figure 2.9: Snapshots obtained from molecular simulations: (a) starting configuration and (b) self-assembled fibrelar structures obtained from molecular simulations [22] .

ample of a so-called bottom-up approach to coarse-graining. Here, to derive bonded interaction potentials for the CG model, atomistic simulations of a single peptide in water were first performed. According to the mapping scheme, distributions of CG bond lengths, $P^{CG}(r, T)$, CG angles, $P^{CG}(\theta, T)$, and CG dihedral angles $P^{CG}(\phi, T)$ were then determined. These distributions were finally converted into potentials (potentials of mean force) through Boltzmann inversion:

$$U^{CG}(r, T) = -k_B T ln(P^{CG}(r, T)/r^2) + C_r \tag{2.1}$$

$$U^{CG}(\theta, T) = -k_B T ln(P^{CG}(\theta, T)/sin(\theta)) + C_\theta \tag{2.2}$$

$$U^{CG}(\phi, T) = -k_B T ln(P^{CG}(\phi, T)) + C_\phi \tag{2.3}$$

For the nonbonded interactions, potentials of mean force were calculated by thermally averaging over bead internal and solvent degrees of freedom from all-atom description simulation of a pair of peptides. The resultant CG model was used to simulate the self-assembly of dipeptides at finite concentration in solution. Despite being at least three orders of magnitude more efficient, the model results were found to be in very good agreement with those obtained using a detailed-atomistic force field model.

Another impressive example of using coarse-grained models to study self-assembly is the work on tethered nanoparticles performed by Glotzer and co-wokers [25]. This used a minimal model for nano building blocks determined as follows. For spherical nanoobjects, a nanoparticle was modeled as a single sphere of diameter $d$. Non-spherical nanoparticles, in contrast, were built by freezing $N_{np}$ spherical subunits (atoms) of diameter $\sigma$, separated by distance $l_0 = 0.97\sigma$, into the desired nanoparticle geometry.

A polymer tether was modeled as a bead-spring chain of $N_p$ monomers with diameter $\sigma$, neighboring monomers along the chain being connected by a FENE potential with average bond length $l_0$. Tethers were permanently connected to specific atoms on the nanoparticles via further FENE potential. Atoms or monomers of the same type were then taken to interact with a 12-6 Lennard-Jones (LJ) potential, whereas purely repulsive Weeks-Chandler-Andersen soft-sphere potentials were used to describe interactions between particles of different type.

Brownian dynamics simulations performed with this model showed that tun-

ing of thermodynamic parameters and architectural features of the nano building blocks can control aspects of local and global nanoparticle ordering. It was also demonstrated that the additional packing constraints, introduced by the nanoparticle geometries and the nano building block topologies, combined with tether and nanoparticle immiscibility, can lead to structures far richer than those known for conventional block copolymer, surfactant, and liquid-crystal systems (Fig.2.10).



(a)                                    (b)
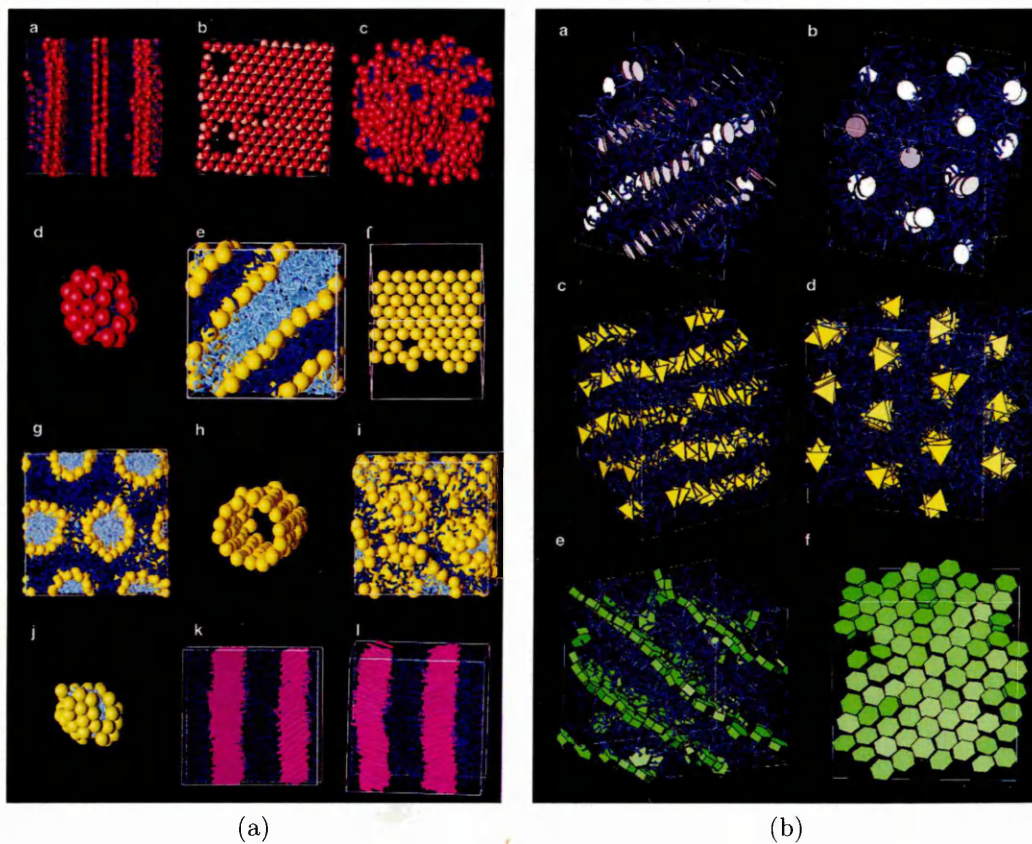
Figure 2.10: Equilibrium structures formed by tethered nanosphere and nanorod building blocks.

Often even more idealized coarse-grained models are used to study molecular self-assembly. For instance, in [26] two models for chromonic molecules were developed and studied. In the first of these, molecules were represented as diamond shaped assemblies comprising of 9 tangent spheres of diameter $\sigma$ rigidly bonded together (Fig.2.11). Here 7 spheres forming the central disc were taken to be hydrophobic, the 2 end spheres being hydrophilic. In the other variant, model chromonic molecules

were taken to be disk shaped and represented by 7 tangent spheres. Here, the 6 outer spheres were hydrophilic and the sphere at the center of each molecule was treated as hydrophobic. Water molecules were modeled as spheres. Attractive interactions between like particles (water-water, hydrophilic-water, and hydrophilic-hydrophilic) were modeled via LJ potentials. Repulsive hydrophobic-hydrophilic and water-hydrophobic interactions were modeled by a truncated and shifted LJ potential.
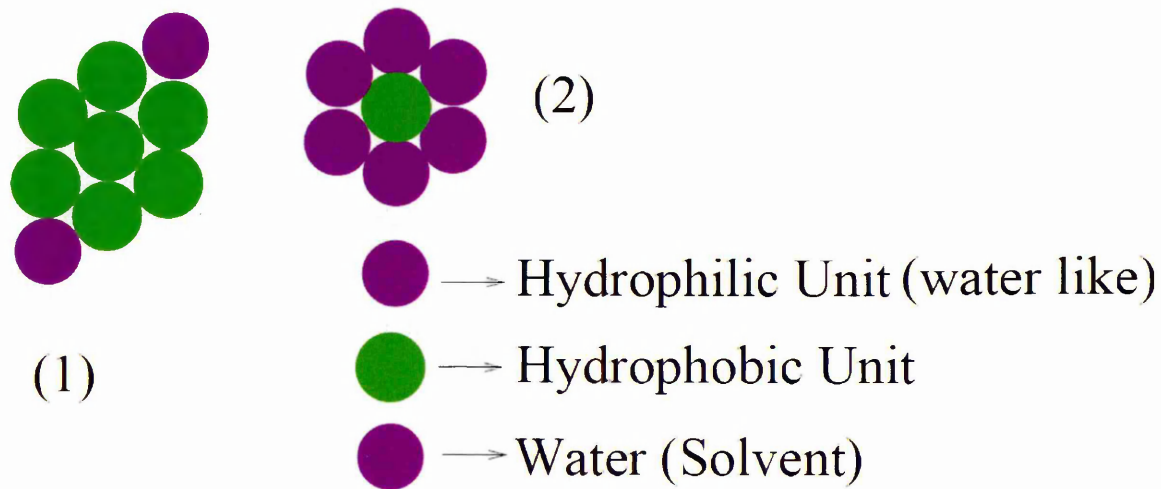


Figure 2.11: A schematic representation of the model chromonic and water molecules used in [26]

On carrying out Monte Carlo simulations with these models, lyotropic LC phases were observed in the first model. At low concentrations the chromonic molecules formed short columns and, with increase in concentration, the lengths and the number of columnar aggregates increased. In contrast, for the second model columnar aggregates proved to be highly unstable and the systems remained isotropic (Fig.2.12).

A closely related (in terms of geometry) model was studied previously by Henderson [27]. Here, the 6 outer spheres were also treated as solvent-like and inner sphere was treated as solvent-hating. However, all interactions were modeled by square-well potentials. The model was used to study the self-assembly of discotic amphiphiles.

(a)                                                    (b)
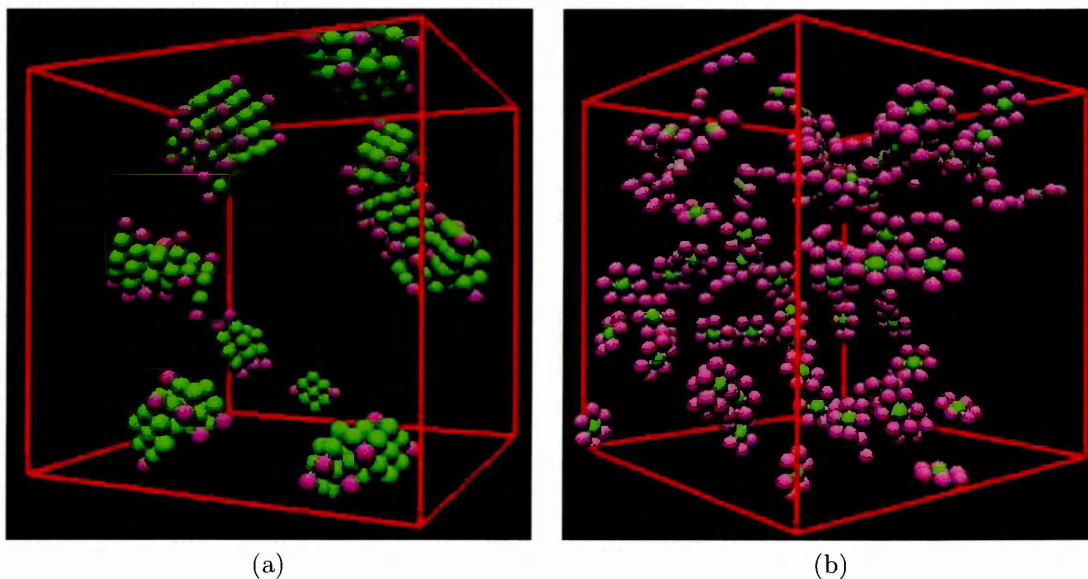
Figure 2.12: In [26] starting from an isotropic initial configuration columnar aggregates were formed by the diamond model (a). Simulations performed with model 2 did not generate columnar aggregates though (b).

The simulation results displayed a strong resemblance to experimentally studied behaviour of discotic solutions. In particular, both nematic and hexagonally ordered columnar phases were observed. Data collected from simulations were in agreement with theory of linear aggregation over a wide range of temperatures and concentrations.

Recently, Stedall, Hanna and co-wokers used CG simulation to study systems based on synthetic peptides (SAFs) [28]. The SAF system consists of two 28-residue $\alpha$-helical sequences that fold to form a helices. The peptide sequences form offset dimers with complementary sticky ends to promote longitudinal assembly into $\alpha$-helical coiled-coils, and, ultimately, fibres. Assembly of the peptide coils depends on specific interactions between the peptide sequences. Hydrophobic interactions between leucine and isoleucine residues stabilise the coiled coils and are supplemented by ionic interactions between glutamic acid and lycine. The offset in assembly is created by the inclusion of aspargines, which have a strong affinity to each other, at different sites on the two peptides.

Self-assembly of these peptides was modeled via coarse-grained representation

in which each peptide sequence was modelled as a rod, with $n$ interaction sites distributed along its length. The peptides, denoted AB and CD, had two distinct halves and, as such the model mimiced the design rules of the self-assembly of the real system where B bonds to C and A bonds to D. The interaction sites, thus, represent the hydrophobic and electrostatic interactions via a relatively simple ruleset.
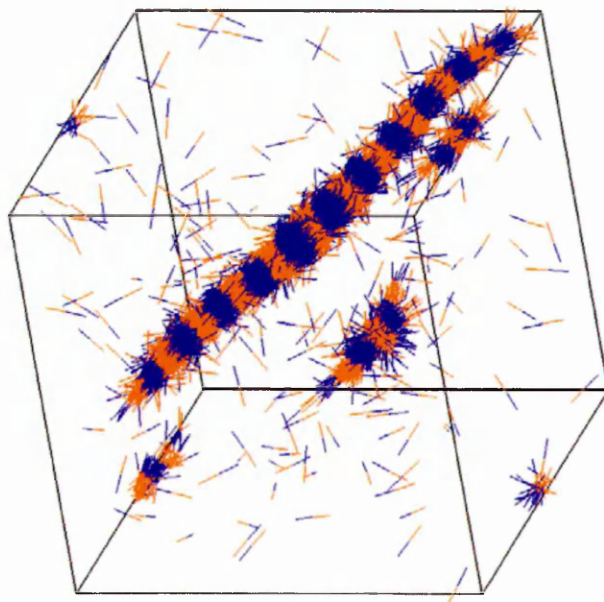


Figure 2.13: Example of fibre formation by homogeneous nucleation from dilute solution in a MC constant-$\mu$VT simulation [28]

Monte Carlo simulations showed that this CG rigid-rod model was able to reproduce some of the growth characteristics of fibres formed from $\alpha$-helical peptide sequences (Fig.2.13). In particular, it was found that lateral and longitudinal growth of the fibre are governed by different mechanisms. The lateral growth was diffusion limited with a very small activation energy for the addition of further units, whereas the longitudinal growth occured via a process of secondary nucleation at the fibre ends. As a result, longitudinal growth generally proceeded more slowly than lateral growth. It was also shown that the aspect ratio of the growing fibre could be controlled by changing temperature and the relative strengths of the AD and BC interactions.

Finally, there have been few recent studies exploring the fibre-forming capabilities of particles with disk-like symmetry. Bolhuis [29] presented coarse-grained model consisting of hard spheres of diameter $\sigma$, decorated with attractive interaction sites on their poles. This specially developed orientation-dependent patch potential not only allowed chain formation but also led to a weak chain-chain interaction. The potential between patches was given by a Lennard-Jones potential modulated by three directional components, favoring parallel alignment of patches.
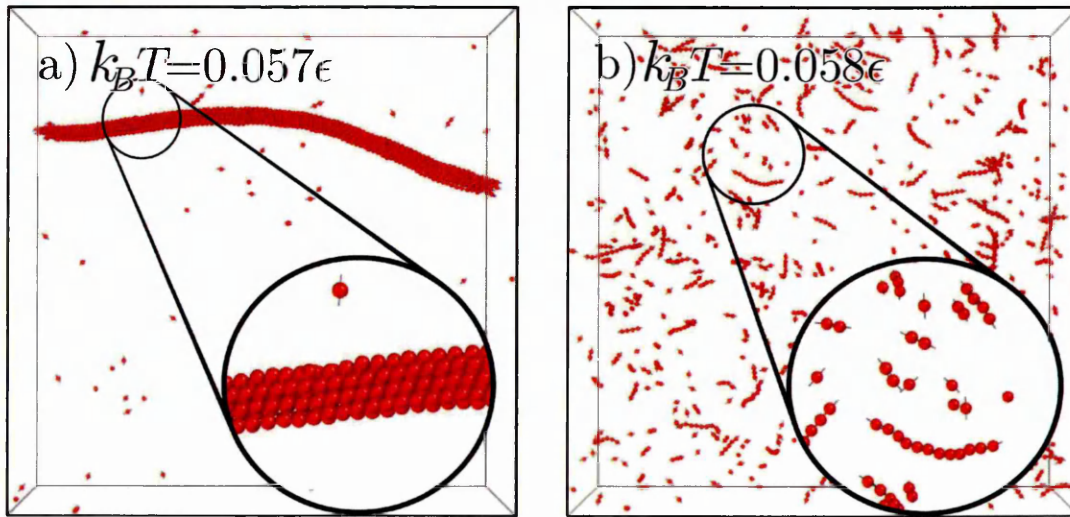


Figure 2.14: Representative configuration at two very close temperatures

Monte Carlo simulations of these patchy particles showed that, by decreasing temperature or increasing density polymerization into chains occurs. Subsequently these polymeric threads undergo a phase transition toward bundles or fibres (Fig.2.14). This bundling was interpreted as a sublimation transition between a polymer gas and a solid bundle. Due to the simplicity of the model used in these simulations, the authors said it was unlikely that their simple patchy particles could yield fibres with an intrinsically limited thickness. They did, though, state that patchy particles appeared to be a powerful tool for efficient modeling of complex, self-assembling systems and that their implementation could readily be improved by incorporating of more specific interactions.

Another example of using spherical patchy particles to study self-assembly is pre-

sented in [30]. In this work the authors studied the kinetic pathways of self-assembly of Janus spheres with hemispherical hydrophobic attraction. It was shown that isomers join to form highly ordered largescale structures, including helical structures. Dynamical interconversion between clusters occured through three major mechanisms: step-by-step addition of individual particles, fusion of smaller clusters into a larger one, and isomerization.

Li and co-workers developed a simple mesoscale simulation model in order to study self-assembly of soft disklike micelles in dilute solutions [31]. Their anisotropic potential was based on the conservative potential in DPD that incorporated some orientation dependence of the particles. It was expressed as:

$$U_{ij} = \frac{\alpha_{ij}^R}{2} \left(1 - r_{ij}\right)^2 - f^\nu \frac{\alpha_{ij}^A}{2} \left(r_{ij} - r_{ij}^2\right), \qquad (2.4)$$

where

$$f = \frac{\left(\mathbf{n}_i \cdot \mathbf{r}_{ij}\right)\left(\mathbf{n}_j \cdot \mathbf{r}_{ij}\right)}{r_{ij}^2} \qquad (2.5)$$

and $\mathbf{n}_i$ and $\mathbf{n}_j$ are unit vectors assigning the orientation to particle $i$ and $j$, respectively.

It was found that the so-defined DPD particles could pack into one-dimensional flexible threads. Depending on the solvent condition and concentration, these threads were found to further self-assemble into flexible hexagonal and twisted hexagonal bundles. However, there is considerable non-physical character in the potential, such as dimensional inconsistency in (2.4) and the absence of $\mathbf{n_i} \cdot \mathbf{n_j}$ term in (2.5). As such, the relevance of this work to experimentally realisable situations is questionable.

# 2.3   Conclusion

Experimental techniques (such as TEM, CryoSEM, AFM) allow direct observation of the growth of nucleated fibres, their elongation and thickening. It is also possible to make some assumptions about the arrangement of possible building blocks in final formed structure based on analysis of spectra data (CD, LD). However, these data describe only the late stages of fibre self-assembly. Key details of early-stage processes remain blocked to empirical observation, because of the inaccessibility of the required spatial and temporal resolution. On the other hand, detailed computer simulations of this problem are also beyond the capability of modern computers. Fully atomistic simulations (using MD or MC) are limited to relatively small sizes (a few dozen monomers), which are inadequate for processes occuring on larger scales. Application of coarse-graining approaches, allows for significant speed-up of simulations. As a result, not only can much larger systems be simulated, but also longer time scales can be accessed. This provides an opportunity to directly observe aggregation and nucleation of monomers into a various complex structures. Although atomistic detail is omitted in these simulations, previously obtained results show reasonable consistence, with both atomistic simulations and experiment. Thus, a coarse-graining approach appears to be a viable and reasonably effective approach to adopt to gain insights into the molecular basis of fibre formation.

# Chapter 3

# Computer simulation techniques

## 3.1 Molecular simulation techniques

Many techniques have been developed for the computer simulation of various physical and biological systems. Generally, the choice of simulation technique is governed by the specifics of the scientific problem being addressed. Often, the time and length scales of the processes occuring in the system are the key determining factors for this choice, as all simulations are limited by the acessible computational resources. Considering molecular self-assembling process, there are two main simulation methods that are extensively used to explore different molecular (and atomistic) systems: Molecular Dynamics (MD) and Monte Carlo (MC). For atomistic detail, MD is a more appropriate technique, as it provides essential information about a system's dynamics (as it works with approximation of the actual trajectories of the particles). The MC method, by contrast, is based on a statistical sampling of phase space, and involves accepting or rejecting randomly generated system states with an appropriate probability. Thus, due to its stochastic nature, time-dependent quantities cannot be analysed in this method. However, MC can be used to negotiate pathways over energy barriers which separate different system states and, thus, to explore phase space efficiently.

Simplification of a system description generally enables access to longer time scales and/or larger systems to be simulated. For instance, explicit calculations of solvent interactions (as in MD) are avoided in Brownian Dynamics method (BD) by treating the solvent as a viscous medium for the solvated particles. This is implemented by introducing stochastic (to account for the Brownian motion) and drag force terms into Newton's equation of motion together with the assumption that the average acceleration of a particle is small and can be neglected (non-inertial dynamics). The resultant first order differential equation can then be integrated with a timestep which is two to four times larger then those used in standard MD. Even longer time scales are accessible in the Dissipative particle dynamics (DPD) method, where the Navier-Stokes behaviour is emergent from large time-step simulation of simple interaction sites.

## 3.2   Molecular dynamics method

Molecular Dynamics is a computer simulation method in which a given sample is considered as a system of interacting particles. This approach often centres on modelling molecular motion. This is achieved by numerical integration of the classical equations of motion:

$$\frac{d^2}{dt^2}\left(m_i \mathbf{r}_i\right) = \mathbf{f}_i \tag{3.1}$$

$$\mathbf{f}_i = -\nabla_{r_i} U \tag{3.2}$$

where $m_i$ is the mass of molecule $i$ and $\mathbf{f}_i$ is the force acting on that molecule .

The basic form of a MD algorithm is as follows:

step 1: set up the parameters that specify the conditions of the run (e.g., initial temperature, pressure, time step) and initialise the system (i.e., give all atoms initial positions and velocities)

step 2: calculate the forces on all particles

step 3: integrate the equations of motion, using the forces calculated on step 2

Steps two and three are then repeated until the system has been equilibrated for the desired length of time.

## 3.2.1 Initialisation

As was mentioned above, MD simulations are started by assigning initial positions and velocities to all particles in the system. The first of these should be implemented in such a way that particles do not overlap significantly. In practice this is often achieved by placing the particles on a low density cubic lattice. In most cases, this cubic lattice is mechanically unstable and melts rapidly to some amorphous configuration.

The velocities may be assigned randomly from a Gaussian distribution, to achieve required initial temperature of the system. For example, for the $x$-component of velocity, this has the following form:

$$\rho\left(v_{ix}\right) = (m_i/2\pi k_B T)^{\frac{1}{2}} \, exp\left(-\frac{1}{2}m_i v_{ix}^2/k_B T\right) \tag{3.3}$$

Alternatively, a uniform distribution can be used, as the Maxwell-Boltzmann distribution of velocities will naturally become established by molecular collisions processes within some equilibration time.

A desired temperature for a system $T$ can be achieved by scaling all velocities with a factor $(T/\mathcal{T})^{\frac{1}{2}}$, where $\mathcal{T}$ is the instantaneous temperature.

In some cases, it is appropriate to use the final configuration from previously performed simulations to initiate a new run (e.g. to explore evolution of the system under different thermodynamic conditions).

### 3.2.2 Integration algorithm

The Velocity-Verlet algorithm is the most popular algorithm for the integration of the equations of motion [32, 33]. Being computationally efficient, it allows long-term energy conservation to be achieved; this is a crucial characteristic for any integration scheme. For translational motion, velocities $\mathbf{v}_i(t)$ and positions $\mathbf{r}_i(t)$ are updated according to the following expressions:

$$\mathbf{v}_i\left(t + \frac{dt}{2}\right) = \mathbf{v}_i(t) + \mathbf{a}_i(t)\frac{dt}{2} \tag{3.4}$$

$$\mathbf{r}_i(t + dt) = \mathbf{r}_i(t) + \mathbf{v}_i\left(t + \frac{dt}{2}\right)dt \tag{3.5}$$

After the forces (and updated accelerations $\mathbf{a}_i(t + dt)$) have been computed, the velocities are updated again:

$$\mathbf{v}_i(t + dt) = \mathbf{v}_i\left(t + \frac{dt}{2}\right) + \mathbf{a}_i(t + dt)\frac{dt}{2} \tag{3.6}$$

To integrate the equations of rotational motion of objects with biaxial symmetry, the method of quaternions can be applied. A quaternion $\mathbf{Q}$ is a set of four scalar quantities

$$\mathbf{Q} = (q_0, q_1, q_2, q_3) \tag{3.7}$$

satisfying the constraint

$$q_0^2 + q_1^2 + q_2^2 + q_3^2 = 1 \tag{3.8}$$

and in the Euler angle convention defined as

$$q_0 = cos\frac{1}{2}\theta cos\frac{1}{2}(\varphi + \psi) \tag{3.9}$$

$$q_1 = sin\frac{1}{2}\theta cos\frac{1}{2}(\varphi - \psi) \tag{3.10}$$

$$q_2 = sin\frac{1}{2}\theta sin\frac{1}{2}(\varphi - \psi) \tag{3.11}$$

$$q_3 = cos\frac{1}{2}\theta sin\frac{1}{2}(\varphi + \psi) \tag{3.12}$$

Rotation of a molecule now can be described in terms of quaternions by the rotation matrix $\mathbf{A}$, which connects body-fixed $\mathbf{u}^b$ and space-fixed coordinates $\mathbf{u}^s$

$$\mathbf{u}^b = \mathbf{A(Q)}\mathbf{u}^s \tag{3.13}$$

where $\mathbf{A(Q)}$ is defined as

$$\mathbf{A} = \begin{pmatrix} q_0^2 + q_1^2 - q_2^2 - q_3^2 & 2(q_1q_2 + q_0q_3) & 2(q_1q_3 - q_0q_2) \\ 2(q_1q_2 - q_0q_3) & q_0^2 - q_1^2 + q_2^2 - q_3^2 & 2(q_2q_3 + q_0q_1) \\ 2(q_1q_3 + q_0q_2) & 2(q_2q_3 - q_0q_1) & q_0^2 - q_1^2 - q_2^2 + q_3^2. \end{pmatrix} \tag{3.14}$$

In terms of quaternions, rotational motion of a molecule is described by the following expression:

$$\dot{\mathbf{Q}} \equiv \begin{pmatrix} \dot{q}_0 \\ \dot{q}_1 \\ \dot{q}_2 \\ \dot{q}_3 \end{pmatrix} = \frac{1}{2} \begin{pmatrix} q_0 & -q_1 & -q_2 & -q_3 \\ q_1 & q_0 & -q_3 & q_2 \\ q_2 & q_3 & q_0 & -q_1 \\ q_3 & -q_2 & q_1 & q_0 \end{pmatrix} \begin{pmatrix} 0 \\ \omega_x^b \\ \omega_y^b \\ \omega_z^b \end{pmatrix} \tag{3.15}$$

where $\omega$ is the angular velocity (in the body-fixed coordinates). It is more convenient to represent the last equation in a shortened form $\dot{\mathbf{Q}} = \frac{1}{2}M_{\alpha\beta}W_\beta$.

The equations of rotational motion in quaternion form are obtained from the Euler equations for a rigid body:

$$\dot{\omega}_x^b = N_x/I_x + \omega_y^b\omega_z^b(I_y - I_z)/I_x,$$

$$\dot{\omega}_y^b = N_y/I_y + \omega_z^b\omega_x^b(I_z - I_x)/I_y, \tag{3.16}$$

$$\dot{\omega}_z^b = N_z/I_z + \omega_x^b \omega_y^b (I_x - I_y)/I_z$$

where $\mathbf{N}$ is the torgue and $\mathbf{I}$ is the inertia moment tensor (in the principal frame). Expressing angular velocities in quaternion form, using (3.15), taking derivatives and substituting these into the Euler equations (3.17) the following equation is obtained

$$\ddot{\mathbf{Q}} = \frac{1}{2}M_{\beta\gamma}\mathcal{T}_\gamma - \mathbf{Q}_\beta(\dot{\mathbf{Q}}_\alpha^T\dot{\mathbf{Q}}_\alpha). \tag{3.17}$$

where $\mathcal{T}$ is the right-hand side of eq. (3.17) with $\mathcal{T}_4 = 0$. Finally, the integrator for $Q_\alpha$ takes the form [34]:

$$Q_\alpha(t + dt) = Q_\alpha(t) + \dot{Q_\alpha}(t)dt + \ddot{Q_\alpha}(t)\frac{dt^2}{2} + f_\alpha(t)\frac{dt^2}{2}. \tag{3.18}$$

Here $f_\alpha$ is a constraint force with the form $f_\alpha = -2\Lambda Q_\alpha$. The condition $Q_\alpha Q_\alpha = 1$ leads to an explicit expression for the coefficient $\Lambda$:

$$(dt)^2\Lambda = 1 - s_1(dt)^2/2 - \sqrt{1 - s_1(dt)^2 - s_2(dt)^3 - (s_3 - s_1^2)(dt)^4/4}, \tag{3.19}$$

where $s_1 = \dot{\mathbf{Q}} \cdot \dot{\mathbf{Q}}$, $s_2 = \dot{\mathbf{Q}} \cdot \ddot{\mathbf{Q}}$ and $s_3 = \ddot{\mathbf{Q}} \cdot \ddot{\mathbf{Q}}$.

The values for $\dot{\mathbf{Q}}$ and $\ddot{\mathbf{Q}}$ are updated accordingly to (3.15) and (3.17) respectively, with angular velocities obtained by solving the Euler equations, Eqs. (3.17).

## 3.3 Practical aspects

### 3.3.1 Boundary conditions and the minimum image convention

In seeking to make efficient use of finite computational resources, most MD simulation utilise systems with relatively small numbers of particles ($10^2$ to $10^6$ particles, compared to $10^{23}$ particles in real systems). In such systems, a significant propor-

tion of the particles are close to the boundaries. Thus, the choice of the boundary conditions is important and should be made so as to minimize its influence on the properties of the system. One of the choices of boundary conditions that is often made in simulations is periodic boundary conditions. In this, the simulation box is treated as a primitive cell of an infinite periodic lattice of its own identical images. This is implemented in practice by applying a simple rule: when a particle crosses one side of the simulation box, its image reappears on the opposite side with the same velocity.

The interactions between particles in these periodic cells are computed accordingly to the 'minimum image convention': a particle from a given cell interacts with the nearest 'image' of a second particle from the neighbouring boxes. For short-range interactions, it is reasonable to truncate potentials beyond a certain cutoff distance $r > r_c$, thereby neglecting weak interactions between particles. An additional requirement is that size of the simulation box $L$ must satisfy the condition $L > 2r_c$ to prevent particles from interacting with two images of any other particle.

### 3.3.2 Verlet Neighbour list

As mentioned above, it is very common to impose an interaction cutoff distance in simulations. In this case, the condition $r < r_c$ should be checked for each pair of particles during the force calculation loop. Considering any individual particle, however, it is clear that many of the particles in the system will not lie within its cutoff distance $r_c$ and that the number of non-interacting particles will grow with increasing system size. Thus, the standard loop procedure is low-efficiency, as it includes a large amount of pointless but computationally expensive operations.

The efficiency of the force calculation loop can be improved, though, by use of the Verlet neighbour list. The basic idea of this approach is that particles with finite velocities will not move too far from their initial positions during a finite timestep. Thus, for each individual particle, a list of neighbour particles, which are within some

distance $r_v > r_c$, can be created. Now, during the force calculation loop, only pairs of particles in this neighbour list need to be considered. Obviously, particles can leave and enter this defined space, so neighbour lists need to be updated occasionally by removing 'old' and adding 'new' particles respectively.

An appropriate value for $r_v$ is best determined in the context of simulation, rather than being predicted in advance. Its value controls the frequency of neighbour list updating. If $r_v$ is too small, then the neighbour list will be updated unnecessarily often. If it is too big, then too many unnecessary comparison operations $(r < r_c)$ will be included in the force calculation loop.

### 3.3.3  Observable Quantities

The aim of any MD or MC simulation is to provide information about the many body properties of a given sample. These thermodynamic and structural properties are often reflected in such quantities as the potential energy, temperature, pressure, orientational order parameter and others. Calculation of all such quantities is based on the ergodic hypothesis, that is that the ensemble average of a given macroscopic property can be obtained by the the time averaging of its instantaneous values. In unperturbed, bulk systems, the potential energy is defined by the sum of all pairwise potentials in the system:

$$E_{pot} = \sum_{i=1}^{N} \sum_{j>i}^{N} U_{ij} \tag{3.20}$$

The total kinetic energy is defined as the sum of the translational and rotational kinetic energies of individual particles:

$$E_{kin} = \sum_{i=1}^{N} \frac{m\mathbf{v_i}^2}{2} + \sum_{i=1}^{N} \frac{I\omega_i^2}{2} \tag{3.21}$$

**Temperature** in the system can be defined in accordance with the equipartition theorem: on average an energy $\frac{1}{2}k_B T$ is associated with each harmonic translational and rotational degree of freedom. Thus, the kinetic temperature $T$ of the mixture

of $N_{disc}$ discs and $N_{sph}$ spheres can be found from the following equation:

$$\sum_{i=1}^{N_{sph}} \frac{m_{sph}\mathbf{v_i}^2}{2} + \sum_{i=1}^{N_{disc}} \frac{m_{disc}\mathbf{v_i}^2}{2} + \sum_{i=1}^{N_{disc}} \frac{I\omega_i^2}{2} = \left(\frac{5}{2}N_{disc} + \frac{3}{2}N_{sph}\right)k_BT \qquad (3.22)$$

**Pressure** is calculated using the virial theorem:

$$P = \rho k_BT + \frac{1}{3V}\sum_{i=1}^{N}\sum_{j>i}^{N}\mathbf{r_{ij}} \cdot \mathbf{F_{ij}} \qquad (3.23)$$

**Orientational order parameter** describes an orientational properties of the system. It is defined as the largest eigenvalue of the $Q$-tensor:

$$Q_{\alpha\beta} = \frac{1}{N}\sum_{i=1}^{N}\left(\frac{3}{2}\hat{\mathbf{u}}_{i\alpha} \cdot \hat{\mathbf{u}}_{i\beta} - \frac{1}{2}\delta_{\alpha\beta}\right) \qquad (3.24)$$

**Moment of inertia** is a measure of an object's resistance to changes to its rotation. It encompasses not only the overall mass of an object, but also the distribution of component masses within the object. Thus, the moment of inertia can be used to characterise an object's shape.

For a rigid object comprising $N$ point masses $m_i$, the moment of inertia tensor (with respect to the origin) has components given by:

$$\mathbf{I} = \begin{bmatrix} I_{11} & I_{12} & I_{13} \\ I_{21} & I_{22} & I_{23} \\ I_{31} & I_{32} & I_{33}. \end{bmatrix} \qquad (3.25)$$

where:

$$I_{11} = I_{xx} = \sum_{i=1}^{N} m_i\left(y_i^2 + z_i^2\right),$$

$$I_{22} = I_{yy} = \sum_{i=1}^{N} m_i\left(x_i^2 + z_i^2\right),$$

$$I_{33} = I_{zz} = \sum_{i=1}^{N} m_i \left( x_i^2 + y_i^2 \right),$$

$$I_{12} = I_{xy} = \sum_{i=1}^{N} m_i x_i y_i, \tag{3.26}$$

$$I_{13} = I_{xz} = \sum_{i=1}^{N} m_i x_i z_i,$$

$$I_{23} = I_{yz} = \sum_{i=1}^{N} m_i y_i z_i.$$

There is a Cartesian coordinate system in which moment of inertia tensor is diagonal, having the form:

$$\mathbf{I} = \begin{bmatrix} I_1 & 0 & 0 \\ 0 & I_2 & 0 \\ 0 & 0 & I_3. \end{bmatrix} \tag{3.27}$$

where the coordinate axes are called the principal axes and the constants $I_1, I_2$ and $I_3$ are called the principal moments of inertia. When all principal moments of inertia are distinct, the principal axes through center of mass are uniquely specified.

**Radial distribution function** (or pair correlation function) $g(r)$ is an another important measure to use to characterise the local structure of a material sample. This function gives the probability of finding a pair of atoms at a distance $r$, relative to the probability expected for a completely random distribution at the same density. In the canonical ensemble, $g(r)$ is defined as:

$$g(\mathbf{r_1}, \mathbf{r_2}) = \frac{N(N-1)}{\rho^2 Z_{NVT}} \int d\mathbf{r_3} d\mathbf{r_4}...d\mathbf{r_N} exp\left( -\beta V(\mathbf{r_1}, \mathbf{r_2}, ...\mathbf{r_N}) \right). \tag{3.28}$$

An equivalent definition takes an ensemble average over pairs:

$$g(r) = \rho^{-2} \left\langle \sum_i \sum_{j \neq i} \delta(\mathbf{r_i}) \delta(\mathbf{r_j} - \mathbf{r}) \right\rangle = \frac{V}{N^2} \left\langle \sum_i \sum_{j \neq i} \delta(\mathbf{r} - \mathbf{r_{ij}}) \right\rangle. \tag{3.29}$$

This last form may be used to calculate $g(r)$ in computer simulations. Numerical results for the radial distribution function can be compared with experimentally obtained information about $g(r)$ (the neutron, the X-ray scattering diffraction data) and thus to be used to test model interaction types and parameters.

**Reduced Units**

For reasons of simplicity, convenience and numerical stability, physical quantities in computer simulations are often expressed in reduced units instead of dimensional ones. The choice of these reduced units is usually closely related to ceratain key parameters of the model. For instance, it is convenient to set the particle's mass to be a unit of mass, as then acceleration is numerically equal to the acting force and so expensive division operation can be omitted. Obviously, if a system has some characteristic length $\sigma_0$ and energy $\epsilon_0$ parameters, it is also convenient to measure all distances in units of $\sigma_0$ and energies in units of $\epsilon_0$. For unchanged system, once these reduced units have been defined, all other quantities should be expressed in accord with these. For instance, the unit of temperature becomes $\epsilon_0/k_B$, where $k_B$ is Boltzmann's constant, the unit of time is equal to $\sqrt{m\sigma_0^2/\epsilon_0}$ and the unit of pressure is $\epsilon_0/\sigma_0^3$.

## 3.4 Intermolecular model potentials

### 3.4.1 Lennard-Jones potential

Realistic interactions between molecules include both attractive and repulsive components. These are mimicked using simple approximation in so-called soft particle models in which the potential comprises an attractive tail at large intermolecular separations and a short range repulsive core.

The Lennard-Jones potential is one of the simplest and widely used examples of such models. It describes the interaction between a pair of neutral, spherical particles as:

$$U_{LJ}(r) = 4\epsilon \left[ \left(\frac{\sigma}{r}\right)^{12} - \left(\frac{\sigma}{r}\right)^{6} \right], \tag{3.30}$$

where $\epsilon$ is the depth of the potential well, $\sigma$ determines the separation of repulsion and $r$ is the interparticle distance.
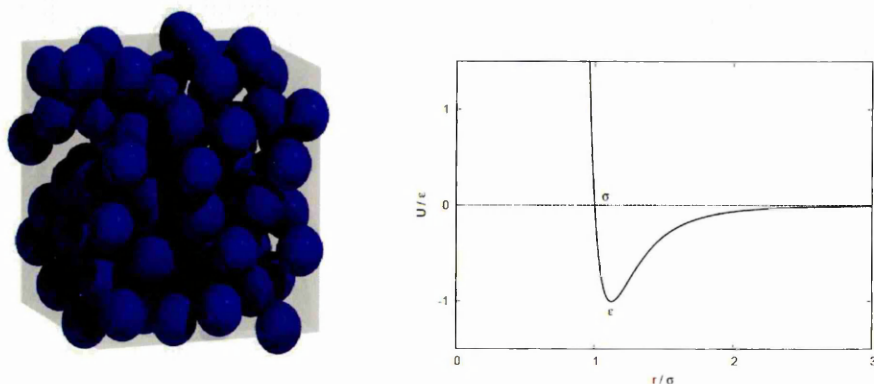


Figure 3.1:  LJ Potential model graph.

The $\left(\frac{1}{r}\right)^{6}$ term describes attraction at intermediate range and comes from the leading term in the quantum-mechanical solution for non-polar, neutral atoms with spherically symmetric electron shells, like e.g. noble gas atoms. The $\left(\frac{1}{r}\right)^{12}$ term describes repulsion at short intermolecular distances, however, unlike attraction term, it does not have any explicit theoretical basis. It is basically an approximation of repulsive interactions and the choise of inverse twelfth power is largely a matter of pragmatism: as the $\left(\frac{1}{r}\right)^{12}$ term is simply the square of $\left(\frac{1}{r}\right)^{6}$, it is easy to compute. Use of this functional form allows to reduce computational costs, maintaining reasonable fit to realistic interatomic potentials at the same time.

### 3.4.2    Gay-Berne potential

Considering each atom as a Lennard-Jones site, one can make a fully-atomistic representation of a given molecule and use this to run reasonably realistic simulations of different molecular systems.  However, in most cases, this approach incurs a

significant computational cost in cases where large system size and simulation time are needed.

To model anisotropic molecules as single-site objects (instead of as multi-site molecules made of Lennard-Jones particles), Gay and Berne [35] proposed an efficient model for representing anisotropic molecular interactions. In this approach, the molecules are represented as soft 'rod-shaped' particles interacting via the Gay-Berne potential. The Gay-Berne potential in itself is a Lennard-Jones type potential with an angular dependence of the shape and energy parameters ($\sigma$ and $\epsilon$ correspondingly). It takes the form:

$$U^{GB}(\mathbf{r_{ij}}, \mathbf{\hat{u}_i}, \mathbf{\hat{u}_j}) = 4\epsilon(\mathbf{\hat{r}_{ij}}, \mathbf{\hat{u}_i}, \mathbf{\hat{u}_j}) \left[ \left( \frac{\sigma_0}{r_{ij} - \sigma(\mathbf{\hat{r}_{ij}}, \mathbf{\hat{u}_i}, \mathbf{\hat{u}_j}) + \sigma_0} \right)^{12} - \left( \frac{\sigma_0}{r_{ij} - \sigma(\mathbf{\hat{r}_{ij}}, \mathbf{\hat{u}_i}, \mathbf{\hat{u}_j}) + \sigma_0} \right)^{6} \right], \quad (3.31)$$

where $\mathbf{\hat{u}_i}$ and $\mathbf{\hat{u}_j}$ are unit vectors describing molecular orientations.
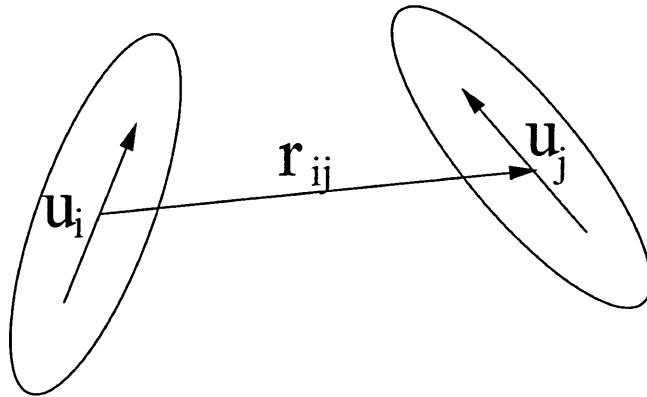


Figure 3.2: Schematic representation of Gay-Berne particles.

The shape and energy parameters are defined, respectively, by:

$$\sigma(\mathbf{\hat{r}_{ij}}, \mathbf{\hat{u}_i}, \mathbf{\hat{u}_j}) = \sigma_0 \left[ 1 - \frac{\chi}{2} \left\{ \frac{(\mathbf{\hat{r}_{ij}} \cdot \mathbf{\hat{u}_i} + \mathbf{\hat{r}_{ij}} \cdot \mathbf{\hat{u}_j})^2}{1 + \chi(\mathbf{\hat{u}_i} \cdot \mathbf{\hat{u}_j})} + \frac{(\mathbf{\hat{r}_{ij}} \cdot \mathbf{\hat{u}_i} - \mathbf{\hat{r}_{ij}} \cdot \mathbf{\hat{u}_j})^2}{1 - \chi(\mathbf{\hat{u}_i} \cdot \mathbf{\hat{u}_j})} \right\} \right]^{-1/2} \quad (3.32)$$

and

$$\epsilon(\hat{\mathbf{u}}_i, \hat{\mathbf{u}}_j) = \epsilon_0 \left[\epsilon_1(\hat{\mathbf{u}}_i, \hat{\mathbf{u}}_j)\right]^\nu \left[\epsilon_2(\hat{\mathbf{r}}_{ij}, \hat{\mathbf{u}}_i, \hat{\mathbf{u}}_j)\right]^\mu \qquad (3.33)$$

with

$$\chi = \frac{(\sigma_e/\sigma_s)^2 - 1}{(\sigma_e/\sigma_s)^2 + 1}. \qquad (3.34)$$

where $\sigma_e$ and $\sigma_s$ are the length and the diameter of the molecule, respectively, and $\sigma_0$ and $\epsilon_0$ are constants.

The terms $\epsilon_1$ and $\epsilon_2$ in the equation for the energy parameter are defined by:

$$\epsilon_1(\hat{\mathbf{u}}_i, \hat{\mathbf{u}}_j) = \left[1 - \chi^2(\hat{\mathbf{u}}_i \cdot \hat{\mathbf{u}}_j)^2\right]^{-1/2}. \qquad (3.35)$$

$$\epsilon_2(\hat{\mathbf{r}}_{ij}, \hat{\mathbf{u}}_i, \hat{\mathbf{u}}_j) = 1 - \frac{\chi'}{2} \left\{ \frac{(\hat{\mathbf{r}}_{ij} \cdot \hat{\mathbf{u}}_i + \hat{\mathbf{r}}_{ij} \cdot \hat{\mathbf{u}}_j)^2}{1 + \chi'(\hat{\mathbf{u}}_i \cdot \hat{\mathbf{u}}_j)} + \frac{(\hat{\mathbf{r}}_{ij} \cdot \hat{\mathbf{u}}_i - \hat{\mathbf{r}}_{ij} \cdot \hat{\mathbf{u}}_j)^2}{1 - \chi'(\hat{\mathbf{u}}_i \cdot \hat{\mathbf{u}}_j)} \right\} \qquad (3.36)$$

where

$$\chi' = \frac{(\epsilon_{ss}/\epsilon_{ee})^{1/\mu} - 1}{(\epsilon_{ss}/\epsilon_{ee})^{1/\mu} + 1}. \qquad (3.37)$$

The parameter $\epsilon_{ss}$ is the depth of the potential for a pair of parallel molecules arranged side-to-side and $\epsilon_{ee}$ is equivalent depth for two parallel molecules arranged end-to-end.

Having an extended set of parameters and being relatively simple model at the same time, the Gay-Berne model is one of the most flexible and computationally efficient models for liquid crystal (LC) simulation [36, 37, 38]. Depending on the chosen shape and energy parameterisation, it can be used to model many different LCs, from linear mesogens to discotic molecules [39, 40] and pear-shaped particles

[41]. For example, the exponents $\mu$ and $\nu$ were originally adjusted to obtain a good fit to the linear four site Lennard-Jones potential. From the same comparison it was found that the elongation of the molecule $\sigma_e/\sigma_s$ should be set to 3, and $\epsilon_{ss}/\epsilon_{ee}$ to 5. A system with $(\sigma_e/\sigma_s = 3; \epsilon_{ss}/\epsilon_{ee} = 5; \mu = 1; \nu = 2)$ parametrisation was studied by Luckhurst et al. [42]. These subsequent simulations demonstrated that the model is able to form a number of different phases, including isotropic, nematic, smectic A, smectic B and crystalline phases. Later, Luckhurst and Simmonds [43] determined an alternative set of parameters to represent the molecule of p-terphenyl, which has a molecular structure typical of many mesogens. Here parameters (4.4; 39.6; 0.74; 0.8)were obtained by fitting the Gay-Berne potential to the contours of a biaxially averaged set of multi-site interaction potentials. Simulations showed that the isotropic and nematic phases, dominated by short range repulsion, are controlled by the shape parameter, whereas the stability of the $S_A$ was critically dependant on the anisotropy in the energy terms.

### 3.4.3 Generalized Gay-Berne potential

Cleaver et al. [44] proposed a generalisation of the Gay-Berne potential for the interaction between two unlike molecules. The shape parameter in the generalised form was found to be:

$$\sigma(\hat{\mathbf{r}}_{ij}, \hat{\mathbf{u}}_i, \hat{\mathbf{u}}_j) = \sigma_0 \left[ 1 - \frac{\chi}{2} \left\{ \frac{(\alpha \hat{\mathbf{r}}_{ij} \cdot \hat{\mathbf{u}}_i + \alpha^{-1} \hat{\mathbf{r}}_{ij} \cdot \hat{\mathbf{u}}_j)^2}{1 + \chi(\hat{\mathbf{u}}_i \cdot \hat{\mathbf{u}}_j)} + \frac{(\alpha \hat{\mathbf{r}}_{ij} \cdot \hat{\mathbf{u}}_i - \alpha^{-1} \hat{\mathbf{r}}_{ij} \cdot \hat{\mathbf{u}}_j)^2}{1 - \chi(\hat{\mathbf{u}}_i \cdot \hat{\mathbf{u}}_j)} \right\} \right]^{-1/2}$$

$$(3.38)$$

Parameters $\chi$ and $\alpha$ here are functions of $l_i, l_j, d_i$ and $d_j$ and, thus, depend on particle shapes. For example, if particle $i$ is a sphere of diameter $d$, so $l_i = d_i = d$, both $\chi$ and $\alpha$ go to zero. The shape parameter, nevertheless, remains finite in this limit and tends to:

$$\sigma(\hat{\mathbf{r}}_{ij}, \hat{\mathbf{u}}_j) = \sigma_0 \left[ 1 - \frac{l_j^2 - d_j^2}{l_j^2 + d^2} (\hat{\mathbf{r}}_{ij} \cdot \hat{\mathbf{u}}_j)^2 \right]^{-1/2}. \tag{3.39}$$

The energy parameter $\epsilon$ in this case is given by:

$$\epsilon(\hat{\mathbf{r}}_{ij}, \hat{\mathbf{u}}_j) = \epsilon_0 \left[ 1 - \left( 1 - \left( \frac{\epsilon_E}{\epsilon_S} \right)^{1/\mu} \right) (\hat{\mathbf{r}}_{ij} \cdot \hat{\mathbf{u}}_j)^2 \right]^{\mu}. \tag{3.40}$$

where the ratio $\epsilon_E/\epsilon_S$ determines the well-depth anisotropy of the interaction.

The form (3.39) was first noted in an aside in Berne and Pechukas original paper [45]. It was understood that there is a continuous route between the rod-rod and rod-sphere shape parameters, corresponding to a gradual shrinking of one of the rods to a sphere. The behaviour of this class of system was investigated through a comprehensive simulation study by Antypov [46]. This showed the effects of adding small spherical particles to a fluid of rods which would otherwise represent a liquid crystalline substance[47].

## 3.4.4   Discotic Gay-Berne potential

A discotic Gay-Berne potential can be derived from original Gay-Berne potential (3.31) simply by considering that a disc is a 'rod-shaped' particle with diameter $d$ being greater than its length $l$. In addition, the $\epsilon_f/\epsilon_e$ ratio can be altered to reflect the relative attractions between two molecules. Obviously, there are three possible variants. If $\epsilon_f > \epsilon_e$, the face-to-face interaction will be enhanced and one can expect the system to have propensity to form a columnar phase. Secondly, if $\epsilon_f < \epsilon_e$, the discs will tend to align such that the edge-to-edge interaction is enhanced; this attraction may conceivably lead to a layered or smectic phase. A third possibility may arise if there is no anisotropy in the attractive forces for parallel molecules ($\epsilon_f = \epsilon_e$); here, it might be expected that only a nematic mesophase will be observed, as is the case for hard ellipsoids and Berne-Kushick-Pechukas particles.

However, it was found that the Gay-Berne potential, given by (3.31), when

parametrized for discs, exhibits unrealistic behavior at small $r$. It is easy to show that, for all arrangements of a pair of molecules, except for the edge-to-edge, the $\sigma(\hat{\mathbf{r}}_{\mathbf{ij}}, \hat{\mathbf{u}}_{\mathbf{i}}, \hat{\mathbf{u}}_{\mathbf{j}})$ term is less than the particle breath $\sigma_e$ and so the potential energy only tends to infinity at negative, unphysical separations. To correct this unrealistic feature, a modified version of the potential was proposed by Bates and Luckhurst [48], where the potential is shifted and scaled by $\sigma_f$ rather than $\sigma_e$:

$$
U_{ij}(\mathbf{r}_{\mathbf{ij}}, \hat{\mathbf{u}}_{\mathbf{i}}, \hat{\mathbf{u}}_{\mathbf{j}}) = 4\epsilon(\hat{\mathbf{r}}_{\mathbf{ij}}, \hat{\mathbf{u}}_{\mathbf{i}}, \hat{\mathbf{u}}_{\mathbf{j}}) \left[ \left( \frac{\sigma_f}{r_{ij} - \sigma(\hat{\mathbf{r}}_{\mathbf{ij}}, \hat{\mathbf{u}}_{\mathbf{i}}, \hat{\mathbf{u}}_{\mathbf{j}}) + \sigma_f} \right)^{12} - \left( \frac{\sigma_f}{r_{ij} - \sigma(\hat{\mathbf{r}}_{\mathbf{ij}}, \hat{\mathbf{u}}_{\mathbf{i}}, \hat{\mathbf{u}}_{\mathbf{j}}) + \sigma_f} \right)^{6} \right] , \tag{3.41}
$$

where $\sigma_f$ defines the thickness of the discs [48].

Figure (3.3) shows the distance dependence of the potential energy for both versions of discotic Gay-Berne potential. It is clear that the modified version posseses many of the same features as the original one (strong face-to-face attraction, distances at which the attractive and repulsive terms cancel). However, the well widths for the modified Gay-Berne model are significantly narrower.
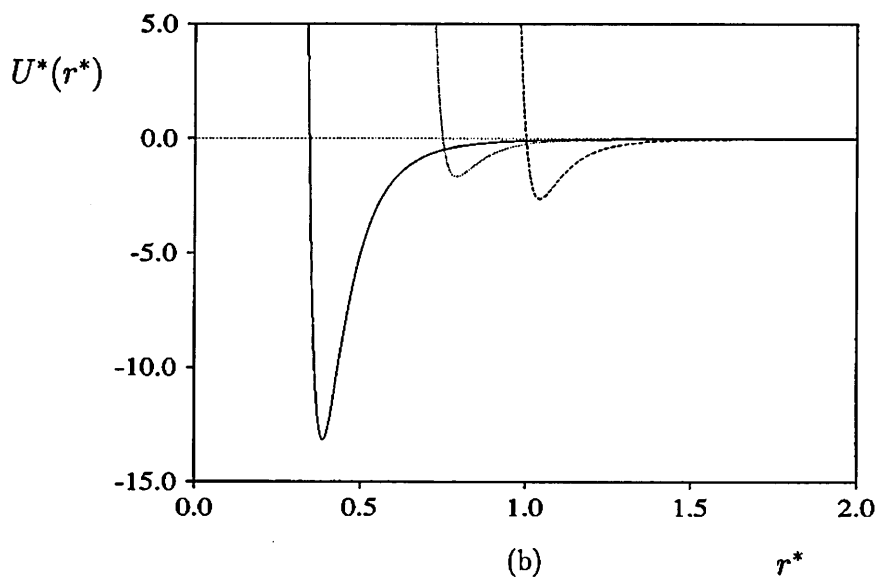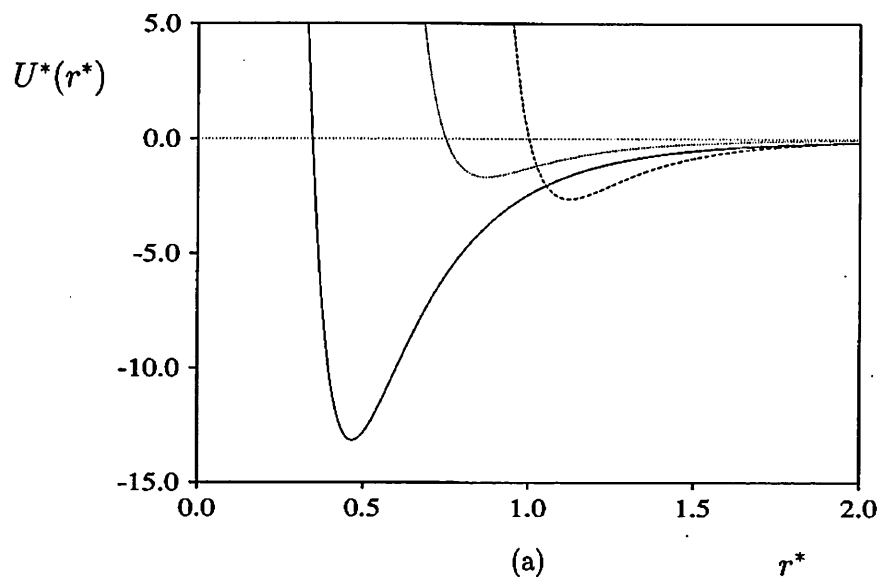
Figure 3.3: Original (a) and Modified (b) discotic Gay-Berne potential for the parametrization $\sigma_f/\sigma_e = 0.345$ , $\epsilon_f/\epsilon_e = 5.0$, $\mu = 1$ and $\nu = 2$; the three curves shown correspond to the face-to-face (solid line), the edge-to-edge (dashes) and the face-to-edge or tee (points) [48]

# Chapter 4

# Preliminary Results

## 4.1 Model Development and Testing

A significant amount of time was spent in the development, testing and modification of an initial MD code with which to conduct some preliminary simulations. The first step was to develop an efficient, bug-free integrator - the central part of MD code. This was achieved by running a series of test NVE (constant energy) simulations. Starting from simple systems (pure LJ spheres systems), and moving to more complex (pure discotic, rod-sphere systems, where rotational motions should be considered) total energy conservation was checked. It was found that for both short times (10 time steps) and long times (few million time steps) the total energy deviations were within $5 \cdot 10^{-5}$ units of energy per particle or 0.003% of the average. This provides confidence that this central part of the MD code was bug-free and both translational and rotational moves were treated correctly.

The second major stage of code development was to improve its efficiency. As was discussed in a previous chapter, the Verlet neighbour list is an effective method to save computational time in the main force calculation loop. After implementation of this technique and performing a series of test simulation runs, results were compared with data obtained with earlier version of the code. As expected, all

observable values (energies, temperature, order parameter) were reproduced; at the same time significant speed-up was achieved (up to 40%). At a later stage, to speed-up simulations of large system sizes, a parallel version of the code was implemented (replica-exchange method, using MPI (Message Passing Interface) library).

After development of the model basis, it was decided to run some preliminary simulations to test not only the numerical values but the physics. To validate the developed code, MD NVT (constant temperature) simulations of a 50/50 rod-sphere mixture system, containing 1000 particles in total, were performed. This type of system had been previously simulated by Antypov [46] and Michel [49]. So as to enable qualitative comparisons to be made between the results sets, the same parameterization was chosen: $\epsilon = 1, \sigma = 1, \sigma_e/\sigma_s = 3, \epsilon_{ss}/\epsilon_{ee} = 5, \kappa' = 5, \epsilon_E = 0.2, \epsilon_S = 1$.
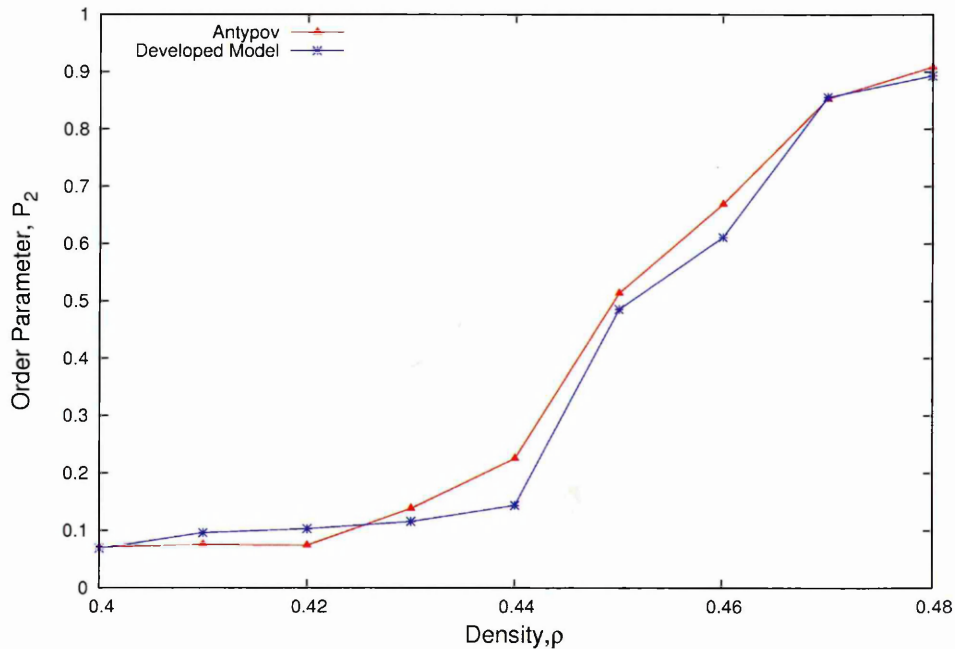


Figure 4.1: Orientational order parameter vs. density for a 50/50 rod-sphere mixture at $T = 0.7$. Results from our code are compared with those achieved previously by Antypov [46].

Starting from low density, a $\rho = 0.22$ system was slowly (by steps of $d\rho = 0.01$) compressed up to density $\rho = 0.48$, keeping temperature constant (T=0.7). At each density, the orientational order parameter was measured for $2 \cdot 10^5$ timesteps
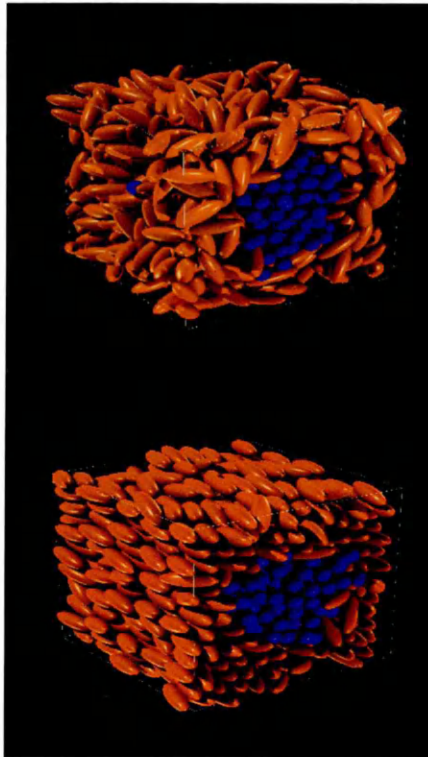
Figure 4.2: Isotropic ($\rho = 0.42$) (top) and LC phase ($\rho = 0.47$) (bottom) for a 50/50 rod-sphere mixture at $T = 0.7$

preceeded by $3 \cdot 10^5$ timesteps of equilibration. The simulations indicated a strong orientational ordering transition in the system, which can be clearly seen (at $\rho = 0.44$) in Fig.4.1, where orientational order parameter vs. density data are presented. Two configuration snapshots taken below and above this transition density are shown on Fig.4.2, suggesting isotropic-smectic transition occured. These results are in excellent agreement with those obtained by Antypov [46] and Michel [49].

To validate the developed code for discotic interactions an additional set of test runs were performed. Here, the aim was to reproduce the well-known and trusted results obtained for discotic Gay-Berne systems by Bates and Luckhurst [48]. In these simulations, systems of 500 discotic particles were cooled down from high temperature and their phase behaviour observed. We used the same range of scaled pressures ($P$=25, 50, 75 and 100) in our simulations as were used in the original paper [48]. At each pressure, the system was found to exhibit isotropic, nematic and columnar mesophases. The transitions between these phases were located from discontinuities

in the second rank order parameter, combined with a visual inspection of configuration snapshots. For instance, the initial ordering transition temperature for the $P = 25$ system was at $T = 2.8$, corresponding to a sharp order parameter rise from 0.13 to 0.38 (Fig.4.3). A second transition at temperature $T = 2.5$ was identified from a sharp change in the gradient of the order parameter vs. temperature data (Fig.4.3).

Configuration snapshots taken at near-transition temperatures confirm that this system underwent isotropic-nematic and nematic-discotic transitions at these temperatures (Fig.4.4). The pressure dependence of the transition temperatures (Fig.4.3-Fig.4.8) was subsequently investigated. These results were found to be in good qualitative and quantitative agreement with those obtained by Bates and Luckhurst et [48] (Fig.4.9). The window of nematic stability broadened and shifted to higher tmperatures with increase in pressure. Again in agreement with Bates and Luckhurst, noticable hysteresis was seen in these systems at the columnar-nematic transition (Fig.4.3-Fig.4.7). Reassuringly, despite our use of a different simulation technique (in comparison to Bates and Luckhurst [48], where MC method was used) and methods for treating rotational motions in the developed model (in comparison to Antypov [46] and Michel [49]) essentially identical results have been obtained.
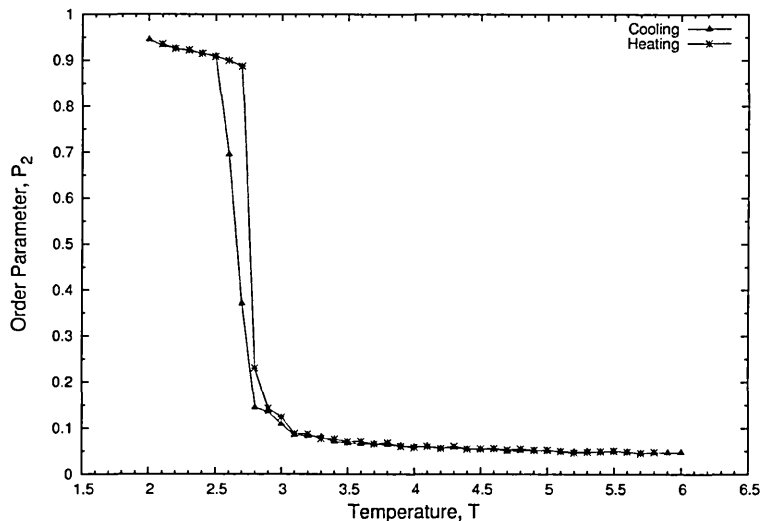


Figure 4.3: Order Parameter vs Temperature for $N = 500$ GB discs, P=25

Figure 4.4: Snapshots from NPT simulation of a 500 particle pure-disc system: isotropic ($T = 3.1$, top), nematic ($T = 2.6$, middle) and discotic phases ($T = 2.3$, bottom) at P=25.
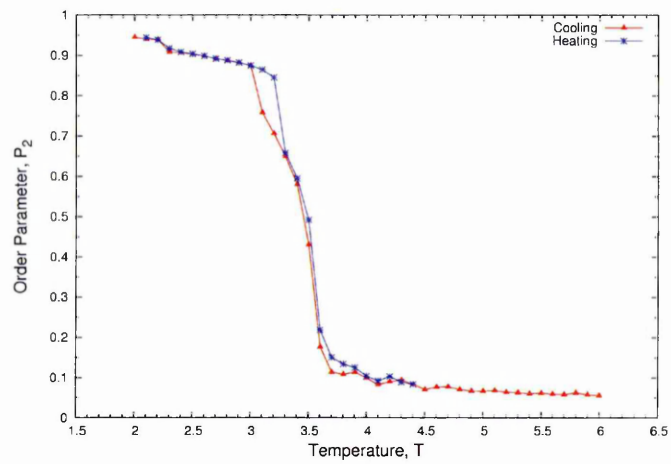
Figure 4.5: Order Parameter vs Temperature for $N = 500$ GB discs, P=50
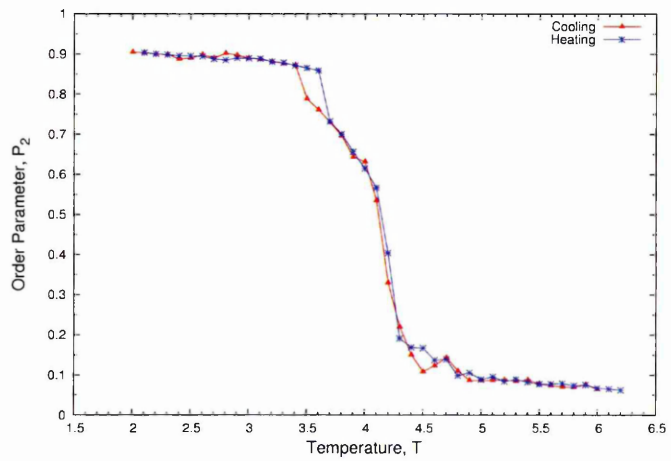


Figure 4.6: Order Parameter vs Temperature for $N = 500$ GB discs, P=75
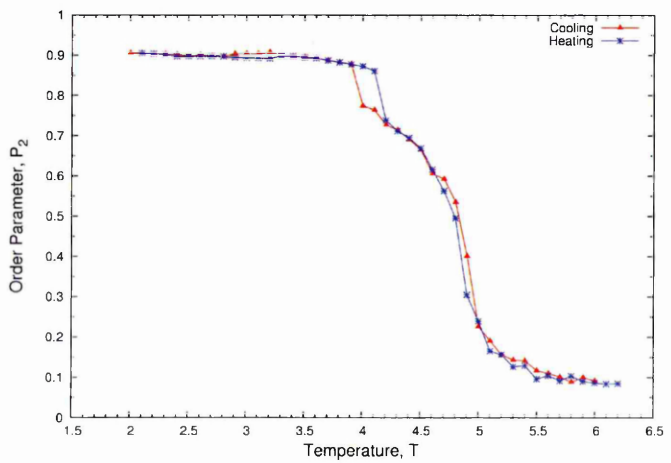


Figure 4.7: Order Parameter vs Temperature for $N = 500$ GB discs, P=100
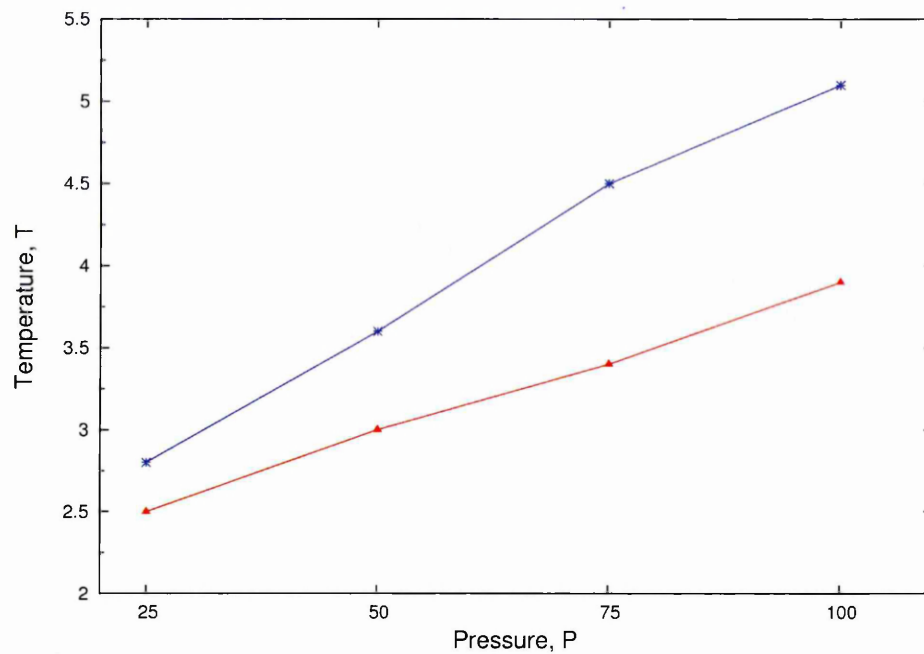
Figure 4.8: The pressure dependence of the transition temperatures on cooling for $N = 500$ discotic GB model systems, isotropic-discotic nematic (blue) and discotic nematic-columnar (red)
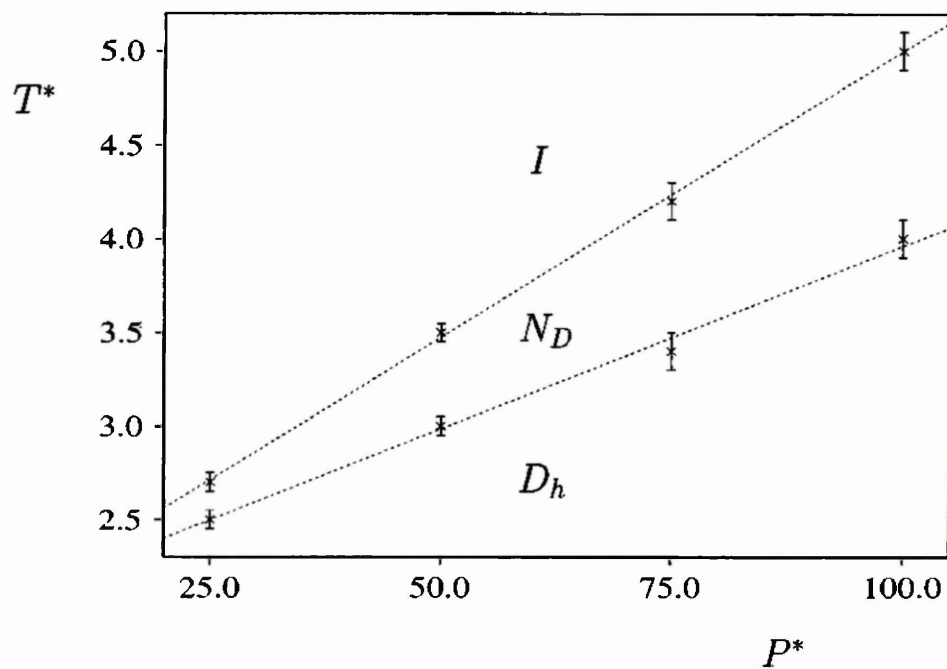


Figure 4.9: Bates and Luckhurst results for the pressure dependence of the transition temperatures for the discotic GB model [48].

## 4.2   Disc-Sphere interaction
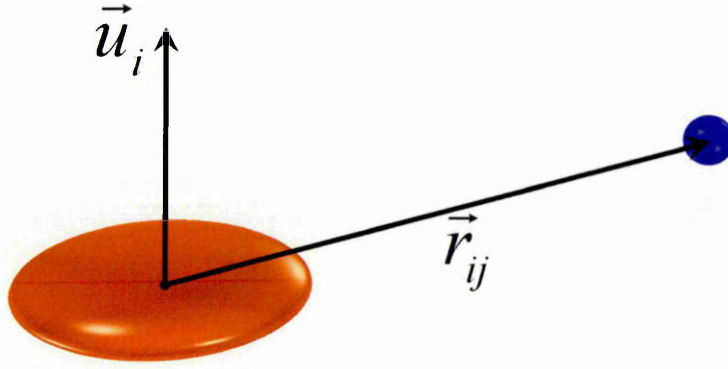


Figure 4.10: Schematic diagram of a Disc and Sphere.

A disc-sphere potential function (Fig.4.11) can be easily derived from the generalised disc-disc potential, by denoting a sphere of diameter $d$ as a disc with its length and diameter set equal to one another $l_i = d_i = d$. The shape and energy parameters ($\sigma$ and $\epsilon$ respectively), according to [44], take the following forms in this case:

$$\sigma(\hat{\mathbf{r}}_{\mathbf{ij}}, \hat{\mathbf{u}}_{\mathbf{j}}) = \sigma_{DS} \left[ 1 - \frac{l_j^2 - d_j^2}{l_j^2 + d^2} (\hat{\mathbf{r}}_{\mathbf{ij}}, \hat{\mathbf{u}}_{\mathbf{j}})^2 \right]^{-1/2} \tag{4.1}$$

$$\epsilon(\hat{\mathbf{r}}_{\mathbf{ij}}, \hat{\mathbf{u}}_{\mathbf{j}}) = \epsilon_{DS} \left[ 1 - \left( 1 - \left( \frac{\epsilon_E}{\epsilon_S} \right)^{1/\mu} \right) (\hat{\mathbf{r}}_{\mathbf{ij}}, \hat{\mathbf{u}}_{\mathbf{j}})^2 \right]^{\mu} \tag{4.2}$$

where the ratio $\frac{\epsilon_E}{\epsilon_S}$ determines the well-depth anisotropy of the interaction. Therefore, the full expression for the disc-sphere potential function takes the following form:

$$U_{ij}^{ds}(\mathbf{r}_{\mathbf{ij}}, \hat{\mathbf{u}}_{\mathbf{i}}) = 4\epsilon(\hat{\mathbf{r}}_{\mathbf{ij}}, \hat{\mathbf{u}}_{\mathbf{i}}) \left[ \left( \frac{\sigma_f}{r_{ij} - \sigma(\hat{\mathbf{r}}_{\mathbf{ij}}, \hat{\mathbf{u}}_{\mathbf{i}}) + \sigma_f} \right)^{12} - \left( \frac{\sigma_f}{r_{ij} - \sigma(\hat{\mathbf{r}}_{\mathbf{ij}}, \hat{\mathbf{u}}_{\mathbf{i}}) + \sigma_f} \right)^{6} \right], \tag{4.3}$$

It is possible to adjust the nature of the disc-sphere interaction by varying the ratio $\frac{\epsilon_E}{\epsilon_S}$. For instance, in the case $\frac{\epsilon_E}{\epsilon_S} = 0.2$, the spheres energetically prefer the edge of the disc and so promote the chromonic self-assembly.
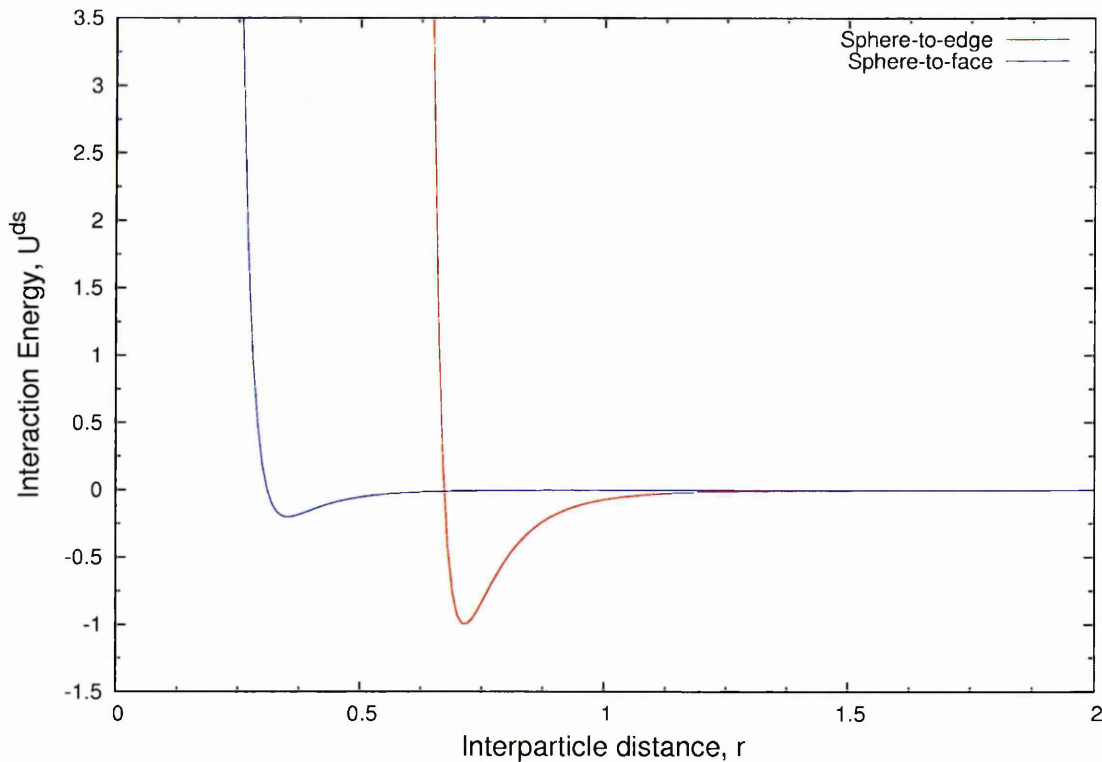


Figure 4.11: Disc-sphere interaction (parameterisation (3,5,2,1)).

To examine the capabilities of this model, a series of preliminary simulations of disc-sphere systems were performed. Starting from high temperature ($T = 2.3$) a small system comprising 1370 particles (70 discs and 1300 spheres) was cooled down in NPT ensemble ($P = 5$). Key model parameters were set as follows: $\sigma_f = l_j = 0.345$, $d_j = 1.0$, $d = 0.345$, $\sigma_{DS} = 0.6725$, $\epsilon_{DS} = 2.63$, $\frac{\epsilon_E}{\epsilon_S} = 0.2$, $\nu = 2$, $\mu = 1$, $k = \frac{\epsilon_{ee}}{\epsilon_{ff}} = 0.2$ (for the disc-disc interactions). For all disc-sphere simulations described in this thesis, the sphere diameter $d$ and the disc length $l$ have been set equal to each other ($d = l = \sigma_f = 0.345$). The parameter $\epsilon_{DS} = 2.63$ was chosen to make the sphere-to-edge and disc edge-to-edge interactions to be of equal strength.

Orientational order parameter measurement made on cooling this system (Fig.4.12) suggested a slow transition from one state (isotropic mixture of discs and spheres)

at high temperature ($T = 2.3$) to another at low temperature ($T = 0.5$). Looking through snapshots of the simulated system, we observed aggregation of individual discs into string-like structures "swimming" in a sea of spheres (Fig.4.13). These linear stacks of discs are consistant with those seen in previous simulations of systems exhibiting chromonic self-assembly [15, 27, 26].
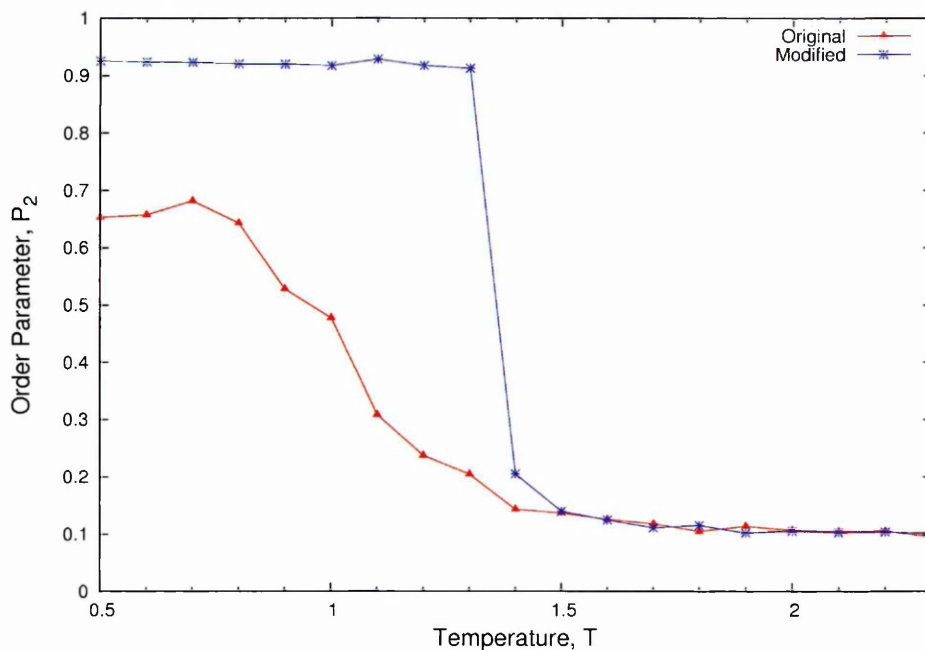


Figure 4.12: Order Parameter vs Temperature in original $R = 1$ (red line) and modified $R = 5$ (blue line) disc-sphere systems involving 1370 particles (70 discs and 1300 spheres)

Subsequently, we performed a series of runs with different concentrations of discs and spheres in both NPT and NVT modes. Depending on temperature, we observed either no changes (high temperatures) or a similar behaviour to that described above (at lower temperatures). These initial results suggested that the parameter set used resulted in the edges of the discs being highly solvophilic. At low temperatures, therefore, the "strings" were effectively isolated from each other, since each was solvated in a layer of spheres, which prevented them from joining laterally (side-by-side).

This led us to the idea that changing the quality of the solvent may give control over the formation of fibrillar structures from aggregated strings. To test this
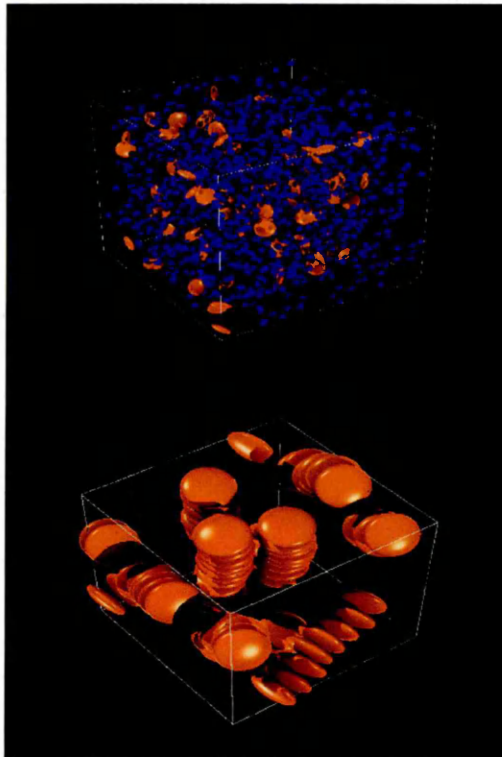
Figure 4.13: Snapshot from 1370 particles NPT simulations of original system at temperature $T = 2.3$ (top) and $T = 0.7$ (bottom, spheres are not shown).

hypothesis, we simulated the same system with slightly different parameters, corresponding to less solvophilic discs. This was achieved by scaling the disc-sphere repulsion term with a constant $R$. A similar approach for reducing the strength of this attractive component has been used in other simulation work [50, 51] exploring the phase separation of symmetric Lennard-Jones particles mixtures. Thus, we have rewritten our disc-sphere interaction potential as:

$$U_{ij}^{ds}(\mathbf{r_{ij}}, \mathbf{\hat{u}_i}) = 4\epsilon(\mathbf{\hat{r}_{ij}}, \mathbf{\hat{u}_i}) \left[ R \left( \frac{\sigma_f}{r_{ij} - \sigma(\mathbf{\hat{r}_{ij}}, \mathbf{\hat{u}_i}) + \sigma_f} \right)^{12} - \left( \frac{\sigma_f}{r_{ij} - \sigma(\mathbf{\hat{r}_{ij}}, \mathbf{\hat{u}_i}) + \sigma_f} \right)^{6} \right], \qquad (4.4)$$

For $R > 1$, the location and depth of the disc-sphere interaction minima are both shifted. If $R$ is sufficiently large, the disc edge-to-edge interaction becomes more

favourable than the sphere-to-edge interaction. Initial simulations of this system demonstrated that for $R = 5$, these changes had a significant impact on the process of self-assembly. While the first stage of this aggregation was similar to that seen previously (formation of stacks of disks), we observed a new second stage behaviour; at low temperatures (below $T = 1.5$), the formed stacks rapidly started to aggregate into a single fibrilar structure. This second-level process was indicated by a sharp rise in the orientational order parameter (Fig.4.12). At first, all threads aligned with each other. However, during subsequent quenching, the structure gradually transformed into a twisted fibril (Fig.4.14).
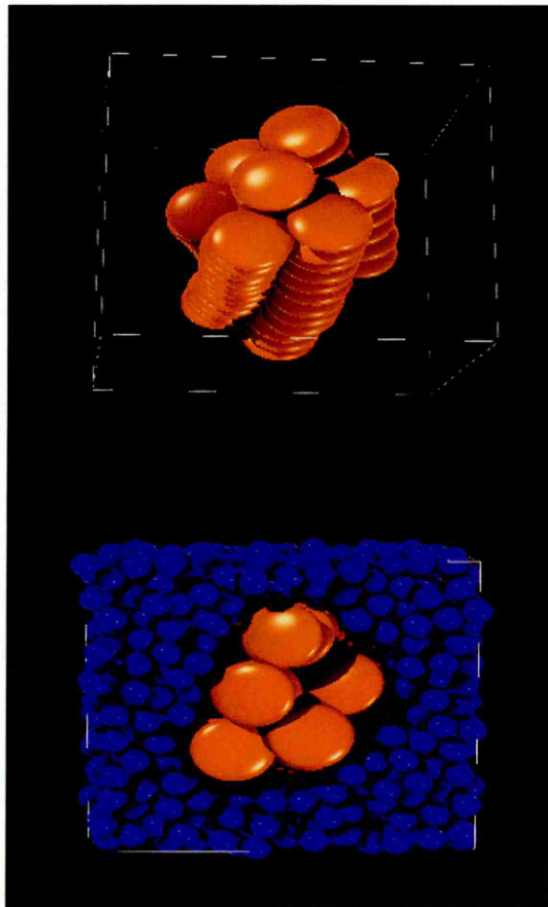


Figure 4.14: Snapshots from 1370 particles NPT ($P = 5$) simulations of modified ($R = 5$) system with stronger repulsion at low temperature $T = 0.7$ .

Thus, while the types of chiral clusters were predicted by the zero temperature energy landscape calculations of Chakrabarti et al. [52], here we show that, in

appropriate conditions, they can be realised in finite-temperature systems. However, it would not be valid to infer too much from the results of simulations of these small systems, as the fibre formed linked through the periodic boundary conditions (Fig.4.14) and thus could have been artificially stabilised. In order to address these stability issues and explore more rigorously the self-assembly mechanisms involved in such systems we present, in the next chapter, a detailed study based on MD simulation of significantly larger systems using the $R = 5$ parametrisation. The behaviour of the $R = 1$ parametrisation is then revisited in chapter 6.

# Chapter 5

# Results of simulations

In this chapter results of simulations of larger disc-sphere systems are presented. A series of constant NVT simulations were performed to determine key model parameters and their influence on system behaviour. The effect of the parameter $k = \epsilon_{ee}/\epsilon_{ff}$, which controls the strength of the anisotropy of the disc-disc interaction, has been investigated. It was found that, for a narrow temperature range, defect-free chiral fibres could freely self-assemble from an initially isotropic configuration. This occured as a result of a complex multistage process. Finally, concentration and system size effects were studied.

## 5.1 Systems with $k = 0.10$

Results obtained from simulations of small systems suggested that the disc-sphere interaction plays an important role in the process of disc self-assembly. We found that changing the quality of the solvent gives control over the formation of fibrillar structures from aggregated threads. One can understand the state adopted by a system as being driven by whether it is energetically preferable for a separate thread to be surrounded by layer of spheres or by other threads. This can be adjusted by changing the ratio between the energy of the disc-disc interaction in edge-to-edge

configuration and the energy of the sphere-disc edge interaction.

Here, as previously, we use an approach where the disc-sphere repulsion term is scaled with a constant $R$. With $R = 5$, threads in a small system aggregated into a twisted fibre. However, as that fibre linked through the periodic boundary conditions, it could have been artificially stabilised.

To exclude this influence of periodic boundary conditions here, a larger simulation box length was used ($Lx = 34.18$); this proved significantly larger than any of the fibre lengths observed in this study. First, a system of total 8788 particles (containing 880 discs) was equilibrated in an NVT ensemble for $7 \cdot 10^6$ MD timesteps at $T = 2.3$. Once memory of the original lattice had been lost, no further transitions were observed in this equilibration run; the system remained isotropic and well-mixed throughout. Based on information obtained from simulations of small systems, we concluded, therefore, that $T = 2.3$ is too high a temperature and that some lower temperature is required for structure formation to be observed.

In order to determine an appropriate temperature regime, a series of further runs was performed. First observable changes were discovered in a run with $T = 2.0$. On cooling to this temperature, it was found that short thread-like assemblies of 2-3 discs occasionally developed. Each of these was found to persist for a relatively short time before dissociating into monomers and dimers.

Performing a slightly deeper quench, to $T = 1.9$, led to more noteworthy self-assembly processes. Here, significantly more and longer threads were observed. Also, while these threads were dynamic objects, with monomers joining and leaving on a regular basis, once established these threads proved long-lived and several could be traced over hundreds of thousands of timesteps. A typical configuration from this run is shown in (Fig. 5.1).This displays very simple chromonic self-assembly of the type previously studied in [15, 27, 26].

Disaggregation of these longer threads commonly involved a split into two shorter threads. Another occasional feature seen at this temperature was lateral associa-
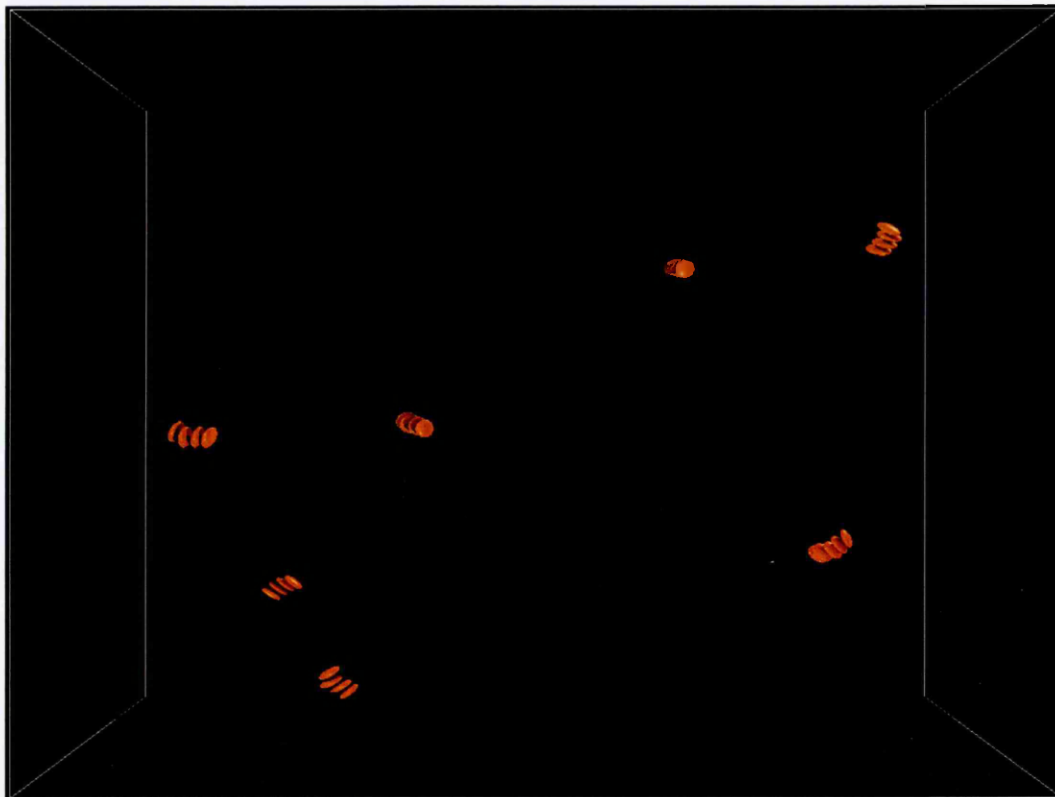
Figure 5.1: A typical configuration from the equilibrated phase of the $T = 1.9$ quench. For clarity, only discs in threads of length 4 or more are shown.

tion, leading to second generation double-thread mini-bundles. At $T = 1.9$, these mini-bundles proved meta-stable since they always re-divided into separate threads. This initial observation of mini-bundle formation was, though, significant since it signposted the general propensity of this system to develop multi-thread assemblies.

To test this hypothesis, we used a lower temperature ($T = 1.7$) in our next simulation run. At this temperature, after an initial period in which numerous individual threads were formed (each comprising up to 8 monomers), several larger bundles were found to develop. The threads in each of these bundles were approximately parallel, leading to nascent fibres which gradually developed both laterally and longitudinally. When these assemblies had relatively few threads (i.e. $\simeq$ 3-5) they exhibited considerably flexibility, the threads exploring various packing arrangements. This flexibility reduced, however, as the bundles grew. Also, subsequent to this, a small number of bundle-bundle aggregation events took place. One of these
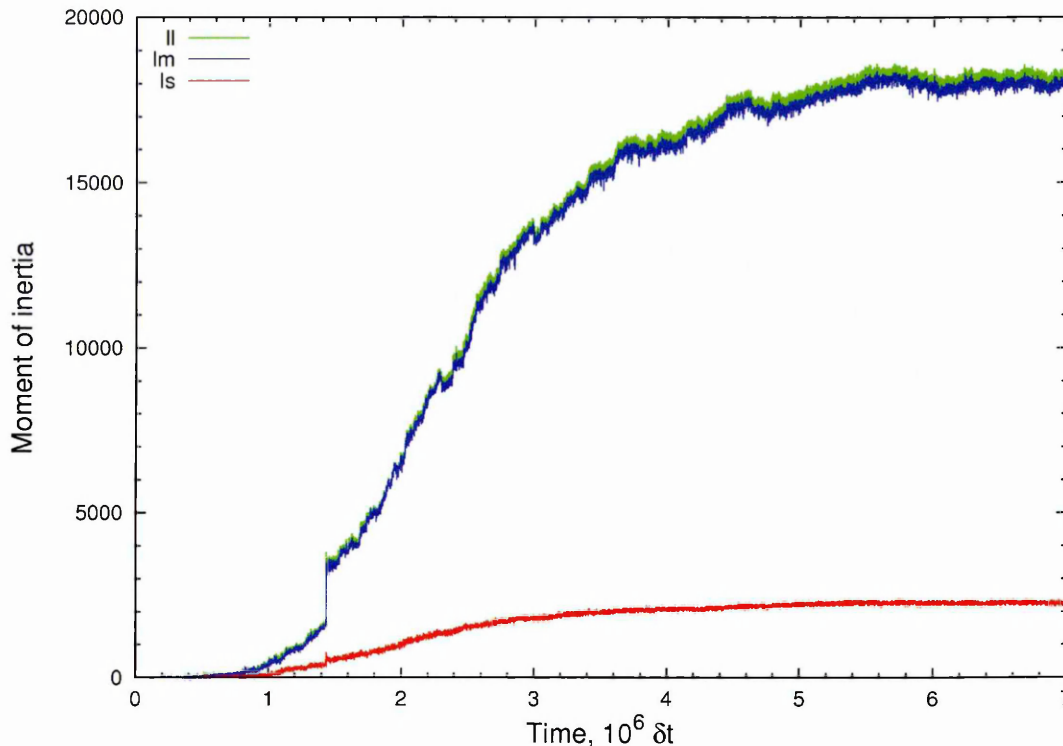
Figure 5.2: Timelines of the principal moments of inertia of the largest cluster in the $T = 1.7$ quench (largest eigenvalue green, middle eigenvalue blue, smallest eigenvalue red.)

is apparent from the jump at $t \simeq 1.4 \times 10^6 \delta t$ in the moment of intertia timelines shown in Fig. 5.2.

These timelines show that, even before this jump, the largest bundle was elongated since two of its moments of inertia were larger than the third. This difference was accentuated by the bundle-bundle aggregation event, showing that the two bundles attached end-to-end. Subsequent to this, the three moments of inertia all grew in near monotonic fashion, but the smallest grew significantly more slowly than the other two. Very little change was seen over the last two million timesteps of the run.

A configuration snapshot from the end of this run is shown in Fig. 5.3. Here, the discs are colour coded according to their orientations, so as to make it easier to recognise differing local packing arrangements. As expected from the moment of inertia data, the final aggregate is certainly fibre-like. However, at least three distinct segments can be identified: a central straight region and twisted segments
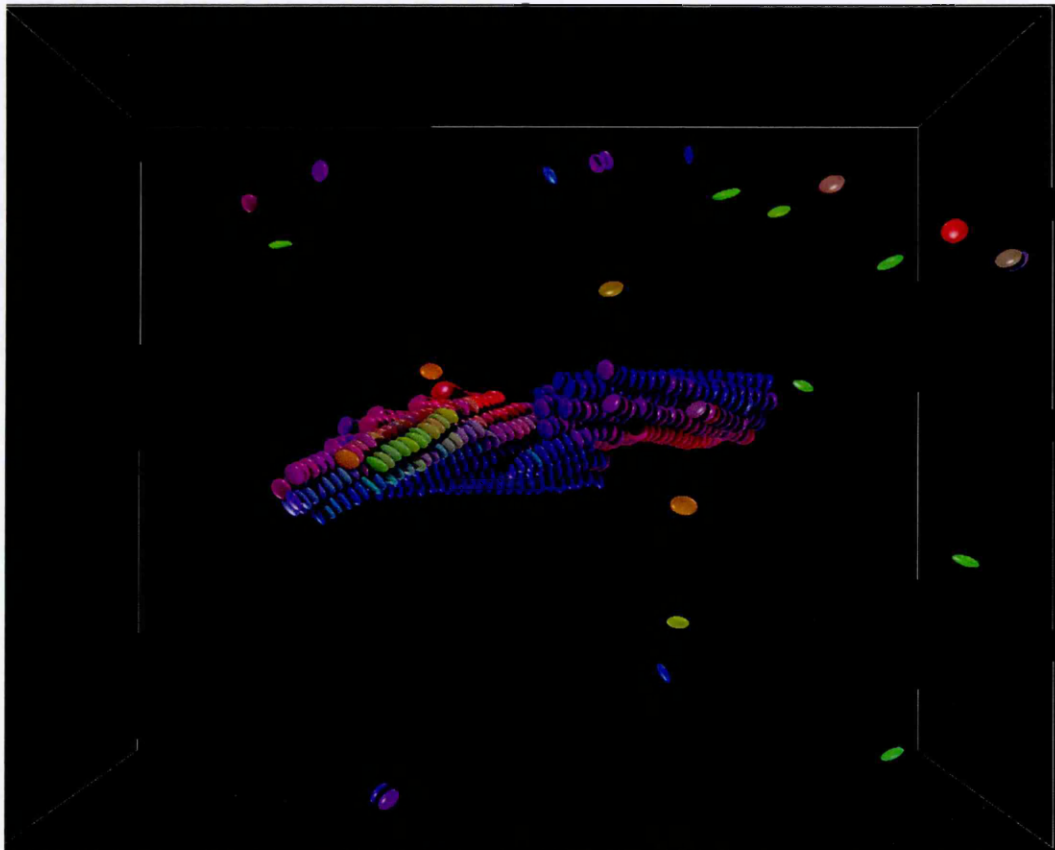
Figure 5.3: Final aggregate formed in the $T = 1.7$ quench. For clarity, no spheres are shown. Discs are colour coded according to their orientation; neighbouring threads in chiral segments therefore have differing colours.

(of opposite handedness) at each end. Stacking defects between these segments can also be identified. Animations of the self-assembly process confirm that this segmental structure originated due to the evolutionary steps experienced by the fibre. Specifically, in this quench three significant multi-thread bundles developed independently in the middle stage of the self-assembly. Each of these grew to a sufficient size that it retained its own local packing arrangement throughout bundle-bundle aggregation. This multi-segment-fibre arrangement was found to be long-lived when the run-time of this simulation was extended, the main defects persisting indefinitely.

This final aggregate obtained from this $T = 1.7$ quench was kinetically arrested - while the thermal energy in the system was sufficient to allow a degree

of single-particle-dissociation type relaxations, the stronger bundle-bundle interaction strengths were too great for larger-scale rearrangements to take place. As a result, the fibre had no kinetically-accessible route by which to adopt a defect-free structure.

In view of this, subsequent quenching runs were undertaken at a range of temperatures intermediate between $T = 1.7$ and 1.9. Of these, the run at $T = 1.82$ proved optimal in that only one multi-thread bundle was nucleated. The final configuration from this run, shown in Fig.5.4 was a defect-free, chiral fibre. As evidenced by the corresponding cluster-size and moment of inertia timelines (Figs. 5.5 and 5.6 respectively) this then grew into an elongated fibre without exhibiting any of the discontinuities seen at $T = 1.7$.
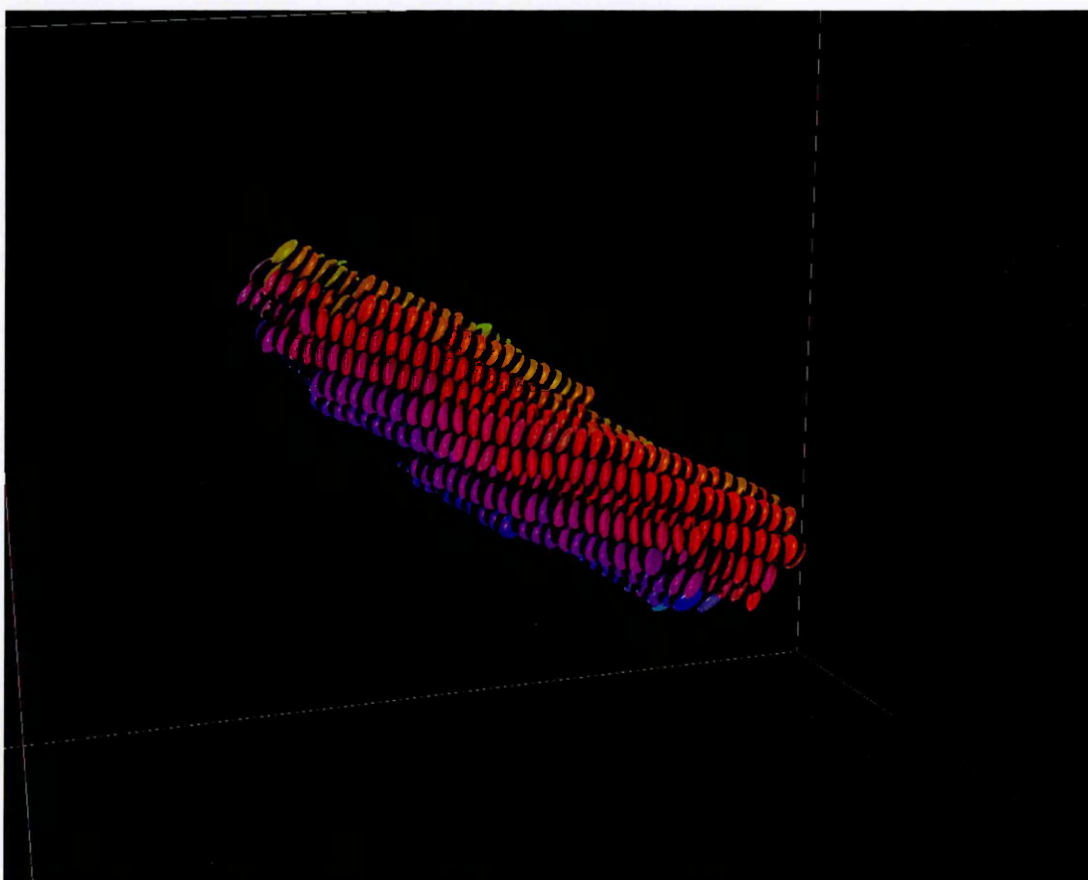


Figure 5.4: Final configuration from the $T = 1.82$ quench. For clarity, no spheres are shown. Discs are colour coded according to their orientation; defect-free helical threads therefore have gradually changing colours.
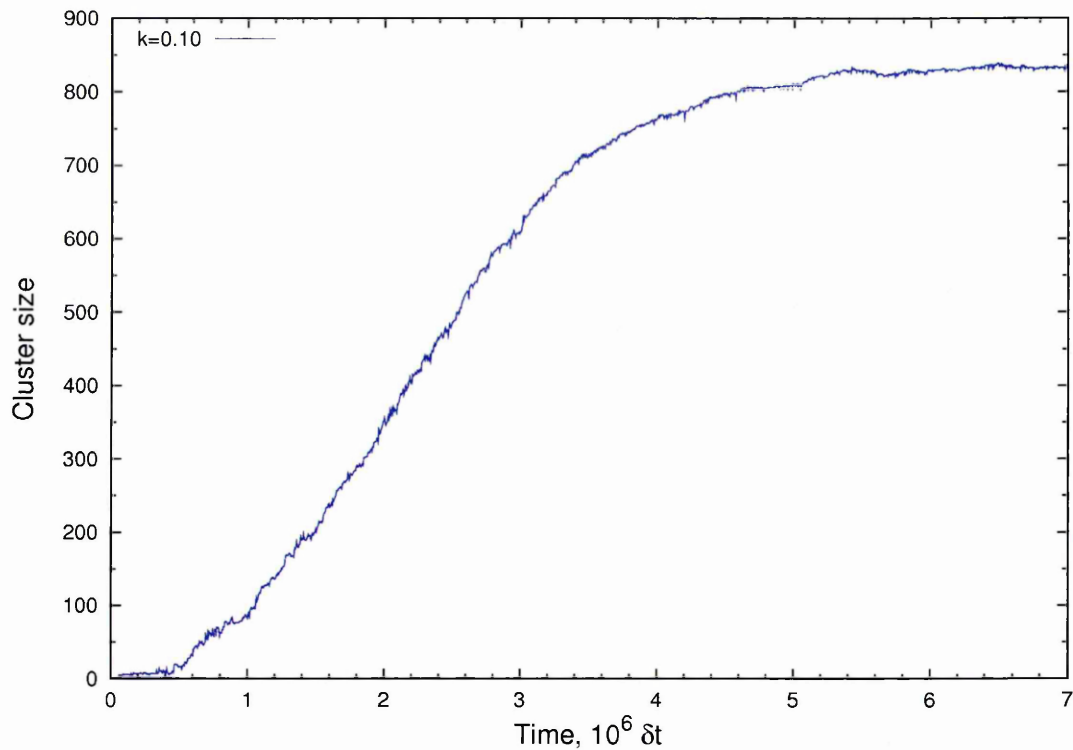
Figure 5.5: Timeline of the number of particles in the biggest cluster in the $T = 1.82$ quench.
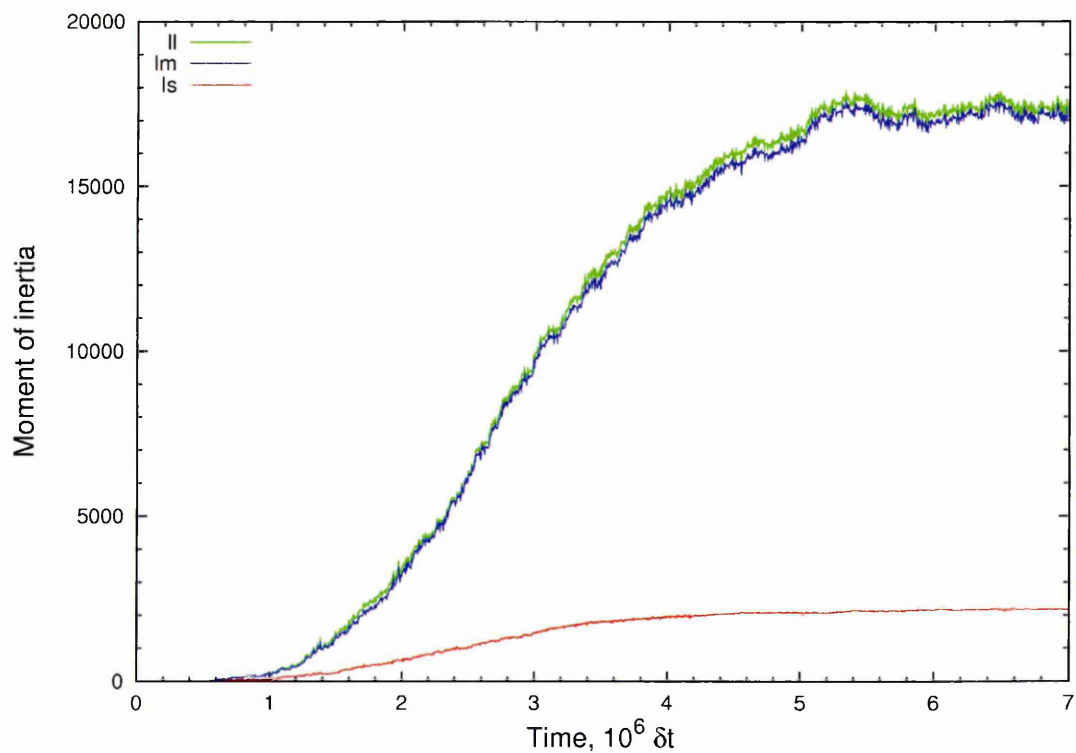


Figure 5.6: Timelines of the principal moments of inertia of the largest cluster in the $T = 1.82$ quench (largest eigenvalue green, middle eigenvalue blue, smallest eigenvalue red.)

To characterise the defect-free chiral fibre more fully, each of its threads was fitted to the locus of a helix with centre-line running along the eigenvector corresponding to the fibre's smallest moment of inertia (Fig.5.7(b)). Using this approach, parametric fits yielded independent helical pitch and radius values for 21 of the fibre's 22 threads (the central thread was found to be straight and so no fit was performed). These fits are given in Table 5.1. These all give a consistent value of $\simeq 32\sigma_{ee}$ for the emergent lengthscale that is the fibre pitch. Furthermore, their radial fit parameters show a tendency to adopt certain preferred values, the first 18 thread radii falling into three distinct groups.
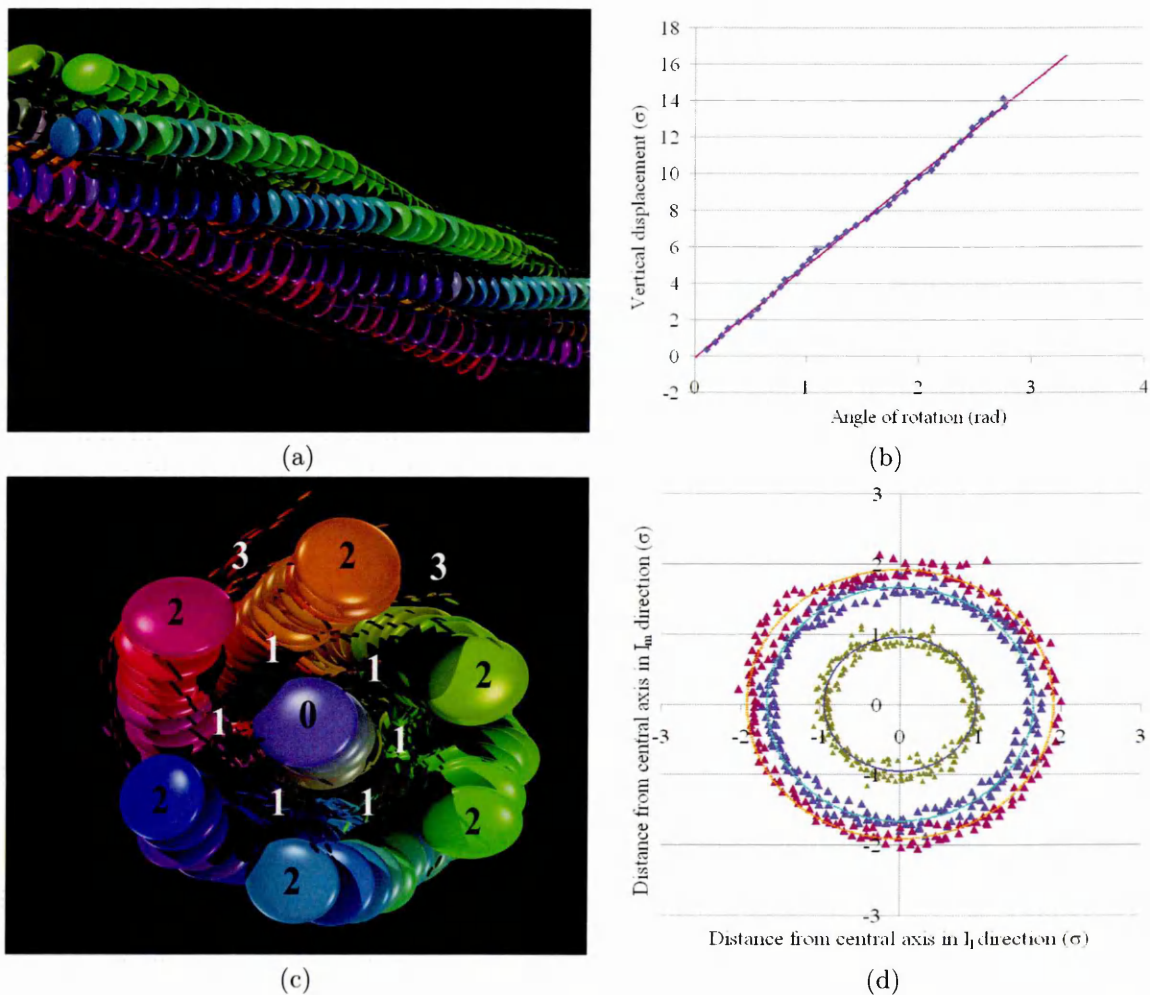


Figure 5.7: Views of the $T = 1.82$ chiral fibre and fit data: (a) side view, showing the particles in Layers 0 and 2 fully resolved and colour coded for orientation; (b) parametric fit of a threads pitch; (c) top view of the fibre; (d) top view, showing particle centres only, projected onto a plane perpendicular to the main thread axis.

Fig.5.7(d) shows all of the disc centres projected onto a plane perpendicular to the fibre axis. This illustrates that the fibre had a straight central thread ("Layer 0") surrounded by six "Layer 1" helical threads. Six "Layer 2" threads then resided in the grooves provided by Layer 1 and, similarly, the locations of the six "Layer 3" threads were templated by the grooves in Layer 2. Finally, three "Layer 4" threads lay in grooves on the outside of the fibre. Snapshots showing the Layer 0 and Layer 2 particles in full and the other particles as short lines are given in Figs.5.7(a) and (c). These both reinforce the absence of defects in this self-assembled structure and, through their orientation-dependent colour coding, show the smooth helices traced out by the Layer 2 threads.

| Thread | Radius $(\sigma_{ee})$ | Pitch $(\sigma_{ee})$ |
|--------|------------------------|------------------------|
| 1 | $0.939 \pm 0.005$ | $32.8 \pm 0.4$ |
| 2 | $0.960 \pm 0.004$ | $30.2 \pm 0.9$ |
| 3 | $0.942 \pm 0.009$ | $31.6 \pm 0.7$ |
| 4 | $0.923 \pm 0.009$ | $33.5 \pm 0.8$ |
| 5 | $0.976 \pm 0.005$ | $30.5 \pm 0.4$ |
| 6 | $1.017 \pm 0.003$ | $31.7 \pm 0.4$ |
| 7 | $1.637 \pm 0.008$ | $32.1 \pm 0.3$ |
| 8 | $1.734 \pm 0.003$ | $31.0 \pm 0.3$ |
| 9 | $1.726 \pm 0.004$ | $31.8 \pm 0.2$ |
| 10 | $1.626 \pm 0.007$ | $33.1 \pm 0.3$ |
| 11 | $1.640 \pm 0.006$ | $31.5 \pm 0.2$ |
| 12 | $1.669 \pm 0.006$ | $31.8 \pm 0.3$ |
| 13 | $1.890 \pm 0.007$ | $31.8 \pm 0.9$ |
| 14 | $1.907 \pm 0.007$ | $32.3 \pm 0.3$ |
| 15 | $1.980 \pm 0.001$ | $31.5 \pm 0.2$ |
| 16 | $1.949 \pm 0.004$ | $32.0 \pm 0.3$ |
| 17 | $1.974 \pm 0.005$ | $31.8 \pm 0.1$ |
| 18 | $1.868 \pm 0.013$ | $33.3 \pm 0.1$ |
| 19 | $2.511 \pm 0.003$ | $32.7 \pm 0.1$ |
| 20 | $2.484 \pm 0.006$ | $33.8 \pm 0.2$ |
| 21 | $2.458 \pm 0.003$ | $30.4 \pm 0.2$ |

Table 5.1: Parametric radius and pitch fits of individual threads of the $T = 1.82$ fibre to ideal helices.

This structural characterisation also indicates why the fibre formed here was chiral. The chirality was founded on the structural stability of a hexagonal 7-thread nucleus comprising a straight central thread sheathed in six columns of slightly tilted discs, the outer threads spiralling around so as to maintain the integrity of the fibre. This arrangement was identified by Chakrabarti et al. as the optimal cluster for $N = 49$ discotic ellipsoids.

The discs in the Layer 1 threads were obliged to tilt because they had to interdigitate (with each-other and with the central thread) in order to achieve their radial displacements from the central axis (note, from Table5.1, that the radial fit values for Layer 1 particles are generally less than $\sigma_{ee}$). Since hexagonal packing requires triplets of neighbouring threads to co-operatively interdigitate, a consistent handedness developed naturally in the stacking adopted at these triplet junctions. This arrangement is characterised by a 7-particle propeller-like motif - this motif is the structurally chiral object, on which the helical fibre is founded. Once formed, the chiral seven-thread core acted as a seed for the subsequent fibre growth. We will describe the complex kinetics of this hierarchical growth process in the concluding section of this chapter.

## 5.2  Systems with $k = 0.075$

On analyzing results for $k = 0.10$ system, we concluded that growth rate is highly important, as it basically determines all of the observed stages of self-assembly. As we have seen, in case of too high temperature, the thermal energy in the system is sufficient to allow for a high degree of single-particle-dissociation type relaxations. This prevents formation of threads and, subsequently, fibres. However, if temperature is too low, bundle-bundle aggregation events take place. This leads to the formation of fibres with defects. Moreover, at low temperature the fibre has no kinetically-accessible route by which to adopt a defect-free structure. Thus, the nucleation of a single defect-free fibre is possible only at a range of temperatures intermediate between these two regimes. We can consider, however, what would happen if we change a strength of disc-disc interaction, making discs face-to-face attraction stronger or weaker. Presumably, this should have an equivalent effect on aggregation as varying the temperature, as the strength of the disc-disc interaction has a direct impact on the stability of the formed stacks. It is less obvious, however, how this parameter will influence higher-level aggregation - we can ask another intriguing question: whether we can grow longer fibres?

To explore the influence of the disc-disc well-depth anisotropy parameter $k$ on the aggregation process we studied disc self-assembly in a range of systems with different $k$ values. It was decided to study system with $k = 0.075$ first, i.e. to make the face-to-face attraction stronger. Again a system comprising a total of 8788 particles (containinig 880 discs) was equilibrated in an NVT ensemble for $7 \cdot 10^6$ MD timesteps at different temperatures.

In the first run temperature was set to $T = 1.8$. Here we observed noticable changes in the early thread-formation phase, compare to $k = 0.10$ systems, where this temperature is close to the optimal 1.82. In the new system, much longer individual threads were formed (up to 12 discs). Similarly, the final fibre was con-
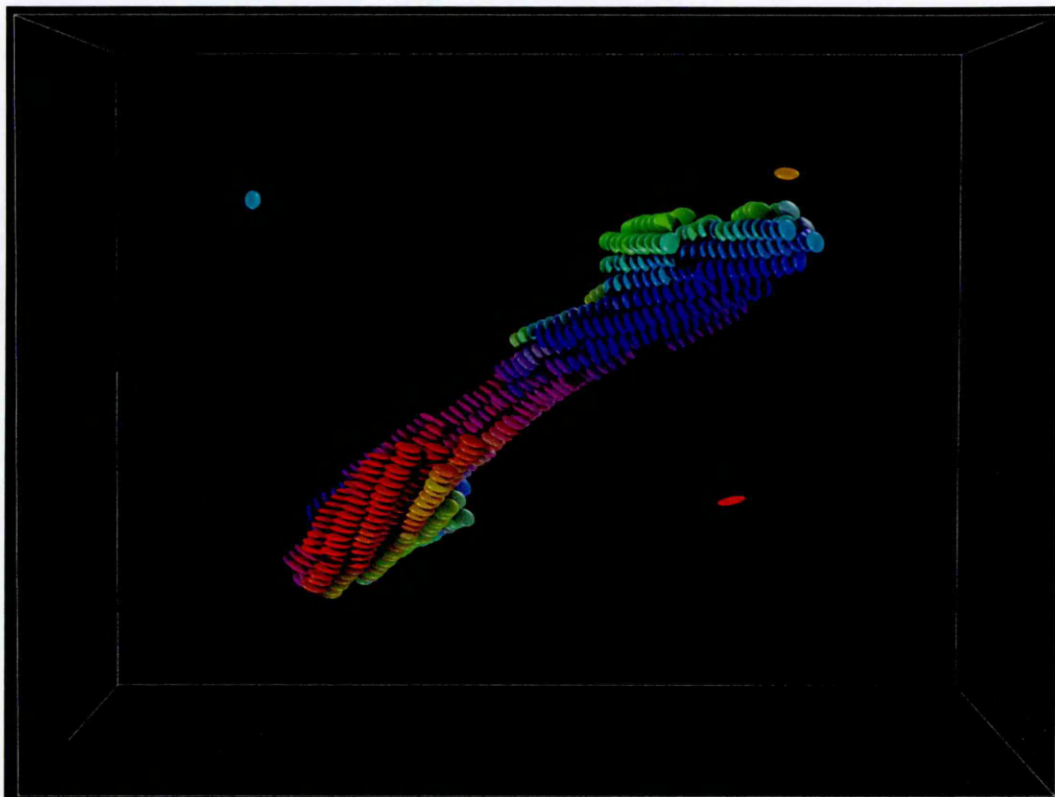
Figure 5.8: Fibre with defects found in the $T = 1.8$ quench of the $k = 0.075$ system.

siderably longer than those observed before. However it contained several deffects (Fig.5.8). This fact alone already confirms that longitudinal fibre growth progressed more rapidly in the case of stronger face-to-face attraction.

However, in order to enable a proper comparison with the $k = 0.1$ system, it was necessary to grow a defect-free fibre. This would provide a more rigorous comparison by which to judge the impact of $k$ on the self-assembly and structure aggregation in these systems. Similarly as in the previously studied system, therefore, subsequent quenching runs were undertaken at a range of temperatures to find an appropriate aggregation regime. Of these, the run at $T = 2.3$ proved to be optimal. The final configuration from this run is shown in Fig.5.9. Although visually it appeared that the formed fibre here had a slightly higher pitch, than that found at $k = 0.1$, fits indicated that the pitch value actually remained virtually unchanged at $P \approx 32\sigma_{ee}$ (Table 5.2). The apparent pitch difference suggested by snapshots arises due to the

outer threads of the larger radius fibre (for $k = 0.10$) necessarily following more helical loci, which makes an illusion of higher pitch.
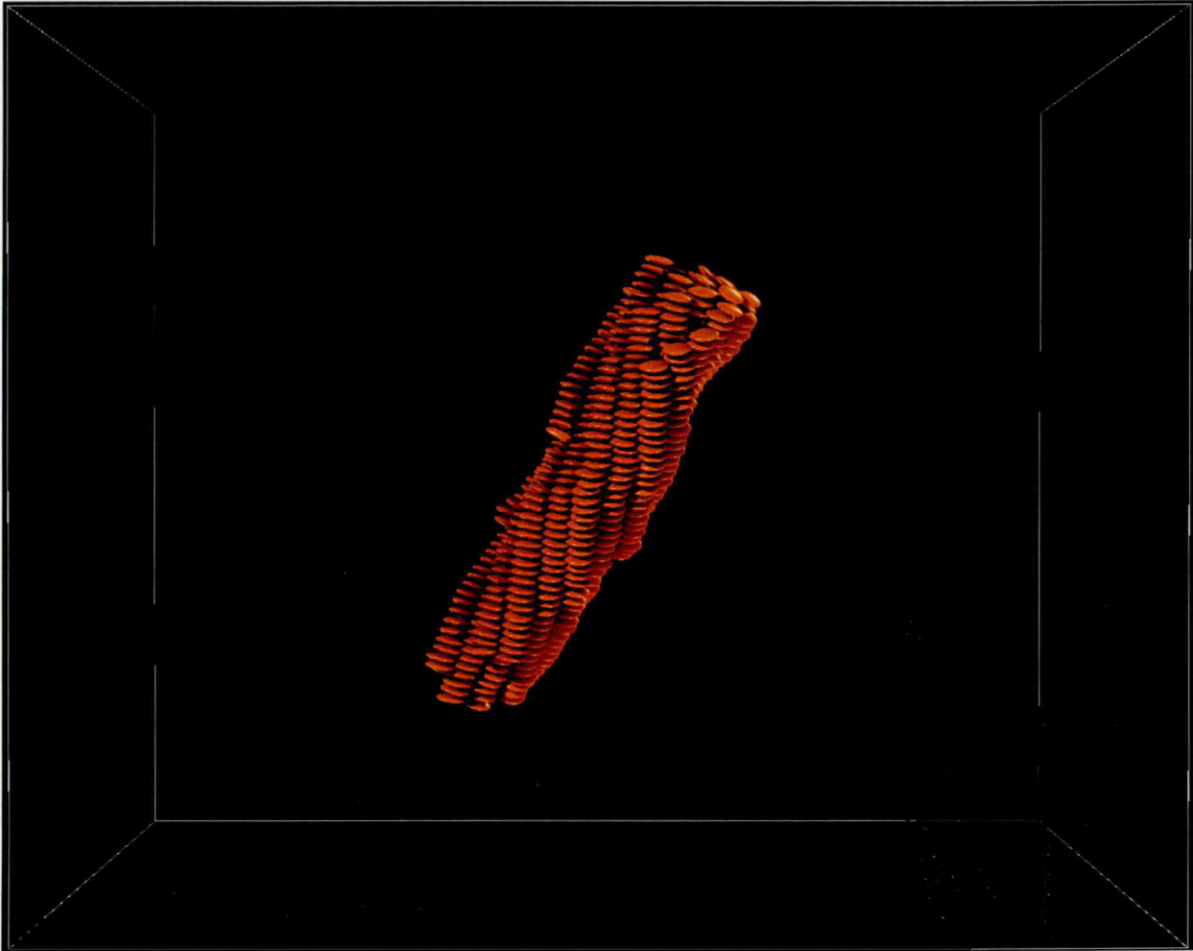


Figure 5.9: Final configuration from the $T = 2.3$ quench of the $k = 0.075$ system. For clarity, no spheres are shown.

Another observation is that the final fibre appears longer and narrower (Fig.5.9), compared to that obtained from the $k = 0.10$ system. This is confirmed numerically by the moment of inertia data (Fig.5.11). Specifically, the two large components increased from 17400 to 22000 whilst the smallest decreased from 2250 to 1990. Considering the fact that fibre growth occured during the same period of time (7000000 timesteps) as for the $k = 0.10$ system, we can state that the elongation growth rate was higher in this system.
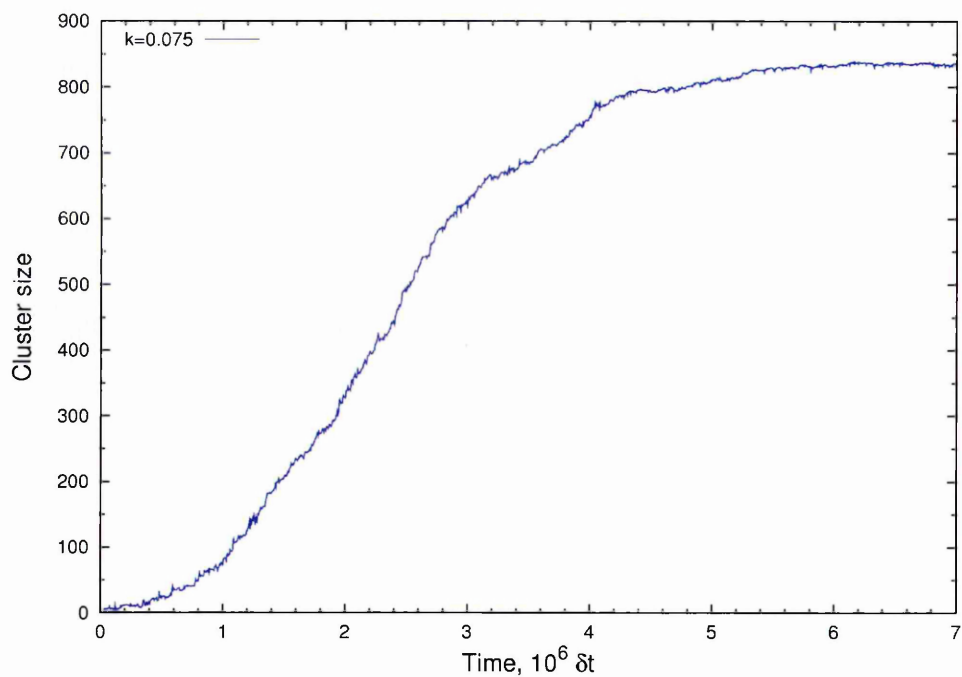
Figure 5.10: Number of particles in the biggest cluster for the $T = 2.3$ quench of the $k = 0.075$ system.
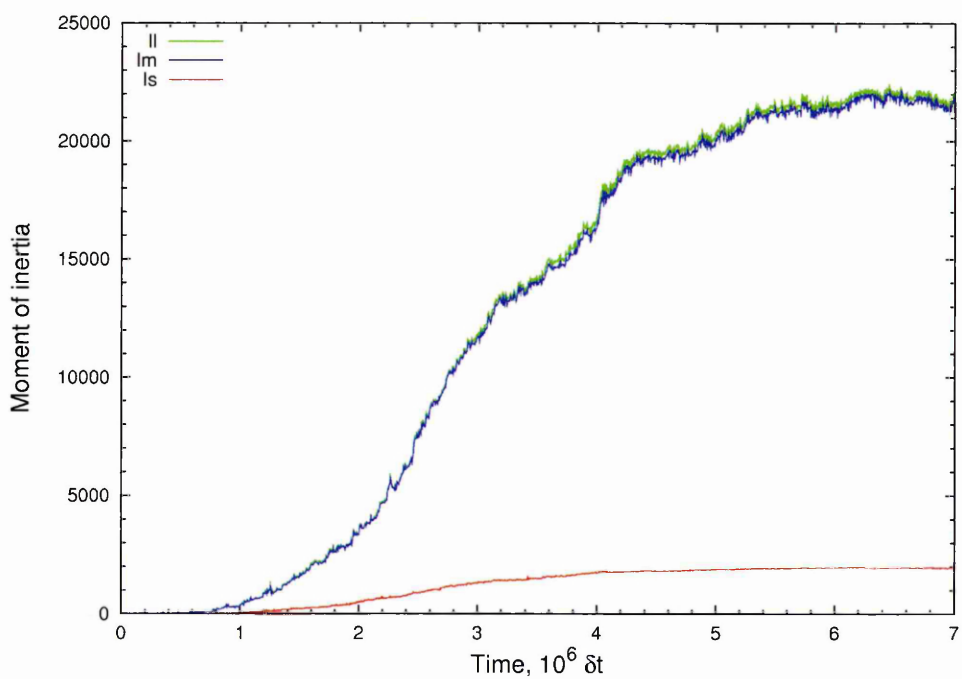


Figure 5.11: Principal Moments of inertia of the biggest cluster for the $T = 2.3$ quench of the $k = 0.075$ system.

Thus, we have found that, while fibre self-assembly is very sensitive to temperature changes, it also progresses diversely in systems with different $k$. This parameter has a strong impact on the dynamics of aggregation. Its influence is more complex than the influence of temperature, as it affects not only the rate of nucleation itself, but also the ratio between rate of longitudinal and lateral growth. To explore this effect systematically, more systems have been studied. Results of these further simulations are presented in the following sections.

| Thread | Radius ($\sigma_{ee}$) | Pitch ($\sigma_{ee}$) |
|--------|------------------------|------------------------|
| 1  | $0.929 \pm 0.010$ | $31.1 \pm 0.5$ |
| 2  | $0.957 \pm 0.009$ | $32.3 \pm 0.3$ |
| 3  | $0.899 \pm 0.015$ | $31.9 \pm 0.4$ |
| 4  | $0.947 \pm 0.006$ | $32.6 \pm 0.6$ |
| 5  | $1.000 \pm 0.008$ | $32.2 \pm 0.1$ |
| 6  | $0.995 \pm 0.009$ | $31.6 \pm 0.2$ |
| 7  | $1.681 \pm 0.002$ | $30.5 \pm 0.8$ |
| 8  | $1.690 \pm 0.004$ | $32.7 \pm 0.9$ |
| 9  | $1.723 \pm 0.007$ | $31.3 \pm 0.7$ |
| 10 | $1.668 \pm 0.011$ | $32.2 \pm 0.5$ |
| 11 | $1.699 \pm 0.004$ | $30.6 \pm 0.1$ |
| 12 | $1.720 \pm 0.005$ | $33.0 \pm 0.6$ |
| 13 | $1.810 \pm 0.009$ | $32.1 \pm 0.3$ |
| 14 | $1.943 \pm 0.006$ | $32.5 \pm 0.9$ |
| 15 | $1.965 \pm 0.006$ | $30.0 \pm 0.9$ |
| 16 | $2.075 \pm 0.007$ | $32.4 \pm 0.8$ |
| 17 | $2.081 \pm 0.008$ | $31.7 \pm 0.3$ |

Table 5.2: Parametric radius and pitch fits of individual threads of the $k = 0.075$ $T = 2.3$ fibre to ideal helices.

## 5.3    Systems with $k = 0.05$

According to the results presented in Section 5.2, it appears that it is possible to use $k$ to adjust the growth modes of fibres, leading to fibres with different length/breath ratios. It was decided to test this assumption further by running additional series of simulations. It was logical to continue to explore effect of strengthening of the face-to-face interaction on the process of self-assembly, so $k = 0.05$ was used in the subsequent set of runs. Here, though, we observed formation and consequent growth of a straight (not-twisted) fibre (Fig.5.12) at $T = 3.2$. This was a surprising outcome, as we had expected the system to follow the previous trend of forming a twisted and more elongated fibre.



(a)                                                            (b)
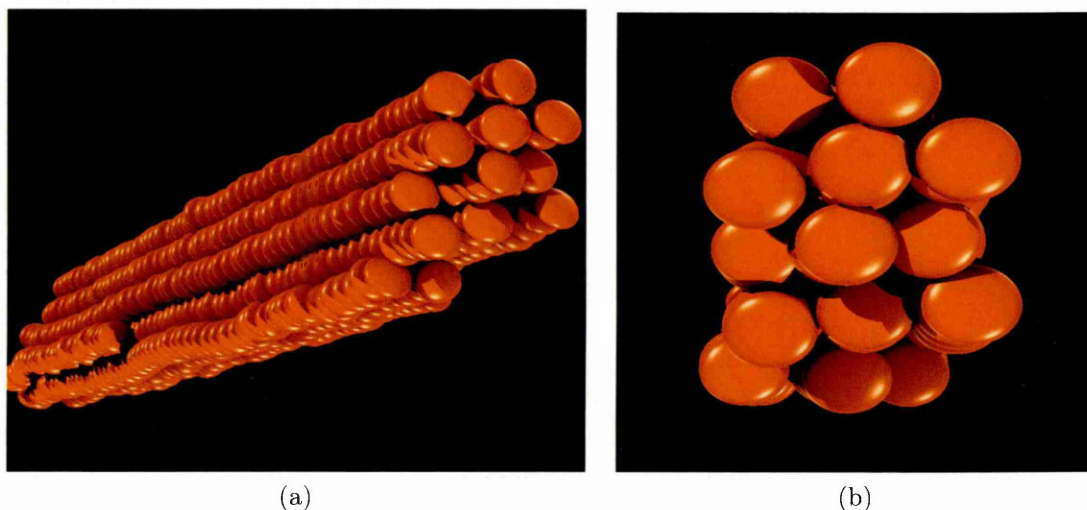
Figure 5.12: Side and top view of the $k = 0.05$ fibre found at $T = 3.2$

Nevertheless, moment of inertia data and snapshots clearly indicated that the formed fibre was considerably longer than the structures observed previously. The largest moment of inertia values increased from 22000 to 34500 and the smallest decreased from 1990 to 1350 (Fig.5.13), compare to $k = 0.075$ case. We also noticed high degree of discontinuity on the Moment of inertia and Number of particles graphs (Fig.5.13, Fig.5.14) after $t = 3 \cdot 10^6$ timesteps. We checked snapshots and found that this was associated with short threads frequently joining and dissociating from the main cluster.

Thus, on the one hand, the obtained results again confirmed our finding that the parameter $k$ has a direct impact on the ratio between longitudinal and lateral growth rates.  Stronger face-to-face attraction between discs makes longitudinal growth more preferable over lateral. On the other hand, we found that influence of $k$ is even greater than previously thought: it also affects local packing within the fibre, leading to a qualitative change in the overall fibre symmetry.
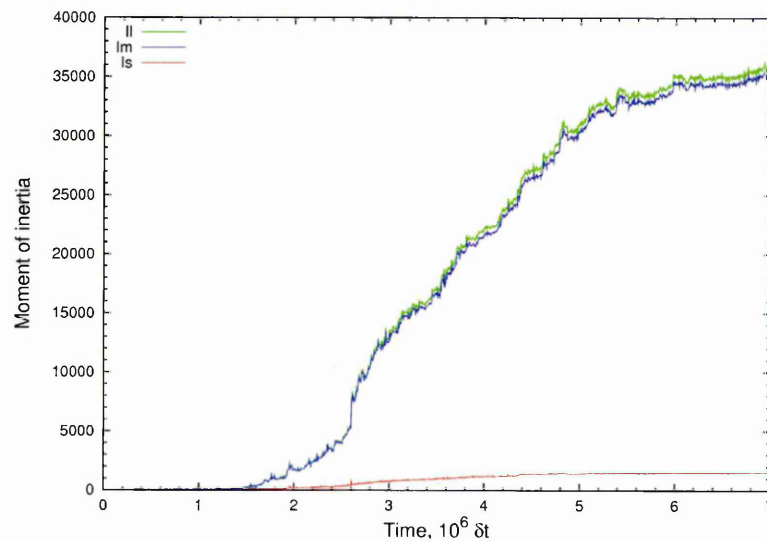


Figure 5.13: Moment of inertia of the biggest cluster for the $T = 3.2$ quench of the $k = 0.05$ system.
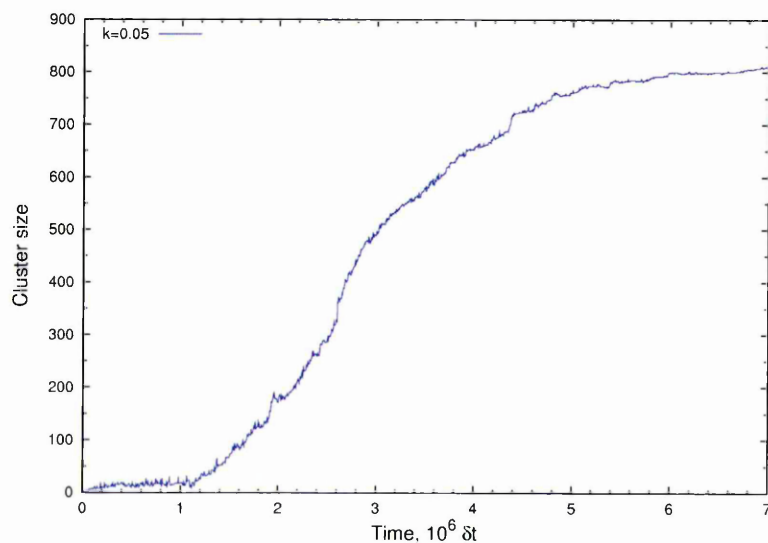


Figure 5.14: Number of particles in the biggest cluster for the $T = 3.2$ quench of the $k = 0.05$ system.

## 5.4 Systems with $k = 0.15$ and $k = 0.20$

In Sections 5.1, 5.2 and 5.3 we have studied self-assembly in systems with relatively strong face-to-face attractions. Importantly, in these runs, a transition between twisted and achiral fibre arrangements has been identified. To gain knowledge about systems with weaker disc-disc interactions additional runs with $k = 0.15$ and $k = 0.20$ were performed. Again, a number of temperatures were considered, optimal fibres being formed at $T = 1.35$ and $T = 1.08$ for $k = 0.15$ and $k = 0.20$, respectively.

We combined these results in a single section, as they demonstrated quite similar behaviour. In both cases, the formed fibres were much shorter and had greater diameters (Fig.5.15), than those described above. It is relatively difficult to distinguish the $k = 0.15$ fibre from the $k = 0.20$ fibre by snaphots alone, but still there is a difference between them. Moment of inertia data show that the fibre formed in the system with the stronger face-to-face interaction ($k = 0.15$) was slightly longer and narrower (Fig.5.16). This, again, confirms our previous observation, that kinetics of the process appears to play a key role in fibre formation.



(a) (b)
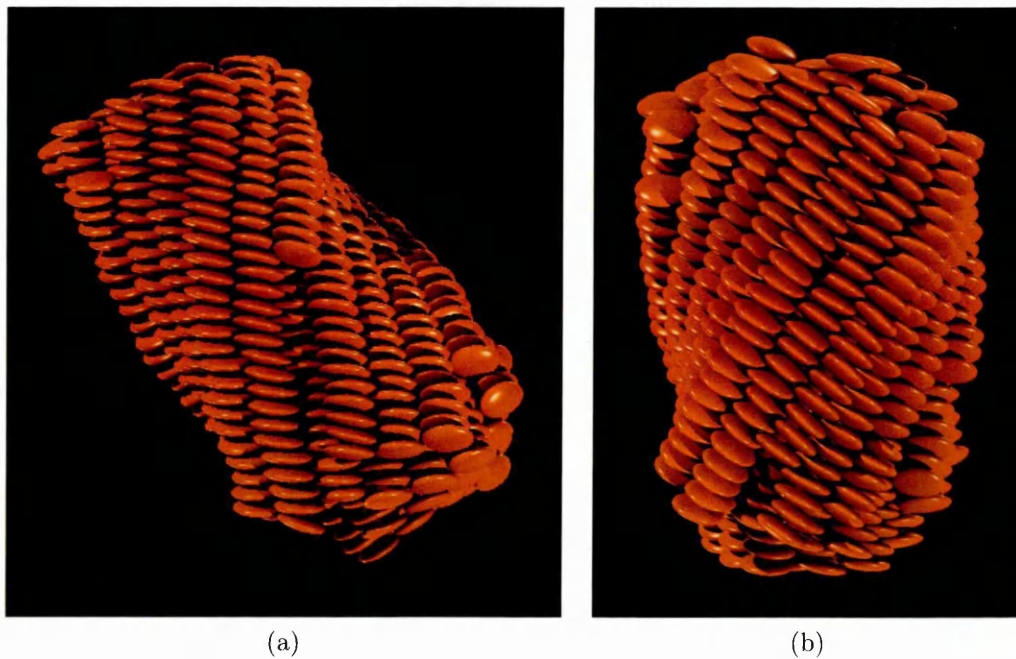
Figure 5.15: Side view of the fibres in $k = 0.15$ $T = 1.35$(a) and $k = 0.20$ $T = 1.08$ (b) systems
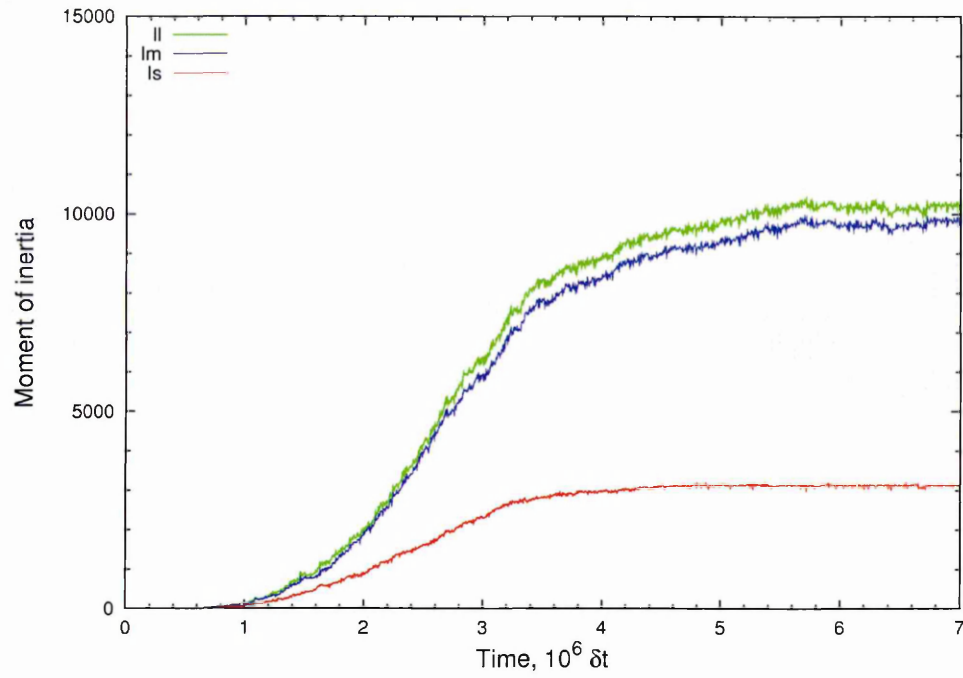
Figure 5.16: Moment of inertia of the biggest cluster for the $T = 1.35$ quench of the $k = 0.15$ system.
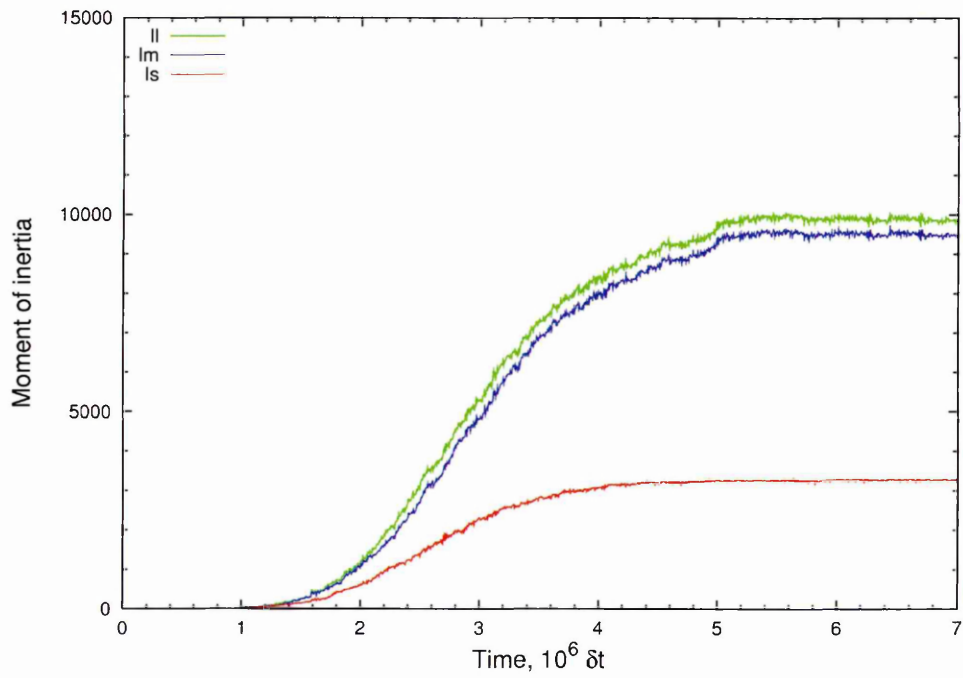


Figure 5.17: Moment of inertia of the biggest cluster for the $T = 1.08$ quench of the $k = 0.20$ system.

For these twisted fibers we also measured pitch values for all the of the long threads. While visually both fibres appear more helical than those for $k = 0.1$ and $k = 0.075$, results from fitting confirmed that the pitch remained unchanged.

| k = 0.15 T = 1.35 | | | k = 0.20 T = 1.08 | | |
|---|---|---|---|---|---|
| Thread | Radius | Pitch | Thread | Radius | Pitch |
| 1 | $0.812 \pm 0.003$ | $30.1 \pm 0.4$ | 1 | $0.729 \pm 0.005$ | $32.8 \pm 0.3$ |
| 2 | $0.885 \pm 0.005$ | $32.2 \pm 0.9$ | 2 | $0.844 \pm 0.004$ | $30.2 \pm 0.5$ |
| 3 | $0.911 \pm 0.009$ | $31.6 \pm 0.7$ | 3 | $0.854 \pm 0.009$ | $31.6 \pm 0.8$ |
| 4 | $1.035 \pm 0.007$ | $34.8 \pm 0.8$ | 4 | $1.068 \pm 0.009$ | $33.5 \pm 0.7$ |
| 5 | $1.064 \pm 0.003$ | $34.1 \pm 0.4$ | 5 | $1.095 \pm 0.005$ | $30.5 \pm 0.3$ |
| 6 | $1.100 \pm 0.005$ | $35.7 \pm 0.4$ | 6 | $1.188 \pm 0.003$ | $31.7 \pm 0.5$ |
| 7 | $1.500 \pm 0.009$ | $31.7 \pm 0.3$ | 7 | $1.441 \pm 0.008$ | $32.1 \pm 0.5$ |
| 8 | $1.529 \pm 0.009$ | $35.0 \pm 0.3$ | 8 | $1.459 \pm 0.003$ | $31.0 \pm 0.1$ |
| 9 | $1.637 \pm 0.003$ | $33.7 \pm 0.2$ | 9 | $1.623 \pm 0.004$ | $31.8 \pm 0.2$ |
| 10 | $1.680 \pm 0.006$ | $31.2 \pm 0.3$ | 10 | $1.642 \pm 0.007$ | $33.1 \pm 0.4$ |
| 11 | $1.747 \pm 0.007$ | $35.1 \pm 0.2$ | 11 | $1.661 \pm 0.006$ | $32.5 \pm 0.5$ |
| 12 | $1.781 \pm 0.008$ | $33.8 \pm 0.3$ | 12 | $1.778 \pm 0.006$ | $30.8 \pm 0.2$ |
| 13 | $1.787 \pm 0.008$ | $32.2 \pm 0.9$ | 13 | $1.800 \pm 0.007$ | $31.6 \pm 0.7$ |
| 14 | $1.825 \pm 0.005$ | $30.3 \pm 0.3$ | 14 | $1.832 \pm 0.007$ | $32.3 \pm 0.3$ |
| 15 | $1.855 \pm 0.003$ | $33.5 \pm 0.2$ | 15 | $1.841 \pm 0.001$ | $31.5 \pm 0.6$ |
| 16 | $2.019 \pm 0.013$ | $31.8 \pm 0.1$ | 16 | $1.996 \pm 0.013$ | $33.3 \pm 0.4$ |
| 17 | $2.035 \pm 0.004$ | $30.7 \pm 0.1$ | 17 | $2.015 \pm 0.003$ | $32.7 \pm 0.1$ |
| 18 | $2.056 \pm 0.005$ | $32.7 \pm 0.2$ | 18 | $2.145 \pm 0.006$ | $30.8 \pm 0.1$ |
| 19 | $2.357 \pm 0.007$ | $30.4 \pm 0.2$ | 19 | $2.249 \pm 0.003$ | $35.4 \pm 0.3$ |
| 20 | $2.367 \pm 0.003$ | $31.4 \pm 0.1$ | 20 | $2.288 \pm 0.005$ | $32.7 \pm 0.5$ |
| 21 | $2.412 \pm 0.005$ | $33.1 \pm 0.2$ | 21 | $2.324 \pm 0.006$ | $33.8 \pm 0.6$ |
| 22 | $2.417 \pm 0.005$ | $32.1 \pm 0.2$ | 22 | $2.339 \pm 0.003$ | $31.4 \pm 0.3$ |
| 23 | $2.464 \pm 0.008$ | $34.1 \pm 0.1$ | 23 | $2.425 \pm 0.004$ | $32.7 \pm 0.2$ |
| 24 | $2.686 \pm 0.007$ | $33.7 \pm 0.2$ | 24 | $2.477 \pm 0.006$ | $31.8 \pm 0.1$ |
| 25 | $2.688 \pm 0.001$ | $32.7 \pm 0.2$ | 25 | $2.508 \pm 0.007$ | $30.4 \pm 0.8$ |
| 26 | $2.701 \pm 0.003$ | $30.2 \pm 0.1$ | 26 | $2.554 \pm 0.005$ | $32.7 \pm 0.9$ |
| 27 | $2.774 \pm 0.007$ | $31.7 \pm 0.2$ | 27 | $2.623 \pm 0.006$ | $33.8 \pm 0.5$ |
|  |  |  | 28 | $2.681 \pm 0.001$ | $34.7 \pm 0.3$ |
|  |  |  | 29 | $2.705 \pm 0.002$ | $32.7 \pm 0.2$ |
|  |  |  | 30 | $2.711 \pm 0.007$ | $33.6 \pm 0.4$ |
|  |  |  | 31 | $2.742 \pm 0.005$ | $31.1 \pm 0.4$ |
|  |  |  | 32 | $2.881 \pm 0.008$ | $30.9 \pm 0.6$ |

Table 5.3: Results of radius and pitch fitting for $k = 0.15$ and $k = 0.20$ fibers.

## 5.5   Pitch adjustment

The fact that the threads in all of the twisted fibres obtained thus far had quite close pitch values suggested that pitch is predetermined by the geometry (i.e. shape) of the buiding blocks (discs). To test this, we investigated whether it is possible to create fibres with different pitch by varying the shape (thickness, diameter) of discs.

As was mentioned in Section 5.1, hexagonal packing requires triplets of neighbouring threads to co-operatively interdigitate. A consistent handedness develops naturally in the stacking adopted at these triplet junctions. A ring of 6 co-operative triplets forms to give propeller-like motif, where outer particles have to tilt as well as interdigitate. Obviously, the flatter discs are, the flatter the 'propeller' we have, as 'blades' are less tilted in this case. Therefore, stacks of these flatter propellers should give a rise to a less twisted structure.

To test this hypothesis, we run an additional simulation with flatter discs (diameter $\sigma = 1.2$ and thickness $\sigma_{dd} = 0.25$). Again, temperatures of quench was varied so as to give a defect-free fibre.



<div align="center">(a)                                                       (b)</div>
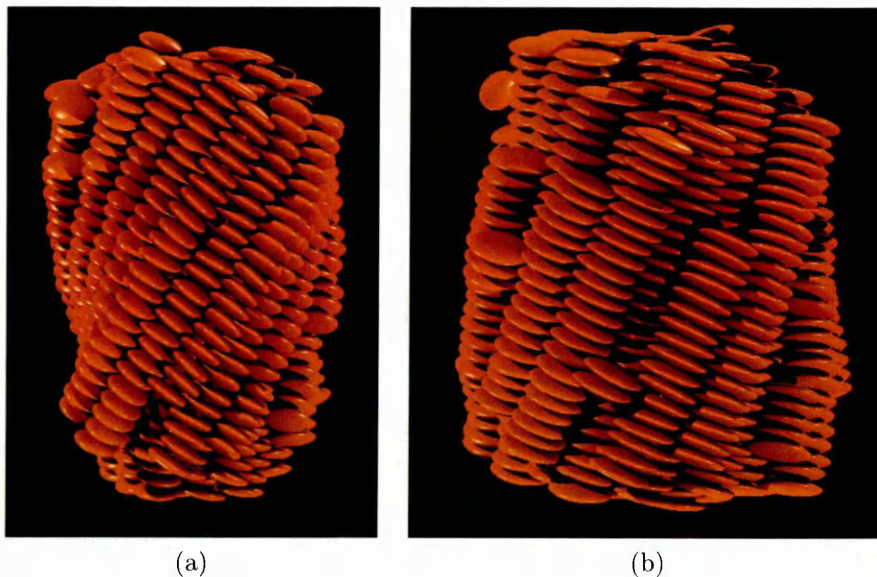
Figure 5.18: Side view of the $k = 0.20, \sigma = 1.0, \sigma_{dd} = 0.345$ $T = 1.08$ and $k = 0.20, \sigma = 1.2, \sigma_{dd} = 0.3$ $T = 1.55$ fibres. It is clearly seen, that second fibre has a higher pitch.

All threads within the resultant fibre were identified and fitted to helical curves. This clearly indicated an increase in the pitch value from $P \approx 32$ to $P \approx 55$ (Table 5.4), so confirming our previous hypothesis.

| $k = 0.20,\ \sigma = 1.0,\ \sigma_{dd} = 0.345\ T = 1.08$ | | | $k = 0.20,\ \sigma = 1.2,\ \sigma_{dd} = 0.3\ T = 1.55$ | | |
|---|---|---|---|---|---|
| Thread | Radius | Pitch | Thread | Radius | Pitch |
| 1 | $0.729 \pm 0.005$ | $32.8 \pm 0.3$ | 1 | $1.137 \pm 0.009$ | $54.6 \pm 0.4$ |
| 2 | $0.844 \pm 0.004$ | $30.2 \pm 0.5$ | 2 | $1.204 \pm 0.007$ | $51.9 \pm 0.2$ |
| 3 | $0.854 \pm 0.009$ | $31.6 \pm 0.8$ | 3 | $1.195 \pm 0.007$ | $58.7 \pm 0.2$ |
| 4 | $1.068 \pm 0.009$ | $33.5 \pm 0.7$ | 4 | $1.231 \pm 0.008$ | $50.5 \pm 0.1$ |
| 5 | $1.095 \pm 0.005$ | $33.5 \pm 0.3$ | 5 | $1.264 \pm 0.006$ | $55.6 \pm 0.2$ |
| 6 | $1.188 \pm 0.003$ | $31.7 \pm 0.5$ | 6 | $1.199 \pm 0.006$ | $50.7 \pm 0.1$ |
| 7 | $1.441 \pm 0.008$ | $32.1 \pm 0.5$ | 7 | $1.781 \pm 0.008$ | $54.8 \pm 0.1$ |
| 8 | $1.459 \pm 0.003$ | $31.0 \pm 0.1$ | 8 | $1.844 \pm 0.003$ | $56.0 \pm 0.1$ |
| 9 | $1.623 \pm 0.004$ | $31.8 \pm 0.2$ | 9 | $1.847 \pm 0.004$ | $50.4 \pm 0.2$ |
| 10 | $1.642 \pm 0.007$ | $33.1 \pm 0.4$ | 10 | $1.963 \pm 0.005$ | $58.4 \pm 0.1$ |
| 11 | $1.661 \pm 0.006$ | $32.5 \pm 0.5$ | 11 | $1.964 \pm 0.006$ | $50.5 \pm 0.1$ |
| 12 | $1.778 \pm 0.006$ | $30.8 \pm 0.2$ | 12 | $2.006 \pm 0.007$ | $55.8 \pm 0.3$ |
| 13 | $1.800 \pm 0.007$ | $31.6 \pm 0.7$ | 13 | $2.093 \pm 0.009$ | $51.5 \pm 0.2$ |
| 14 | $1.832 \pm 0.007$ | $32.3 \pm 0.3$ | 14 | $2.110 \pm 0.011$ | $54.7 \pm 0.3$ |
| 15 | $1.841 \pm 0.001$ | $31.5 \pm 0.6$ | 15 | $2.202 \pm 0.006$ | $53.0 \pm 0.5$ |
| 16 | $1.996 \pm 0.013$ | $33.3 \pm 0.4$ | 16 | $2.218 \pm 0.009$ | $53.2 \pm 0.7$ |
| 17 | $2.015 \pm 0.003$ | $32.7 \pm 0.5$ | 17 | $2.296 \pm 0.010$ | $62.1 \pm 0.9$ |
| 18 | $2.145 \pm 0.006$ | $30.8 \pm 0.6$ | 18 | $2.299 \pm 0.010$ | $54.1 \pm 0.2$ |
| 19 | $2.249 \pm 0.003$ | $35.4 \pm 0.3$ | 19 | $2.790 \pm 0.009$ | $59.2 \pm 0.3$ |
| 20 | $2.288 \pm 0.005$ | $32.7 \pm 0.5$ | 20 | $2.801 \pm 0.007$ | $52.8 \pm 0.6$ |
| 21 | $2.324 \pm 0.006$ | $33.8 \pm 0.6$ | 21 | $2.824 \pm 0.006$ | $56.7 \pm 0.5$ |
| 22 | $2.339 \pm 0.003$ | $31.4 \pm 0.3$ | 22 | $2.841 \pm 0.007$ | $55.2 \pm 0.4$ |
| 23 | $2.425 \pm 0.004$ | $32.7 \pm 0.2$ | 23 | $2.883 \pm 0.005$ | $53.3 \pm 0.3$ |
| 24 | $2.477 \pm 0.006$ | $31.8 \pm 0.1$ | 24 | $2.945 \pm 0.005$ | $59.2 \pm 0.2$ |
| 25 | $2.508 \pm 0.007$ | $30.4 \pm 0.8$ | 25 | $2.995 \pm 0.008$ | $54.4 \pm 0.6$ |
| 26 | $2.554 \pm 0.005$ | $32.7 \pm 0.9$ | 26 | $3.006 \pm 0.009$ | $55.7 \pm 0.8$ |
| 27 | $2.623 \pm 0.006$ | $33.8 \pm 0.5$ | 27 | $3.026 \pm 0.012$ | $53.8 \pm 0.3$ |
| 28 | $2.681 \pm 0.001$ | $34.7 \pm 0.3$ | 28 | $3.184 \pm 0.007$ | $51.1 \pm 0.9$ |
| 29 | $2.705 \pm 0.002$ | $32.7 \pm 0.2$ | 29 | $3.017 \pm 0.007$ | $56.3 \pm 0.7$ |
| 30 | $2.711 \pm 0.007$ | $33.6 \pm 0.4$ | 30 | $3.071 \pm 0.010$ | $53.9 \pm 0.2$ |
| 31 | $2.742 \pm 0.005$ | $31.1 \pm 0.4$ | 31 | $3.157 \pm 0.011$ | $50.7 \pm 0.5$ |
| 32 | $2.881 \pm 0.008$ | $30.9 \pm 0.6$ | | | |

Table 5.4: Results of radius and pitch fitting for $k = 0.20$ fibres with different particle shape.

## 5.6    System size and concentration effects

The observation of fibre self-assembly poses an interesting question about the possibility of mechanisms limiting lateral growth. At first, it appears that a fibre can grow in size until the supply of free monomers is depleted. However, it appears from experiments on some systems [1-9], that after some time lateral growth stops and fibre diameters become fixed. A number of different explanations have been suggested to explain this observed finite fibre width, including the influence of long-range interactions [53], kinetic limitations to the bundle size [54], and in-plane shear elastic stresses, arising due to chirality [55]. The first two of these were originally proposed for the systems involving aggregation of charged particles. As there are no such intercations in our model, but the formed fibres do posses chirality, the last hypothesises appears to be the most relevant for our systems.

To characterise the possible presence of shear elastic stresses, we measured the average in-thread interaction strengths within our twisted fibres. We found, that for $k \geq 0.1$ this shows a marked dependence on radial layer number, the 12 threads in the third layer being 10% more weakly bound than those in the core (Fig.5.19). This trend is consistent with the notion that fibre radius may be self-limited, provided that the strain induced in the outer threads is sufficient.
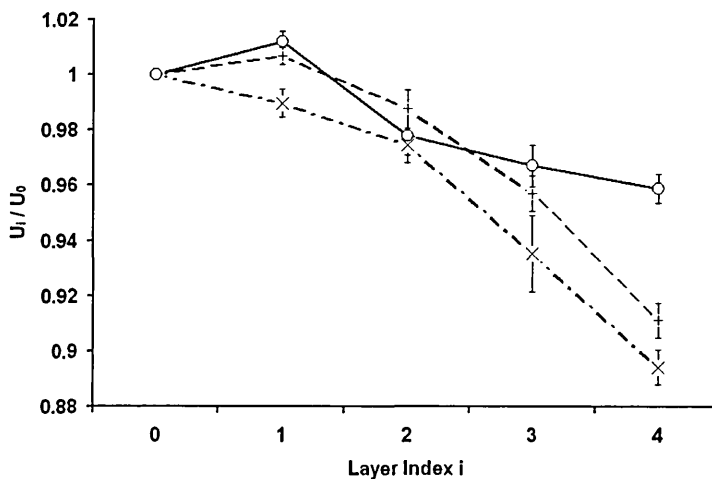


Figure 5.19: Relative in-thread interaction strengths for particles in different radial layers of completed threads: $k = 0.1$ circles; $k = 0.15$ pluses; $k = 0.2$ crosses;

To explore this effect, we ran an additional simulation of a larger system with $N = 19652$ particles ($N_{discs} = 1965$) with $k = 0.075$ at $T = 2.3$. This reproduces the conditions (relative concentration of discs, temperature) of the previously-studied $k = 0.075$ system. Similar to the original-size system, a sigle twisted fibre self-assembled in this run. Due to the higher number of available monomers though, this fibre could continue to grow beyond the previously observed dimensions, both laterally and longitudinally. As a result, the formed fibre was noticably larger, but no limitations of lateral growth were found. Thus, our first conclusion is that there is either no limit on fibre diameter in our systems or the size of this enlarged system is still insufficient to probe this phenomenon. However, after an additional few million timesteps of simulation we noticed that a slight jump occured in the disc orientational order parameter value (Fig.5.20).
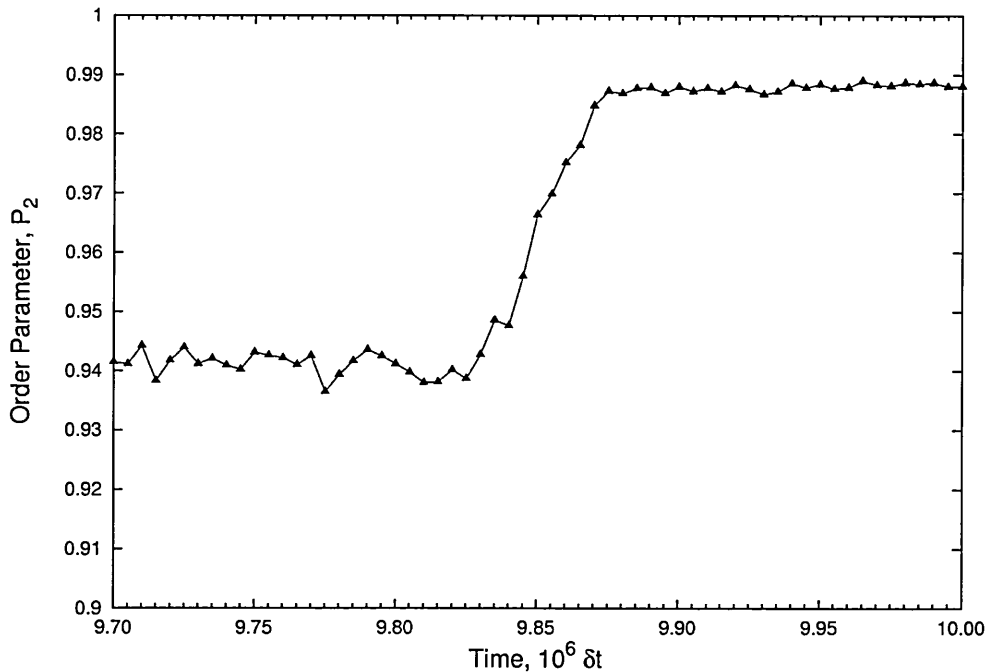


Figure 5.20: Order parameter data vs time for the $k = 0.075$, $N = 19652$ ($N_{discs} = 1965$) $T = 2.3$ system.

Visual inspection of configurational snapshots confirmed these data. In a period between $9.8 \cdot 10^6$ and $9.9 \cdot 10^6$ timesteps the initially twisted fibre underwent a transition to a straight one (Fig.5.21). Importantly, despite these significant structural changes, the fibre size (number of discs) remained stable (Tab.5.5).



(a) t=9855000
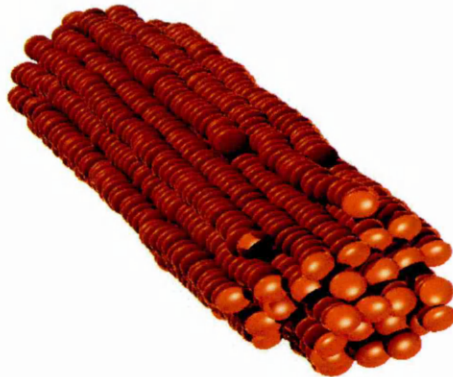


(b) t=9900000

Figure 5.21: Straightening transition of a fibre in the $k = 0.075$, $N = 19652$ ($N_{discs} = 1965$) $T = 2.3$ system.

To probe the mechanism of this transition, we used post-processing to measure the total energy of the interactions between the discs within the fibre and found that it decreased during the transformation (Fig.5.22). Thus, one can infer that there had been a free energy barrier between the twisted and the more stable straight states. Presumably, the height of this barrier reduces with lateral growth of a fibre, due to the increasingly strained outer threads, thus increasing the probability of

the transition.  From this, we can refine our previous inference that the radius of twisted fibres should be limited in our systems, since they become unstable and straightening once they achieve a certain radius.

| Timestep | Order Parameter | Number of Monomers |
|----------|-----------------|--------------------|
| 9820000 | 0.940174 | 1896 |
| 9825000 | 0.93869 | 1896 |
| 9830000 | 0.942755 | 1895 |
| 9835000 | 0.947625 | 1894 |
| 9845000 | 0.955973 | 1894 |
| 9850000 | 0.966373 | 1894 |
| 9855000 | 0.969856 | 1894 |
| 9860000 | 0.975185 | 1893 |
| 9865000 | 0.978078 | 1893 |
| 9870000 | 0.984805 | 1894 |
| 9875000 | 0.987234 | 1894 |
| 9880000 | 0.986855 | 1895 |
| 9885000 | 0.987715 | 1895 |
| 9890000 | 0.987877 | 1896 |
| 9895000 | 0.986896 | 1895 |
| 9900000 | 0.987996 | 1897 |

Table 5.5: Order parameter data combined with number of discs in the big fibre simulation with $k = 0.075$, $N = 19652$ ($N_{discs} = 1965$) $T = 2.3$.
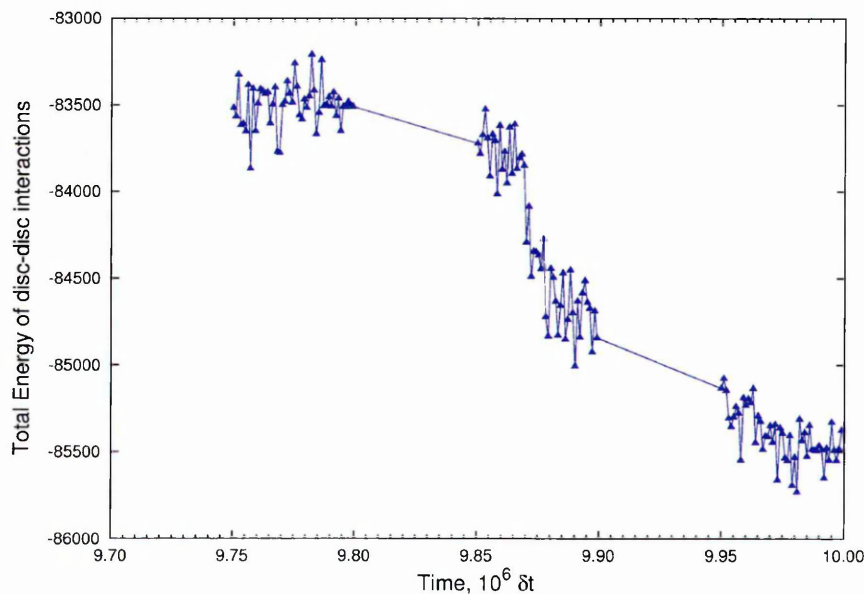


Figure 5.22: Total energy of disc-disc interactions in the big fibre simulation with $k = 0.075$, $N = 19652$ ($N_{discs} = 1965$) $T = 2.3$. Only stored values are shown (for the first 50000 $dt$ from each 100000 $dt$ cycle)

To test the role of induced strain in the fibre straightening process, we additionally measured the distribution of energy within the individual threads and studied how this changed during the transition. For each thread, the total energy of the disc-disc interactions was calculated and divided by the number of discs in the thread. These results qualitatively confirm the notion that straightening reduces the strain in individual threads, as the distribution of average per particle energies flattens out during the transition (Fig.5.23).
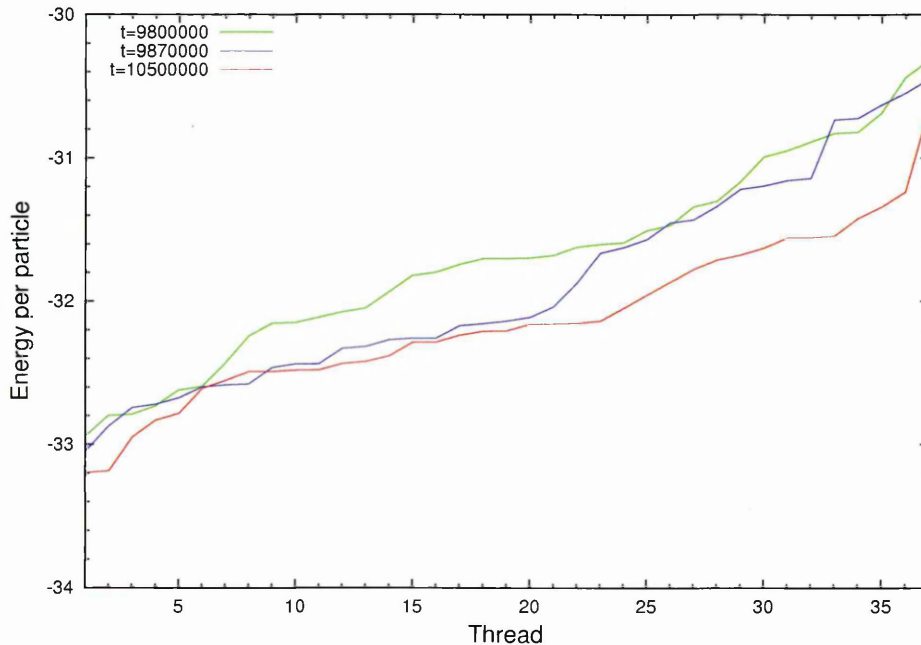


Figure 5.23: Distribution of energies within threads in the large fibre for the $k = 0.075$, $N = 19652$ ($N_{discs} = 1965$) $T = 2.3$ system. Timesteps before, in the middle of and after the transition are shown.

To probe this further we also studied a number of systems with doubled concentration of discs, i.e. $N_{total} = 8788$ and $N_{discs} = 1600$. In the first runs with this concentration we needed to find an optimal temperature again. As the concentration of discs was increased, the probability of nucleation got higher and, so, higher temperatures were required to grow a single defect-free fibre. After few test runs at different temperatures, finally, at $T = 2.42$ an appropriate growth mode was achieved for $k = 0.075$. In this system, the formed fibre remained twisted for a very long time. However, at $t = 17.5 \cdot 10^6 dt$ it too underwent a transition to

a straight state.  This result demonstrates that it is possible to observe the fibre straightening transition with even fever ( i.e.  lower than 1900) discs in the fibre. In-thread and interthread energies were measured to gain a better understanding of the straightening process.  The ratio of these two energies was found to increase during the transition (Fig.5.24).
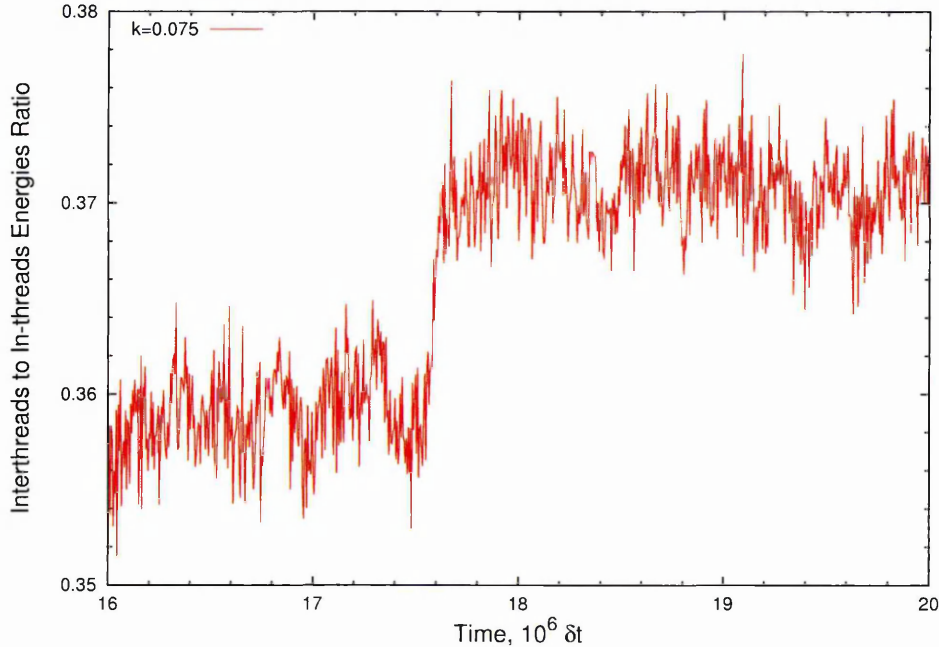


Figure 5.24: Ratio between interthread and in-thread energies for the large fibre in case of $k = 0.075$.

This means that the observed reduction of total energy was mainly driven by a decrease in the interaction energy between the threads (the interthread energy). Thus, one can state that the fibre sacrificed thread interdigitation in favour of thread orientaitional order.  This finding indicates that our previous conjecture, that un-twisting is driven by the desire to reduce in-thread stress is over simplistic.  We, therefore, should in first place consider the influence of the interthread contribution to the total energy of disc-disc interactions.  So as to enable quantitative compar-isons to be made between systems with different $k$, we also need to take into account that each system has its own optimal temperature $T_{optimal}$ (Fig.5.25).  This can be accounted for by scaling energies with $1/k_B T_{optimal}$.  Calculations show, that as $k$ is

increased, the interdigitation contribution becomes stronger, while the face-to-face interactions become less significant (Tab.5.6). This means that the temperature normalised energy barrier, associated with interthread energy, grows with increased $k$. Thus for $k \geq 0.075$ untwisting should become less likely.

| $k \cdot T_{optimal}$ | $0.05 \cdot 3.2$ | $0.075 \cdot 2.3$ | $0.10 \cdot 1.815$ | $0.15 \cdot 1.35$ | $0.20 \cdot 1.08$ |
|---|---|---|---|---|---|
| $U_{ff}/T_{optimal}$ | 16.43 | 15.25 | 14.49 | 12.99 | 12.18 |
| $U_{ee}/T_{optimal}$ | 0.82 | 1.14 | 1.48 | 1.95 | 2.43 |

Table 5.6: Energy calculations data for different $k$.

This hypothesis was confirmed by an additional run in a $k = 0.1$ double concentration system at $T = 1.95$. Here, no straightening transition was observed during a $50 \cdot 10^6$ timesteps run. We plot a diagram, which summarises our findings regarding to the formation of twisted and straight fibres on Fig.5.25. This will be discussed within a context of the next (concluding) section of this chapter.
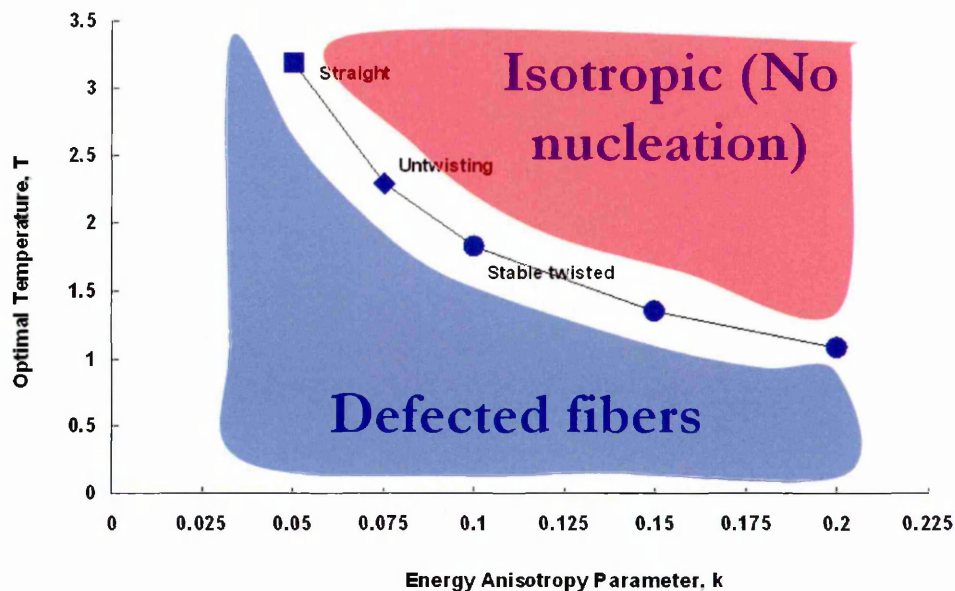


Figure 5.25: Optimal temperature for systems with different $k$.

## 5.7   Summary and conclusions

In this chapter we have presented the results from series of constant NVT simulations of various disc-sphere systems, conducted in order to gain understanding of fibre-formation processes. We found that the self-assembly of a fibre is a complex, hierarchical process, which requires certain physical conditions to be met. With $R = 1$, cooling initially isotropic mixtures led to the development of numerous linear stacks of discs, consistent with previous simulations of chromonic self assembly [15, 27, 26]. These stacks were well solvated and did not condense into a single aggregate on further cooling - lateral aggregation of the stacks was inhibited by the strongly associated solvation shells. However, changes in the disc-sphere interaction did trigger this aggregation: in systems with $R = 5$, where the rims of the discs were rather less solvophilic, further assembly of stacks was observed.

On gently cooling such systems, the equilibrium arrangement was a solution of monomer discs and length-polydisperse chromonic stacks. Deep quenching promoted the development of multi-stack clusters which eventually coalesced, each such simulation leading to a single aggregate which comprised virtually all of the discs. These final aggregates were generally fibrillar (i.e. approximately cylindrical) but contained stacking defects, some sections having opposing chiralities and others zero chirality. For a narrow temperature range between the chromonic stack and misshape fibre regions, however, defect-free chiral fibres could freely self-assemble on quenching an initially isotropic configuration.

The process of defect-free fibre self-assembly involved a certain hierarchy of intermediate steps and competing growth mechanisms. We have identified these by performing cluster-evolution analysis using configurational snapshots of the $k = 0.1$ system. To display the findings, we have divised a colour scheme, in which each disc is coloured according to the role it plays in the fibre formation process. Initially, this required analysis of the final configuration of the fibre. All of the discs in each

simulation were numbered and those belonging to threads in the final fibre, were stored in a corresponding series of arrays. By applying a cluster recognition algorithm based on these arrays, we were then able to characterise particles and threads in earlier configuration.
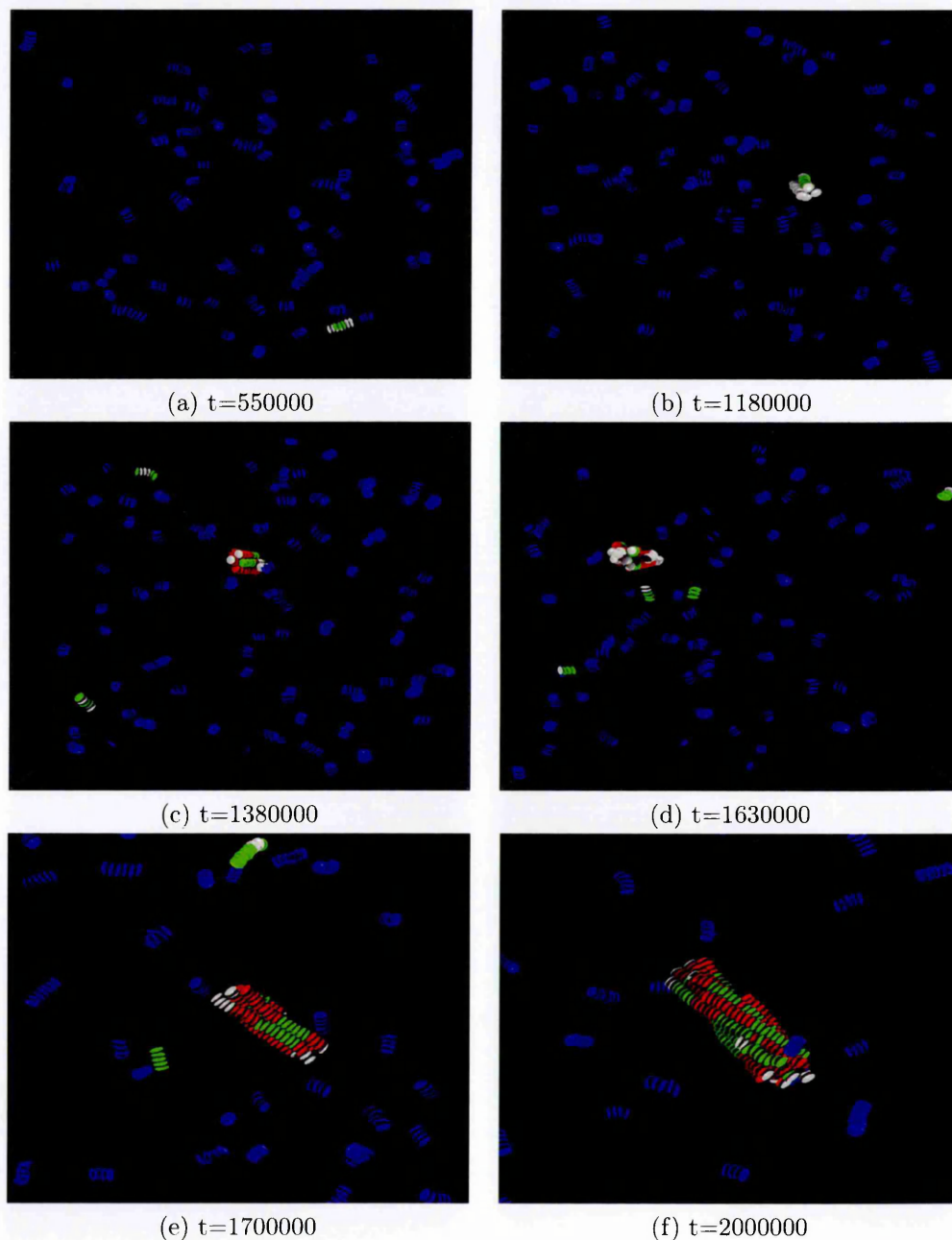


Figure 5.26: Stages of hierarchical self-assembly in $k = 0.1$ ($N_{total} = 8788$, $N_{discs} = 880$). Discs which join the fibre as a pre-existing stable stack are colored green; particles which did not join as stacks but which will continue to reside in their current thread - red; other peripheral particles which will be shed to solution or other threads - white; stacks having no relation to the final configuration - blue.

In the early stages, the initially monomeric discs underwent chromonic self-assembly and formed numerous orientationally disordered stacks (Fig.5.26(a)). These were the first level of supramolecular entity required for fibre formation. The longest of these stacks were, effectively, flexible cylinders with length to breadth ratio 2-3. The vast majority of these stacks (i.e. all those colored blue (Fig.5.26) did not join the aggregating fibre directly - they simply dissociated in solution. However, occasional stack-stack association proved crucial to the fibre nucleation process.

As the population of stacks grew, two- and three-stack bundles occasionally developed (Fig.5.26(b)). These bundles were very dynamic and, in most cases, dissociated into independent stacks. Where bundles were longer-lived, though, their parent stacks commonly adopted an intertwined side-by side arrangement. Fig.5.26 (c),(d),(e) show the early stages of what became the dominant bundle. This comprised several threads made up of identifiable parent stacks (green), discs which had joined as monomers (red) and unstable discs (white) which would go on to be shed to solution or to other threads. For most parameterizations, such embryonic fibres exhibited considerable flexibility. Animations show the constituent threads exploring alternative interdigitations, the aggregates switching en masse between right-handed, left-handed and achiral arrangements.

Monomer discs were highly disfavoured from initiating new threads on the sides of growing fibres - due to their shape, monomer discs tend to self-poison lateral fibre growth [56]. Thus, in virtually all cases, fibre broadening was initiated by a previously solvated stack docking into a helical or linear groove running along the side of the fibre. These previously-identified stacks of 4 or more discs are also coloured green in Fig.5.26. These additive lateral stacks subsequently either dissociated back into solution or grew along the templating groove. Recently aggregated particles and stacks retained a significant degree of flexibility after joining the fibre. This proved crucial to them achieving defect-free consistency with the core nucleus. Typically, however, only 25 percent of the discs in any final fibre could be identified as both
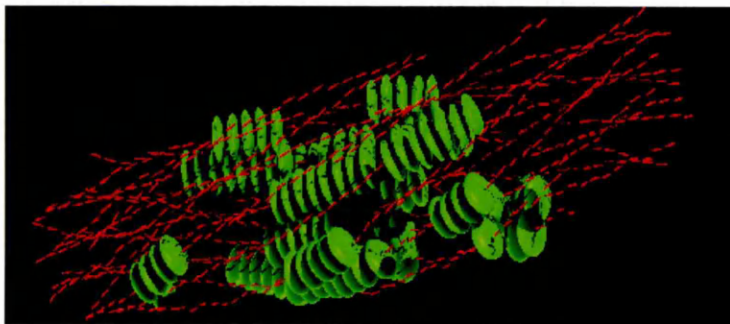
Figure 5.27: Final configuration of fibre in $k = 0.1$ $T = 1.825$ system at $t = 7 \cdot 10^6 dt$. Particles which joined as pre-existing stacks are shown in green.

joining as a stack of 4 particles or more and residing in a single thread of the final fibre (Fig.5.27).

It was very rare for stacks to join pre-existing threads. Rather, the dominant growth modes were longitudinal thread extension via monomer and small group addition and discs hopping between the ends of neighboring threads. As the bundle grew into a fibre, the frequency of en masse rearrangements decreased. Eventually, the aggregate size became sufficient for the symmetry of its nucleus to become locked in for the remainder of the self assembly process (Fig.5.26(f)). The locking-in event could be clearly characterised by the associated attenuation of order parameter fluctuations (Fig.5.28).
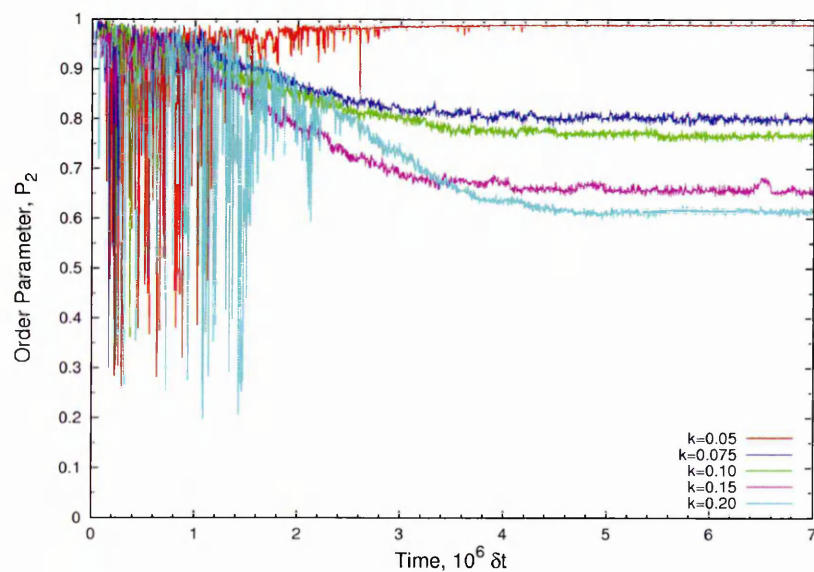


Figure 5.28: Order parameter data for the biggest cluster in different systems.

If more than one fixed-symmetry nucleus developed because, for example, a system was quenched too deeply, it was the subsequent coalescence of these potentially incompatible nuclei that led to misshapen fibre formation. Since all nuclei initiate via bundling of parent stacks, it is clear that limiting the stack number density is key to restricting fibre defects. This was achieved by following kinetic crossover ideas [57], whereby the yield of states which are thermodynamically stable but kinetically inaccessible is optimised at intermediate temperatures.The optimal temperature $T_{optimal}$, at which the defect-free fibres formed, decreased with increasing $k$. Thus, for instance, $T_{optimal} = 3.2$ in $k = 0.05$ system , while for $k = 0.20$ this temperature $T_{optimal} = 1.08$, ( recall Fig.5.25).

Provided that the correct temperature regime was accessed, fibre symmetry and growth modes were reproducibly dependent on the choice of disc-disc interaction parameter $k$. This parameter defines the strength of the face-to-face attraction between discs. For strong face-face interactions ($k = 0.05$) (i.e. relatively stiff threads) the resultant fibre was highly extended and achiral (Fig.5.29).

Further weakening of the face-face interaction ($k = 0.075$ to $k = 0.2$) led to progressively shorter and wider chiral fibres (Fig.5.30). The structures obtained here also show a remarkable resemblance to the experimental helical mesostructures (Fig.5.31) reported in [58] .

We conclude from this, that the observed $k$-dependence of the fibre shapes is due to the effect of $k$ on the relative accretion rates of the competing growth processes. This follows from analysis of the lateral and elongation growth rates, as characterised by timelines of the fibre moment of inertia tensor components for different $k$ (Fig.5.32, Fig.5.33). These show that higher $k$ (weaker face-to-face attraction) is associated with a reduced longitudinal growth rate and increased lateral growth rate.
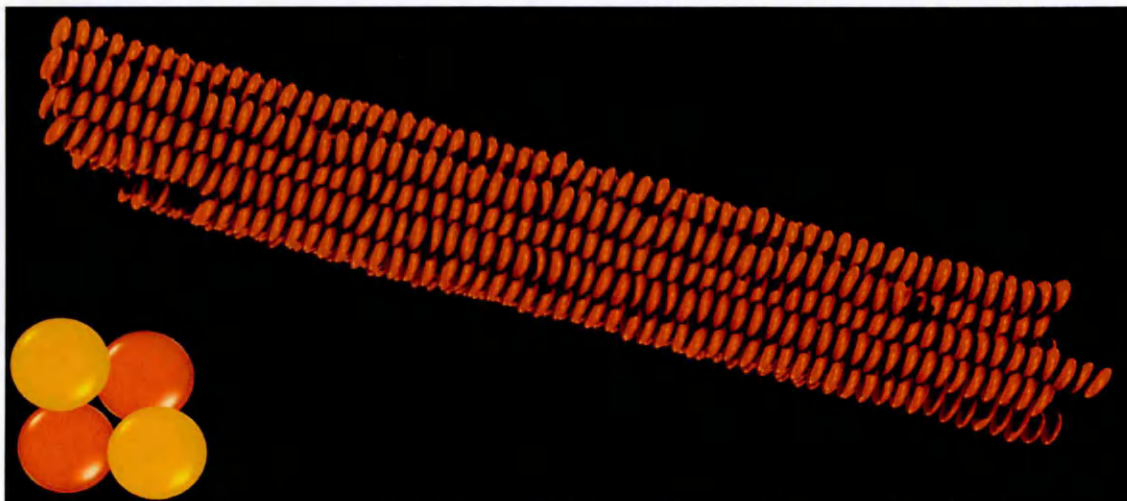
Figure 5.29: Snapshots of final fibre in $k = 0.05$ $T = 3.2$ system at $t = 7 \cdot 10^6 dt$
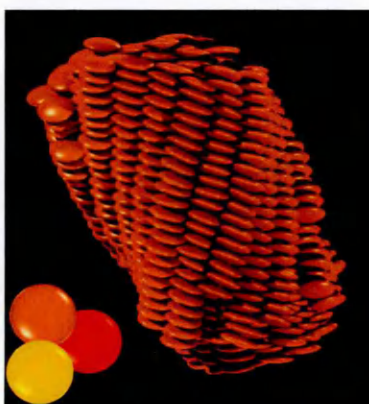


(a) $k = 0.20$



(b) $k = 0.075$
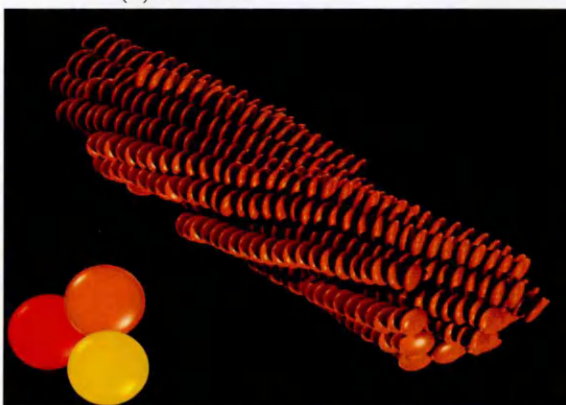


(c) $k = 0.10$



(d) $k = 0.15$

Figure 5.30: Snapshots of final fibres obtained with different $k$ values. Schematics show thread interdigitations.

(a) (b)
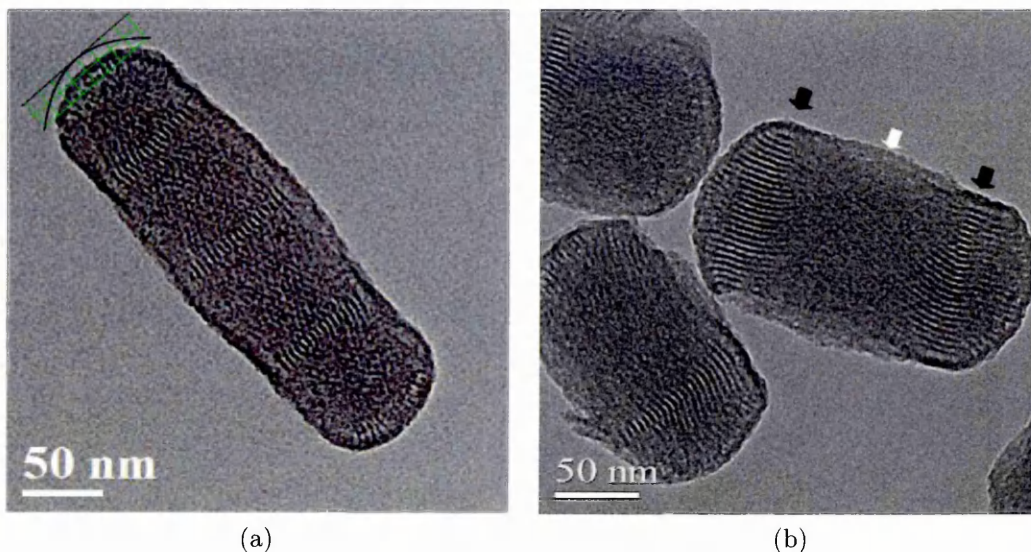
Figure 5.31: TEM images of S1 (a) and calcined sample (b) described in [58]. This paper reports the synthesis of helical mesoporous materials by using achiral surfactants. At high magnification images show a periodic fringes, indicative of chiral channels within the helical rods (the fringes indicated by dark and white arrows). Each helical rod possesses two rounded ends viewing along the direction perpendicular to the rods, while the shape of the end (cross section) shows a hexagonal plane. Particle-shape influence on the final structure was mentioned, as was the effect of surfactant size on the resultant helical pitch.
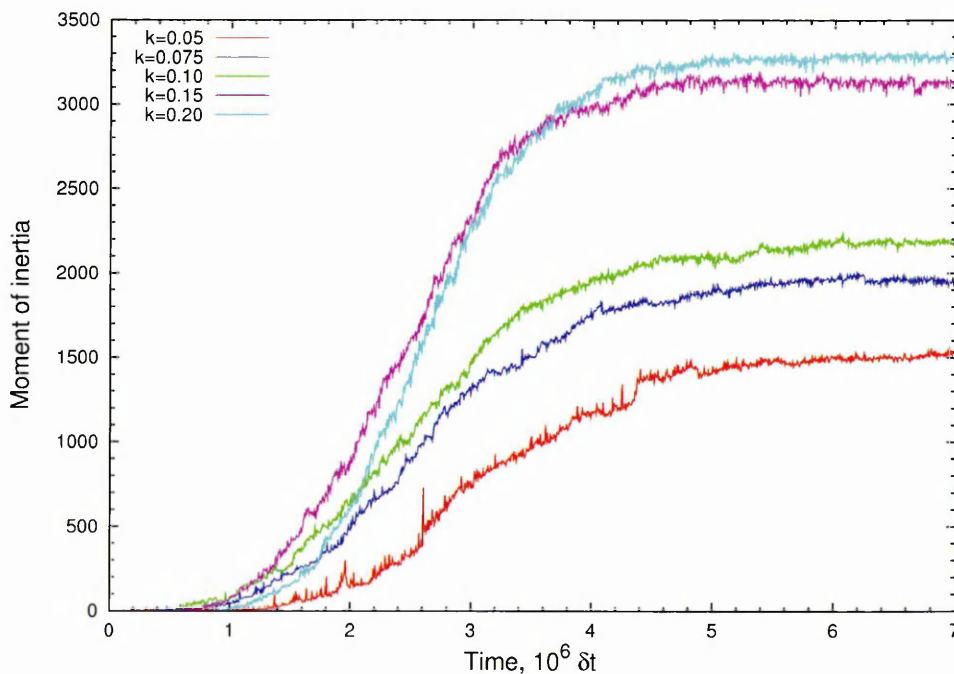


Figure 5.32: Smallest component of moment of inertia for the biggest cluster in different systems.
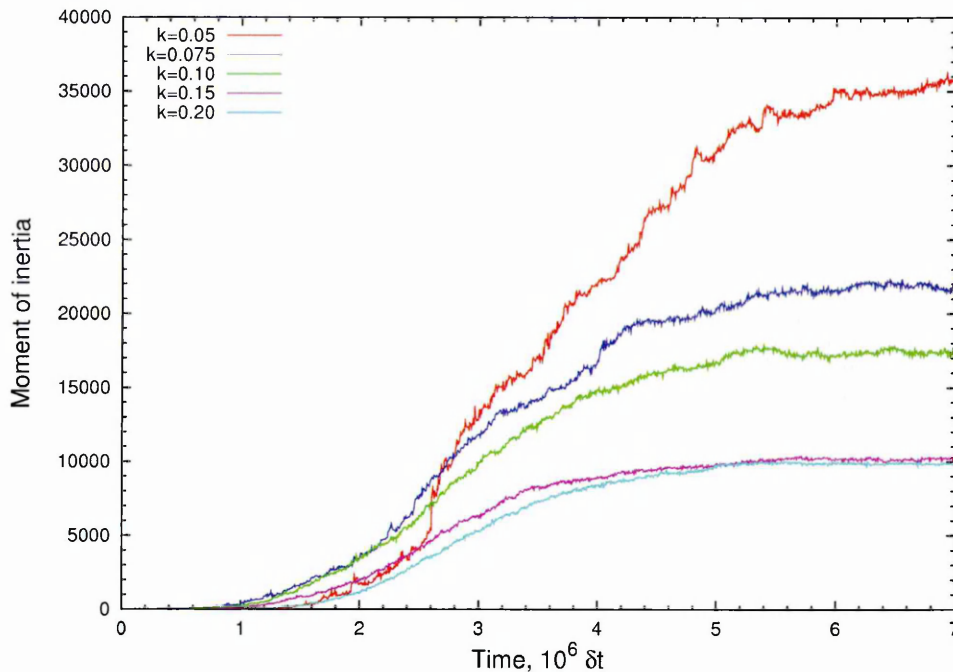
Figure 5.33:  Largest component of moment of inertia for the biggest cluster in different systems.

However, as we showed in Section 5.6, the influence of $k$ on fibre formation is actually even more complex due to the additional possibility of fibre unwinding. We found that the temperature-normalised energy barrier between the two possible fibre states (twisted and straight), lowers with decreasing $k$. This is explained by the fact that the strength of the edge-to-edge interactions between discs is the same in all systems ($\epsilon_{ee} \approx 2.63$), i.e. does not vary with $k$. However, as the optimal temperature $T_{optimal}$ does depend on $k$, the interthread interaction does change in terms of $k_b T$. This was confirmed by simulations (see previous section) which showed that a chiral fibre can exhibit a straightening transition in the case of $k = 0.075$, provided it contains sufficient threads. That we did not observe this transformation in other systems, suggests that the straightening transition is inaccessible to systems with higher $k$ due to the strengthening of the interthread energies.

Thus, as simulation data and animations show, self-assembly of a defect-free fibre is a complex, multi-stage process, which only succeeds provided certain conditions are met. In particular, the temperature needs to be controlled so as to limit

the system to a single nucleation event. We also identified that fibre shape has a kinetic control mechanism due to the differential aggregation rates of longitudinal and lateral growth modes. These aggregation rates can be varied, by controlling the strength of the interparticle interaction parameters. Additionally, the resultant pitch of the twisted fibre can be adjusted by using particles with different shape. We believe that results of this work provide a comprehensive insight into the mechanisms of fibre formation and provide considerable insight into the processes involved in experimental fibre forming systems.

# Chapter 6

# Self-assembly of solvent-stabilised structures

In Chapter 5, we described the self-assembly of fibrillar structures by systems with a moderate strength solvophilic interaction at the rim of the disc-shaped particles. These fibres comprised discs only, and no spheres were involved in the final structures. Here, we consider second class of aggregation which we have observed in disc-sphere systems: simulations that lead to assemblies which contain both discs and spheres.

We probe this behavior here by studying systems with strongly solvophilic rims. Additionally, we investigate the effect of breaking the cylindrical symmetry of the disc-sphere interactions, so that the solvophilic strength is able to vary around the rim.

In view of the increase in scope, implied by the consideration of this additional parameter, the approach adopted here is somewhat different from that adopted in the previous chapter. Specifically, we limit ourselves here to assessing the range of structures accessible to these systems; in-depth investigation of the underlying kinetic pathways involved in each of these is, though, beyond the scope of this thesis.

## 6.1  Self-assembly in systems with different repulsion strengths

A solvent plays significant role in the self-assembly of solvent-stabilised structures. A solvent molecules act here as linkers, making considerable contributions to the overall stability of the assemblies. As an example of such a structure, solvent-stabilized molecular capsules can be considered, where water molecules stabilise a structure by hydrogen-bonding between building blocks [59, 60, 61].

With the disc-sphere systems studied in this thesis, we also found cases where the solvent particles could play a similar stabilising role, leading to the formation of assemblies which contained both discs and spheres. We initially identified this behaviour when we studied self-assembly in large-size systems with different repulsion strengths ($R = 0.5$, $R = 1$, $R = 1.5$ and $R = 2$). All major parameters were the same as those used previously: $N_{total} = 8788$, $N_{discs} = 880$, $\epsilon = 1$, $\epsilon_{DS} = 2.63$, $k = 0.1$. For these systems, the strength of the solvophilic interaction at the rim of the disc-shaped particles was increased, in comparison with these described in Chapter 5 (where $R = 5$).

We first discovered solvent-stabilised structures when we tried to reproduce the behavior of the small $R = 1$ systems considered in our preliminary simulations (recall Chapter 4). As for the small system, we set the temperature to $T = 0.7$. Again, the discs aggregated into stacks quite rapidly and, after $t = 60000dt$, almost no free monomers were left. In these larger simulations, however, a second level process became observable. As the spheres had a strong attraction to the disc rims, they acted to promote subsequent side-by-side aggregation of stacks. As a result, a typical assembly comprised highly-ordered columns of threads, joined by layers of spheres (Fig.6.1 (a)). At this low temperature, a significant number of these aggregates formed in the system, and gradually these all coalesced to give a single mis-shaped solvent-containing structure (Fig.6.2).

(a)                                             (b)
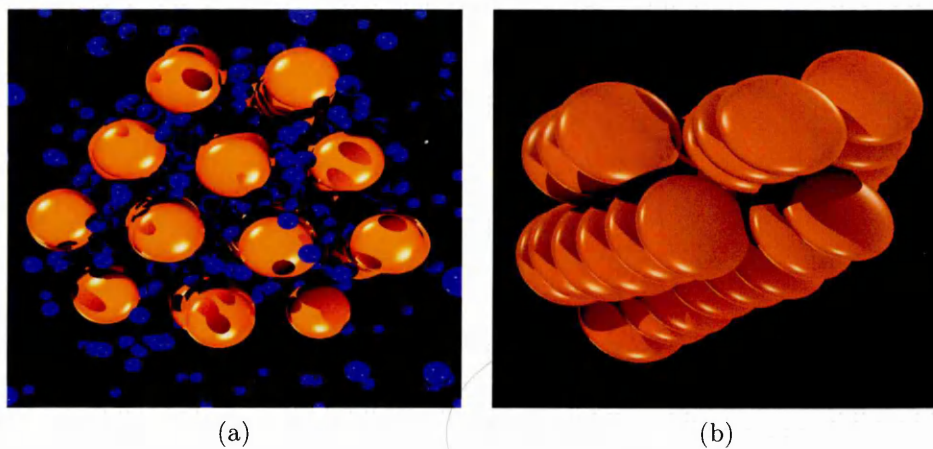
Figure 6.1: Typical clusters in $R = 1$ (a) and $R = 2$ (b) ( also $R = 5$) systems at $T = 0.7$. In the first snapshot discs are made smaller for clarity.
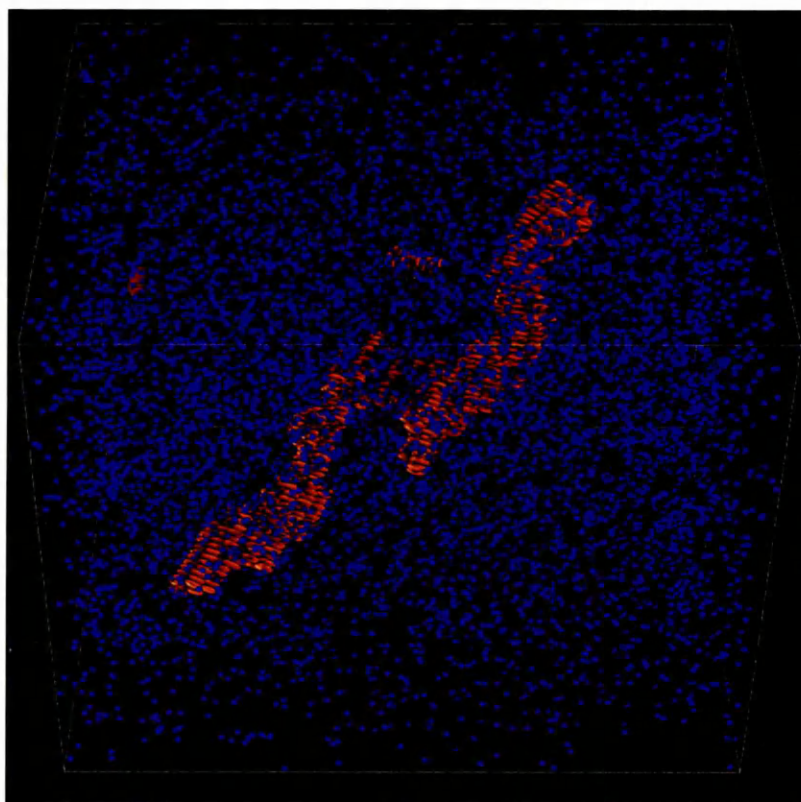


Figure 6.2: Misshaped solvent-containing fibre in $R = 1$ system at $T = 0.7$ after $t = 1.2 \cdot 10^6 dt$

Similar structures were observed at low temperatures ($T = 0.7$) with $R = 0.5$ and $R = 1.5$. However, with $R = 2$ the disc-disc interaction became dominant and aggregation of threads into short solvent-free fibres occured (Fig.6.1 (b)). This scenario was also seen in $R = 5$, $T = 0.7$ system, of course, where the disc-disc

interaction was even more dominant.

We also studied the large-system behaviour of the strongly solvophilic system ($R = 1$) at higher temperatures, in order to compare its results with those from the $k = 0.1$ $R = 5$ system (described in Chapter 5). Surprisingly, we found that at the same temperature as for the $R = 5$ system (i.e. $T = 1.82$), the solvent-free fibre can be formed even with $R = 1$. Therefore, following the approach we adopted for disc-disc interactions, we considered it would be more appropriate to categorise the strength of the disc-sphere interactions in terms of $k_B T$.

We also made an attempt to determine the temperature of crossover between the two different types of assembly. To identify this transitional temperature, we ran an additional series of simulations with $R = 1$ at increasing temperatures, starting from $T = 0.85$ in steps of $dT = 0.05$. From this, we found that this transition temperature lies in a range between $T = 1.35$ and $T = 1.40$. This temperature range proved too low, however, for the system to be restricted to a single nucleation event, and either misshaped solvent-containing or misshaped solvent free fibres formed.

Thus, we conclude that the effect of the parameter $R$ becomes increasingly apparent at low temperatures, where it influences the formation of solvent-stabilised structures, comprising both threads of discs and spheres. However, at higher temperatures, this behaviour appears to be metastable with respect to the type of defect-free disc fibres observed in the previous chapter.

# 6.2 'Tanh' potential

As we have just shown, it is possible to access solvent-stabilised structures using systems with cylindrically symmetric disk-sphere interactions. In the remainder of this chapter, we investigate how this behaviour can be extended by giving additional orientational dependence to the interparticle interactions. Specifically, we study the effect of modulating the disc-sphere energy parameter around the rim of the disc. This approach is similar to that which was applied by Michel [49], to model amphiphilic behaviour in rod-sphere systems. In Michel's model, the rod-sphere energy parameter incorporated a tanh function of the dot product between the interparticle and orientation vectors $\hat{\mathbf{r}}_{ij}$ and $\hat{\mathbf{u}}_j$.

Following Michel, therefore, we write:

$$\epsilon(\hat{\mathbf{r}}_{ij} \cdot \hat{\mathbf{u}}_j)_{tanh} = a + b \cdot \tanh\left(\frac{(\hat{\mathbf{r}}_{ij} \cdot \hat{\mathbf{u}}_j) - S}{l}\right). \tag{6.1}$$

where $S = 1 - \frac{2H}{100}$, $a = (\epsilon_{min} + \epsilon_{max})/2$ and $b = (\epsilon_{max} - \epsilon_{min})/2$. One can tune the parameters $a, b$ and $l$ to control the shape of the resultant energy parameter function. The parameter $l$ can change the slope of the growth part, $b$ controls the amplitude of the switch and $a$ is just a shifting value along the ordinate axis. The $S$ value can be used to set the location of the transition position either to positive or negative values of $\hat{\mathbf{r}}_{ij} \cdot \hat{\mathbf{u}}_j$. $\epsilon_{max}$ and $\epsilon_{min}$ define the levels of the potential. The parameter $H$ defines the extent of the solvophobic region.

Using the angular dependent potential, eqn. (6.1), Michel broke head-tail symmetry in his system to obtain an interaction where spheres favoured one end of the rods. This gave something analogous to the amphiphilic behaviour exhibited by molecules with hydrophilic and hydrophobic parts.

In order to break the symmetry of our model, we introduce an additional vector $\hat{\mathbf{u}}_{imin}$, which points towards the solvophilic rim region (i.e $\hat{\mathbf{u}}_{imin}$ is perpendicular to $\hat{\mathbf{u}}_i$, see Fig.6.3).
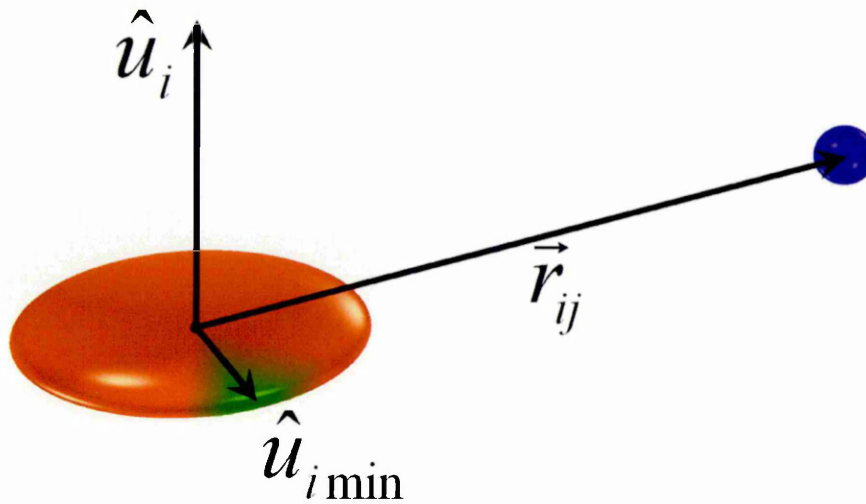
Figure 6.3: Orientation and position vectors in our modified disc-sphere model.

Modulating the energy parameter of the disc-sphere interaction using the above tanh function of the dot product $(\hat{\mathbf{r}}_{\mathbf{ij}} \cdot \hat{\mathbf{u}}_{\mathbf{imin}})$, we then obtain an interaction in which spheres favour only part of the rim of the disc. Accordingly, the resultant disc-sphere potential function takes the form:

$$U_{ij}^{ds}(\hat{\mathbf{r}}_{\mathbf{ij}}, \hat{\mathbf{u}}_{\mathbf{i}}, \hat{\mathbf{u}}_{\mathbf{imin}}) = 4\epsilon_{ds}(\hat{\mathbf{r}}_{\mathbf{ij}}, \hat{\mathbf{u}}_{\mathbf{i}})\epsilon_{tanh}(\hat{\mathbf{r}}_{\mathbf{ij}}, \hat{\mathbf{u}}_{\mathbf{imin}}) \left[ \left( \frac{\sigma_0}{r_{ij} - \sigma_{ds}(\hat{\mathbf{r}}_{\mathbf{ij}}, \hat{\mathbf{u}}_{\mathbf{i}}, \hat{\mathbf{u}}_{\mathbf{j}}) + \sigma_0} \right)^{12} - \right.$$
$$\left. \left( \frac{\sigma_0}{r_{ij} - \sigma_{ds}(\hat{\mathbf{r}}_{\mathbf{ij}}, \hat{\mathbf{u}}_{\mathbf{i}}, \hat{\mathbf{u}}_{\mathbf{j}}) + \sigma_0} \right)^{6} \right] \quad (6.2)$$

The additional functionality offered by this potential allows us to consider, at a coarse-grained level, the effects of rudimentary chemical detail on the solvent-stabilised structures accessible to our disc-sphere systems.

## 6.3    Effect of the size of the solvophilic region

To examine the behaviour of the modified tanh potential model, a further series of simulations was undertaken. These simulations were performed in the constant NVE and NVT ensembles using the MD algorithm described previously. In order to assess the capability of this model, systems with different $H$ values were studied, in particular: $H = 80$, $H = 50$, $H = 20$, $H = 10$ and $H = 5$ (Fig.6.4, Fig.6.5).



(a) Original model, $R = 1$, $k = 0.1$, $k'_{DS} = 0.2$, $\epsilon_{DS} = 2.63$

(b) Original model, side view

(c) $H = 80$, $a = 2.6$, $b = 2.4$, $l = 1/10$, $k = 0.1$, $k'_{DS} = 0.2$, $\epsilon_{DS} = 2.0$

(d) $H = 80$, side view

(e) $H = 50$, $a = 2.6$, $b = 2.4$, $l = 1/10$, $k = 0.1$, $k'_{DS} = 0.2$, $\epsilon_{DS} = 2.0$

(f) $H = 50$, side view
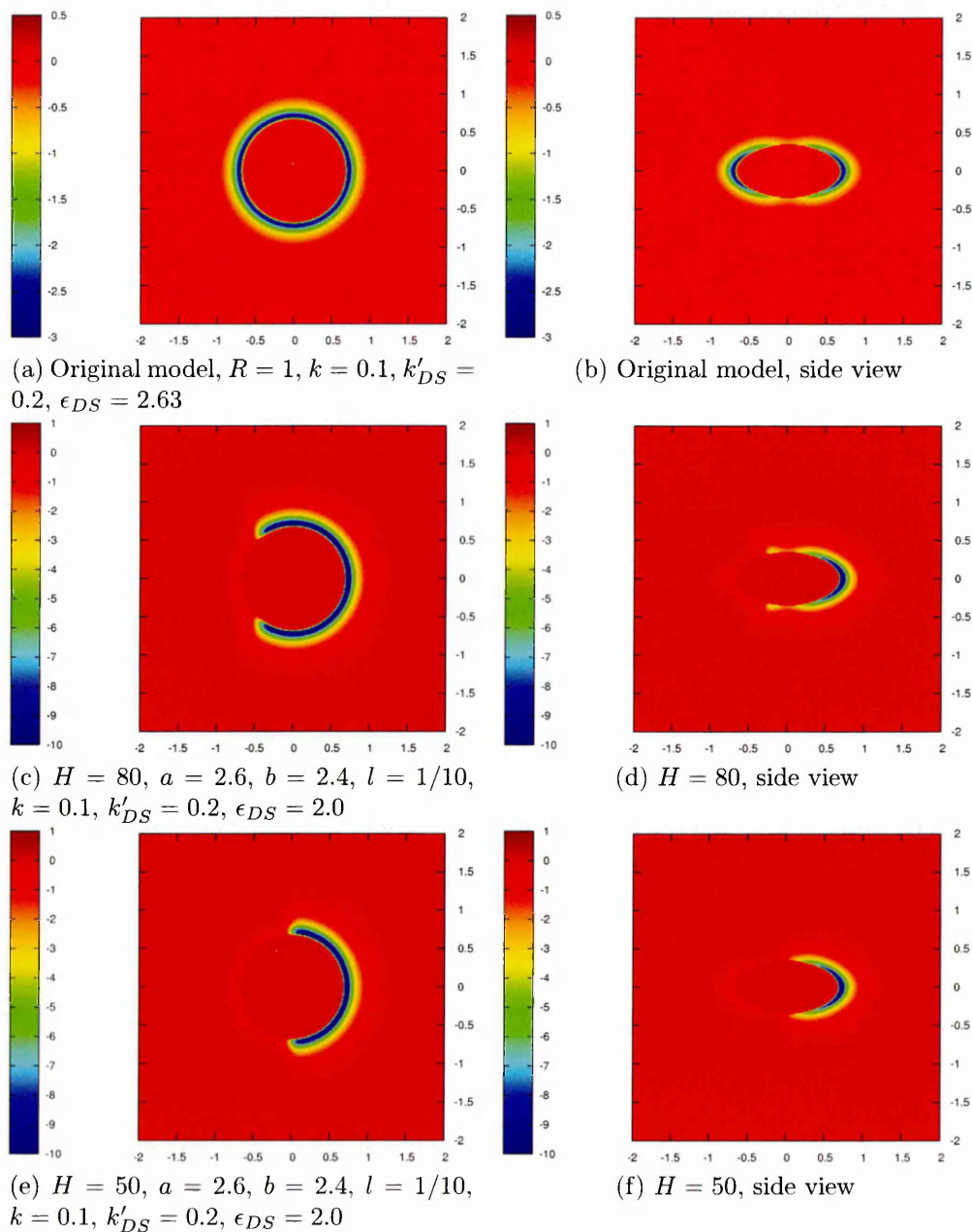
Figure 6.4: Contour plots of modified disc-sphere potentials, studied in this chapter.

(a) $H = 20$, $a = 2.6$, $b = 2.4$, $l = 1/10$, $k = 0.1$, $k'_{DS} = 0.2$, $\epsilon_{DS} = 2.0$

(b) $H = 20$, side view

(c) $H = 10$, $a = 2.6$, $b = 2.4$, $l = 1/10$, $k = 0.1$, $k'_{DS} = 0.2$, $\epsilon_{DS} = 2.0$

(d) $H = 10$, side view

(e) $H = 5$, $a = 24$, $b = 24$, $l = 1/3$, $k = 0.05$, $k'_{DS} = 0.2$, $\epsilon_{DS} = 1.0$

(f) $H = 5$, side view
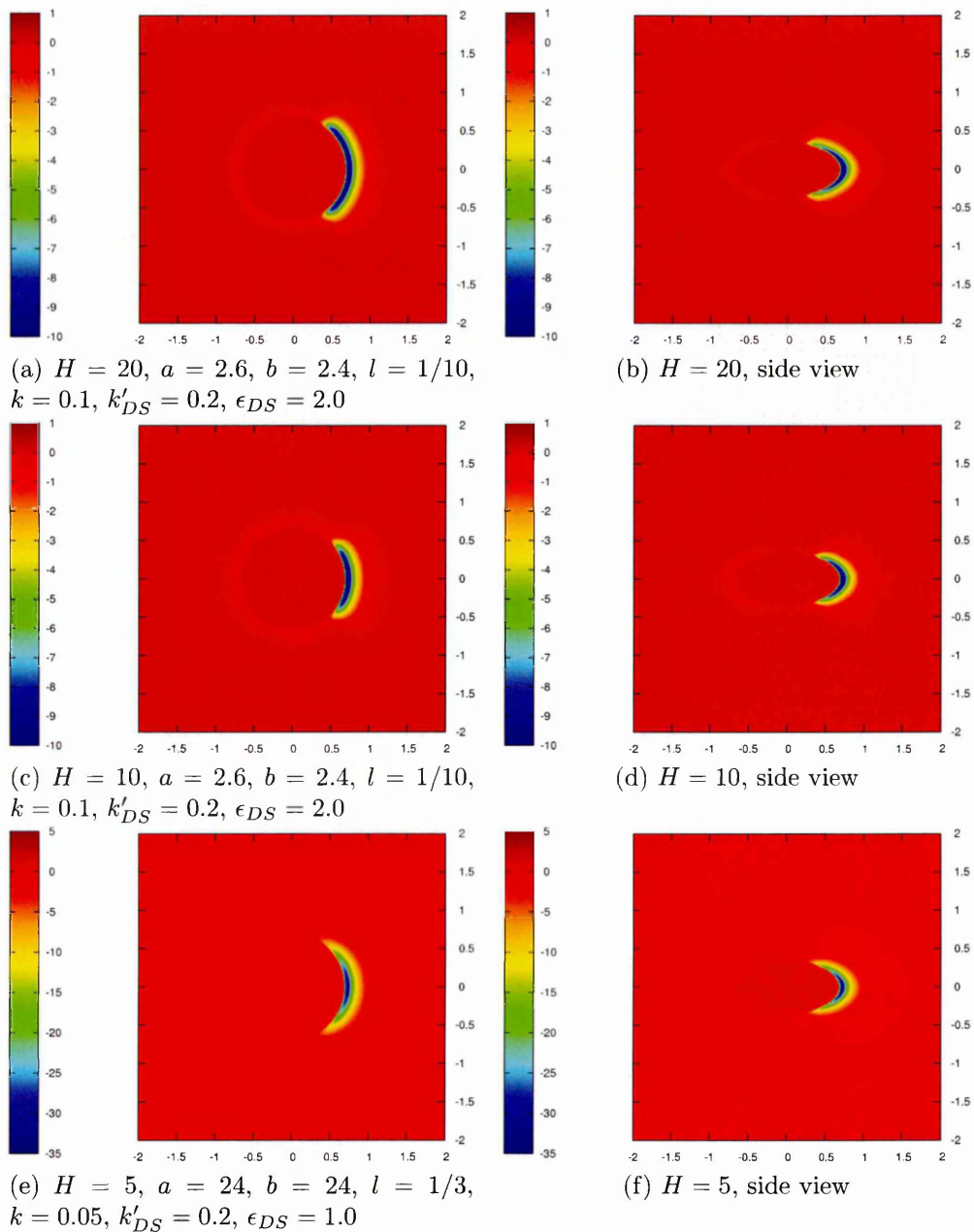
Figure 6.5: Contour plots of modified disc-sphere potentials, studied in this chapter.

These figures show that the parameter $H$ gives a direct control on the extent of the solvophilic region around the rim of the discs. The crossover between solvophilic and solvophobic regions is controlled by $l$.Thus, in Fig.6.5 e) and f), where $l$ is increased to $1/3$, this crossover is significantly more diffuse than it is in the other cases, where $l = 1/10$.

## 6.3.1   H=80 ('Toblerone')

Firstly, a $H80K10$ system (defined as $H = 80$ and $k = 0.1$) with a total of $N = 4000$ particles (with 600 disks) was studied in a series of NVT runs. With this parametrisation, a large part of each disc's edge ($H = 80$) was solvophilic. As for the systems studied in the previous chapter, we found that it was important to control the temperature so as to access an appropriate nucleation rate. At high temperatures ($T = 4.0$) no nucleation occured and the system stayed isotropic (no orientational order). When a simulation was carried out at a reduced temperature of $T = 3.4$, we found that the discs condensed into a dense droplet, comprising both discs and spheres, however no further self-assembly was observed. Thus, in the next run we reduced the temperature further to $T = 2.9$. This run finally showed that ordered structures can be formed as well. However, as a number of nuclei developed in this system, the subsequent coalescence of these nuclei led to misshape structure formation. Finally, we managed to find a temperature ($T = 3.1$) at which system was limited to a single nucleation event (formation of a droplet) with subsequent growth of the ordered structure.

To characterise the developing droplet, a cluster identification analysis was performed using a separation parameter of $r_{cd} = 1.3\sigma$. This was used to identify all of the discs within the forming structure. We also used orientational order parameter data to characterise structural changes in the system.

Fig.6.6 shows that the cluster grew slowly in the first $1 \cdot 10^6 dt$ steps, accumulating $\sim 70$ discs in that time. No significant changes in system behaviour were apparent from the cluster size and order parameter time lines, though, until $t = 1.25 \cdot 10^6$ (Fig.6.7), where strong orientational ordering occured.

To gain a better understanding of this event we analysed snapshots of the droplet before, during and after this ordering transition (Fig.6.8). Whilst some local structure is apparent in the $t = 500000dt$ snapshot, the $t = 1.25 \cdot 10^6 dt$ configuration indicates an ordered central core lined by ordered outer stacks. Here, the ordering
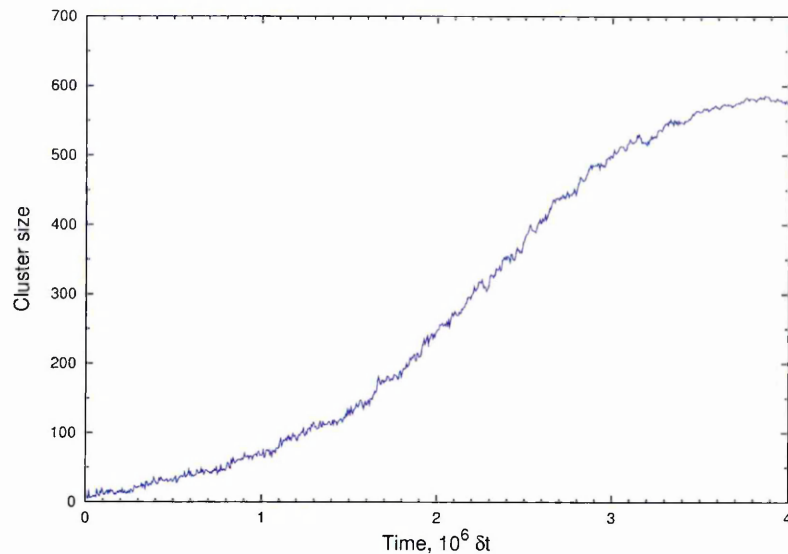
Figure 6.6: Number of Particles in the biggest cluster in $H80K10\ T = 3.1$ system.
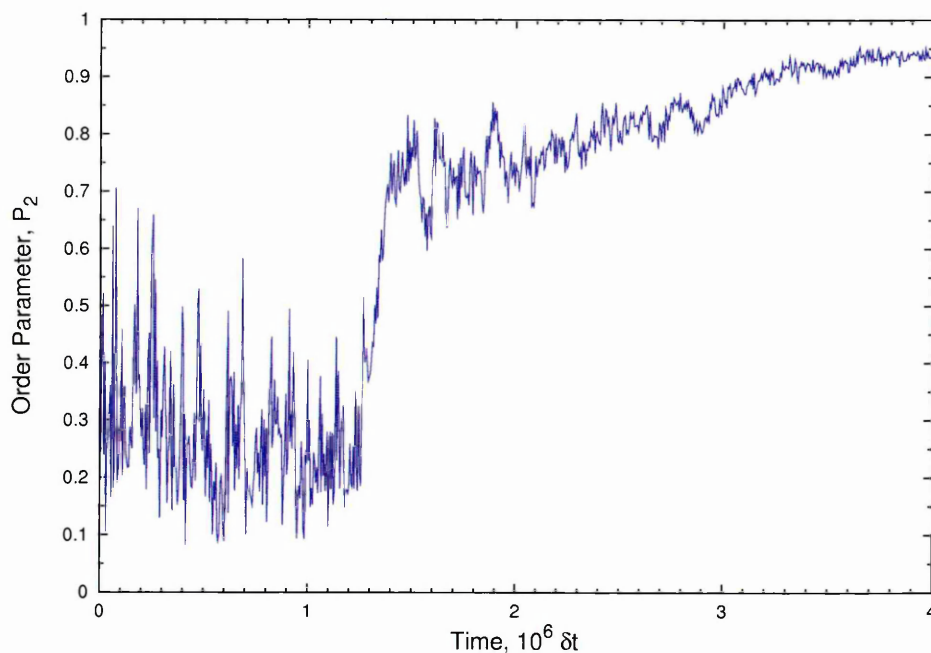


Figure 6.7: Order parameter value vs time for the biggest cluster in $H80K10\ T = 3.1$ system.

in the central core initiated subsequent ordering of the outer stacks and the droplet finally transformed to the highly-ordered triangular-shape structure ('toblerone') at $t = 1.55 \cdot 10^6 dt$ (Fig.6.8.c) . This structure is even more apparent from the alternative visualisation shown in Fig.6.8.d. Here, disc centres are shown as orange lines, solvent particles as blue dots and solvophobic axes $(-\hat{\mathbf{u}}_{\mathbf{imin}})$ as green lines. Thus,

it is apparent that the highly ordered central triangular part of the structure had a strongly solvophobic core (Fig.6.8.c). The outside of this triple-threaded core was, in contrast, strongly solvated. The outer stacks in this structure were, therefore, not in direct contact with the central core. Further, the solvophobic vectors for these outer stacks were oriented to the outside, i.e. away from the dense solvent layer between the core and the outer stacks.



(a) t=500000

(b) t=1250000

(c) t=1550000

(d) t=1600000
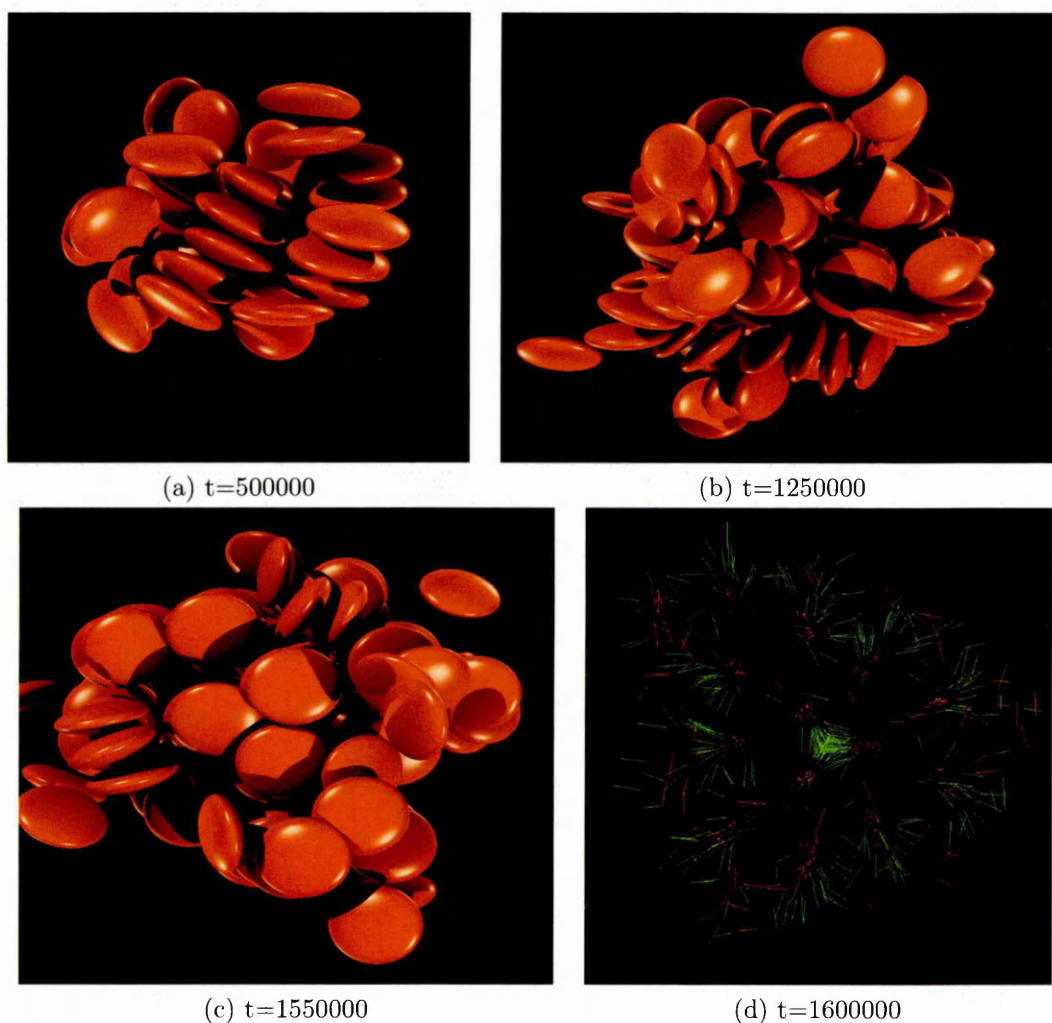
Figure 6.8: Cluster Transition in $H80K10$ $T = 3.1$ system

Radial distribution function data also clearly reflect these structural changes (Fig.6.9, Fig.6.10). The positions of major peaks in these correspond to the strutural arrangement of discs within a 'toblerone'. First of all, they indicate stacking of discs (first and second peak) and the preferred spacing between columns of disks (third

and subsequent peaks). Also, one can see a gradual increase in peak values over a time. A noticeable jump between the $t = 1 \cdot 10^6$ and $t = 2 \cdot 10^6$ RDF graphs and the gradual decrease of RDF values at long-range also indicate separation of the system into a disc-rich droplet or 'toblerone' and a lower density surrounding medium.
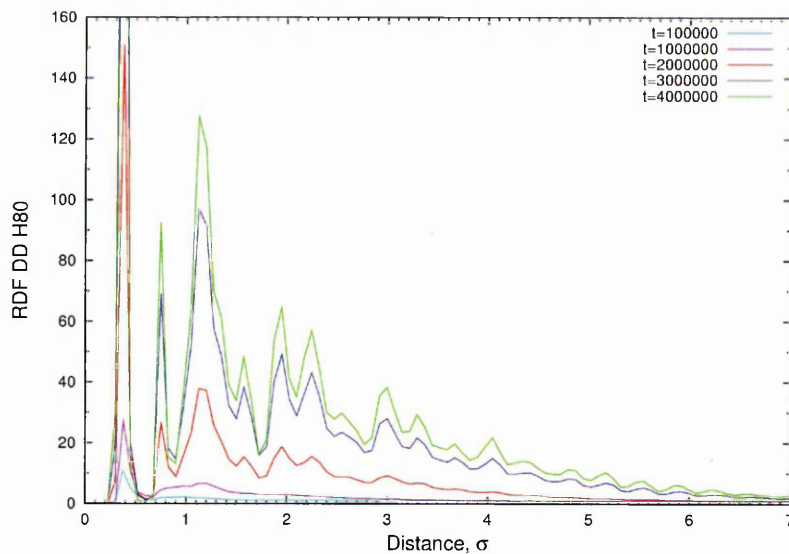


Figure 6.9: Radial Distribution Function for Discs for $H80K10$ $T = 3.1$ system
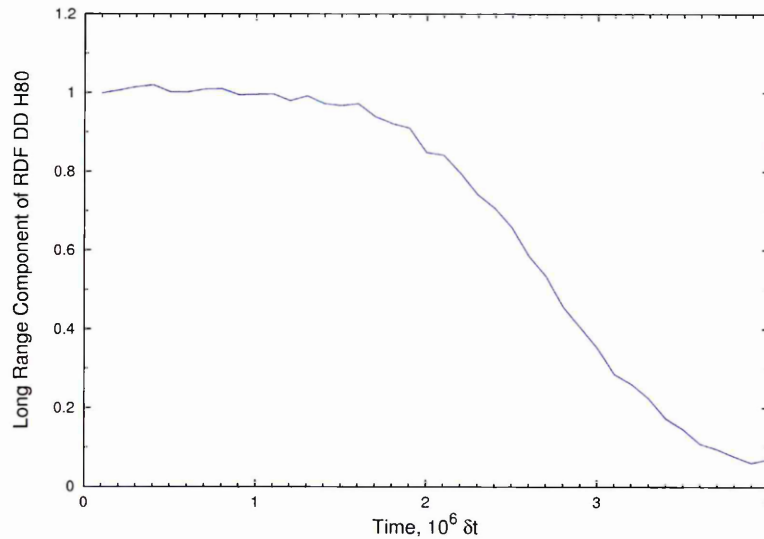


Figure 6.10: Radial Distribution Function (long range) for $H80K10$ $T = 3.1$ system.

Transition from a droplet to a 'toblerone' was the first major stage in the overall process of self-assembly for this system. It was definitely a key event, as it changed the kinetics of the process and initiated a new phase of self-assembly. This is clearly

seen from the moment of inertia and number of particles graphs (Fig.6.11, Fig.6.6). Once the initial 'toblerone' structure had been formed (at approximately $t = 1.6 \cdot 10^6$), its further growth appears mainly to have been by addition of disc monomers on to the ends of existing columns. This is characterised by the two larger moment of inertia components rapidly increasing, indicating elongation of the structure. Also, the overall aggregation rate increased after the transition (as judged by the change in slope of the number of particles graph (Fig.6.6).

It is noteworthy that the moment of inertia timelines obtained here differ from those obtained in Chapter 5. Additionally, we introduce a normalised moment of inertia, where each component is normalised to the sum of $I_l + I_m + I_s$. There is an increasing gap between the $I_l$ and $I_m$ timelines, reflecting changes in the shape of the structure cross-section as it grew from nearly cylindrical to rectangular. This is explained by the lateral growth mode: occasionally discs joined cluster laterally to initiate development of a new column, which could later be accomodated into the main structure. We note, indeed that the final structure in this particular simulation had two triangular cores (Fig.6.12).

A final note to make here is that even though this system exhibited 'fibre-like' structure, the mechanism by which it grew was different from that found in the previous chapter. Firstly, the initiation of the structure was via an amorphous droplet, rather than bundling of pre-existing threads. Also, lateral growth was initiated by occasional monomer seeding, rather than by adhesion of preexisting threads. Essentially, then, there were no free-forming stacks in this system, so both the growth and assembly modes were different.
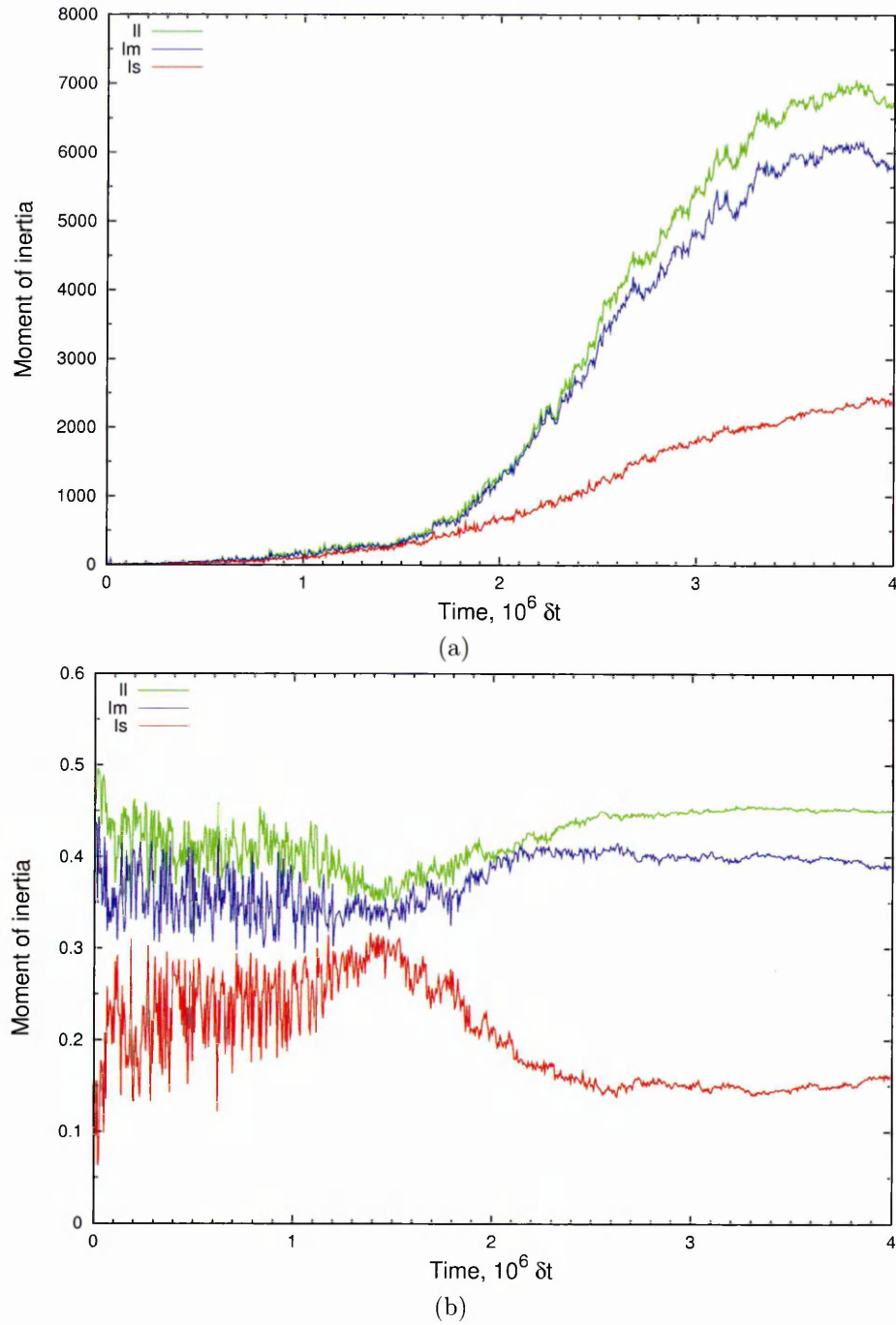
Figure 6.11: Moment of inertia (a) Normalised Moment of inertia (b) in $H80K10$ $T = 3.1$ system
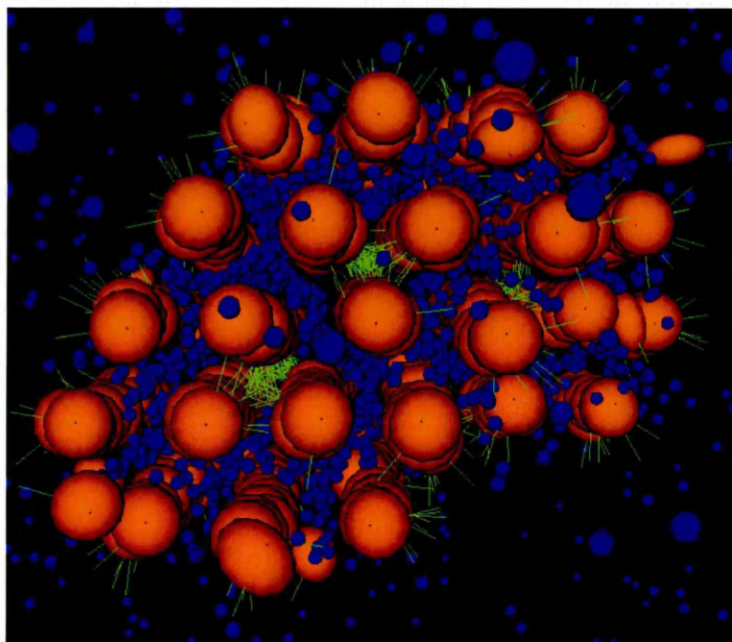
Figure 6.12: Final configuration at $t = 4 \cdot 10^6$ in $H80K10$ $T = 3.1$ system. Disks and spheres are 30% smaller (compare to real size) for clarity
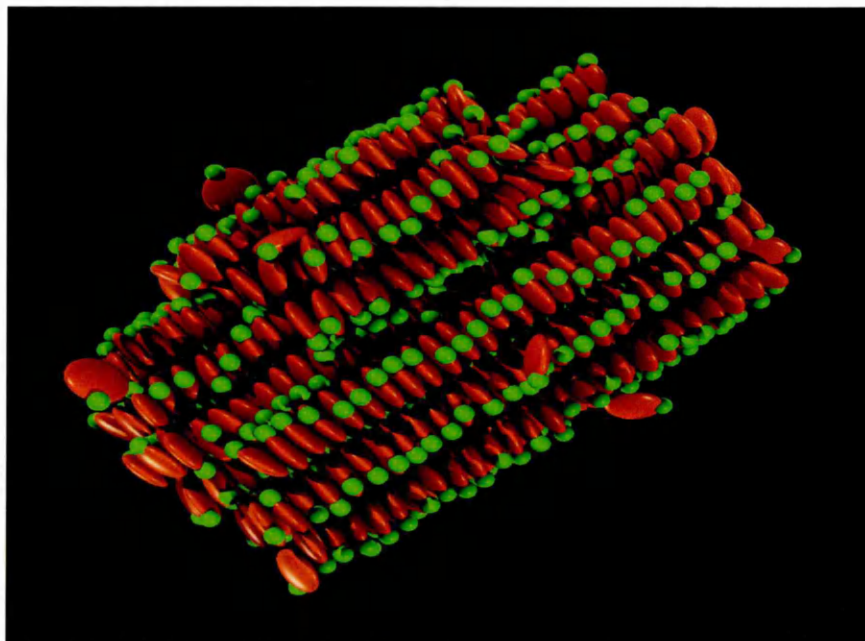


Figure 6.13: Final configuration at $t = 4 \cdot 10^6$ in $H80K10$ $T = 3.1$ system, side view. This figure clearly shows the strong orientation of solvophobic regions (marked with green spheres) in the outer stacks.

## 6.3.2   H=50 and H=20 ('Layer')

On analyzing the results obtained in the previous section, we concluded that temperature has a strong impact on the process of self-assembly in the $H = 80$ system. As we saw, high thermal energy in the system prevents formation of an amorphous droplet and its subsequent ordering into the essential structure required to initiate the second stage of the self-assembly. However, if temperature is too low, a number of aggregation events take place. This leads to the formation of structures with defects. Thus, the nucleation of a single defect-free structure is possible only at a range of temperatures intermediate between these two regimes.

Knowing this, we ran NVT simulations at different temperatures, in order to find an optimal value in $H = 50$ and $H = 20$ systems. Here, if we observed a few aggregates forming in the system, it was an indication that the temperature should be increased. Alternatively, if no droplet was formed, the temperature was decreased in the subsequent simulation. To enable qualitative comparisons to be made with the results the previous systems all parameters were kept same (except for the value of $H$).

We studied the behaviour of the $H50K10$ system in a series of NVT runs. With this parametrisation half of each disc's edge ($H = 50$) was solvophilic and half solvophobic. After a number of attempts, we found the optimal temperature for this system was $T = 2.9$.

Similarly to the $H = 80$ system, the early stages of the self-assembly were characterised by the slow formation and growth of a droplet over a period of $t = 700000dt$. As judged by the number of particles graph (Fig.6.14)), this initial droplet comprised $\sim 50$ discs. This droplet subsequently underwent a transformation into an ordered structure , as indicated by the rise of the orientational order parameter value between $t = 700000dt$ and $t = 1 \cdot 10^6 dt$ (Fig.6.15).
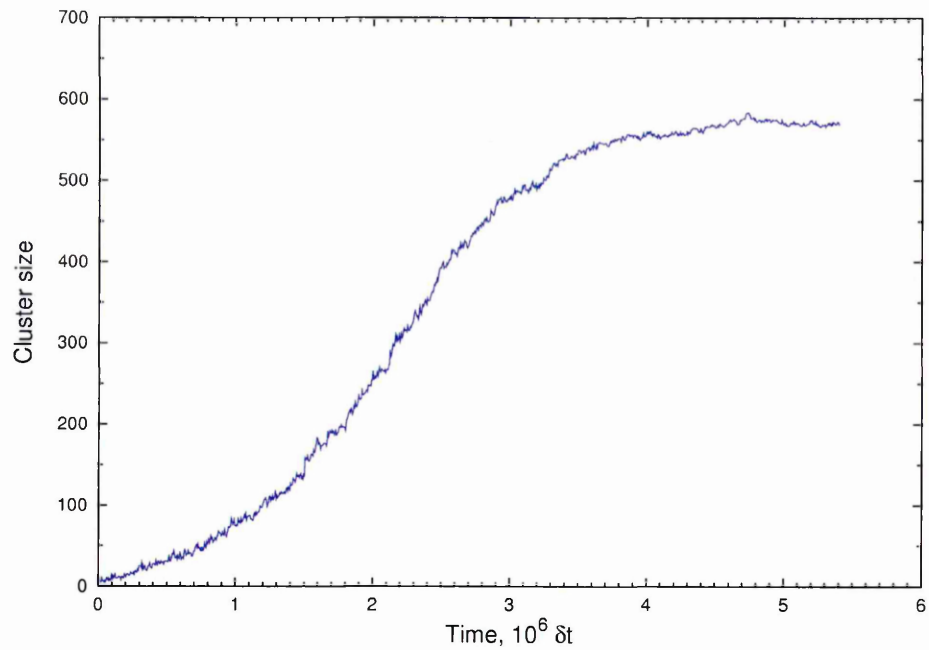
Figure 6.14: Number of Particles in the biggest cluster in $H50K10\ T = 2.90$ system.
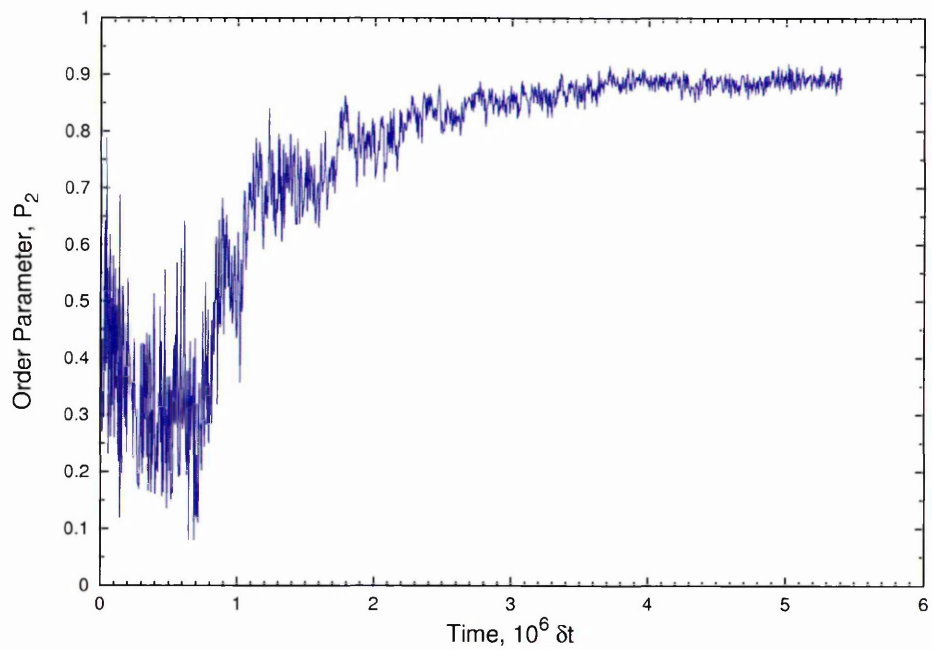


Figure 6.15: Order parameter value vs time for the biggest cluster in $H50K10$ $T = 2.90$ system.

The RDF's for $H80K10$ (Fig.6.9) and $H50K10$ (Fig.6.16) systems are quite similar for the first $2 \cdot 10^6$ timesteps, and start to differ only at later times (peaks $\approx 20\%$ lower for $H50K10$ at $t \geq 3 \cdot 10^6 dt$). This means that while the structure of the initial droplet appears to have been similar in the two systems, subsequent reorganisation of discs progressed differently, due to the difference in the respective size of solvophilic regions. Snapshots showed that the shape of the initial structure was indeed different from 'toblerone' in this system. It was rather flat and the aggregate could be compared to a small bilayer, locally having a nearly square arrangement of strands (Fig.6.17).
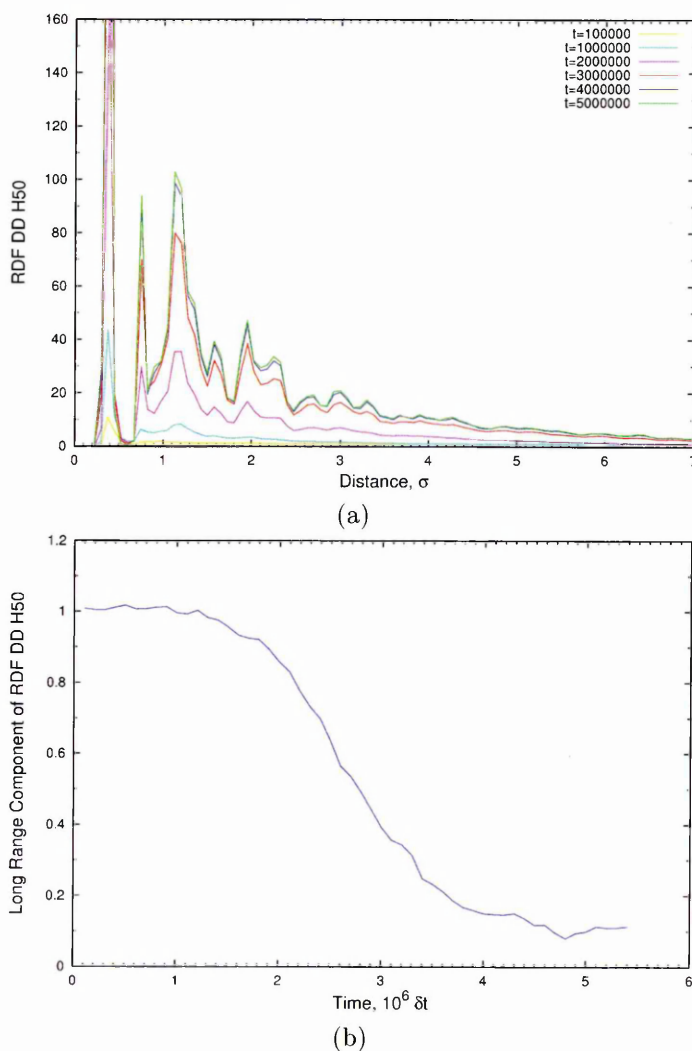


Figure 6.16: Radial Distribution Function for Discs in $H50K10$ $T = 2.90$ system (a), its long-range component (b)
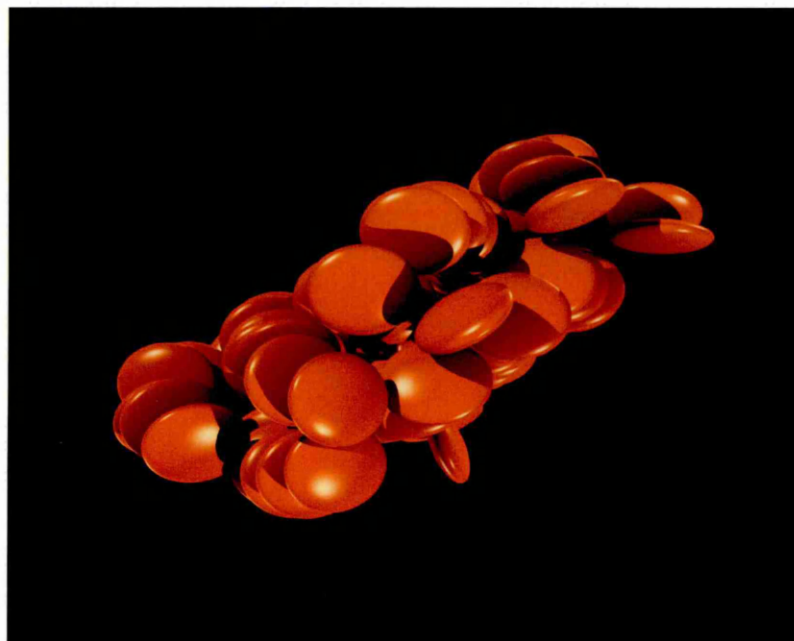
(a)
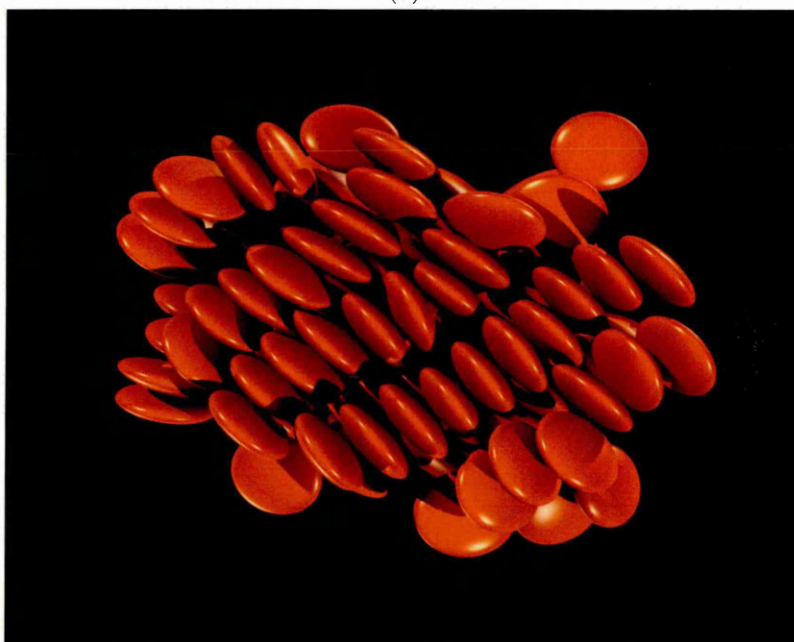


(b)

Figure 6.17: Small bilayer in $H50K10$ $T = 2.9$ system system at $t = 1.1 \cdot 10^6 dt$ top view (a), side view (b).

Once the initial bilayer structure had been formed, the mechanism by which it grew was similar to that of the $H80K10$ system: elongation of existing columns combined with lateral growth, initiated by occasional monomer seeding. Nevertheless, the moment of inertia timelines differ from what was seen for $H80K10$ system, as here they consistently adopted values characterstic of a flat rectangular structure $(I_l > I_m > I_s)$ (Fig.6.18), instead of initial cuboid-like and later rectangular fibre shape observed with $H = 80$ $(I_l \approx I_m > I_s)$.
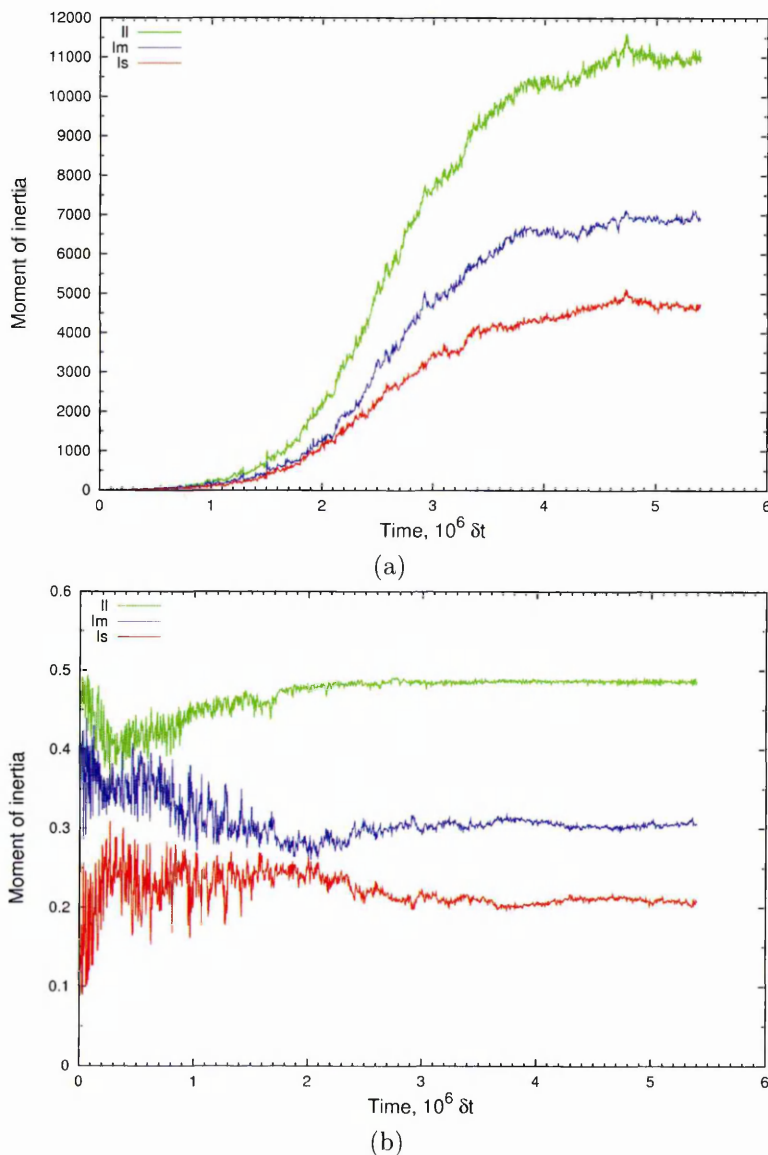


Figure 6.18: Moment of inertia (a) and Normalised Moment of inertia (b) for the largest cluster in $H50K10$ $T = 2.90$ system.

The final structure from the $H50K10$ simulation is presented on Fig.6.19. Here, the positions of the solvophobic axes $(-\hat{\mathbf{u}}_{\mathbf{imin}}$ ) are marked with green spheres. The snapshot shows that the local square arrangement of stacks ultimately led to a bilayer sheet-like structure. In this, the solvophobic vectors are oriented to the outside, i.e. away from the dense solvent layer between the sheets. The solvophilic sites are very well ordered, leading to the lines of green spheres seen in Fig.6.19.
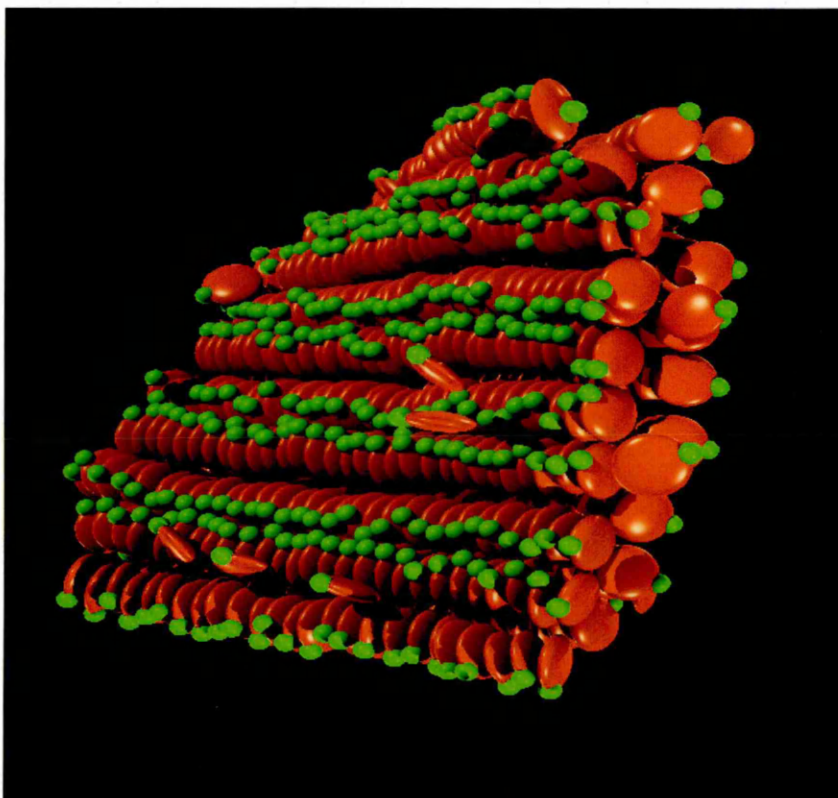


Figure 6.19: Final configuration in $H50K10\ T = 2.90$ system at $t = 5.5 \cdot 10^6$. Spheres are not shown. Green spheres are used to show the location of the solvophobic rim regions $(-\hat{\mathbf{u}}_{\mathbf{imin}}$ ).

Using a similar approach to that described above, we also studied the behaviour of the $H20K10$ system. The optimal temperature for this system was found to be $T = 2.55$. For this system we first noticed that the droplet's growth and ordering took considerably longer time to establish. Thus, the number of discs (Fig.6.20)and orientational order parameter (Fig.6.21) timelines showed that the growth of the initial structure took $t \approx 2.5 \cdot 10^6 dt$. The shape of this initial structure was rect-

angular and bilayer-type, like in the $H50K10$ system, but the kinetics of its subsequent growth was different, though. Specifically, the moment of inertia timelines (Fig.6.22) indicated a more elongated rectangular structure, than in $H = 50$ system ($I_m^{H20} > I_m^{H50}$ and $I_s^{H20} < I_s^{H50}$).
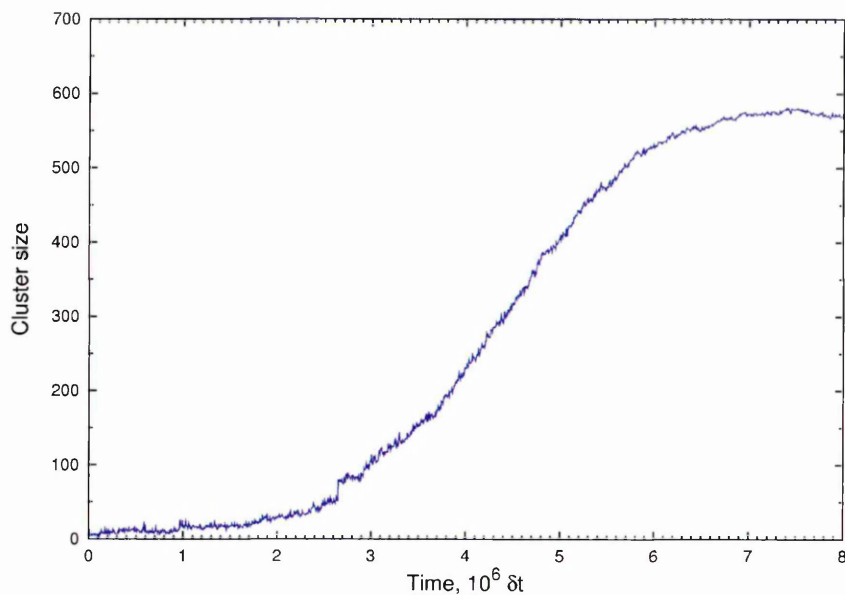


Figure 6.20: Number of Particles in the biggest cluster in $H20K10$ $T = 2.55$ system.
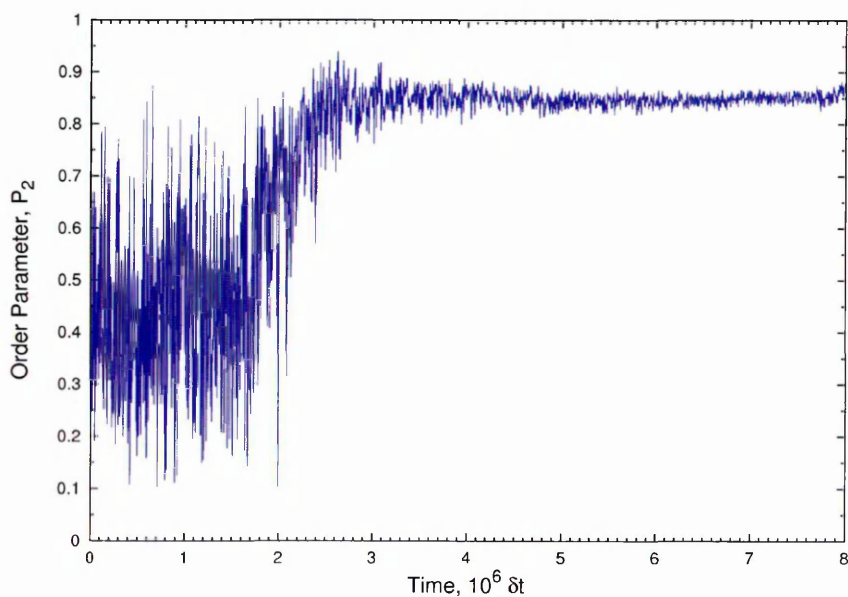


Figure 6.21: Order parameter value vs time for the biggest cluster in $H20K10$ $T = 2.55$ system.

(a)



(b)
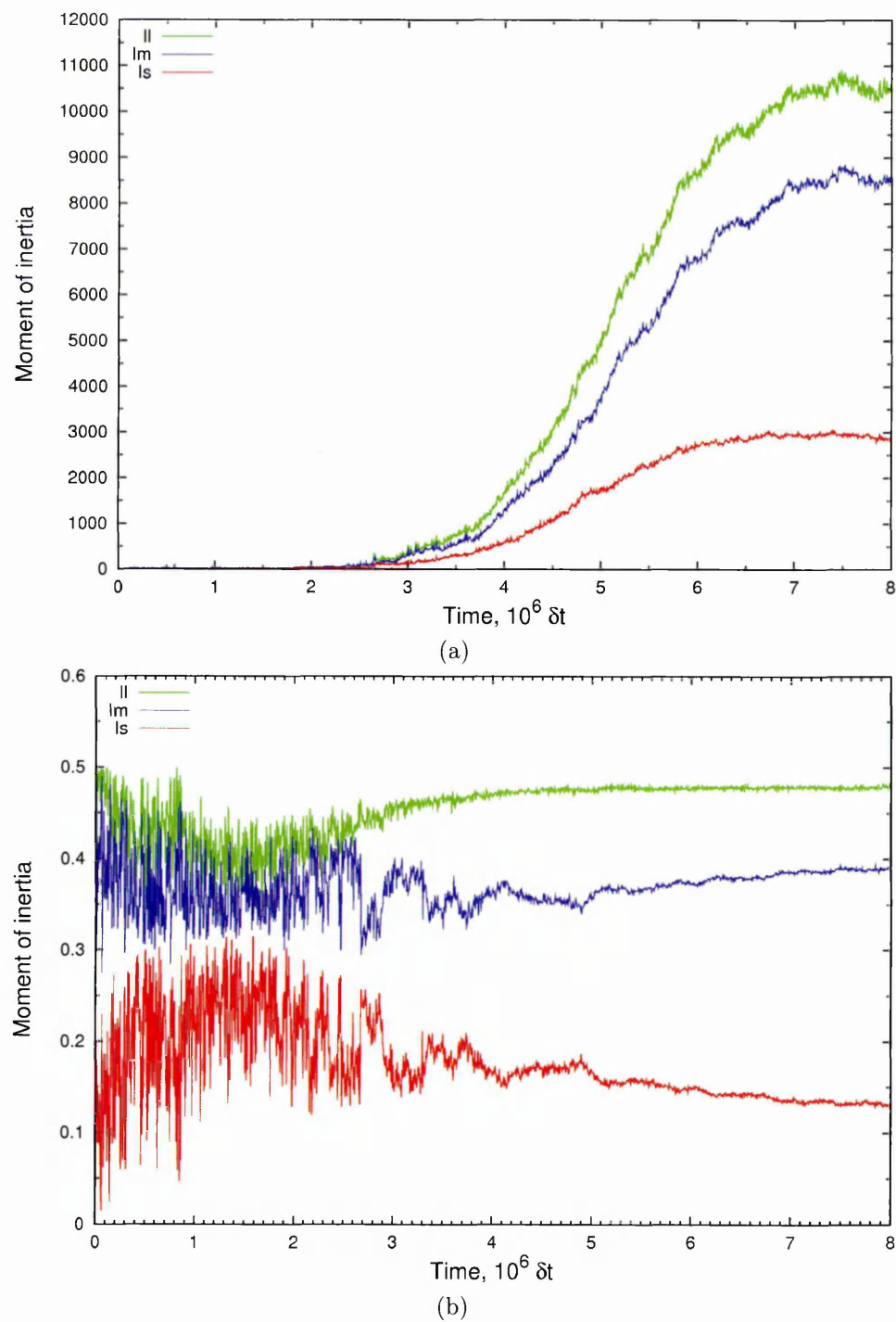
Figure 6.22: Moment of inertia (a) and Normalised Moment of inertia (b) for the largest cluster in $H20K10$ $T = 2.55$ system.

The RDF also indicated some structural differences between the aggregates in the $H = 50$ and $H = 20$ systems. This reflected a higher number of interdigitated discs in the latter (more peaks near $r = 1.0\sigma$). The snapshot of the final configuration clearly shows closer packing of stacks, with no gaps between the stacks running along and face of the bilayer (Fig.6.24).
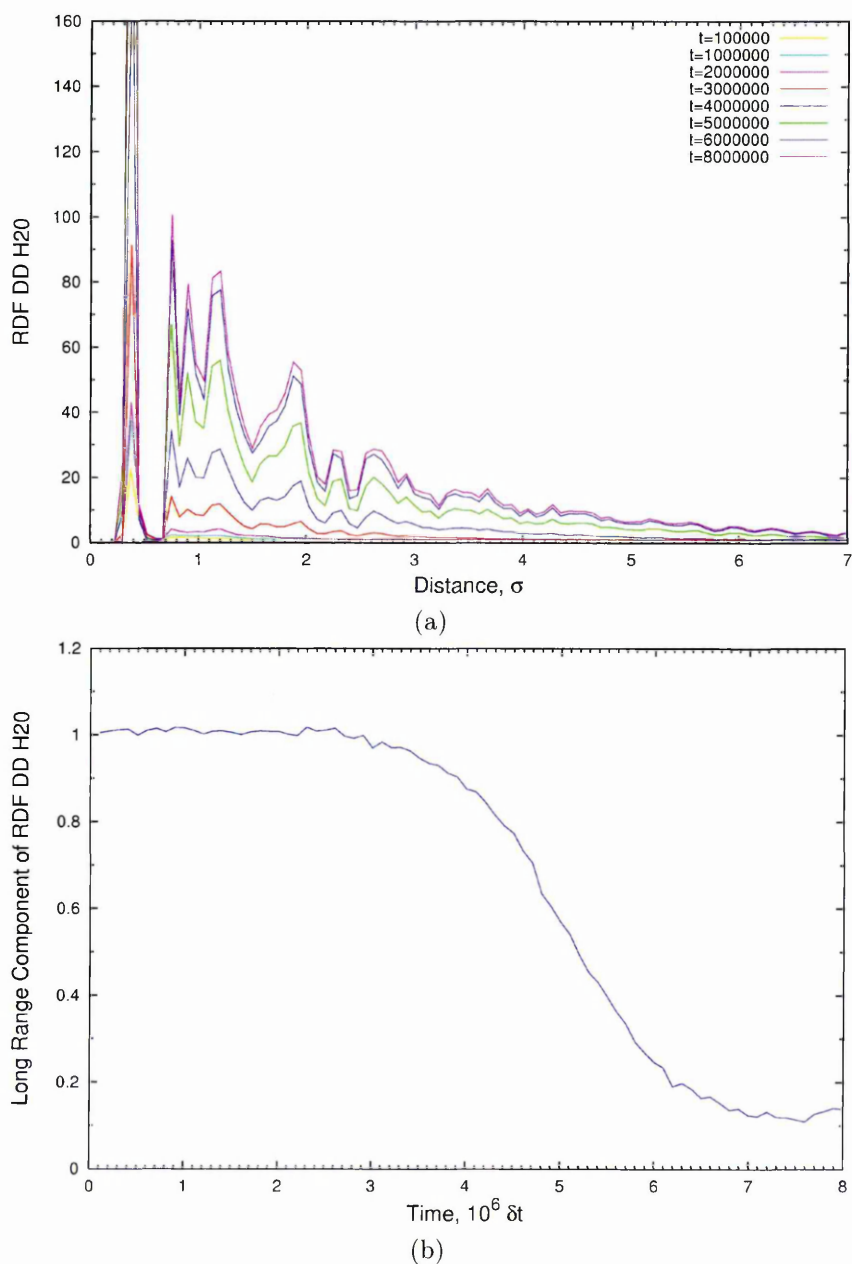


Figure 6.23: Radial Distribution Function for Disks in $H20K10$ $T = 2.55$ system (a), its long-range component (b)
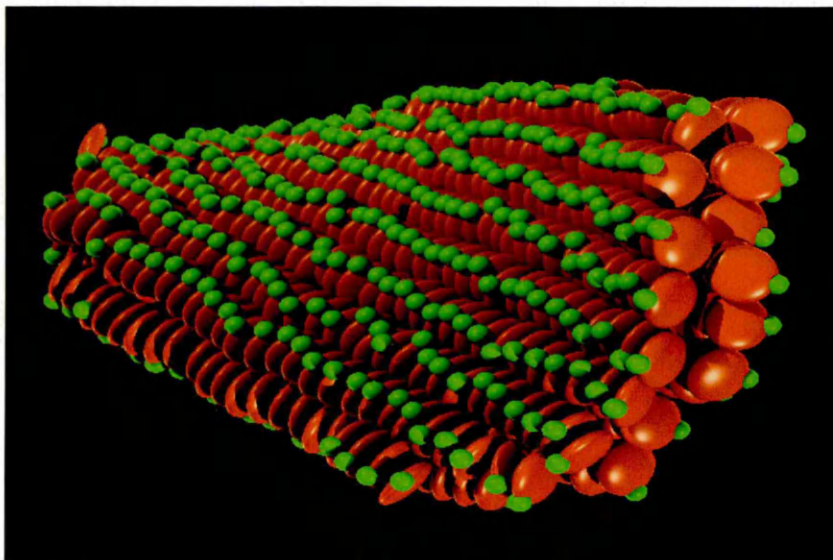
Figure 6.24: Final configuration in $H20K10$ $T = 2.55$ system at $t = 8 \cdot 10^6$ (b). Spheres are not shown for a clarity.

Interestingly, the final structures in the $H50$ and $H20$ systems were both found to possess large lengthscale chirality in the form of a twist. This was not so clear at the early stage of self-assembly, as the columns were not long enough for structural properties to be gauged. However, as the bilayers grew larger, the presence of chirality became noticable (Fig.6.19, Fig.6.24). In the $H20K10$ system (NVT run, $T = 2.55$) this twist is particularly apparent. This was confirmed by orientational order parameter data, obtained for the final configurations (on average, it was 0.85 for $H20K10$ system and 0.90 for $H50K10$ system). While the number of discs in the bilayers was almost equal in the two cases, the lower order parameter for the $H = 20$ system reflects that it has more twisted superstructure. This means that $H$ parameter has a direct effect on the curvature of a structure. The origin of this twist is presumed to be relevant to the degree of inter-thread interdigitation.

Thus, the results presented in this section have demonstrated, that the parameter $H$ has a significant impact on both the kinetics of the self-assembly and the resultant structural properties. While structural changes reflect the symmetry of the disc-sphere interaction, the influence of the latter on the kinetics is less obvious. We assume, however, that this influence is related to the fact that discs with larger

solvophilic regions have a higher probability of joining the cluster, since they have a wider range of possible orientations, which are able to activate a strong disc-sphere interaction. Therefore, it appears logical that self-assembly of discs with smaller solvophilic regions takes a longer time.

### 6.3.3 H=10 ('Cord')

On decreasing the solvophilic region from $H = 80$ to $H = 50$ we observed a transition from one shape to another ('toblerone' to bilayer). Although final configuration remained of the bilayer type at $H = 20$, the overall twist of the structure increased, indicating that a transition to another shape may possibly be accessed at even smaller $H$. To test this hypothesis, we used $H = 10$ in the following runs.

Firstly, we found an optimal temperature for this system was $T = 2.23$. As the number of particles (Fig.6.25) and orientational order parameter (Fig.6.26) timelines showed, the development of an initial ordered structure again took a long time in this system ($t \approx 2 \cdot 10^6 dt$). Interestingly, the number of discs in the droplet was particularly low ($N \approx 20$). At the same time, the structure was more ordered than it had been in all previously studied systems (order parameter $P_2 > 0.9$).
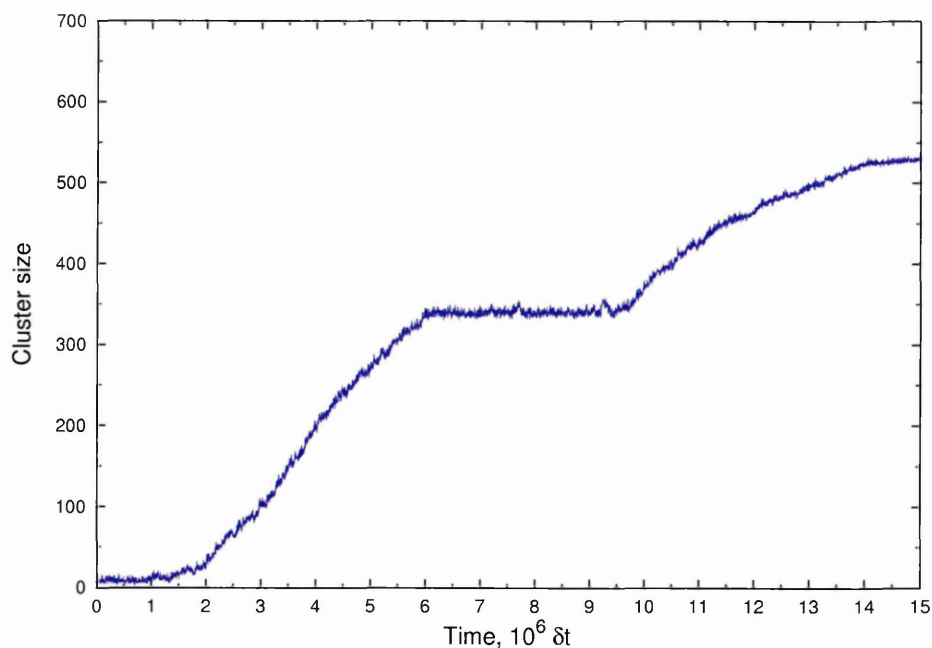


Figure 6.25: Number of Particles in the biggest cluster in $H10K10\ T = 2.23$ system.
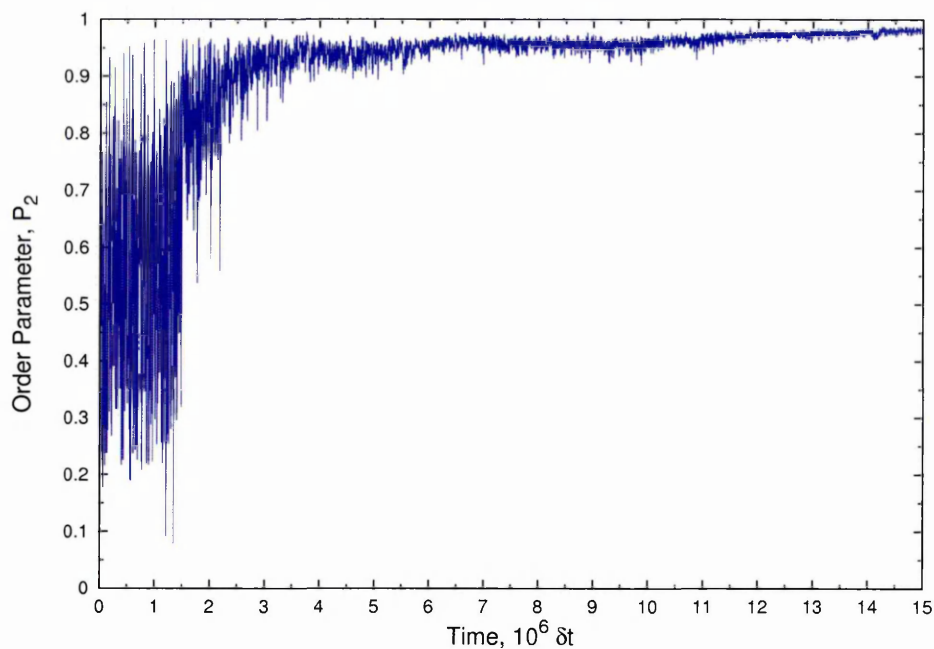
Figure 6.26:  Order parameter value vs time for the biggest cluster in $H10K10$ $T = 2.23$ system.

Snapshots of this initial structure showed, that it consisted of four strongly ori-

entated columns of discs, with a core of spheres between them (Fig.6.27).



(a)                                                            (b)
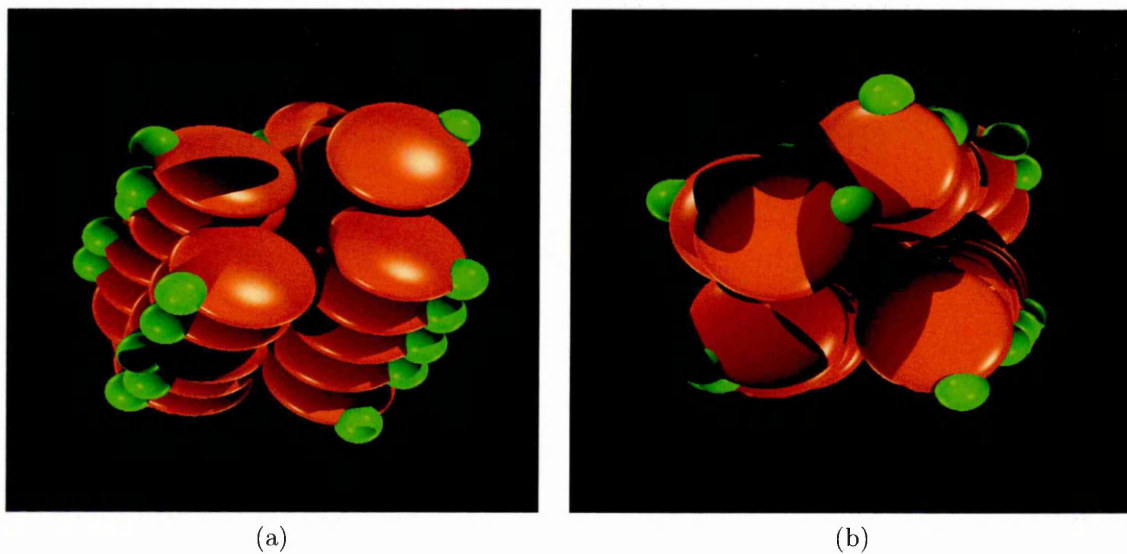
Figure 6.27: Small cluster in $H10K10$ $T = 2.23$ system system at $t = 2 \cdot 10^6 dt$ angle view (a), top view (b). Solvophobic regions are marked with green spheres. Solvent spheres are not shown.

Moment of inertia timelines showed that this structure grew further from $t = 2 \cdot 10^6 dt$ to $t = 6 \cdot 10^6 dt$, where this growth stopped. Values of the moment of inertia components were characteristic of an elongating cylindrical structure ($I_l \approx I_m >> I_s$). This was very different from what had been seen in the systems studied previously, indicating significant changes in the second stage of self-assembly.



(a)



(b)
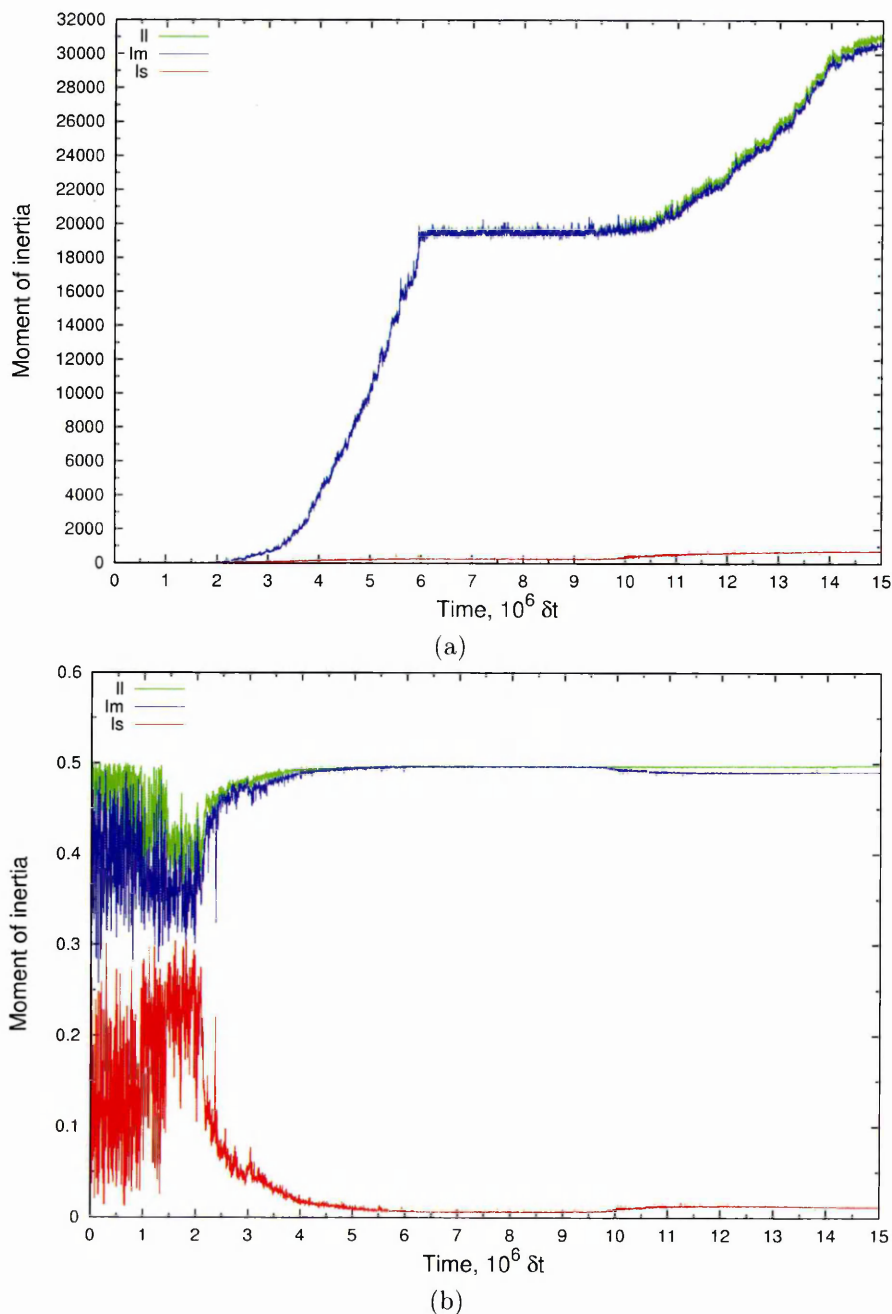
Figure 6.28: Moment of inertia (a) and Normalised Moment of inertia (b) for the largest cluster in $H10K10$ $T = 2.23$ system.

We checked snapshots and found that the the cessation of the structure's growth after $t = 6 \cdot 10^6 dt$ was associated with it reaching the boundaries of the simulation box (Fig.6.29). Thus, in this system not only was the structure a different shape (nearly cylindrical or cord-like), but also the growth modes were changed. Elongation of existing columns became the only dominating mechanism of second-stage self-assembly in this system, as no lateral growth was observed.
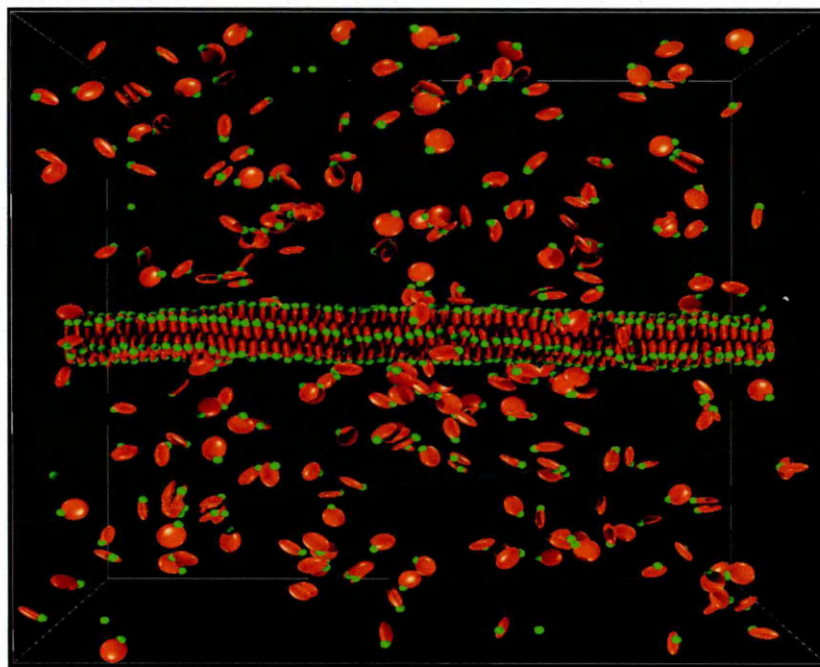


Figure 6.29: Snapshot from $H10K10\ T = 2.23$ system at $t = 7 \cdot 10^6$

This cord-like configuration maintained its shape for a few millions timesteps, until $t = 9.5 \cdot 10^6$, where a new column growth was spontaneously initiated. This triggered further self-assembly of free monomers to form a double-cord structure (Fig.6.31(b)). This stage is clearly seen on the moment of inertia and number of particles graphs by the rise of values after a period of time, in which the graph lines were flat (Fig.6.28, Fig.6.25). However, as judged by the slope of these timelines, this growth was slower, which can be explained by the decreased concentration of avalable monomers.
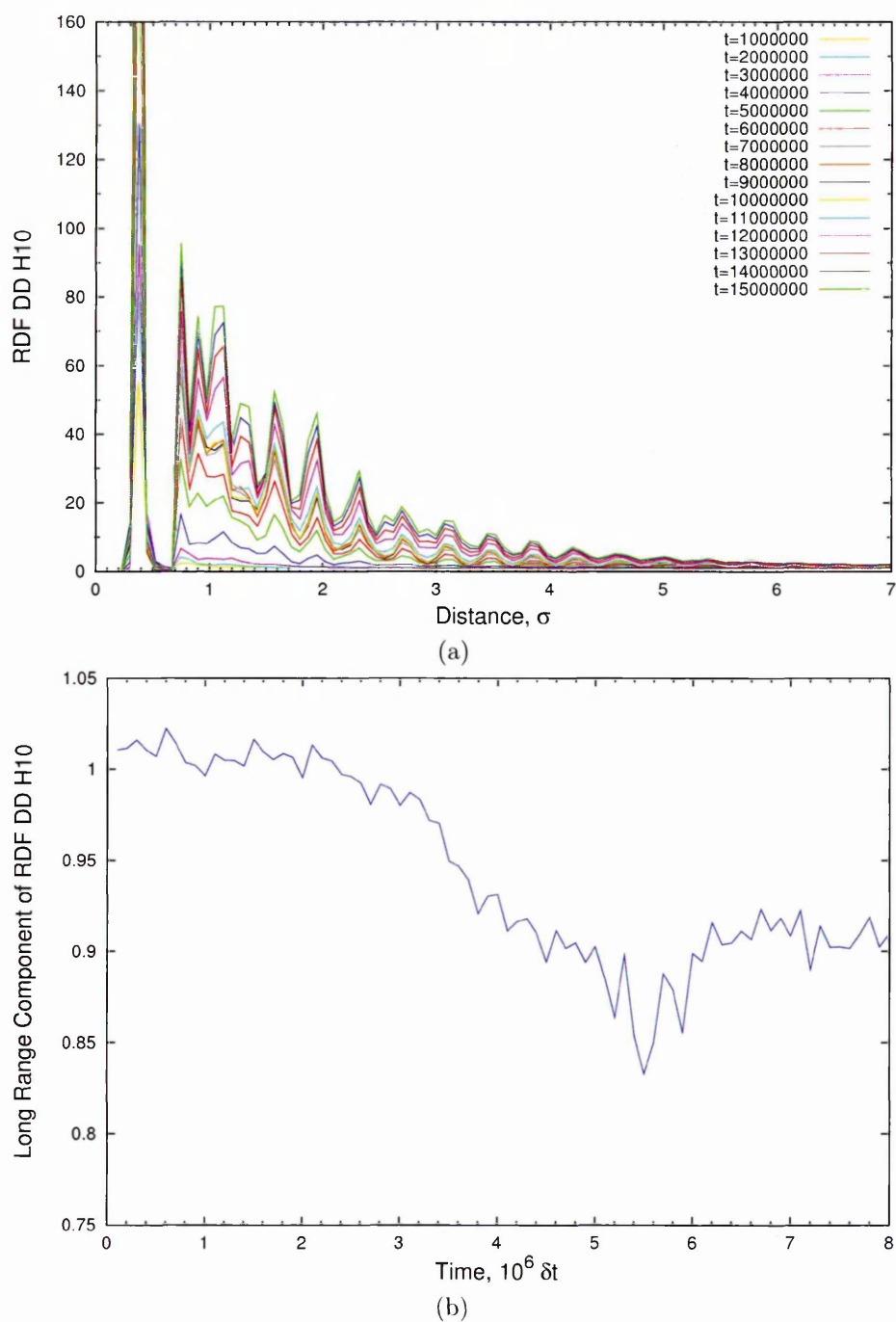
Figure 6.30: Radial Distribution Function for Disks in $H10K10$ $T = 2.23$ system correspond to the strongly-ordered structure, with many distinct peaks being present (a). RDF's long-range component (b)
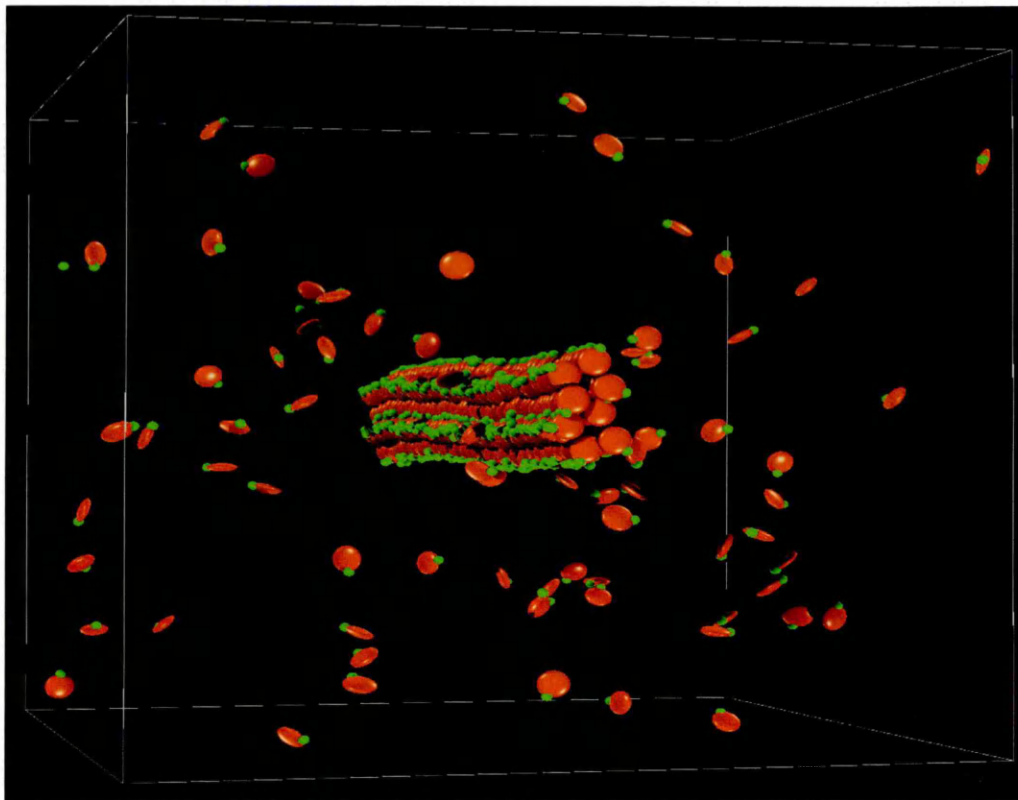
Figure 6.31: Snapshot from $H10K10$ $T = 2.23$ system at $t = 15 \cdot 10^6$

These results confirmed our finding that the parameter $H$ has a direct impact on the local packing within the overall structure. Decreasing the size of the hydrophilic region around the disc's rim leads to a qualitative change in the overall symmetry of the structure. Thus, for these systems with essentially square local packing of disc stacks, we have seen bilayer-like, twisted-bilayer-like and cord-like superstructures. We also found that $H$ influences the kinetics of self-assembly: initial nucleation and subsequent growth take longer time in system with lower $H$.

## 6.3.4   H=5 ('Triple helix')

Finally, we studied the behaviour of the $H5K10$ system. With this parametrisation only a small region of each disc's edge ($H = 5$) was solvophilic. Unlike the other systems studied previosly in this chapter, here we observed formation of the solvent-free fibre, i.e. of the type described in Chapter 5. While the outcome of this simulation was somewhat unexpected, this result, in general, is consistent with those obtained earlier. This becomes more clear if we take into consideration that the original undecorated rim model is, in fact, a close approximation of the $H = 5$ one, since the solvophilic region is relatively small.

However, on experimenting with the parameters, we found that when the interaction between the discs and spheres was strengthened further, the system behaviour changed, and a new form of disc-sphere aggregate was obtained. This is best illustrated by simulation performed in the NVT ensemble with the following parameters: $N_{total} = 4000, N_{discs} = 400, \epsilon = 1, \epsilon_{DS} = 1, k = 0.05, H = 5, a = 24, b = 24, l = 1/3$. Compared to the previously studied systems, here not only was the solvophilic disc-sphere interaction much stronger, but also the discs had a stronger attraction in the face-to-face configuration. As a result, the number of nucleation events increased, and a much higher temperature was required ($T = 5.19$) to achieve an appropriate nucleation rate. To accurately integrate equations of motion, and especially to treat rotational motions correctly, the timestep was reduced to $dt = 0.0005$ (instead of $dt = 0.0015$) and $l$ was changed to $l = 1/3$.

In general, the initial mechanism of self-assembly found here remained similar to that observed in the previously studied systems. The early stages of the self-assembly were characterised by the slow formation and growth of a droplet over a period of $t = 8.5 \cdot 10^6 dt$. As judged by the number of particles graph (Fig.6.32)), this initial droplet comprised $\sim 20$ discs. Snapshots of the simulation box indicated that the aggregate was constantly transforming and rearranging until $t = 9 \cdot 10^6 dt$, at which point it underwent a transformation into an ordered structure. This is apparent from

the orientational order parameter graph, which shows that discs within the cluster became more ordered, with the average value $P_2$ increasing to 0.75 and becoming less volatile (Fig.6.33).
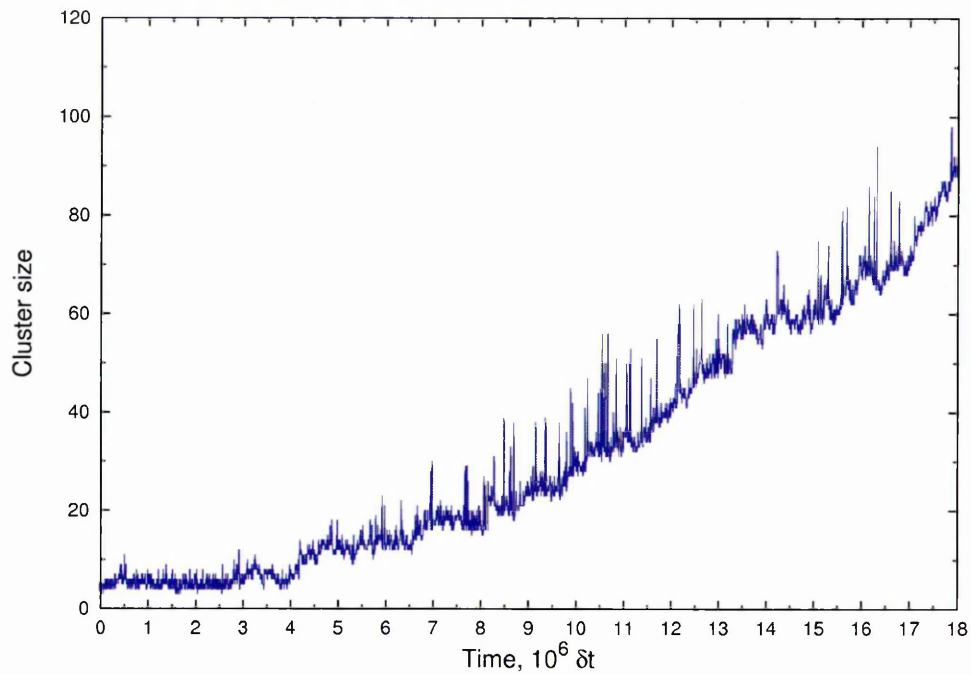


Figure 6.32: Number of discs in the largest cluster in $H5K5\ T = 5.19$ system
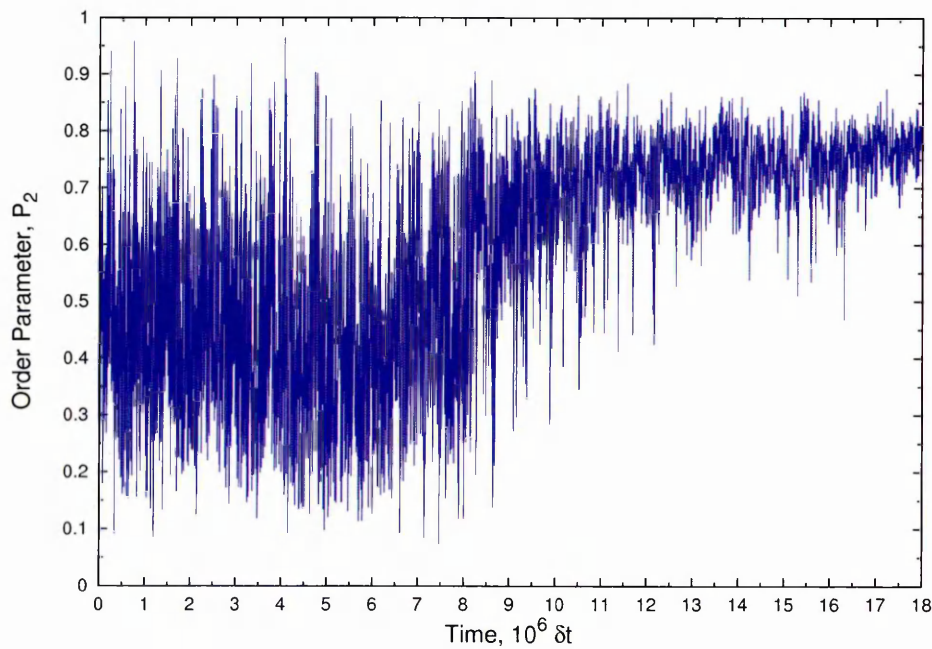


Figure 6.33: Order parameter for the biggest cluster in $H5K5\ T = 5.19$ system.

It can be seen from the moment of inertia graph (Fig.6.34 b)) that the droplet initially had a nearly spherical shape ($I_l$, $I_m$ and $I_s$ are at their closest to $1/3$). However, data measured at later times (Fig.6.34 a)) indicate a cylindrical cluster shape after ordering ($I_l \approx I_m >> I_s$).
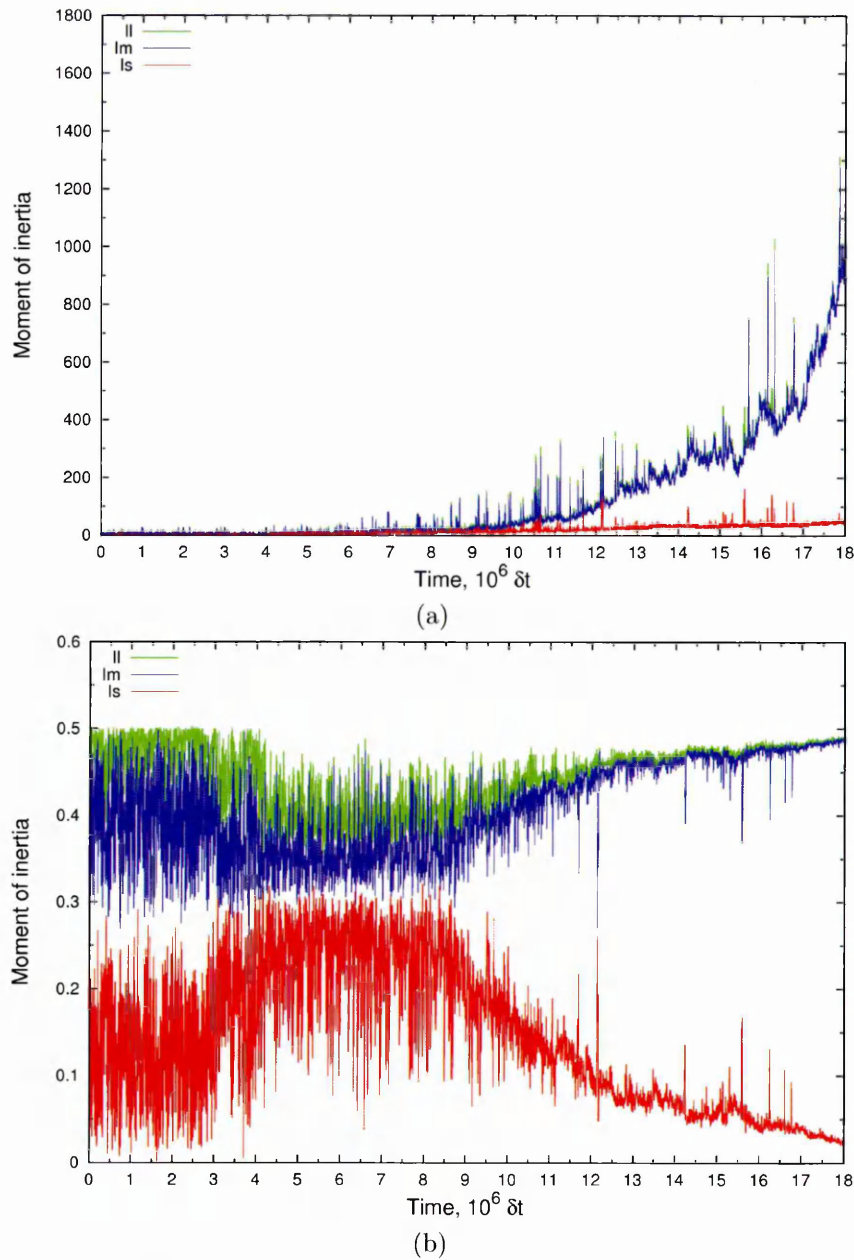


Figure 6.34: Moment of inertia (a) and Normalised Moment of inertia (b) for the largest cluster in $H5K5$ $T = 5.19$ system.

The RDF for $H5K5$ indicate apparently different structural characteristics of this initial ordered aggregate. It shows just a few peaks with relatively low magnitudes (Fig.6.35). Snapshots show that the shape of the initial structure was indeed different from any observed previously. The aggregate had three slightly twisted columns of discs and water spheres in the centre. (Fig.6.36).



(a)



(b)
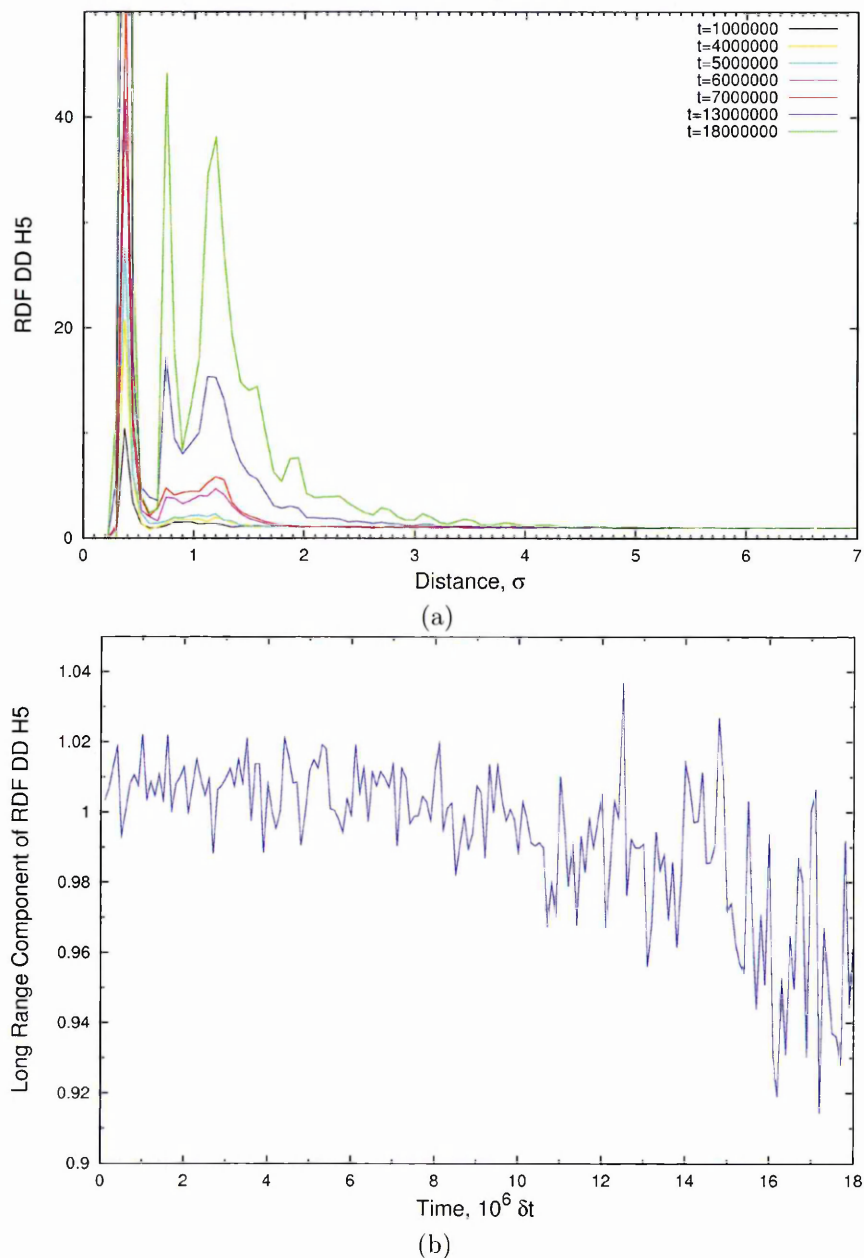
Figure 6.35: Radial Distribution Function for Disks in $H5K5$ $T = 5.19$ system (a), its long-range component (b)
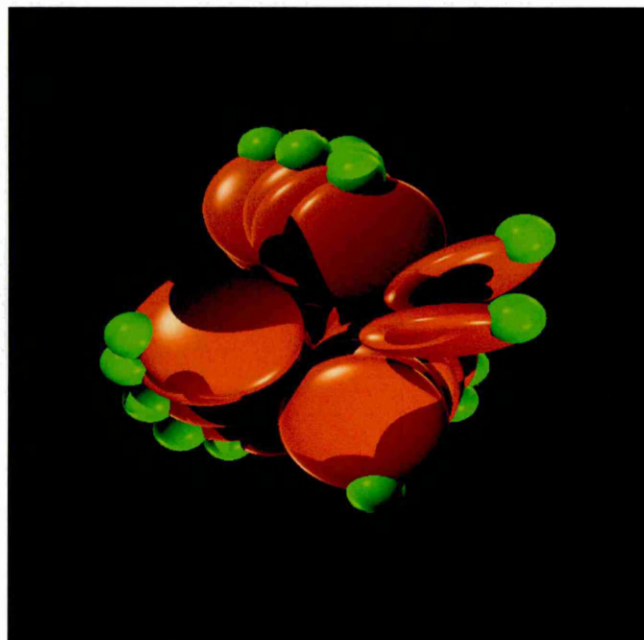
(a)
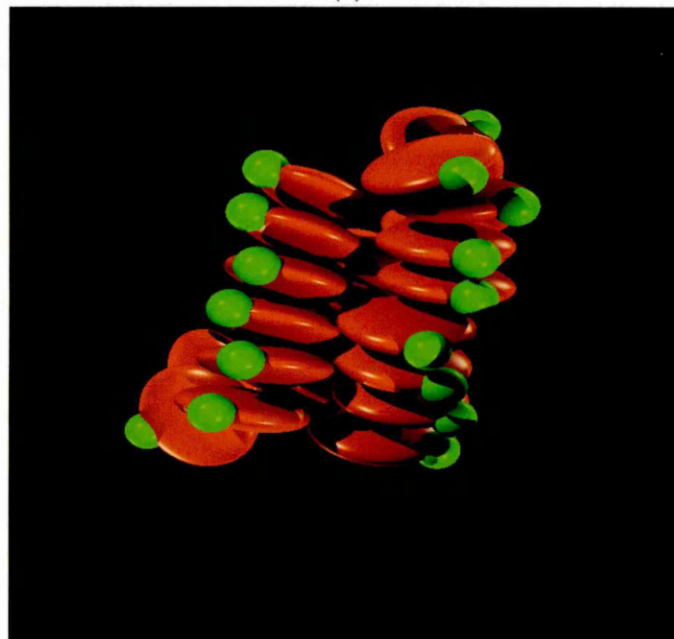


(b)

Figure 6.36: Small triple-helix aggregate in $H5K5$ $T = 5.19$ system system at $t = 9 \cdot 10^6 dt$ top view (a), side view (b).

We subsequently observed slow elongation of this initial triple-helix by monomer addition of discs to the ends of existing columns. The number of discs graph (Fig.6.32) illustrates slow cluster growth over time, from 20 to above 90 monomers (Fig.6.37). There are many short-lived spikes on a graph. However, it needs to be

clarified, that these peaks do not actually indicate group of particles joining or leaving the cluster. These are a noise signals, arising when cluster recognition algorithm includes extra discs in a list. This occurs in situations where monomeric discs are close enough to a structure, but actually are not part of it.
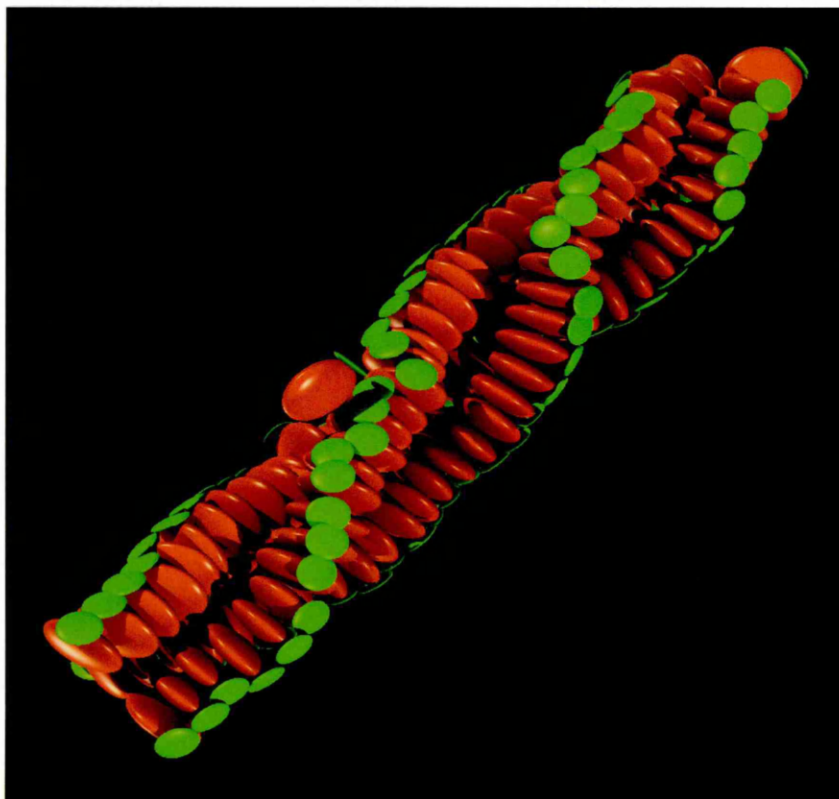


Figure 6.37: Triple helix in $H5K5$ $T = 5.19$ system at $t = 18 \cdot 10^6 dt$. Spheres are not shown for clarity. Green circles indicating opposite direction of $\hat{\mathbf{u}}_{\mathbf{imin}}$ vector

# 6.4  Conclusions

In this chapter, a novel disc-sphere interaction model has been developed based on a mixture of Gay-Berne and Lennard-Jones particles. This mixture involved the use of the Lennard-Jones potential for the spheres, the constant well-depth Gay- Berne potential for the disc particles and finally, a modified version of the Gay- Berne potential for the disc-sphere interaction. This disc-sphere potential has been adjusted in order to incorporate more complex amphiphilic behaviour into the system. In this, one segment of each disc's rim was strongly attracted to the solvent sphere, the other segment being only weakly attracted. The relative size of these segments can be easily tuned by varying single parameter $H$. This, then, provided the opportunity to study the self-assembly of particles with different solvophilic properties.

From the simulations presented in this chapter, it appears that the model was suitable for studying the effects of molecular interaction parameters on self-assembly processes. We identified a new self-assembly pathway, leading to the formation of complex structures from discotic monomers. It involved formation of an initial amorphous aggregate of nearly spherical shape and its rearrangement to an ordered structure, and finally its growth by monomeric addition.

The model proved to be capable of showing significant changes in behaviour due to variation of the $H$ parameter. Different types of structure were found, depending on the value of $H$ ('Toblerone', bilayer, cord, triple-helix). We also found that the parameter $H$ has an influence on the kinetics of self-assembly: initial nucleation and subsequent growth of the structure took longer time in systems with lower $H$. We assumed, that this can be explained by the fact that discs with smaller solvophilic region have a lower probability of joining a cluster, as there are fewer possible orientations to achieve an optimal disc-sphere interaction in this case.

# Chapter 7

# Self-assembly in constant NPT systems

In the previous chapter, we described the self-assembly of fibrillar structures by systems with a strongly solvophilic interaction at the rim of the disc-shaped particles. In these systems, we observed formation of assemblies which contained both discs and spheres. While it appears that the structural changes observed in these systems appropriately reflect the symmetry of the disc-sphere interactions used, the structures themselves demonstrate some unrealistic features. In particular, rather than the outer stacks of each structure having their solvophobic parts residing inside the structure (hiding from solvent) they are generally oriented towards the free solvent regions of the simulation box. Secondly, the solvent spheres incorporated into the structures are visually more densely packed than those in the remainder of simulation box. Thus, it could be argued that we observed self-assembly in the gas medium, rather than in solvent, due to the constant volume constrained used in Chapter 6. In order to explore these issues, we conducted an additional series of NPT simulations.

## 7.1    Single solvent system

To examine the capabilities of the tanh model in denser systems, a series of additional simulations was performed. Starting from high temperature $(T = 3.3)$ a small system comprising 1370 particles (70 discs and 1300 spheres) was cooled down in the NPT ensemble $(P = 20)$. Key model parameters were set as follows: $\epsilon_{DS} = 1$, $\epsilon_D = 1$, $\nu = 2$, $\mu = 1$, $a = 2.6$, $b = 2.4$, $l = 1/10$, $k' = 0.1$, $k'_{DS} = 0.2$.

Firstly, an $H = 80$ system was studied. Orientational order parameter measurements made on cooling this system (Fig.7.1, red line) suggested a transition from one state (isotropic mixture of discs and spheres) at high temperature $(T = 3.3)$ to an ordered arrangement at low temperature $(T = 0.8)$.
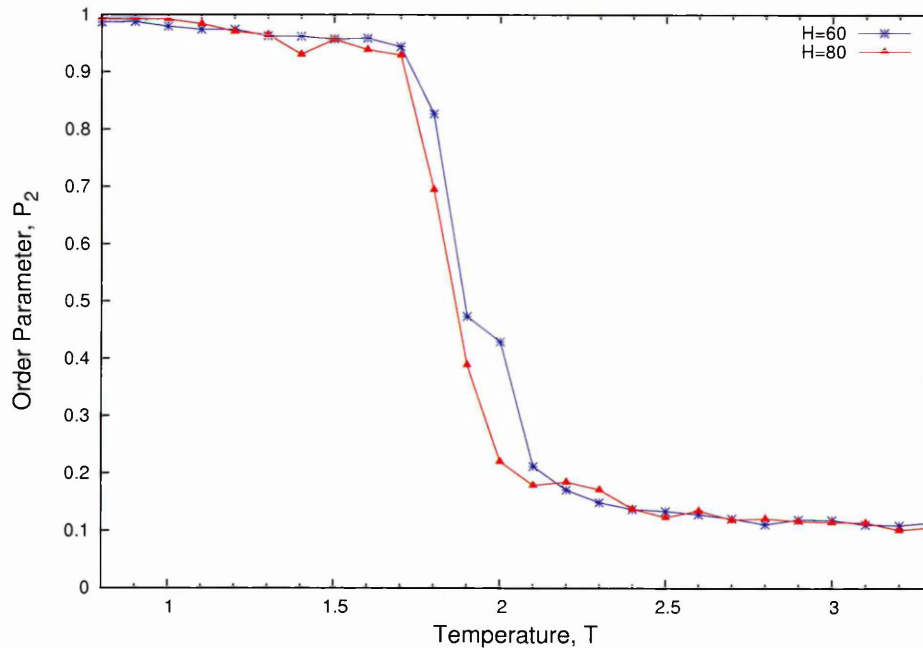


Figure 7.1: Order Parameter vs Temperature in $H = 80$ (red line) and $H = 60$ (blue line) in NPT simulations of disc-sphere systems involving 1370 particles (70 discs and 1300 spheres)

Snapshots from this system confirmed assembly of individual discs into an aggregate of string-like structures (Fig.7.2 a)). In this respect, system's behaviour was reminiscent of the late stage of self-assembly in $R = 1$ system, described in Chapter 5. As it is seen from the snapshot at $T = 1.7$, the hydrophobic regions were ran-

domly oriented at this stage. However, on further cooling, the interaction with the solvent spheres drove dissociation of the initial aggregate into dimeric ribbon structures at $T = 0.8$ (Fig.7.2 b)). In these, the hydrophobic regions were well hidden from the solvent. Thus, the aggregation observed here was very different from the 'toblerone' seen in the $H80K10$ NVT simulations. This can be understood from the inability of the NPT system to separate into rare and dense phases and, thus, the high solvent concentration 'boundary condition' imposed on the aggregates formed.

To test the capability of the model to show changes in system behaviour due to variation of the $H$ parameter in this ensemble, we also studied a system with $H = 60$. Orientational order parameter data (Fig.7.1, blue line) and snapshots (Fig.7.3 a)) again indicate a two-stage process. The first stage of this assembly was similar to that seen previously (aggregation of mutually aligned stacks with randomly oriented hydrophobic regions). However, a different type of aggregate developed in the second stage. Rather than forming ribbons from pairs of threads, the larger solvophobic region in this system enabled the development of a four-stacked fibre at $T = 0.8$ (Fig.7.3 b)). This fibre is strongly analogous to a conventional worm-like micelle in that the solvophobic disc regions are all oriented towards its core.

As in the NVT simulations presented in the previous chapter, we have confirmed that the parameter $H$ has a direct impact on the local packing and overall structure, in the NPT ensemble. Nevertheless, the pathway by which these structures form, and the structures themselves differ markedly from these identified in the previous chapter for identical model parameterisations.

The very strong ensemble-dependence observed here has a clearly identifiable origin; in our NVT-ensemble simulations of decorated-rim systems, phase separation into sub volumes with differing packing fraction was regularly observed. This mechanism is not accessible to constant NPT systems, however. We have already highlighted the importance of kinetic pathways to structure formation in the systems studied in this thesis, so this finding is not a great surprise. It does, though, have
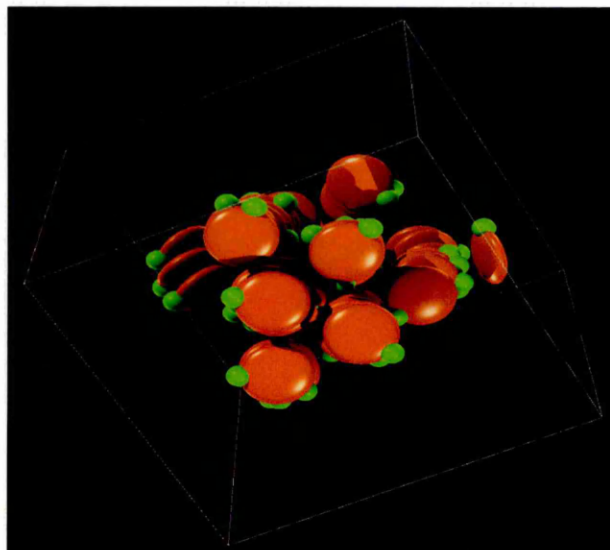
(a)
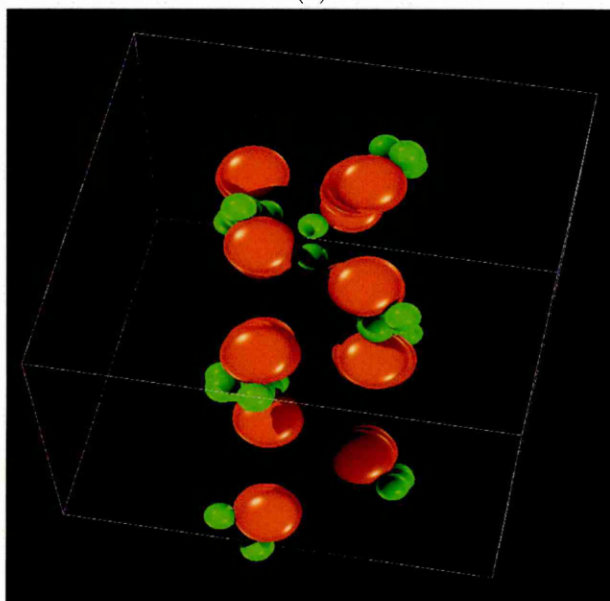


(b)

Figure 7.2: Snapshot from 1370 particles NPT simulations of $H = 80$ system at temperature $T = 1.7$ (a) and $T = 0.8$ (b) (solvent spheres are not shown).

implications for the applicability of the results of Chapter 6 to real-world behaviour, since the constant NPT ensemble is the closest to most fluid phase experiments.

In respect of this latter point, we note recent experimental studies on complex solvent-stabilised structures formed by drying systems [62]. These 'micropottery' systems, like our NVT simulations, involve rare-dense interfaces and rely on complex solvent-solute arrangements to stabilise their structures.
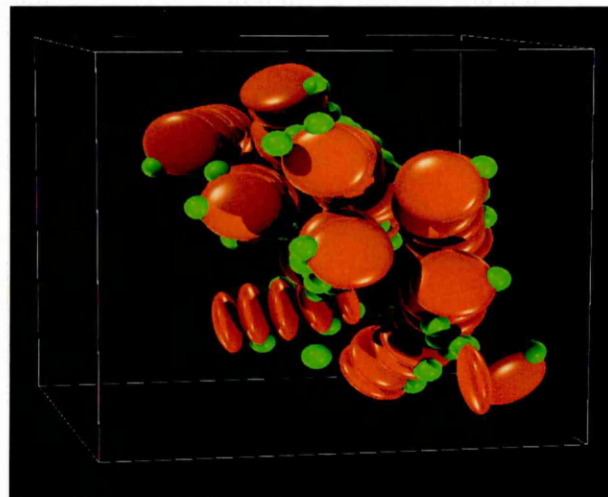
(a)
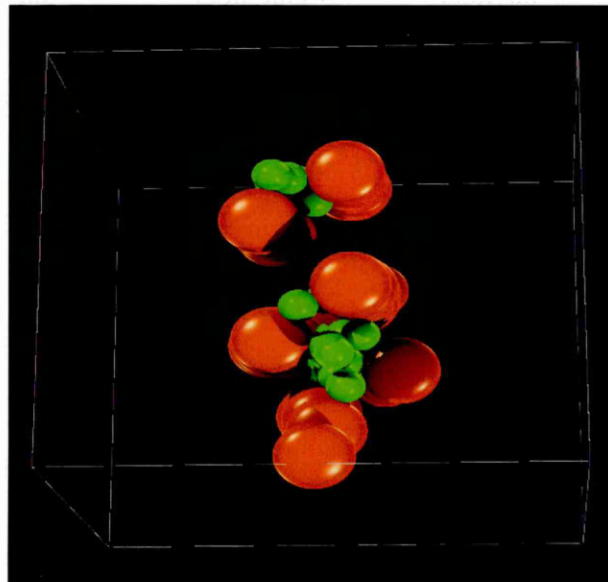


(b)

Figure 7.3: Snapshot from 1370 particles NPT simulations of $H = 60$ system at temperature $T = 1.7$ (a) and $T = 0.8$ (b). Centres of hydrophobic regions marked with green sphere. Solvent spheres are not shown.

Having made this qualitative justification for the strong ensemble-dependence of our systems, however, it is clearly pertinent to ask whether the family of solvent-containing structures found in the previous chapter has any more general relevance beyond the micropottery behaviour. To this end, we have performed a brief investigation of three component systems in which two species of spheres (one 'oil'-like and one 'water'-like) are combined with decorated discs in the NPT ensemble. This study makes up the remainder of this Chapter.

## 7.2  Self-assembly of decorated discs in a two-component solvent

In this section, we consider the behaviour of systems in which discs with tanh-function variation of their rim potentials are mixed with two dissimilar types of solvent particle. This is achieved by designating our original solvent as water and the new solvent as oil. The oil-water interaction being described via repulsive LJ potential ($r_{cut} = 2^{(1/6)}\sigma_{DS}$) also known as the WCA potential [63]. The symmetries of the two sets of disc-sphere interactions are then arranged such as that oil particles have a philic interaction in rim regions where water particles are phobic and vice versa.

In order to study self-assembly of structures in these systems, a series of simulations of systems with different $H$ values were performed. Simulations were carried in the NPT ensemble ($P = 20$) and subject to gradual temperature quenching. Key model parameters were set as follows: $N_{total} = 4000$, $N_{discs} = 200$, $N_{water} = 3040$, $N_{oil} = 760$, $\epsilon_{DS} = 1$, $\epsilon_D = 1$, $\nu = 2$, $\mu = 1$, $a = 2.6$, $b = 2.4$, $l = 1/10$, $k' = 0.1$, $k'_{DS} = 0.2$. The starting configuaration for each quench was a random mixture of water and oil spheres and discs at $T = 3.0$. $H$ values of 90, 80 and 60 were considered but, so as to keep this investigation at a tractable level, only one value of $N_{water}/N_{oil}$ was attempted.

As previously, all of these systems exhibited two stages of self-assembly. Like the single-solvent NPT systems, the first stage involved formation of stacks of discs from monomers. Interestingly, we again found that the $H$ parameter had an influence on strength of the self-assembly. Thus, as evidenced by the orientational order parameter data (Fig.7.4), the stack alignment occured at different temperatures in each of the systems (at $T = 2.3$ for $H = 60$, $T = 2.2$ for $H = 80$ and at $T = 1.9$ for $H = 90$). We found that the presence of oil spheres had additional impact on stack aggregation, as the formed structures differed from those observed

in the single-solvent NPT systems. Here, a bilayer-like structure was formed with $H = 60$ (Fig.7.5), a single aggregate with squared internal structure in the $H = 80$ system (Fig.7.6) (instead of dimeric ribbons in $H80$ NPT). Finally, an aggregate with triangular internal arrengement was observed in the $H = 90$ system (Fig.7.7). This structure is close to the 'toblerone' core seen for $H = 80$ in our NVT simulations.
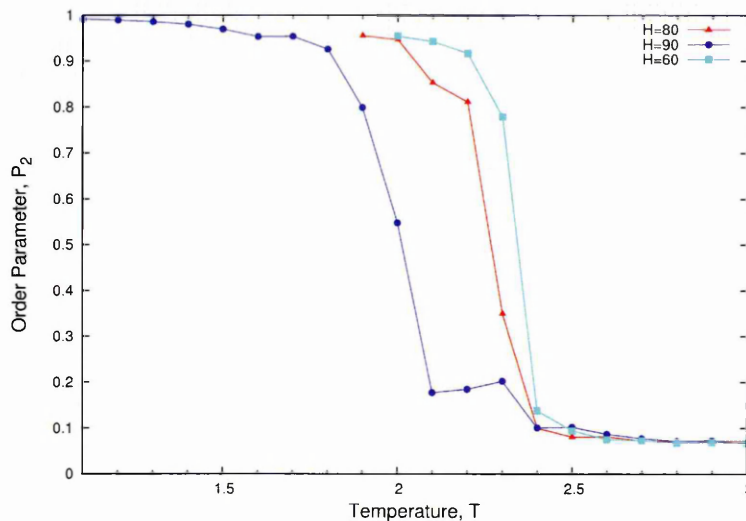


Figure 7.4: Order Parameter vs Temperature in $H = 60$ (light blue line), $H = 80$ (red line) and $H = 90$ (blue line) systems.
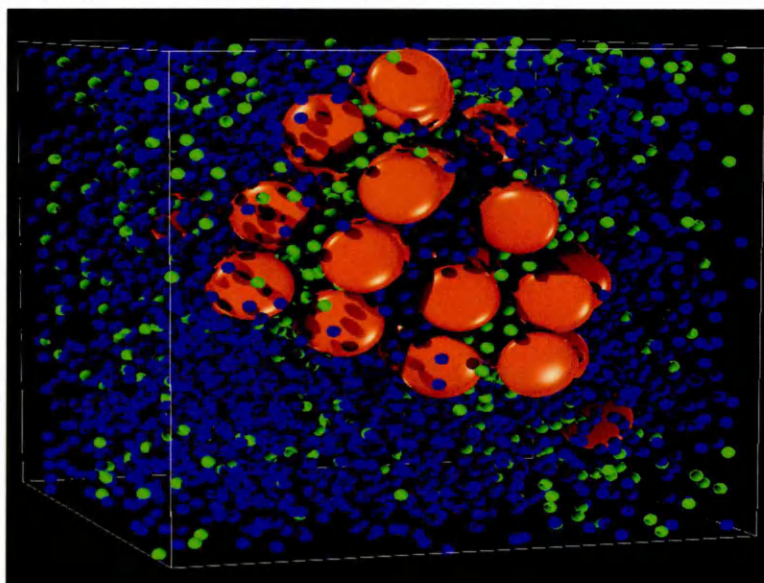


Figure 7.5: Final configuration after $t = 2.17 \cdot 10^6 dt$ timesteps in $O20W80H60$ system at $T = 2.0$. Water spheres (blue) and oil spheres (green) are made 50% smaller for clarity.
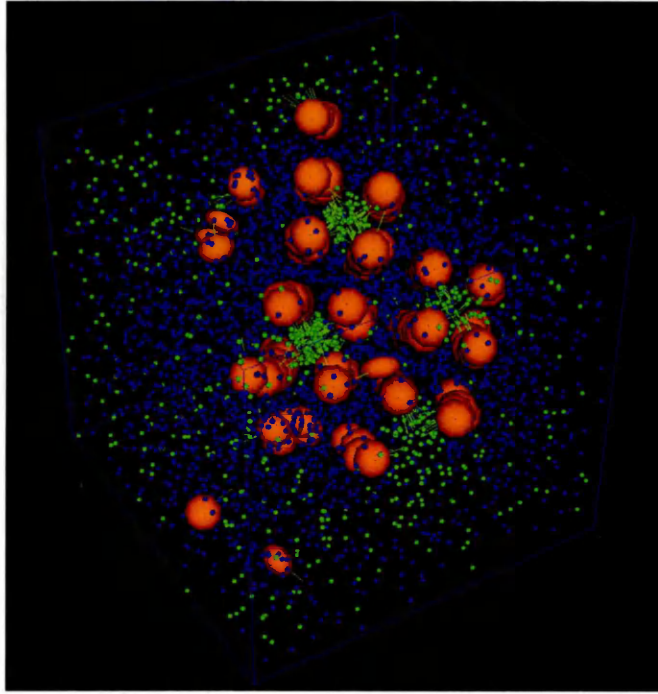
Figure 7.6: Final configuration after $t = 2.2 \cdot 10^6 dt$ timesteps in $O20W80H80$ system at $T = 1.9$. Water spheres (blue) and oil spheres (green) are made 70% smaller for clarity. Discs 30% smaller.
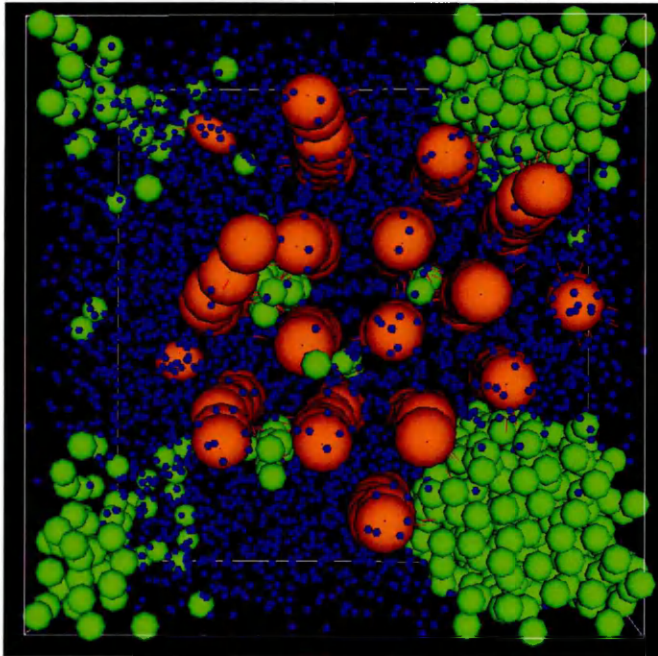


Figure 7.7: Final configuration after $t = 3.8 \cdot 10^6 dt$ timesteps in $O20W80H90$ system at $T = 1.1$. Water spheres (blue) are made 70% smaller for clarity, oil spheres are coloured green. Discs 30% smaller.

These results again confirm our finding that the parameter $H$ has a direct impact on the local packing within the overall structure. Essentially, introducing a mixed solvent provides a mechanism by which the systems can exhibit either full phase separation or microphase separated behaviour. This manifests itself differently for each $H$ value. For $H = 60$, the interlayer space is preferentially occupied by oil-spheres and the outer faces of the bilayer are hydrophilic. In $H = 80$, each square arrangement of columns is stabilised by a core of oil spheres and a water-rich matrix links the square fibres together. For $H = 90$, in comparison, the oil-rich cores of the triangular sub-fibres are relatively narrow, with a consequence that the remainder of the oil spheres phase-separate into a separate sub-volume.

The simulations presented in this section are not indeed to give a systematic and comprehensive understanding of decorated-disc aggregation in oil-water mixtures. Rather, they are intended to provide a comparison with the NVT and NPT disc plus single-solvent systems presented in the last two chapters. In respect of this, it is clear that the types of complex solvent-stabilised structures observed in NVT in Chapter 5, but absent from two-component NPT systems, can be regained by introducing a further solvent species. We conclude, therefore, that liquid-state experimental studies should be able to access such behaviour, provided that appropriate mixed-solvents are employed.

# Chapter 8

# Conclusions and Further Work

In this Chapter, the principal results of this Thesis are summarised and discussed, and suggestions for future work are made.

## 8.1 Conclusions

An understanding of fibre self-assembly phenomena is of considerable biomedical and technological importance. However, analysis of literature has shown that, to date, early-stage processes of fibre formation are poorly explored. On the one hand, key details of early self-assembly remain blocked to experimental observation, because of the inaccessibility of the required spatial and temporal resolution. On the other hand, detailed computer simulations of this problem are also beyond the capability of modern computers. In most of the presented full-atomistic simulations of molecular self-assembly, the number of molecules (building blocks) used is limited to a few dozens. This is inadequate for studies of processes occuring on larger length- and timescales. Thus, it is necessary to gain computational efficiency in order to access larger length and time scales in simulations. Application of coarse-graining approaches appears to be a viable and reasonably effective methodology to adopt to achieve this and so gain insights into the molecular basis of processes such as fibre

formation.

We implemented this approach in this thesis by representing each molecule with a single-site particle. Thus, a fibre-forming system was considered here as a mixture of oblate Gay-Berne ellipsoids in a solvent of Lennard-Jones spheres. Avoiding chemical specificity, the model focused on global properties and generic phenomena.

The results of the initial simulations (described in Chapter 4) indicated that this simple molecular model is able to qualitatively reproduce some essential behaviour of real systems (such as stacking, solvophilic/solvophobic effects). These properties are central to the processes of self-assembly and led to the formation of the different structures observed in these preliminary simulations. In particular, cooling initially isotropic mixtures led to the development of numerous linear stacks of discs, consistent with previous simulations of chromonic self assembly [15, 27, 26]. However, even more significantly, we identified that in certain conditions (deeper quenching of less solvated discs) self-assembly of multi-threaded fibre aggregates occurs.

Following from these initial results, Chapter 5 presents results from a series of constant NVT simulations of various disc-sphere systems, conducted in order to gain a deeper understanding of fibre-formation processes. From these, we found that fibre self-assembly is a complex, multistage process, which is based around an evolving hierarchy of intermediate steps and competing growth mechanisms. Defect-free fibre growth involves the following stages: 1) chromonic self-assembly of monomeric discs; 2) formation of a flexible bundle from formed stacks; 3) locking-in of the spontaneous bundle chirality (left-handed, right-handed, straight) 4) lateral growth of the fibre by the docking of new stacks and longitudinal growth by addition of the monomers. We found that the relative rates of these aggregation processes could be varied by changing the strength of the interparticle interaction parameter $k$. Thus, defect-free fibres with a range of different length/breadth ratios was achievable, provided that temperature was controlled so as to limit each system to a single nucleation event. The resultant pitch of the twisted fibre proved independent of $k$ but could

be adjusted by using particles with different shape. Finally, we studied possible mechanisms, which might limit lateral fibre growth. For chiral fibres, it has been argued that fibre radii should be self-limiting due to the strains experienced by the increasingly helical outer strands [55]. However, most of our simulations showed that this effect appears to be insuficient to render the outer threads unstable. Instead, we found that chiral fibres can exhibit a straightening transition, provided a) they contain sufficient threads and b) they form at a sufficiently high temperature. We concluded, then, that the existence of this transition is associated with the structure being able to cross the temperature-normalised free energy barrier between the two possible fibre states (twisted and straight).

In Chapter 6, we introduced a modified disc-sphere potential, comprising a sharp switch between solvophobic and solvophilic rim regions, and used it to study the consequent range of structures accessible. In this model, one segment of each disc's rim was strongly attracted to the solvent spheres, the other segment being only weakly attracted. The relative size of these segments could be easily tuned by varying the single parameter $H$. In constant NVT simulations we identified a new self-assembly pathway for this system, leading to the formation of complex solvent-containing structures from discotic monomers. This involved formation of an initial amorphous aggregate of nearly spherical shape, its rearrangement to an ordered structure and, finally, its growth by monomeric addition. This model proved capable of showing changes in system behaviour in response to variation of the $H$ parameter. An increase of the hydrophilic region size resulted in an increase in the number of solvent spheres packed around hydrophilic group. As a consequence of this change, different structure shapes were observed ('Toblerone', bilayer-sheet, cord, triple-helix). We also found that the parameter $H$ had an influence on the kinetics of self-assembly: initial nucleation and subsequent growth of the structure took longer in systems with lower $H$.

Finally, in Chapter 7, we described results of two additional series of NPT sim-

ulations, conducted in order to address some unrealistic features of the structures, obtained in Chapter 6. In particular, the outer stacks of each structure in the NVT simulations had their solvophobic sites oriented towards the free solvent region of the simulation box. On moving to the NPT ensemble, a different range of structures was found, due to the inability of the system to separate into rare and dense phases. We again confirmed that the parameter $H$ has a direct impact on the local packing within the overall structures. Here, self-assembly firstly involved formation of stacks of discs (instead of formation of a droplet). These stacks subsequently aggregated into different ordered structures, depending on the size of hydrophobic region. While NPT simulations of systems involving a single-solvent species only yielded rather simple aggregates, it was found that a rich variety of complex solvent-stabilised aggregates, similar to those seen in our NVT simulations, could be achieved if a two-component 'oil and water' solvent was employed.

## 8.2   Further Work

Despite its relative simplicity, the model developed here has produced encouraging results and has opened up several possible directions for further research:

- While some progress has been made in studying the effects which limit lateral growth of fibres, it would be of considerable interest to investigate this in more detail.

- Study of the straight-to-twisted transition in defect-free fibres

- Study of self-assembly of particles with a distribution of shapes (i.e. with slightly different aspect ratios), in order to make closer approximation to possible real nanoparticle systems

- Study of growing fibres using an ensemble in which free monomers are constantly injected into the system

- Improvement of the fibre growth-modes analysis algorithm

The modified versions of the model, which were introduced in Chapter 6 and 7, have also shown interesting behaviour. In terms of future work, it would be desirable to:

- Conduct comprehensive studies of NVT and NPT systems of larger size, as they have been the subject of only a partial investigation here

- Investigate a wider range of relative concentrations in the mixed solvent systems

- Develop and study a model with several solvophobic/solvophilic regions

- Alternatively, develop and study the behaviour of a two-site model, in which the aromatic group of a peptide is represented by a disc and the tail part with a rod

The initial aim of the study was to try to "gain insight into the underlying basis of fibre self-assembly". Given what we have learned, we now know that this is a rather imprecise aim, since we have found a number of fibre-types (as well as some other aggregates) and, importantly, shown that their formation mechanisms vary considerably. Indeed, self-assembly kinetics appear to be directly related to structure in many of the systems considered here. This goes some why to explaining the sensitivity of experimental fibre-forming systems to processing conditions.

By performing a detailed kinetic analysis of the initial system presented in Chapter 5, we have gained a precise understanding of the combination of inter-linked processes involved in a single hierarchical self-assembly process. It is to be hoped that this will be taken up by experimentalists as it could be directly applicable to suitably tuned colloidal or nanoparticle systems. More generally, we have shown that generic simulation is capable of identifying mechanisms and bottle-necks in

multi-stage self-assembly processes and, thus, giving understanding of relevance to experimentally inaccessible situations.

# Appendix A

# Derivation of Forces and Torques

## A.1 Calculation of forces for Lennard-Jones particles

In the case of two spherical particles $i$ and $j$ interacting via the Lennard-Jones potential the force is calculated as:

$$\mathbf{f}_{ij} = -\frac{dU_{LJ}(r_{ij})}{dr_{ij}} \frac{\mathbf{r}_{ij}}{r_{ij}} = \frac{24\epsilon}{r_{ij}} \left[ 2 \left( \frac{\sigma}{r_{ij}} \right)^{12} - \left( \frac{\sigma}{r_{ij}} \right)^{6} \right] \hat{\mathbf{r}}_{ij} \tag{A.1}$$

where $r_{ij}$ is the separation between the two particles $i$ and $j$.

If a cutoff scheme at a distance $r_c$ is applied to the system, the potential becomes

$$U_{SS}(r_{ij}) = \begin{cases} U_{LJ}(r_{ij}) - U_{LJ}(r_c) & (r_{ij} \leq r_c) \\ 0 & (r_{ij} > r_c) \end{cases} \tag{A.2}$$

The net force $\mathbf{F}_i$ on particle $i$ is then given by a simple vectorial sum over pairwise forces between $i$ and its neighbouring particles specified by the cutoff spherical range.

$$\mathbf{F}_i = \sum_j \mathbf{f}_{ij} = -\sum_j \nabla_{\mathbf{r}_{ij}} U_{SS}(r_{ij}) \tag{A.3}$$

## A.2 Calculation of forces and torques for discotic Gay-Berne particles

### A.2.1 Derivation of the forces and torques

Consider two discotic Gay-Berne particles $i$ and $j$ with centre of mass position vectors $\mathbf{r}_i$ and $\mathbf{r}_j$, respectively. The distance between the two particles is defined by the intermolecular vector $\mathbf{r}_{ij} = \mathbf{r}_j - \mathbf{r}_i$. The orientation of the particles is described by two unit vectors $\hat{\mathbf{u}}_i$ and $\hat{\mathbf{u}}_j$, parallel to the symmetry axes of the molecules.

As for the case of the Lennard-Jones fluid, a truncated and shifted form of $U_{ij}$, $U_{RR}$ is considered when applying a cutoff scheme. In the conventional approach to the calculation of forces and torques, the orientation dependance of $U_{RR}(\hat{\mathbf{r}}_{ij}, \hat{\mathbf{u}}_i, \hat{\mathbf{u}}_j)$ can be written in terms of scalar products of unit vectors $\hat{\mathbf{r}}_{ij}$, $\hat{\mathbf{u}}_i$ and $\hat{\mathbf{u}}_j$:

$$U_{RR}(r,a,b,c) = 4\epsilon(r,a,b,c)\left[\left(\frac{\sigma_f}{r-\sigma(r,a,b,c)+\sigma_f}\right)^{12} - \left(\frac{\sigma_f}{r-\sigma(r,a,b,c)+\sigma_f}\right)^{6}\right] - $$
$$4\epsilon(r,a,b,c)\left[\left(\frac{\sigma_f}{r_c-\sigma(r,a,b,c)+\sigma_f}\right)^{12} - \left(\frac{\sigma_f}{r_c-\sigma(r,a,b,c)+\sigma_f}\right)^{6}\right].$$

with $r = \hat{\mathbf{r}}_{ij} \cdot \mathbf{r}_{ij}$, $a = \hat{\mathbf{u}}_i \cdot \mathbf{r}_{ij}$, $b = \hat{\mathbf{u}}_j \cdot \mathbf{r}_{ij}$ and $c = \hat{\mathbf{u}}_i \cdot \hat{\mathbf{u}}_j$.

Note that the energy and shape parameters $\epsilon$ and $\sigma$ remain functions of $r$ and not $r_c$ being dependant upon scalar products of the form $\mathbf{r}_{ij} \cdot \hat{\mathbf{u}}_i$.

Considering this formulation of the potential, the force calculation is straightforward and, according to Newton's third law on the action-reaction principle, can be written as:

$$\mathbf{f}_i = -\mathbf{f}_j = \mathbf{f}_{ij} = -\nabla_{\mathbf{r}_{ij}}U_{RR} = -\left(\frac{\partial U_{RR}}{\partial r_{ij}^x}, \frac{\partial U_{RR}}{\partial r_{ij}^y}, \frac{\partial U_{RR}}{\partial r_{ij}^z}\right) \tag{A.4}$$

In order to express $\mathbf{f}_{ij}$ as a function of unit vectors $\hat{\mathbf{r}}_{ij}$, $\hat{\mathbf{u}}_i$ and $\hat{\mathbf{u}}_j$, the chain rule can be applied such that

$$\mathbf{f}_{ij} = -\sum_s \frac{\partial U_{RR}}{\partial(\mathbf{s} \cdot \mathbf{r}_{ij})} \nabla_{\mathbf{r}_{ij}}(\mathbf{s} \cdot \mathbf{r}_{ij}) \qquad (A.5)$$

where the sum over $\mathbf{s}$ represents the sum over all the scalar products of unit vectors involving $\mathbf{r}_{ij}$, namely $a$, $b$ and $r$.

Furthermore, it can found that,

$$\nabla_{\mathbf{r}_{ij}}(\mathbf{s} \cdot \mathbf{r}_{ij}) = \left(\frac{\partial r_{ij}^x s^x}{\partial r_{ij}^x}, \frac{\partial r_{ij}^y s^y}{\partial r_{ij}^y}, \frac{\partial r_{ij}^z s^z}{\partial r_{ij}^z}\right) = (s^x, s^y, s^z) = \mathbf{s} \qquad (A.6)$$

Therefore, Eqn. A.5 becomes:

$$\mathbf{f}_{ij} = -\frac{\partial U_{RR}}{\partial r}\hat{\mathbf{r}}_{ij} - \frac{\partial U_{RR}}{\partial a}\hat{\mathbf{u}}_i - \frac{\partial U_{RR}}{\partial b}\hat{\mathbf{u}}_j \qquad (A.7)$$

For the rotational motion, in the case of the discotic Gay-Berne potential, the particle is axially symmetric and the torque acting on particle $i$ can be expressed as:

$$\tau_i = \sum_j \tau_{ij} = \hat{\mathbf{u}}_i \times \mathbf{g}_i = \hat{\mathbf{u}}_i \times \sum_j \mathbf{g}_{ij} \qquad (A.8)$$

$$\mathbf{g}_{ij} = -\nabla_{\hat{\mathbf{u}}_i} U_{RR} \qquad (A.9)$$

Here, $\mathbf{g}_i$ is defined as the gorque and is the derivatives of the potential $U_{RR}$ with respect to the orientational vector $\hat{\mathbf{u}}_i$. This is the rotational equivalent to the translational force $\mathbf{F}_i$ defined as the derivative of $U_{RR}$ with respect to $\mathbf{r}_i$.

As for the translational motion, the chain rule can be used to expand the expressions for the gorques such as:

$$\mathbf{g}_{ij} = -\nabla_{\hat{\mathbf{u}}_i} U_{RR} = -\sum_s \frac{\partial U_{RR}}{\partial(\mathbf{s} \cdot \hat{\mathbf{u}}_i)}(\mathbf{s} \cdot \hat{\mathbf{u}}_i) \qquad (A.10)$$

$$\mathbf{g}_{ij} = -\frac{\partial U_{RR}}{\partial a}\mathbf{r}_{ij} - \frac{\partial U_{RR}}{\partial c}\hat{\mathbf{u}}_j \qquad (A.11)$$

## A.2.2 Explicit analytical forms of all necessary derivatives

Using the standard definition of the discotic Gay-Berne potential, the partial derivatives $\frac{\partial U_{RR}}{\partial r}$, $\frac{\partial U_{RR}}{\partial a}$, $\frac{\partial U_{RR}}{\partial b}$ and $\frac{\partial U_{RR}}{\partial c}$ are given below.

$$\begin{aligned}
\frac{\partial U_{RR}}{\partial r} &= 4\epsilon \left[ \frac{\mu\chi'}{\epsilon_2 r^3} \left( \frac{(a+b)^2}{1+\chi'c} + \frac{(a-b)^2}{1-\chi'c} \right)(A - A_c) - \frac{B}{\sigma_f} \right. \\
&\left. - \frac{\sigma^3\chi}{2\sigma_f\sigma_0^2 r^3} \left( \frac{(a+b)^2}{1+\chi c} + \frac{(a-b)^2}{1-\chi c} \right)(B - B_c) \right]
\end{aligned} \qquad (A.12)$$

$$\begin{aligned}
\frac{\partial U_{RR}}{\partial a} &= 4\epsilon \left[ -\frac{\mu\chi'}{\epsilon_2 r^2} \left( \frac{a+b}{1+\chi'c} + \frac{a-b}{1-\chi'c} \right)(A - A_c) \right. \\
&\left. + \frac{\sigma^3\chi}{2\sigma_f\sigma_0^2 r^2} \left( \frac{a+b}{1+\chi c} + \frac{a-b}{1-\chi c} \right)(B - B_c) \right]
\end{aligned} \qquad (A.13)$$

$$\begin{aligned}
\frac{\partial U_{RR}}{\partial b} &= 4\epsilon \left[ -\frac{\mu\chi'}{\epsilon_2 r^2} \left( \frac{a+b}{1+\chi'c} - \frac{a-b}{1-\chi'c} \right)(A - A_c) \right. \\
&\left. + \frac{\sigma^3\chi}{2\sigma_f\sigma_0^2 r^2} \left( \frac{a+b}{1+\chi c} - \frac{a-b}{1-\chi c} \right)(B - B_c) \right]
\end{aligned} \qquad (A.14)$$

$$\begin{aligned}
\frac{\partial U_{RR}}{\partial c} &= 4\epsilon \left[ (A - A_c) \left( \nu\epsilon_1^2\chi^2 c + \frac{\mu\chi'^2}{2\epsilon_2 r^2} \left( \left(\frac{a+b}{1+\chi'c}\right)^2 - \left(\frac{a-b}{1-\chi'c}\right)^2 \right) \right) \right. \\
&\left. - (B - B_c)\frac{\sigma^3\chi^2}{4\sigma_f\sigma_0^2 r^2} \left( \left(\frac{a+b}{1+\chi c}\right)^2 - \left(\frac{a-b}{1-\chi c}\right)^2 \right) \right]
\end{aligned} \qquad (A.15)$$

where $A$, $A_c$, $B$, $B_c$ are defined as:

$$
\begin{aligned}
A &= \left(\frac{\sigma_f}{r - \sigma(r,a,b,c) + \sigma_f}\right)^{12} - \left(\frac{\sigma_f}{r - \sigma(r,a,b,c) + \sigma_f}\right)^{6} \\
A_c &= \left(\frac{\sigma_f}{r_c - \sigma(r,a,b,c) + \sigma_f}\right)^{12} - \left(\frac{\sigma_f}{r_c - \sigma(r,a,b,c) + \sigma_f}\right)^{6} \\
B &= 12\left(\frac{\sigma_f}{r - \sigma(r,a,b,c) + \sigma_f}\right)^{13} - 6\left(\frac{\sigma_f}{r - \sigma(r,a,b,c) + \sigma_f}\right)^{7} \\
B_c &= 12\left(\frac{\sigma_f}{r_c - \sigma(r,a,b,c) + \sigma_f}\right)^{13} - 6\left(\frac{\sigma_f}{r_c - \sigma(r,a,b,c) + \sigma_f}\right)^{7}
\end{aligned}
$$

## A.3 Calculation of forces and torques for the disc-sphere interaction

### A.3.1 Original model

The explicit forms of the force and torque exerted on a discotic Gay-Berne particle $i$ by a Lennard-Jones particle $j$ are evaluated by applying Eqn. A.5 to the following disc-sphere potential

$$
U_{RS}(r,a) = 4\epsilon(r,a)\left[R\left(\frac{\sigma_f}{r - \sigma(r,a) + \sigma_f}\right)^{12} - \left(\frac{\sigma_f}{r - \sigma(r,a) + \sigma_f}\right)^{6}\right] -
$$
$$
4\epsilon(r,a)\left[R\left(\frac{\sigma_f}{r_c - \sigma(r,a) + \sigma_f}\right)^{12} - \left(\frac{\sigma_f}{r_c - \sigma(r,a) + \sigma_f}\right)^{6}\right]. \quad \text{(A.16)}
$$

For this interaction, we have

$$
\mathbf{f}_{ij} = -\frac{\partial U_{RS}}{\partial r}\hat{\mathbf{r}}_{ij} - \frac{\partial U_{RS}}{\partial a}\hat{\mathbf{u}}_i. \quad \text{(A.17)}
$$

While the torque acting upon the disc is given by

$$\tau_{ij} = -\hat{\mathbf{u}}_i \times \frac{\partial U_{RS}}{\partial a} \mathbf{r}_{ij} \tag{A.18}$$

Using the same methodology as previously, one can find:

$$\frac{\partial U_{RS}}{\partial r} = 4\epsilon \left[ \frac{2\mu\chi''a^2}{(1 - \chi''\frac{a^2}{r^2})r^3}(A - A_c) - \frac{\sigma^3\chi a^2}{\sigma_f\sigma_{DS}^2 r^3}(B - B_c) - \frac{B}{\sigma_f} \right] \tag{A.19}$$

$$\frac{\partial U_{RS}}{\partial a} = 4\epsilon \left[ \frac{2\mu\chi''a}{(1 - \chi''\frac{a^2}{r^2})r^2}(A_c - A) + \frac{\sigma^3\chi a}{\sigma_f\sigma_{DS}^2 r^2}(B - B_c) \right] \tag{A.20}$$

where $A$, $A_c$, $B$, $B_c$ are defined as:

$$A = R\left( \frac{\sigma_f}{r - \sigma(r, a) + \sigma_f} \right)^{12} - \left( \frac{\sigma_f}{r - \sigma(r, a) + \sigma_f} \right)^{6}$$

$$A_c = R\left( \frac{\sigma_f}{r_c - \sigma(r, a) + \sigma_f} \right)^{12} - \left( \frac{\sigma_f}{r_c - \sigma(r, a) + \sigma_f} \right)^{6}$$

$$B = 12R\left( \frac{\sigma_f}{r - \sigma(r, a) + \sigma_f} \right)^{13} - 6\left( \frac{\sigma_f}{r - \sigma(r, a) + \sigma_f} \right)^{7}$$

$$B_c = 12R\left( \frac{\sigma_f}{r_c - \sigma(r, a) + \sigma_f} \right)^{13} - 6\left( \frac{\sigma_f}{r_c - \sigma(r, a) + \sigma_f} \right)^{7}$$

## A.3.2 Tanh model

In this model disc-sphere potential has the following form:

$$U_{RS}(r, a, d) = 4\epsilon(r, a)\epsilon_{tanh}(r, d) \left[ \left( \frac{\sigma_f}{r - \sigma(r, a) + \sigma_f} \right)^{12} - \left( \frac{\sigma_f}{r - \sigma(r, a) + \sigma_f} \right)^{6} \right] -$$
$$4\epsilon(r, a)\epsilon_{tanh}(r, d) \left[ \left( \frac{\sigma_f}{r_c - \sigma(r, a) + \sigma_f} \right)^{12} - \left( \frac{\sigma_f}{r_c - \sigma(r, a) + \sigma_f} \right)^{6} \right] \tag{A.21}$$

Accordinig to the (A.5) and (A.8):

$$\mathbf{f}_{ij} = -\frac{\partial U_{RS}}{\partial r} \hat{\mathbf{r}}_{ij} - \frac{\partial U_{RS}}{\partial a} \hat{\mathbf{u}}_i - \frac{\partial U_{RS}}{\partial d} \hat{\mathbf{u}}_{imin}, \tag{A.22}$$

$$\tau_{ij} = -\hat{\mathbf{u}}_i \times \frac{\partial U_{RS}}{\partial a} \mathbf{r}_{ij} - \hat{\mathbf{u}}_{imin} \times \frac{\partial U_{RS}}{\partial d} \mathbf{r}_{ij}. \tag{A.23}$$

The derivatives for the tanh model are defined by:

$$\frac{\partial U_{RS}}{\partial r} = 4\epsilon \cdot \epsilon_{tanh} \left[ \frac{2\mu\chi''a^2}{(1 - \chi''\frac{a^2}{r^2})r^3}(A - A_c) - \frac{\sigma^3\chi a^2}{\sigma_f\sigma_{DS}^2 r^3}(B - B_c) - \frac{B}{\sigma_f} \right] -$$
$$4\epsilon (A - A_c) \left[ \frac{b_t}{rl} \left( 1 - tanh^2 \left( \frac{d - S}{l} \right) \right) \right] d \tag{A.24}$$

$$\frac{\partial U_{RS}}{\partial a} = 4\epsilon \cdot \epsilon_{tanh} \left[ \frac{2\mu\chi''a}{(1 - \chi''\frac{a^2}{r^2})r^2}(A_c - A) + \frac{\sigma^3\chi a}{\sigma_f\sigma_{DS}^2 r^2}(B - B_c) \right] \tag{A.25}$$

$$\frac{\partial U_{RS}}{\partial d} = 4\epsilon \left[ \frac{b_t}{rl} \left( 1 - tanh^2 \left( \frac{d - S}{l} \right) \right) \right] (A - A_c) \tag{A.26}$$

where $a$, $A$, $A_c$, $B$, $B_c$ are defined as in the original model and $d = \hat{\mathbf{r}}_{ij} \cdot \hat{\mathbf{u}}_{imin}$.

# Appendix B

# Video files

In support of the text description of simulations provided in Chapter 5, here we additionally provide video animations for some of them (see DVD in envelope at last page).

File **k10T1815Timeline.mpg**:

Animation of the $k = 0.1$ $T = 1.82$ system (Section 1, Chapter 5), produced from snapshots made every 500 timesteps. Here, threads of length 4 and longer are shown only. Spheres are not shown for clarity. Note the key stages of defect-free fibre self-assembly (timesteps given approximately):

1) chromonic self-assembly of monomeric discs from $t = 17500dt$;

2) formation of a flexible bundle from formed stacks at $t = 1180000dt$;

3) locking of the spontaneous bundle chirality to the right-handed at $t = 1700000dt$

File **k10T1815CTimeline.mpg**:

As before, with the difference that the simulation box is centered on the centre-of-mass of the largest aggregate. This causes some 'jumps' in the early stages, but gives a better view of the late stages.

Largest cluster is centered.

File **k10T1815ColourTimeline.mpg**:

The same as in the first file, but with application of a colour scheme, in which each disc is coloured accord to the role it plays in the fibre formation process. Discs which join the fibre as a pre-existing stable stack are colored green; particles which did not join as stacks but which will continue to reside in their current thread - red; other peripheral particles which will be shed to solution or other threads - white; stacks having no relation to the final configuration - blue.

File **k10T190Timeline.mpg**:

Animation of $k = 0.10$ $T = 1.90$ system. Note mini-bundle formation at $t = 4820000dt$ and its subsequent disaggregation into separate threads at $t = 4920000dt$.

File **k075BigStr.mpg**:

Animation of straightening fibre in $k = 0.075$ $T = 2.3$ system (Section 6, Chapter 5) from $t = 9800000dt$ to $t = 9900000dt$. Snapshots were produced at each 5000 timesteps.

# Bibliography

[1] Rein V. Ulijn, Nurguse Bibi, Vineetha Jayawarna, Paul D. Thornton, Simon J. Todd, Robert J. Mart, Andrew M. Smith, and Julie E. Gough. Bioresponsive hydrogels. *Materials Today*, 10(4):40–48, 4 2007.

[2] Yong Qiu and Kinam Park. Environment-sensitive hydrogels for drug delivery. *Advanced Drug Delivery Reviews*, 53(3):321–339, 12/31 2001.

[3] Giorgio Colombo, Patricia Soto, and Ehud Gazit. Peptide self-assembly at the nanoscale: a challenging target for computational and experimental biotechnology. *Trends in biotechnology*, 25(5):211–218, MAY 2007 2007. PT: J; TC: 36; UT: WOS:000246428500006.

[4] Meital Reches and Ehud Gazit. Casting metal nanowires within discrete self-assembled peptide nanotubes. *Science*, 300(5619):625–627, April 25 2003.

[5] Meital Reches and Ehud Gazit. Formation of closed-cage nanostructures by self-assembly of aromatic dipeptides. *Nano Letters*, 4(4):581–585, 04/01 2004. doi: 10.1021/nl035159z.

[6] A. Mahler, M. Reches, M. Rechter, S. Cohen, and E. Gazit. Rigid, self-assembled hydrogel composed of a modified aromatic dipeptide. *Advanced Materials*, 18(11):1365–1370, JUN 6 2006. PT: J; UT: ISI:000238203300004.

[7] V. Jayawarna, M. Ali, T. A. Jowitt, A. E. Miller, A. Saiani, J. E. Gough, and R. V. Ulijn. Nanostructured hydrogels for three-dimensional cell culture

through self-assembly of fluorenylmethoxycarbonyl-dipeptides. *Advanced Materials*, 18(5):611–614, MAR 3 2006. PT: J; UT: ISI:000236379200014.

[8] Z. M. Yang, K. M. Xu, L. Wang, H. W. Gu, H. Wei, M. J. Zhang, and B. Xu. Self-assembly of small molecules affords multifunctional supramolecular hydrogels for topically treating simulated uranium wounds. *Chemical Communications*, (35):4414–4416, 2005. PT: J; UT: ISI:000231555800007.

[9] Andrew M. Smith, Richard J. Williams, Claire Tang, Paolo Coppo, Richard F. Collins, Michael L. Turner, Alberto Saiani, and Rein V. Ulijn. Fmoc-diphenylalanine self assembles to a hydrogel via a novel architecture based on pi-pi interlocked beta-sheets. *Advanced Materials*, 20(1):37–41, JAN 7 2008. PT: J; UT: ISI:000252866800004.

[10] T. Kowalewski and D. M. Holtzman. In situ atomic force microscopy study of alzheimer's beta-amyloid peptide on different substrates: New insights into mechanism of beta-sheet formation. *Proceedings of the National Academy of Sciences of the United States of America*, 96(7):3688–3693, MAR 30 1999 1999. PT: J; CT: National-Academy-of-Sciences Colloquium on Geology, Mineralogy, and Human Welfare; CY: NOV 08-09, 1998; CL: ARNOLD MABEL BECKMAN CTR, IRVINE, CALIFORNIA; SP: Natl Acad Sci; TC: 194; UT: WOS:000079507900063.

[11] H. A. Lashuel, D. Hartley, B. M. Petre, T. Walz, and P. T. Lansbury. Neurodegenerative disease - amyloid pores from pathogenic mutations. *Nature*, 418(6895):291–291, JUL 18 2002 2002. PT: J; TC: 487; UT: WOS:000176868000031.

[12] H. A. Lashuel, S. R. LaBrenz, L. Woo, L. C. Serpell, and J. W. Kelly. Protofilaments, filaments, ribbons, and fibrils from peptidomimetic self-assembly: Implications for amyloid fibril formation and materials science. *Journal of the*

*American Chemical Society*, 122(22):5262–5277, JUN 7 2000 2000. PT: J; TC: 159; UT: WOS:000087540500005.

[13] D. M. Marini, W. Hwang, D. A. Lauffenburger, S. G. Zhang, and R. D. Kamm. Left-handed helical ribbon intermediates in the self-assembly of a beta-sheet peptide. *Nano Letters*, 2(4):295–299, APR 2002 2002. PT: J; TC: 127; UT: WOS:000175041800008.

[14] Elizabeth H. C. Bromley, Kevin J. Channon, Patrick J. S. King, Zahra N. Mahmoud, Eleanor F. Banwell, Michael F. Butler, Matthew P. Crump, Timothy R. Dafforn, Matthew R. Hicks, Jonathan D. Hirst, Alison Rodger, and Derek N. Woolfson. Assembly pathway of a designed alpha-helical protein fiber. *Biophysical journal*, 98(8):1668–1676, APR 21 2010 2010. PT: J; TC: 7; UT: WOS:000276939800035.

[15] Fatima Chami and Mark R. Wilson. Molecular order in a chromonic liquid crystal: A molecular simulation study of the anionic azo dye sunset yellow. *Journal of the American Chemical Society*, 132(22):7794–7802, JUN 9 2010. PT: J; NR: 58; TC: 7; J9: J AM CHEM SOC; PG: 9; GA: 611RA; UT: ISI:000278837100039.

[16] S. Tsonchev, A. Troisi, G. C. Schatz, and M. A. Ratner. All-atom numerical studies of self-assembly of zwitterionic peptide amphiphiles. *Journal of Physical Chemistry B*, 108(39):15278–15284, SEP 30 2004 2004. PT: J; TC: 20; UT: WOS:000224070200069.

[17] W. M. Hwang, D. M. Marini, R. D. Kamm, and S. Q. Zhang. Supramolecular structure of helical ribbons self-assembled from a beta-sheet peptide. *Journal of Chemical Physics*, 118(1):389–397, JAN 1 2003 2003. PT: J; TC: 45; UT: WOS:000179879500046.

[18] One-Sun Lee, Samuel I. Stupp, and George C. Schatz. Atomistic molecular dynamics simulations of peptide amphiphile self-assembly into cylindrical nanofibers. *Journal of the American Chemical Society*, 133(10):3677–3683, MAR 16 2011 2011. PT: J; TC: 0; UT: WOS:000288410100068.

[19] S. J. Marrink, A. H. de Vries, and A. E. Mark. Coarse grained model for semi-quantitative lipid simulations. *Journal of Physical Chemistry B*, 108(2):750–760, JAN 15 2004. PT: J; UT: ISI:000187951700035.

[20] Hung D. Nguyen and Carol K. Hall. Molecular dynamics simulations of spontaneous fibril formation by random-coil peptides. *Proceedings of the National Academy of Sciences of the United States of America*, 101(46):16180–16185, November 16 2004.

[21] A. V. Smith and C. K. Hall. alpha-helix formation: Discontinuous molecular dynamics on an intermediate-resolution protein model. *Proteins-Structure Function and Genetics*, 44(3):344–360, AUG 15 2001. PT: J; UT: ISI:000170121500019.

[22] Giovanni Bellesia and Joan-Emma Shea. Self-assembly of beta-sheet forming peptides into chiral fibrillar aggregates. *Journal of Chemical Physics*, 126(24):245104-1–245104-11, JUN 28 2007. PT: J; UT: ISI:000247625800068.

[23] Alessandra Villa, Christine Peter, and Nico F. A. van der Vegt. Self-assembling dipeptides: conformational sampling in solvent-free coarse-grained simulation. *Physical Chemistry Chemical Physics*, 11(12):2077–2086, 2009. PT: J; UT: ISI:000264097700021.

[24] Alessandra Villa, Nico F. A. van der Vegt, and Christine Peter. Self-assembling dipeptides: including solvent degrees of freedom in a coarse-grained model. *Physical Chemistry Chemical Physics*, 11(12):2068–2076, 2009. PT: J; UT: ISI:000264097700020.

[25] Z. L. Zhang, M. A. Horsch, M. H. Lamm, and S. C. Glotzer. Tethered nano building blocks: Toward a conceptual framework for nanoparticle self-assembly. *Nano Letters*, 3(10):1341–1346, OCT 2003 2003. PT: J; TC: 121; UT: WOS:000185863500005.

[26] PK Maiti, Y. Lansac, MA Glaser, and NA Clark. Isodesmic self-assembly in lyotropic chromonic systems rid b-6335-2009. *Liquid Crystals*, 29(5):619–626, MAY 2002. PT: J; NR: 22; TC: 19; J9: LIQ CRYST; PG: 8; GA: 552AA; UT: WOS:000175595100001.

[27] RG EDWARDS, JR HENDERSON, and RL PINNING. Simulation of self-assembly and lyotropic liquid-crystal phases in model discotic solutions. *Molecular Physics*, 86(4):567–598, NOV 1995. PT: J; NR: 20; TC: 13; J9: MOL PHYS; PG: 32; GA: TF209; UT: WOS:A1995TF20900004.

[28] T. P. Stedall, M. F. Butler, D. N. Woolfson, and S. Hanna. Computer simulations of the growth of synthetic peptide fibres. *European Physical Journal E*, 34(1):5, JAN 2011. PT: J; NR: 37; TC: 0; J9: EUR PHYS J E; PG: 16; GA: 737DJ; UT: WOS:000288548600008.

[29] B. A. H. m. Huisman, P. G. Bolhuis, and A. Fasolino. Phase transition to bundles of flexible supramolecular polymers rid c-7222-2011. *Physical Review Letters*, 100(18):188301, MAY 9 2008. PT: J; NR: 14; TC: 17; J9: PHYS REV LETT; PG: 4; GA: 299QZ; UT: WOS:000255771400070.

[30] Qian Chen, Jonathan K. Whitmer, Shan Jiang, Sung Chul Bae, Erik Luijten, and Steve Granick. Supracolloidal reaction kinetics of janus spheres. *Science*, 331(6014):199–202, JAN 14 2011 2011. PT: J; TC: 9; UT: WOS:000286433100038.

[31] Zhan-Wei Li, Zhao-Yan Sun, and Zhong-Yuan Lu. Simulation model for hierarchical self-assembly of soft disklike particles. *Journal of Physical Chemistry*

*B*, 114(7):2353–2358, FEB 25 2010. PT: J; NR: 42; TC: 1; J9: J PHYS CHEM
B; PG: 6; GA: 556GP; UT: WOS:000274578500003.

[32] M.P. Allen and D.J. Tildesley. *Computer simulation of liquids.* Oxford University Press, 1987.

[33] W. C. Swope, H. C. Andersen, P. H. Berens, and K. R. Wilson. A computer-simulation method for the calculation of equilibrium-constants for the formation of physical clusters of molecules - application to small water clusters. *Journal of Chemical Physics*, 76(1):637–649, 1982 1982. PT: J; TC: 1069; UT: WOS:A1982MW46500084.

[34] N. S. Martys and R. D. Mountain. Velocity verlet algorithm for dissipative-particle-dynamics-based models of suspensions. *Physical Review E*, 59(3):3733–3736, MAR 1999. PT: J; PN: Part B; UT: ISI:000079233500083.

[35] J. G. Gay and B. J. Berne. Modification of the overlap potential to mimic a linear site-site potential. *Journal of Chemical Physics*, 74(6):3316–3319, 1981. PT: J; UT: ISI:A1981LJ34700029.

[36] C. Zannoni. Molecular design and computer simulations of novel mesophases rid e-3129-2010. *Journal of Materials Chemistry*, 11(11):2637–2646, 2001. PT: J; CT: Molecular Topology in Liquid Crystals, Materials Chemistry Discussion No 4; CY: SEP 11-14, 2001; CL: GRASMERE, ENGLAND; NR: 111; TC: 83; J9: J MATER CHEM; PG: 10; GA: 484YU; UT: WOS:000171721100002.

[37] M. R. Wilson. Progress in computer simulations of liquid crystals. *International Reviews in Physical Chemistry*, 24(3-4):421–455, DEC 21 2005 2005. PT: J; TC: 65; UT: WOS:000234420800002.

[38] CM Care and DJ Cleaver. Computer simulation of liquid crystals. *Reports on Progress in Physics*, 68(11):2665–2700, NOV 2005. PT: J; NR: 257; TC: 77; J9: REP PROG PHYS; PG: 36; GA: 989TU; UT: WOS:000233697600004.

[39] H. Zewdie. Computer simulation studies of liquid crystals: A new cor-
     ner potential for cylindrically symmetric particles. *Journal of Chemi-
     cal Physics*, 108(5):2117–2133, FEB 1 1998 1998. PT: J; TC: 18; UT:
     WOS:000071748000044.

[40] H. Zewdie. Computer-simulation studies of diskotic liquid crystals. *Physical
     Review E*, 57(2):1793–1805, FEB 1998. PT: J; NR: 34; TC: 38; J9: PHYS REV
     E; PN: Part a; PG: 13; GA: YY127; UT: WOS:000072116000078.

[41] F. Barmes, M. Ricci, C. Zannoni, and D. J. Cleaver. Computer simulations of
     hard pear-shaped particles. *Physical Review E*, 68(2):021708, AUG 2003 2003.
     PT: J; PN: Part 1; TC: 8; UT: WOS:000185193900057.

[42] G. R. Luckhurst, R. A. Stephens, and R. W. Phippen. Computer-simulation
     studies of anisotropic systems .19. mesophases formed by the gay-berne model
     mesogen. *Liquid Crystals*, 8(4):451–464, OCT 1990 1990. PT: J; TC: 185; UT:
     WOS:A1990EC32300001.

[43] G. R. Luckhurst and P. S. J. Simmonds. Computer-simulation studies of
     anisotropic systems .21. parametrization of the gay-berne potential for model
     mesogens. *Molecular Physics*, 80(2):233–252, OCT 10 1993 1993. PT: J; TC:
     92; UT: WOS:A1993MB07100002.

[44] D. J. Cleaver, C. M. Care, M. P. Allen, and M. P. Neal. Extension and gen-
     eralization of the gay-berne potential. *Physical Review E*, 54(1):559–567, JUL
     1996. PT: J; UT: ISI:A1996UY73400070.

[45] BJ BERNE and P. PECHUKAS. Gaussian model potentials for molecular-
     interactions. *Journal of Chemical Physics*, 56(8):4213–, 1972. PT: J; NR: 5; TC:
     362; J9: J CHEM PHYS; PG: 0; GA: M2680; UT: WOS:A1972M268000067.

[46] Dmytro Antypov. Computer simulation of rod-sphere mixtures, 2003.

[47] D. Antypov and D. J. Cleaver. The effect of spherical additives on a liquid crystal colloid. *Journal of Physics-Condensed Matter*, 16(19):S1887–S1900, MAY 19 2004 2004. PT: J; SI: SI; CT: Workshop on Liquid Crystal Colloid Dispersions; CY: AUG, 2003; CL: Bled, SLOVENIA; SP: ESF PESC Exploratory; TC: 9; UT: WOS:000221833600003.

[48] M. A. Bates and G. R. Luckhurst. Computer simulation studies of anisotropic systems .26. monte carlo investigations of a gay-berne discotic at constant pressure. *Journal of Chemical Physics*, 104(17):6696–6709, MAY 1 1996. PT: J; UT: ISI:A1996UG68000031.

[49] David Michel. Computer simulation of self-assembling amphiphilic systems, 2006.

[50] E. Diaz-Herrera, J. Alejandre, G. Ramirez-Santiago, and F. Forstmann. Interfacial tension behavior of binary and ternary mixtures of partially miscible lennard-jones fluids: A molecular dynamics simulation. *Journal of Chemical Physics*, 110(16):8084–8089, APR 22 1999. PT: J; UT: WOS:000079739600049.

[51] W. SCOTT, F. MULLERPLATHE, and WF VANGUNSTEREN. Molecular-dynamics study of the mixing and demixing of a binary lennard-jones fluid rid a-1922-2010. *Molecular Physics*, 82(5):1049–1062, AUG 10 1994. PT: J; UT: WOS:A1994PC69700014.

[52] Dwaipayan Chakrabarti, Szilard N. Fejer, and David J. Wales. Rational design of helical architectures rid f-1977-2011. *Proceedings of the National Academy of Sciences of the United States of America*, 106(48):20164–20167, DEC 1 2009. PT: J; UT: WOS:000272254400009.

[53] ML Henle and PA Pincus. Equilibrium bundle size of rodlike polyelectrolytes with counterion-induced attractive interactions. *Physical Review E,*

71(6):060801, JUN 2005. PT: J; NR: 33; TC: 37; J9: PHYS REV E; PN: Part 1; PG: 4; GA: 942HW; UT: WOS:000230274500006.

[54] BY Ha and AJ Liu. Kinetics of bundle growth in dna condensation. *Europhysics Letters*, 46(5):624–630, JUN 1 1999. PT: J; NR: 28; TC: 55; J9: EUROPHYS LETT; PG: 7; GA: 202LH; UT: WOS:000080653400012.

[55] Gregory M. Grason and Robijn F. Bruinsma. Chirality and equilibrium biopolymer bundles. *Physical Review Letters*, 99(9):098101, AUG 31 2007. PT: J; UT: WOS:000249155500046.

[56] T. Schilling and D. Frenkel. Self-poisoning of crystal nuclei in hard-rod liquids rid a-4950-2009. *Physical Review Letters*, 92(8):085505, FEB 27 2004. PT: J; UT: WOS:000189266100030.

[57] Robert L. Jack, Michael F. Hagan, and David Chandler. Fluctuation-dissipation ratios in the dynamics of self-assembly. *Physical Review E*, 76(2):021119, AUG 2007. PT: J; PN: Part 1; UT: WOS:000249154600024.

[58] Sui Yang, Lingzhi Zhao, Chengzhong Yu, Xufeng Zhou, Jiawei Tang, Pei Yuan, Daoyong Chen, and Dongyuan Zhao. On the origin of helical mesostructures rid e-5796-2010. *Journal of the American Chemical Society*, 128(32):10460–10466, AUG 16 2006. PT: J; UT: WOS:000239618700029.

[59] JL Atwood, LJ Barbour, and A. Jerga. Organization of the interior of molecular capsules by hydrogen bonding. *Proceedings of the National Academy of Sciences of the United States of America*, 99(8):4837–4841, APR 16 2002. PT: J; UT: WOS:000175087000020.

[60] A. Shivanyuk, JC Friese, S. Doring, and J. Rebek. Solvent-stabilized molecular capsules. *Journal of Organic Chemistry*, 68(17):6489–6496, AUG 22 2003. PT: J; UT: WOS:000184833500003.

[61] H. Mansikkamaki, M. Nissinen, CA Schalley, and K. Rissanen. Self-assembling resorcinarene capsules: solid and gas phase studies on encapsulation of small alkyl ammonium cations rid b-5688-2008. *New Journal of Chemistry*, 27(1):88–97, 2003. PT: J; UT: WOS:000180272200016.

[62] JS Raut, P. Bhattad, AC Kulkarni, and VM Naik. "micro-pottery"-marangoni effect driven assembly of amphiphilic fibers. *Langmuir*, 21(2):516–519, JAN 18 2005. PT: J; UT: WOS:000226343100005.

[63] JD WEEKS, D. CHANDLER, and HC ANDERSEN. Role of repulsive forces in determining equilibrium structure of simple liquids. *Journal of Chemical Physics*, 54(12):5237–+, 1971. PT: J; UT: WOS:A1971J630300035.